CRANFIELD UNIVERSITY

THEODOROS TRIANTAFYLLOU

THE EFFECT OF INLET FLOW DISTORTION ON INSTALLED GAS TURBINE PERFORMANCE

School of Aerospace, Transport and Manufacturing
Propulsion Engineering Centre

PhD Thesis
Academic Year: 2017 – 2018

Supervisors: Prof. Dr P. Pilidis, Dr T. Nikolaidis
March 2018

CRANFIELD UNIVERSITY

School of Aerospace, Transport and Manufacturing
Propulsion Engineering Centre

PhD Thesis

Academic Year 2017 - 2018

THEODOROS TRIANTAFYLLOU

THE EFFECT OF INLET FLOW DISTORTION ON INSTALLED GAS TURBINE PERFORMANCE

Supervisors: Prof. Dr P. Pilidis, Dr T. Nikolaidis
March 2018

It is the journey that counts .....

K. Kavafis

ABSTRACT

Military aircraft are often subjected to severe flight manoeuvres with high Angles of Attack (AOA) and Angles of Sideslip (AOSS). These flight attitudes induce non-uniform in flow conditions to their installed gas turbine engines which may include distortion of inlet total pressure and total temperature at the Aerodynamic Interface Plane (AIP).

When the downstream compression system of the engine experiences such distorted inflow conditions its operation is significantly affected in that its aerodynamic performance is reduced along with its stall margin. Also the blade stress levels of the compression system increase and vibration becomes an issue. A large, complex facility is required to accurately test how the actual engines response to such distorted conditions. In addition to the engine support facilities, a full-scale inlet is needed to house the engine and a large secondary air supply system is needed to generate flight speed and altitude conditions relative to the inlet. As it can be easily imagined, the cost of this type of full scale testing is remarkably high.

The objective of the present study is to develop a numerical method for the estimation of the installed gas turbine engine performance variations due to airflow distortion. This method will also provide the means to assess the compatibility of an airframe-engine set at a specific operating envelope, given the geometry of the upstream intake and the performance simulation model of the under examination gas turbine engine.

In the present work, the distorted conditions at the interface between the intake and the engine have been numerically calculated with Computational Fluid Dynamics (CFD), where 27 different aircraft flight attitudes have been tested. As a baseline set of airframe-engine, were chosen an airframe inspired by the General Dynamics/LMAERO F-16 aircraft, equipped with a Pratt and Whitney F100-PW-229-like gas turbine engine. Also, the specified flow field was resolved by a commercial CFD code.

The steady state total pressure distortion induced to the AIP due to the aircraft's flight attitude was estimated in terms of distortion descriptors. These

parameters were then correlated to the surge margin of the downstream compression system. Following this methodology, it was concluded whether each one of the tested flight attitudes induced enough distortion to the AIP so as to surge the engine's FAN. Also the engine's performance variations due to airflow distortion have been also estimated in terms of net thrust changes.

The obtained results justify the anticipated behaviour of the engine with degraded performance, in terms of resulted net thrust, when the aircraft flies with Angle of Sideslip (AOSS). Having the FAN shaft rotational speed as the controlled parameter, the net thrust percentage change between the uninstalled condition of the engine with rather uniform inflow and that when the engine is installed and exposed to different flight attitudes varies between -1.76% to -22.56% depending on the flight Mach number and the aircraft's flight attitude. Finally, all the results were combined and performance maps have been created that correlate the aircraft's flight attitude with the engine's net thrust.

KEYWORDS

Airflow Distortion, Total Pressure Distortion, Aircraft Intake, Intake Pressure Recovery, Distortion Descriptors, Gas Turbine Performance, Surge Margin, Fan Stability

PUBLICATIONS

1. Triantafyllou T, Nikolaidis T, Diakostefanis M & Pilidis P, (2015), Total Pressure Distortion Levels at the Aerodynamic Interface Plane of a Military Aircraft, *The Aeronautical Journal, -New Series-*, *Vol 119, Issue 1219, pp1147-1166.*

2. T Triantafyllou, T Nikolaidis, M Diakostefanis and P Pilidis. (2016) Numerical simulation of the airflow over a military aircraft with active intake. *Proceedings of the Institution of Mechanical Engineers, Part G: Journal of Aerospace Engineering, 2016, Vol 231, Issue 8, pp1369-1390.*

3. Triantafyllou T, Nikolaidis T and Diakostefanis M, (2017) Effect of inlet flow distortion on installed gas turbine performance. In: *ISABE 2017 conference paper*, ISABE, Paper ID 21336, 2017.

4. T. Triantafyllou, T. Nikolaidis, M. Diakostefanis, P. Pilidis, (2017) Stability Assessment of an Airflow Distorted Military Engine's FAN, *Proceedings of the Institution of Mechanical Engineers, Part G: Journal of Aerospace Engineering, SAGE Publications, June 2017.*

ACKNOWLEDGEMENTS

Finally this resourch journey has reached its destination! When I started working on this project, reaching the finish line seemed quite distant to my mind. The only thing I used to vision was the accomplishment of the next target set. Following that step by step process this research work has come to its conclusion.

The completion of this work has been a significant milestone in my entire life. Therefore, I would like to acknowledge the help of all the people who have contributed to the successful conclusion of this research work.

I would like to express my special appreciation and thanks to my supervisors Professor Dr. Periclis Pilidis and Dr. Theoklis Nikolaidis. I would like to thank them for encouraging my research and for being always there when I needed them. Their advice on my research efforts has been priceless.

A special thanks to my beloved wife Stella for standing by me and for providing me the ''space'' I needed to complete this study. Also I would like to apologize to my little angels Christina and Giorgo for not spending all of my free time with them due to my engagement to this research work. I promise I will try to make up for lost time.

Last but not least, I would like to dedicate this work to the memory of my father Giorgo and to my mother Christina who made me who I am...

TABLE OF CONTENTS

LIST OF FIGURES

LIST OF TABLES

NOMENCLATURE

Symbols

A [m^2]	Area
M [-]	Mach number
N [rpm]	Rotational Speed
P [Pa]	Total Pressure
p [Pa]	Static Pressure
R [J/(mol·K)]	Gas Constant
T [K]	Total Temperature
t [K]	Static Temperature
W [Kg/s]	Mass Flow Rate
Z [-]	Surge Margin Parameter

Greek Symbols

Δ [-]	Difference and Loss
θ [˚]	Circumferential Angle

Abbreviations

AIP	Aerodynamic Interface Plane
AOA	Angle of Attack
AOSS	Angle of Side Slip
CC	Combustion Chamber
CFD	Computational Fluid Dynamics
CM	Corrected Mass Flow
CR	Contraction Ratio
DNS	Direct Numerical Simulation
DP	Design Point
FPR	Fan Pressure Ratio
HCF	High Cycle Fatigue
HPC	High Pressure Compressor

HPT	High Pressure Turbine
LES	Large Eddies Simulation
LPDE	Linear Partial Differential Equations
LPT	Low Pressure Turbine
MPR	Multiple Per Revolution
NDMF	Non Dimensional Mass Flow
OD	Off Design
OEM	Original Equipment Manufacturer
OPR	Overall Pressure Ratio
PAV	Ring Average Total Pressure
PAVLOW	Average Total Pressure of the Low Pressure Region
PFAV	Face Average Total Pressure
PCN	Relative Rotational Speed
PDE	Partial Differential Equations
PRDS	Distorted Surge Pressure Ratio
PRF	Pressure Recovery Factor
PRS	Surge Pressure Ratio
PR	Pressure Ratio
PW	Pratt & Whitney
RANS	Reynolds Averaged Navier-Stokes
RSM	Reynolds Stresses Model
SFC	Specific Fuel Consumption
SLS	Sea Level Static
SM	Surge Margin
TET	Turbine Entry Temperature
T/O	Take off
VTOL	Vertical Take-off and Landing

Subscripts

c	Circumferential

h	Hub
L	Low Pressure Shaft
r	Radial
t	Tip
dist	Distorted

1 INTRODUCTION

1.1 Background

The integration of a gas turbine engine into an airframe is a challenging engineering task during which the designers need to take into consideration many different aspects.

Civil aircraft manufacturers are undertaking great efforts to reduce the aircraft drag and thereby to realize lower fuel consumption. In order to reach this objective, industry and research establishments are investigating extensively those zones of an aircraft where different components are joined together. One such zone is formed by the components of wing/pylon/nacelle/engine.

In military applications the highly integrated propulsion systems serve the requirements for high maneuverability and flights in the supersonic regime. Along with that is the desire for reduced engine signature which will provide acceptable survivability to the whole aircraft design when it operates in a hostile environment.

The knowledge about the related aerodynamic phenomena and their control is continuously updated and the "optimum" integration of these components can contribute to a very large extent to the success of an aircraft [1]. And this success when achieved is mainly attributed to the air-intake system which acts as the link between the airframe and the engine. It is this subsystem of the propulsion system that conditions the airflow before it reaches the Aerodynamic Interface Plane (AIP) as it is called the boundary surface between the end of the intake and the engine front face.

The airflow that reaches the compression system of an engine which is highly embedded into the airframe structure, especially in military applications, is by no means totally uniform. The flight conditions in conjunction with the lengthy and curved, in some cases, intake system create different non uniformities which are covered under the term air flow distortion.

As it will be discussed later on in further detail (chapter 6), this airflow distortion has a great impact on the stability of the compression system and depending on its severity it may cause the depletion of the FAN surge margin.

Another side effect of the distorted flow which is the subject of the present work is the change in the engine's performance. The non uniform distribution of the total pressure on the AIP creates differences in the output of the engine when compared with the respective one calculated based on a uniform total pressure at the compressor inlet.

1.2 Project Objectives

An installed gas turbine engine eventually operates under various inflow conditions which cause total pressure nonuniformities at the AIP. These distorted conditions cause the thermodynamic parameters of the flow to alter throughout the gas path and subsequently the performance of the engine will adapt to these conditions accordingly.

The main objective of the present work was the establishment of a methodology which, when followed, would provide the means to assess the installed gas turbine engine performance variations, due to airflow distortion, given its upstream intake geometry and the operating flight conditions.

This objective was achieved through the accomplishment of the following three subtasks, namely;

- The selection of specific aircraft flight conditions (altitude, speed, attitude). These flight conditions were chosen to be studied having as a basic criteria to be representative of the flight envelope of the under examination airframe-engine system and also to be manageable by the research tools that was planned to be used. To be more specific, the selected flight attitudes were rather modest as far as the selected Angles of Attack (AOA) and Angles of Sideslip (AOSS) are concerned so that they can be captured by steady state CFD simulations. These flight conditions were then tied together with their resulted non uniform flow characteristics at the AIP which was an indication of the level of distortion that the engine experiences.
- The investigation of the effect of that flow distortion on the downstream compression system. At this stage the total pressure distortion was quantified in terms of distortion descriptors. These distortion descriptors were then correlated to the loss in surge pressure ratio due to the distorted conditions. In that

way it was examined how this distorted flow affect the characteristics of the low compression system which is the first engine's component that experiences the disturbed flow conditions.

- The estimation of the engine's performance variations due to this aforementioned distortion. At this final stage it was calculated how the engine's performance realized these non-uniformities that are present at the AIP in terms of resulted net thrust. These flow non uniformities were translated into intake pressure recovery and mass flow rate variations and they were finally introduced into the engine's performance simulation model to facilitate the net thrust calculations at the respective flight conditions.

1.3 Originality

The present study provides a holistic methodology for the evaluation of the total pressure distortion effect on the performance of an installed gas turbine engine.

A geometry model has been created exclusively for the purpose of the current research work, representing a military aircraft with an intake that provides the airflow with the oportunity to travel all the way up to the engine's face. This geometry model has been exposed, in CFD, to different incoming flow conditions representing thus different flight conditions of the aircraft. Different flight attitudes were considered by changing accordingly the direction of the incoming flow in the computational domain.

The integration between the airframe and the engine has been implied through the definition of the intake's exit as a pressure outlet boundary in the CFD case. The coupling between the airframe and the engine in CFD has been achieved by setting the static pressure at this point in such a way as to cause the same amount of mass flow to enter the intake as what is demanded by the operating at these conditions power plant.

In the post processing of this CFD case, patterns of distortion at the engine's face has been obtained. Based on the CFD results, the fan stability was assessed

following the guidelines of SAE ARP 1420 [20] and AIR 1419 [10]. Along with that, the engine's performance in terms of resulted net thrust was estimated in Turbomatch (gas turbine performance simulation software).

When everything is considered, this methodology enhances the existing engine-inlet compatibility analysis and design methodology (ARP-1420) through the use of modeling and simulation.

1.4 Research Approach

In the context of the present research work the following engineering tools have been used:

- First, the baseline engine was modeled and its performance was predicted at the desired operating conditions using the TURBOMATCH scheme [70],[71]. This is a Cranfield University gas turbine engine simulation software, which was developed by Palmer [2]. It facilitates design point and off-design performance calculations for aero (civil and military) and industrial engines.
- Then, some of the TURBOMATCH results were used as initial boundary conditions for a higher fidelity simulation tool. At this stage the highly 3-D texture of the flow field at the AIP which is representative of the total pressure distortion, was captured using CFD. In CFD, the set of basic equations that govern fluid flow were discretized and solved numerically within a finite computational domain. FLUENT [32], a commercial CFD solver based on finite volume methodology (FVM) was used throughout the present study and the turbulence model selected was the k-ε realizable.
- The geometry and mesh depicting the airframe and the surrounding domain was created in ANSYS ICEM CFD [45], a software that is widely used in engineering applications.
- At the next stage, the distortion profiles were quantified with the use of different descriptors. Distortion intensity, multiple per revolution and extent are the most characteristic ones. These descriptors were then correlated to the loss in surge pressure ratio for the engine's FAN and in that way the distortion effect was communicated to the running characteristics of the downstream FAN component.

- Finally, the performance characteristics of the engine based on the altered, due to distortion, flow parameters were calculated using again the TURBOMATCH scheme.

The entire research approach in a work flow chart format is presented in fig. 1-1 below.

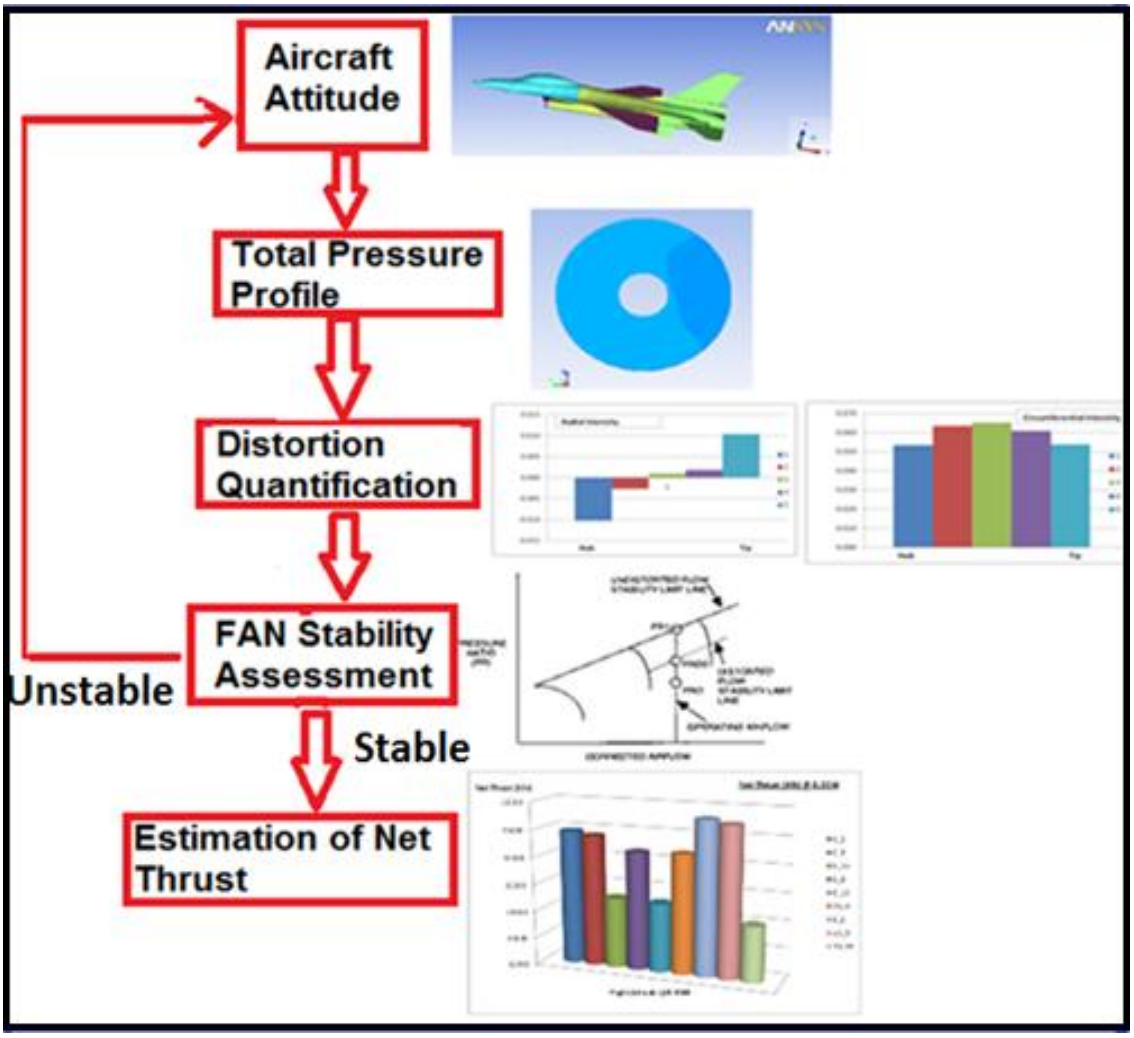

Figure 1-1 Research Aproach in a Work Flow Chart

1.5 Thesis Outline

The present work comprises an effort to estimate the effect of inlet airflow distortion on the installed gas turbine engine's performance. In chapter 2, the airflow distortion terms utilized throughout the research work are analyzed. Gas turbine performance simulation methods of different fidelity are quoted in this

chapter and Turbomatch is briefly presented as one of the basic tools utilized herein. Another important engineering tool described in this chapter is Computational Fluid Dynamics (CFD). CFD represents a method to numerically analyse flow fields which has been used successfully for a wide range of applications. At the end of this chapter a review of prior investigations covering similar aspects of the same research area with the current project, is also cited.

Chapter 3 provides background and includes fundamentals of CFD as well as the relevant CFD modeling considerations for the application scenarios investigated in this study. The pre-processing steps of the CFD cases pertinent to the present study are described along with the settings selected in their solving procedure. The baseline airframe geometry is introduced and the way has been followed in the creation of the intake geometry, embedded in the airframe, is also described. The aircraft's geometry presenting a full scale military aircraft is exposed to different incoming flows in the computational domain, simulating thus different aircraft flight attitudes.

The flow results from the numerical solution of the computational flow domain are presented in chapter 4. The presented flow results refer to both the domain around the aircraft model and the flow field within the intake which comprises the area of interest for the present study. The tested conditions that are covered herein refer to 27 different aircraft flight scenarios:

- Three different flight Mach numbers -0.35M, 0.6M and 0.85M- at 20000ft altitude.
- Nine combinations of Angles of Attack (AOA) and Angles of Sideslip (AOSS) at each one of the above tested flight Mach numbers (AOA and AOSS varied in the range of 0 to 16 degrees).

These specific conditions were selected among the entire flight envelope of this aircraft because they comprise a rather mild sample of its operating conditions, suitable for the testing of a newly developed model like the one described herein.

The obtained results are focused on the distribution of the total pressure at the Aerodynamic Interface Plane (AIP), which is the analytical boundary between the airframe and the power plant. These results are in the form of total pressure contours.

These colorful images representing the airflow distortion levels at the AIP are translated into numbers in chapter 5. The total pressure profiles are quantified in terms of distortion descriptors, following the guidelines of SAE AIR 1419 [10] and SAE ARP 1420 [20]. Also in this chapter it is presented how the distortion descriptors vary with the aircraft's flight attitude.

In chapter 6 the distortion descriptors related to each tested flight attitude are correlated to the loss in surge pressure ratio of the engine's fan component. Through that correlation an estimation of its surge margin depletion due to the distorted condition that experiences is accomplished. In that way it is clarified whether any of the tested flight attitudes causes the operating point on the fan map to move outside its stability area.

Next, in chapter 7 the engine's performance in terms of resulted net thrust is assessed fulfilling in that way the main objective of the present study. This performance assessment was accomplished with the aid of Turbomatch scheme. In this chapter performance maps are also created which tie together the aircraft's flight attitude with the resulted net thrust.

Finally all the conclusions along with recommendations for future work are presented in chapter 8.

2 LITERATURE REVIEW

The scope of this work is to study the effect of total pressure distortion on installed gas turbine performance. For the purpose of this study, as a baseline airframe configuration has been chosen a military aircraft inspired by the General Dynamics/LMAERO F-16 aircraft which is assumed to be equipped with a F100-PW-229-equivalent gas turbine engine. This specific airframe has been exposed in a CFD environment to different directions of incoming flow resembling thus different aircraft flight attitudes. The numerically predicted results has been focused on the distribution of the total pressure at the engine's face

2.1 Gas Turbine Engine Performance Modeling and Simulation

Modeling and simulation applications are of great importance throughout the whole gas turbine engine lifespan. The nature of the models may differ at each life-cycle phase, to reflect the respective specific needs. The propulsion system lifecycle can be subdivided into the following phases [4]:

- Preliminary design;
- Design and verification;
- Development and validation;
- Post certification and in-service support.

During the first of the above mentioned phases, the cost of research, development and implementation of new technology on gas turbine engines is extremely high. One of the main reasons behind this high development cost is the need to perform extensive hardware tests, scaled or not. Preliminary design and development costs could potentially be reduced by replacing some of the large-scale tests with numerically calculated simulation tools.

So, a more wide use of higher fidelity simulation tools, would certainly reduce the costs directly associated with testing, and would also enable the effects of design changes to be studied in detail, before a commitment to a final design is made. In other words, by simulating gas turbine systems, in sufficient detail early in the design

process, covering steady state and transient behavior, critical design and cost issues can be identified and resolved in time, before hardware is built.

Engine performance simulation is extensively used not only during the development process of a new gas turbine engine but throughout its life span as well. It can be used by the engine designers in multiple tasks some of which are quoted below.

- To estimate the design point performance of the engine and to see if the target requirements are met;
- To explore the off-design performance and to define the critical areas in the operating envelope of the engine;
- To predict the performance variation of the gas turbine as the operational conditions change [3];
- To observe the interaction between the different components of the engine and to realize the effect of a design change upon the performance of the whole design.

Engine performance simulation is also used in the post certification phase of an engine and when it is already in service. At this stage the need to estimate the level of degradation of the engine due to its usage may be present. In that sense, it comprises a very important part of the engine health monitoring system[3].

Based on the level of fidelity that can be achieved, the performance models can be split into different categories, according to the level of discretization of space [4].

- The models developed first belong to the 0-D category because the averaged fluid characteristics are computed at discrete positions inside the engine, generally at the inlet and the outlet of each engine component (compressor, combustion chamber, turbine, and exhaust nozzle).
- The next generation of model is the 1-D type and introduces continuity in the computation in that the fluid characteristics are still averaged in each plane, where plane means a fluid section perpendicular to the engine axis. They are computed along a mean line, representing the average trajectory of the fluid inside the engine.

- 2-D and 3-D models extend this description by discretizing the whole flow path inside the engine, and not just the mean line of 1-D models. 2-D models consider there is symmetry of revolution for the stream, while 3-D models make no simplification and use the complete equations of conservation.

Although the higher fidelity simulations may provide more accurate results since they enclose less assumptions and empirical adjustments, they are computationally expensive. This additional computational effort may not be necessary when practically identical results can be obtained in seconds using a lower fidelity but carefully crafted model [6].

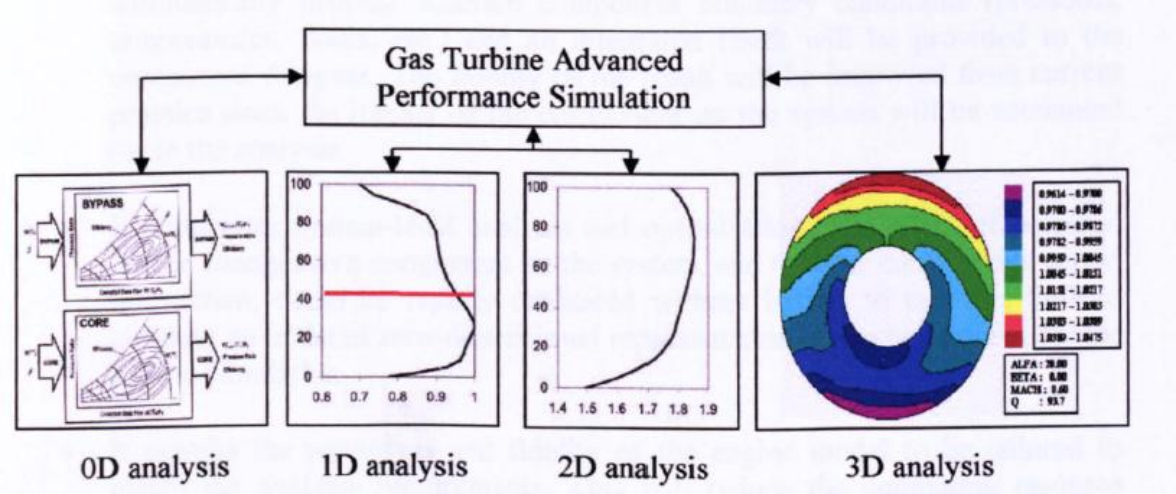

Figure 2-1 Categories of Engine Performance Simulation Models [5]

2.2 TURBOMATCH Scheme

TURBOMATCH is a Cranfield University gas turbine engine simulation software [70], which was initially developed by Palmer[2] and it facilitates design point (DP), off-design (OD) and transient operation performance calculations for aero (civil and military) and industrial engines.

In this software, by means of ''codewords'', various preprogrammed routines known as ''bricks'' can be called up to simulate the action of the different engine's components. The gas turbine performance is calculated by using component characteristic maps for compressors, combustion chambers, turbines (both compressor turbines and free turbines) and a map providing the velocity coefficient for exhaust nozzles. A number of default compressor and turbine maps are

embedded in the Turbomatch database and the user may call up in the input file the one that is closer to the examined engine's characteristics.

A user can simulate virtually any engine configuration merely by changing the data in the input file. In the off-design performance simulation process the user may also declare which engine's parameter will be the driving one, e.g. Turbine Entry Temperature (TET), Compressor's Percentage of Design Rotational Speed (PCN), fuel flow, and which other parameters, e.g. Compressor Surge Margin Parameter (Z), components' efficiencies, will vary so that the engine conforms to continuity and power balance restrictions.

Turbomatch program has been used for Cranfield' s research activities and it has been proven reliable, accurate, and extremely flexible [57], [70].

2.3 Aircraft-Engine Integration

Propulsion-airframe integration is the process of locating the power plant and designing its installation to meet many operating requirements while minimizing drag and weight penalties [11].

When a gas turbine engine is installed on an aircraft it usually requires a number of accessories attached to it and different connections are made to facilitate the interaction with various aircraft systems. The complete installation comprising of the engine, the jet pipe and the accessories, and in some installations the thrust reverser, form the aircraft power plant [8]. All these units, along with an air intake system which conditions the airflow reaching the compressor, must be properly integrated to assure an acceptable operation.

The power plant location and aircraft configuration are design choices and this depends upon the duties that the aircraft has to perform. In some of the existent configurations the Turbojet engine power plants are in the form of pod installations that are attached to the wings by pylons or attached to the sides of the rear fuselage by short stub wings. They also may be buried in the fuselage or wings and embedded in the surrounding structure.

Some aircrafts have a combination of rear fuselage and tail mounted power plants while others, as shown in fig. 2-2, have wing-mounted pod installations with a

third engine buried in the tail structure. Turbo-propeller engines, on the other hand, are normally limited to installation in the wings or nose of an aircraft [8].

Figure 2-2 Tail and Wing-Mounted Pod Installation [7]

The position of the power plant must not affect the operation of the air intake, and the exhaust gases must be discharged away of the aircraft and its control surfaces. Any installation must also be such so as the produced drag effect is kept at minimum levels. Supersonic aircrafts usually have the power plants embedded in the aircraft for aerodynamic reasons. Vertical lift aircraft can use either the buried installation or the podded power plant, or in some instances both types may be combined in one aircraft [8].

2.3.1 Installed vs. Uninstalled Gas Turbine Performance Considerations

Usually performance targets are stipulated as uninstalled, in which case the engine performance quoted stands for the behavior of the propulsion system located from the engine intake flange to the engine exhaust or propelling nozzle flange. When the installed engine performance needs to be quoted then the magnitude of all installation effects must be considered, as follows [3]:

- Plant or airframe intake pressure loss
- Plant exhaust or airframe jet pipe pressure loss
- Auxiliary power off-take (gas turbine accessory power requirements should be accounted even for uninstalled performance)
- Bleed off-take

- Whether the thrust and SFC include any pod drag

Propulsion system performance in total is assessed normally by evaluating intake system's performance in terms of total pressure recovery and installed engine performance at the corresponding value of AIP area weighted average total pressure.

Engine thrust, fuel consumption, airflow and acceleration/deceleration times at appropriate inlet/engine operating conditions, are established by treating the AIP airflow as an equivalent one-dimensional flow. Assessment procedures take into consideration changes in engine and matched engine-component performance resulting from losses of inlet total pressure and account for control interactions [10].

These assessment procedures provide acceptable results only in cases where the AIP airflow pattern is adequately uniform and the turbulence levels are substantially low. In these cases the flow distortion does not need to be accounted for since the resulted difference in the performance can be safely considered as negligible.

On the other hand, when the flow distortion levels are significant, assessments of installed engine performance based simply on averaged total pressure values may be insufficient. Depending on the severity of the problem, the engine stability expressed in terms of compressor surge margin may be threatened long before the above mentioned method has predicted.

2.4 Gas Turbine Engine Control

The gas turbine engine's performance is highly related to a control system which works behind the scenes. The control design enables smooth and safe operation of the engine from one steady-state to another through implementation of various limits and provides the engine with the capability of operating at or near their mechanical or thermodynamic limitations.

Real time sensing of engine's thrust is not feasible outside the engine test cell when the engine operates airborne. In practice, the flight crew becomes aware about the thrust output of their engine through some inferred thrust measurement

techniques which are implemented to facilitate the control and management of engine thrust.

Regarding the nowadays aircraft engine, the more complex their constructive solution is, the bigger the number of their parameters is. Considering an engine as a controlled object, one has to identify among these parameters the most important of them, the easiest to be measured and, in the mean time, to separate them in two classes: control parameters and controlled parameters. There is a multitude of eligible controlled parameters (output parameters, such as thrust, fuel consumption, spool(s) speed, combustor's temperature etc.), but only a few eligible control parameters (input parameters, such as fuel flow rate, nozzle's exit area and/or inlet's area). It results a great number of possible combinations of control programs (command laws) connecting the input and the output parameters, in order to make the engine a safe-operating aircraft part. For a human user (a pilot) it is impossible to assure an appropriate co-ordination of these multiples command laws, so it is compulsory to use some specific automatic control systems (controllers) to keep the output parameters in the desired range, whatever the flight conditions are [72].

The following three parameters are used today as a means of measuring and controlling engine thrust relative to the prevailing operating conditions [50]:

1. Engine Pressure Ratio (EPR);
2. Integrated Engine Pressure Ratio (IEPR);
3. Non dimensional FAN Speed (N1/$\sqrt{T_2}$, where N1 is the rotational speed of the FAN shaft and T2 is the FAN inlet total temperature).

The first technique (which is used on Pratt & Whitney engines) uses the gas generator pressure ratio, typically Pt5/Pt2, where Pt5 is the jet pipe total pressure (Pt7 in fig. 2-3 below) and Pt2 is the compressor inlet total pressure. This parameter is a measure of the airflow through the core section of the engine.

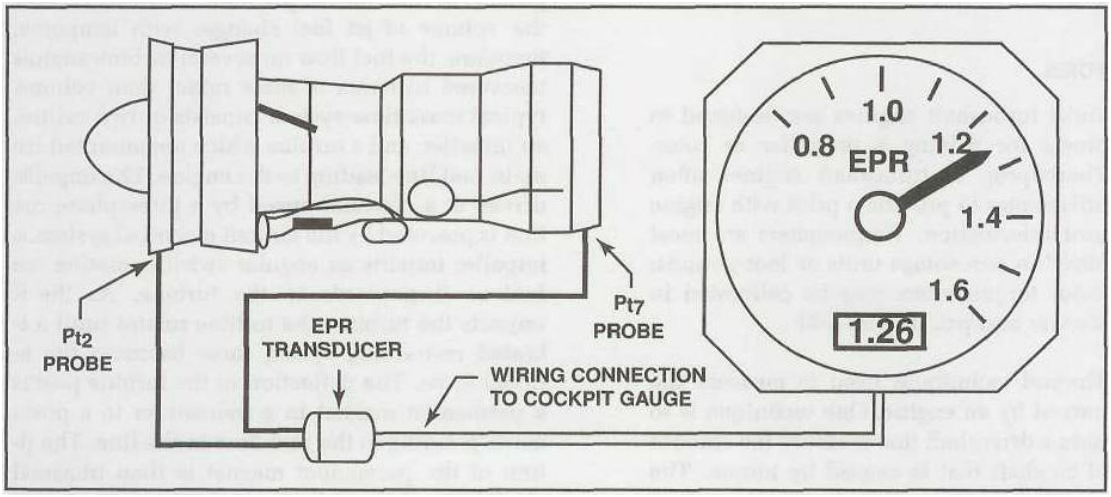

Figure 2-3 An Engine Pressure Ratio (EPR) gauge is used to indicate the power output of a turbojet/turbofan engine [8]

The second technique combines the core EPR with the fan pressure ratio algebraically and it was first introduced by Rolls-Royce on their high-bypass ratio turbofans [8]. This approach seems to be more representative of the engine thrust since the majority of the engine thrust is delivered by the fan.

The third thrust measurement technique is based on the fact that the airflow through the fan which is proportional to the non dimensional fan speed N1/$\sqrt{T_2}$ is a measure of the total engine airflow. The General Electric Company uses this parameter to monitor the engine's thrust [8]. It is worth mentioning that on some Pratt & Whitney engines, the non dimensional FAN speed is also used as a back-up for thrust management should EPR become unavailable.

Ideally, engine thrust should be a linear function of throttle position to provide the required thrust rating at the same throttle position independent of the operational flight condition. This angular deflection of the throttle lever is often referred to as power lever angle (PLA) or throttle resolver angle (TRA) and it has a range from 0 to 100%.

Since airflow through the engine and hence thrust is proportional to inlet total pressure and inversely proportional to the square root of absolute inlet total temperature, the thrust generated by the gas turbine engine varies significantly over the operational flight envelope.

Prior to the introduction of electronic engine controls, the flight crew would have been required to maintain the necessary thrust rating by adjusting the throttle setting as the engine inlet conditions changed following takeoff and throughout the climb to altitude. This process added a considerable workload to the flight crew and increased the chances for an engine abuse as far as its operating limits were concerned.

In modern fuel control systems, thrust settings for each of the above ratings are computed automatically using look-up tables based on the current flight and engine inlet conditions. Throttle settings corresponding to any required rating are therefore managed by the fuel control system which trims the gas generator speed governor set point until the correct rating is obtained. This operation of the control system relieves the flight crew of additional workload and allows them to concentrate on flying the aircraft.

Figure 2-4 shows a block diagram of this concept where PLA represents a percentage of maximum (takeoff) thrust required. The prevailing flight conditions defined by the measured engine inlet parameters are used to generate a specific thrust rating that corresponds to the PLA set by the flight crew. The concept shown is representative of both the EPR and fan speed thrust management control modes.

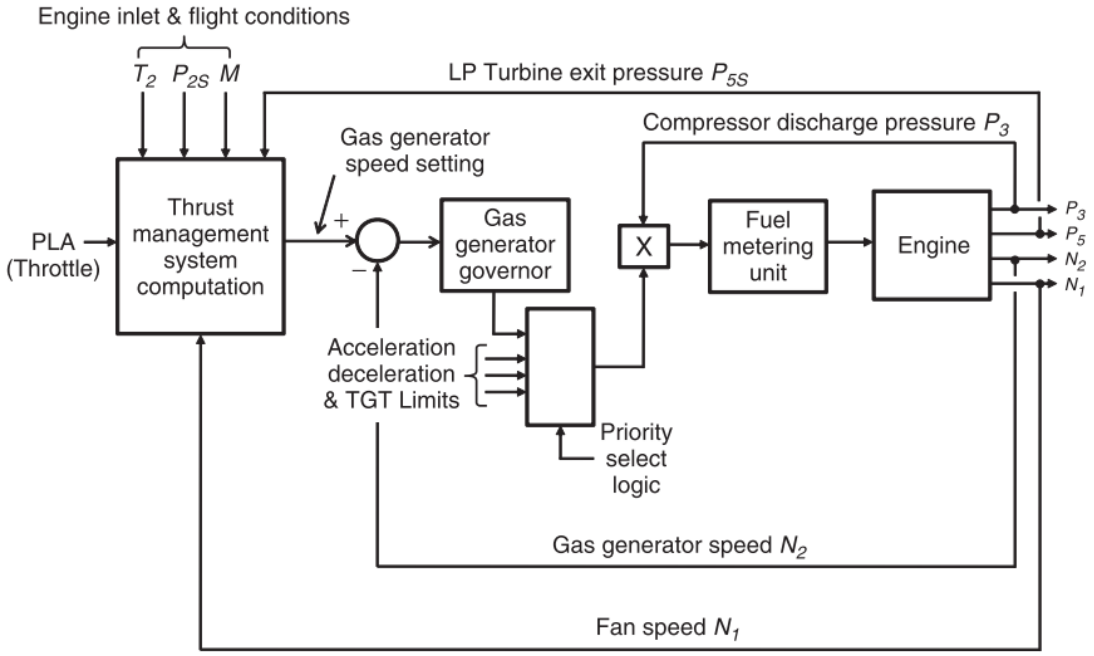

Figure 2-4 Thrust management system block diagram [8].

2.4.1 Need of Air Intake System

All air breathing engines installed in an aircraft must be provided with an air intake and a ducting system to diffuse the air from free stream velocity to a lower velocity acceptable for further processing by other engine components [12].

The task of an intake system is to ensure a smooth running and efficient propulsion by providing airflow at the engine AIP at a proper quantity and at the best quality, keeping the distortion and the pressure losses at the lowest possible level.

In accordance with the flight Mach number this requires either acceleration or deceleration of the air inside the intake in order to match the engine flow condition demands. Usually the airflow entering subsonic compressors or fans must be of low Mach number, of the order 0.4-0.5 or less even if the aircraft speed is much higher than this range [13]. Thus, the intake system in most of the cases acts as a diffuser. In addition, the flow entering the engine should be as uniform as possible in order to ensure stable engine operation.

The compression in a subsonic intake consists of two components:

- The Pre-entry compression which is always isentropic and takes place outside the intake duct.
- The Internal compression or the compression in the diffuser which is not isentropic.

Based on the above, one may think that the best approach would be to design an intake system for maximum pre-entry compression. However trying to maximize pre-entry compression may result in boundary layer separation within the internal compression. As such, designers try to optimize between external and internal compression.

Depending on the application, military or civil, the size and shape of the intake may significantly vary. In cases where the high speed and agility of the aircraft is of high priority, the engine is fully embedded in the airframe. The intake in these applications is required to be lengthy and sometimes curved putting the designers into great concerns about the additional losses which will eventually limit the output of the engine. An example of such an installation is presented in fig. 2-5.

In civil applications, on the other hand, the intake systems are more 'conventional' with limited length and without any bends and shape changes.

During the first stages of the development of an aircraft, one of the airframe designers' concerns is the choice of a proper intake system which will provide acceptable levels of thrust and drag in the whole design. In aero engines, maximum thrust will be obtained by designing the air intake to transform kinetic energy of the flow, as it arrives in front of the air intake, into potential energy, in terms of total pressure at the AIP, with no flow separations and with the best possible efficiency.

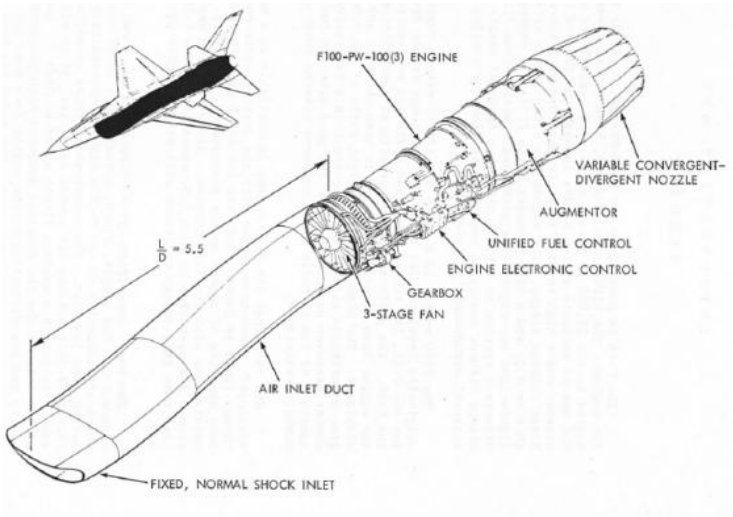

Figure 2-5 The F100 engine in the F-16 Aircraft with its Belly-mounted Intake [49]

Flow separation in an intake system can get initiated at three possible locations:

- External to the intake on the nacelle
- Within the diffuser's internal surface
- On the centre body or the hub

Separation on the nacelle would lead to increase in overall drag of the aircraft whereas separation within the diffuser's geometry may lead to higher total pressure losses and therefore lower diffuser efficiency.

Efficiency or total pressure recovery is a parameter that is calculated by taking the ratio of the total pressure in front of the engine to that of the upstream flow. Minimum drag will be obtained with air intakes that are sized to accommodate just the airflow that the engine needs at critical regimes [14].

Supersonic intakes are characterised by the presence of shocks. In supersonic intakes internal, external or mixed compression may take place, depending upon the location of the shocks. As their names imply In internal compression, shocks are located within the intake's geometry and in external compression shocks are located outside the intake. In mixed compression though shocks are located within as well as outside the intake's geometry.

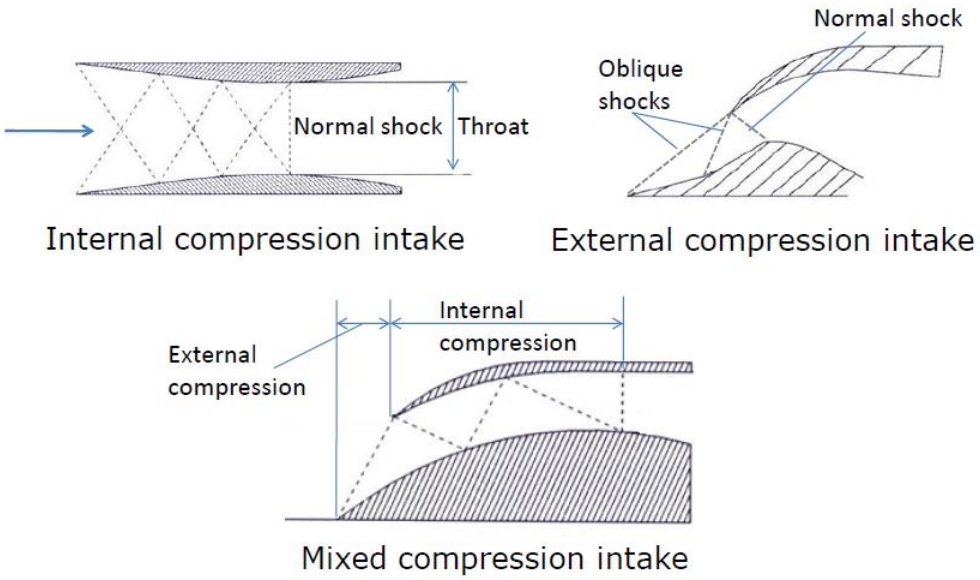

Figure 2-6 Supersonic Intakes [46]

2.4.2 Flow Ratio

Mass flow (w), measured in Kg/s, is a property of the internal flow which is amongst the primary concerns of the air intake system designers. It is defined by [15]

$$w = \rho \times A \times c \qquad \text{(eq. 2-1)}$$

where **ρ** is the air density, in Kg/m^3,

A is the cross sectional area at a given station of the internal flow, in m^2 and

C is the flow velocity in m/s, which is assumed uniform at the plane of interest.

Usually in the study of air intake systems the principal stations are those at upstream infinity, denoted by suffix (∞), at the intake entrance, denoted by (c), and at the engine face denoted by (f).

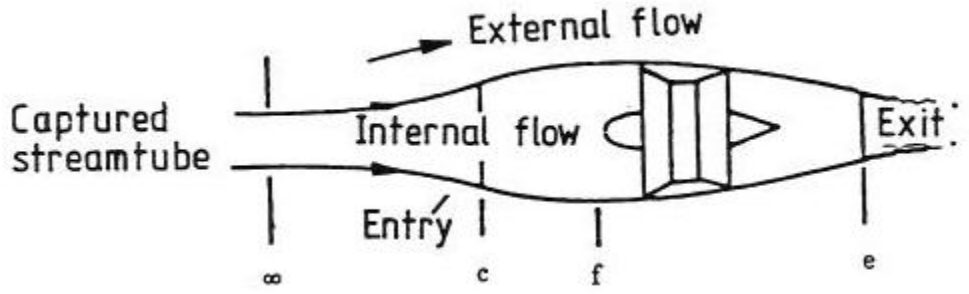

Figure 2-7 Flow Stations for a Complete Engine Nacelle [15]

The captured stream tube in front of an intake divides the airflow into internal and external, with the internal entering the engine and the external going around it. If we assume that there are no additional flow inputs or off takes from the intake the product of equation (2.1) will be constant throughout the internal flow stream tube (principle of continuity), thus:

$$\rho_\infty \times A_\infty \times c_\infty = \rho_c \times A_c \times c_c = \rho_f \times A_f \times c_f \qquad \text{(eq. 2-2)}$$

When the stream tube arrives undisturbed at the entry of the intake (c) then this condition is covered under the term full flow [15].

$$A_\infty = A_c \qquad \text{(eq. 2-3)}$$

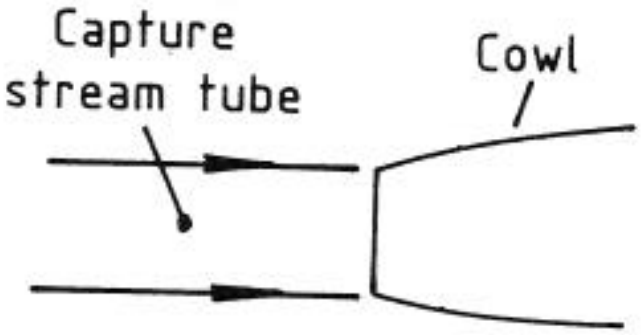

Figure 2-8 Full Flow Condition [15]

And from equation (2.2) we get that:

$$full\ \ flow = \rho_{\infty} \times A_c \times c_{\infty} = \rho_c \times A_c \times c_c \quad \text{(eq. 2-4)}$$

The term **flow ratio** refers to the actual flow defined by the stream tube area at upstream infinity (∞) related to full flow. It is also called capture area ratio [15].

$$flow\ ratio = \frac{\rho_{\infty} c_{\infty} A_{\infty}}{\rho_{\infty} c_{\infty} A_c} = \frac{A_{\infty}}{A_c} \quad \text{(eq. 2-5)}$$

From equation (2.5) becomes obvious that in full flow condition the flow ratio equals to unity. When the flow ratio is greater than one then the cross sectional area at the upstream infinity station (∞) is greater than the cross sectional area at the entry of the intake and the intake operates in suction mode. At this condition there is a high demand for mass flow from the engine but the aircraft is either stationary (like when at rest on the ground) or moving forward with a slow forward speed (like when in takeoff or climb). Respectively, at high flight speeds where the engine's demand in flow is less than that provided by the flow stream tube, the flow ratio is less than unity and the intake is in spillage mode [16].

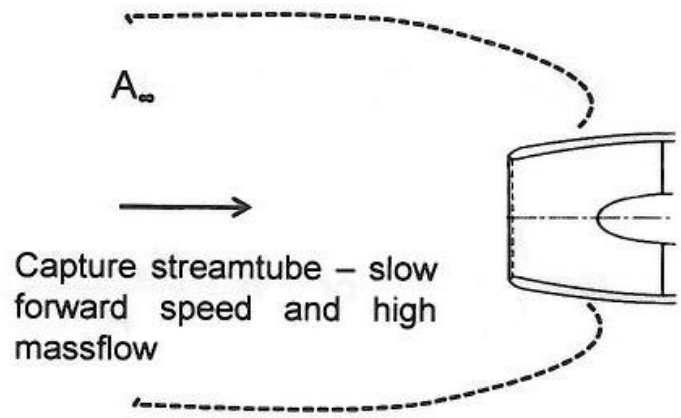

Figure 2-9 Suction Mode [15]

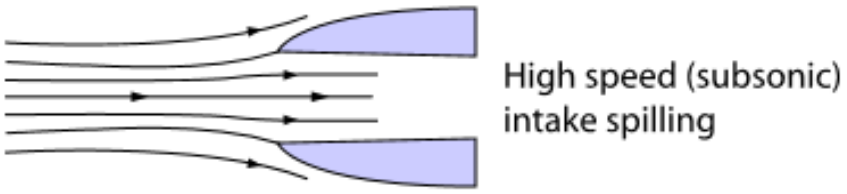

Figure 2-10 Spillage Mode [73]

2.4.3 Air Intake Pressure Recovery Factor

The basic air-intake performance is based on the ability to convert the approaching air flow with a Mach number and pressure to a lower mach number and increased pressure. It needs to do this as efficiently as possible with the lowest reduction in the available total pressure.

In a sub-sonic intake at design condition the losses in total pressure are primarily due to viscous friction losses along the intake approach, nacelle and duct wetted surfaces. For supersonic configurations there is also the loss in total pressure due to the shock waves. Under high subsonic velocity (or manoeuvring) conditions, there are additional losses due to local supersonic regions, shock interactions and flow separations.

As it was discussed before, a basic definition of the intake efficiency is the total pressure ratio between the engine face and upstream of the intake entrance and is referred to as the pressure recovery factor (PRF):

$$PRF = \frac{P_f}{P_\alpha} \qquad \text{(eq. 2-6)}$$

where $\mathbf{P_\alpha}$ is the total pressure of the approaching flow;

$\mathbf{P_f}$ is the total pressure at the engine face.

The higher this value the lower the total pressure losses and the more efficient is the intake system. The loss in total pressure for the intake depends on the details of the installation, namely whether it is a podded, embedded or propeller installation. The losses are mostly due to friction along the intake approach, on the duct wetted surfaces and due to shocks.

For example, for a sub-sonic intake close to the fuselage, under some conditions, the large captured streamtube will interact with the intake approach surfaces and will result in a loss in total pressure.

The loss within the duct from the intake entry plane to the fan face strongly depends on the length and shape of the diffuser duct. The intake must be designed to treat the air very carefully, which means very gentle turns and slow diffusion, to prevent the airflow from separating from the inlet walls and forming eddies and vortices which are causes for pressure loss. This can be important for military applications where the engines are required to be highly embedded. In these applications the presence also of aircraft surface ahead of the intake, wetted by the internal flow, makes things worse in terms of additional losses.

Another important factor related to the total pressure losses is the boundary layer growth in the direction of movement of the internal flow. The flow near the intake walls is slower than the flow in the main part of the intake. In fact, the molecules right next to the wall are effectively stuck to the wall because of friction. This layer of low energy air causes many problems in the intake flow because the higher downstream pressure feeds upstream and causes the flow to separate off the wall [47]. Boundary layers on the intake compression surfaces and internal duct surfaces are best dealt with by bleed systems [15].

The effect of Pressure recovery on engine thrust depends on the characteristics of the engine. It is usually assumed that loss of total pressure in the intake is translated directly to loss of engine thrust by relationship of the form

$$\frac{\Delta X}{X} = \frac{\mathrm{K}\Delta P}{P_{\infty}} \qquad \text{(eq. 2-7)}$$

Where **X** refers to the thrust and **K** is a factor the value of which depends on the type of engine but is greater than unity and generally closer to 1.5 [17].

2.4.4 Preliminary Design Concerns of Air Intake Systems

In the design of an air intake system it is important to ensure that the intake provides an adequate supply of air to the engine, not only at the design point but under the entire operating envelope, with pressure recovery sufficient for the particular operational condition and without an unacceptable drag penalty.

To ensure that these requirements are met over the operational span is called matching: matching is thus a necessary follow-on and complement to the basic study of on-design performance [17].

In subsonic intakes, which as their name implies are used in aircrafts that fly at subsonic speeds, matching is usually not a great problem, though not completely automatic. The essential change from one flight condition to another is the variation in flow ratio, illustrated in broad terms in Figure 2.11. The following comments apply.

(a) High speed cruise. This is usually the design-point condition, with flow ratio less than 1.0, usually in the range 0.5 to 0.8 [17]. Internal duct performance is generally at its best.

(b) Climb. The lower flight speed and, probably, higher engine power lead to a higher flow ratio, probably greater than 1.0. In this condition, lip and throat design play significant role and allow this condition to be accepted without flow separation. The term throat refers to the section of the intake with the smallest cross sectional area.

(c) Ground running. For the extreme static condition (flow ratio infinite) an auxiliary inlet system is probably required. The extra inlet can be arranged to close automatically when the flow ratio falls below a certain value, usually during the take-off run. This is the matching device normally required for a subsonic intake.

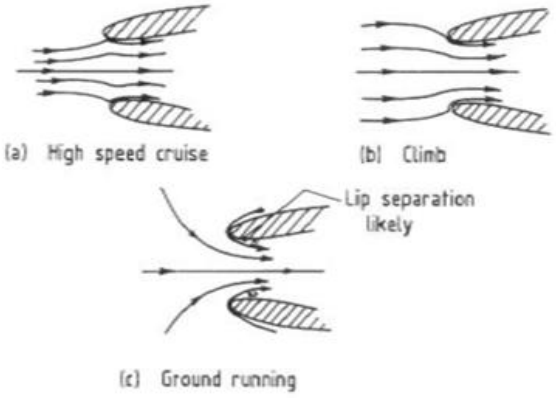

Figure 2-11 Range of Flight Conditions for Subsonic Intake [17]

In supersonic intakes things are more complicated. First of all the geometry of the intake is different than in subsonic cases. The shape of lips is the result of a compromise between sharpness, to reduce drag penalty, and roundness to avoid separations especially at takeoff. Variable geometry in terms of moving surfaces in the intake duct is in some cases inevitable. Wedges are added to the structure to guide properly the occurrence of shocks which will separate the intakes into external, internal or mixed compression configurations.

Finally, fixed geometry intakes that need to operate in subsonic, transonic and supersonic areas are sized for a high subsonic Mach number condition, in the order of 0.9 in the tropopause, using a throat Mach number not greater than about 0.8 [17]. One such intake configuration is the one that the present study deals with.

2.5 Inlet Flow Distortion

The gas turbine engine, when installed on an aircraft, should remain aerodynamically compatible with the air intake throughout the entire aircraft flight

envelope. This task is far more challenging in fighter aircrafts, where both the installation requirements and the operating conditions are more demanding.

When the whole system operates near the design point conditions undesired situations such as compressor stall or engine surge are highly unlikely to occur since the behaviour of the engine at these conditions has been well predicted in the design process. In other regions of the flight envelope though, or in non-standard atmospheric conditions, serious deteriorations in flow quality can occur, causing different malfunctioning of the propulsion system. In these latter cases, the intake flow may be non-uniform at the AIP plane in terms of total pressure or total temperature or in a combination of these parameters. These spatial variations are usually covered under the term "inlet flow distortion".

2.5.1 Sources and Forms of Distortion

Even today the compatibility issue of a new fighter aircraft throughout its entire flight envelope cannot be predicted with certainty at the beginning of the design process. This is mainly due to the fact that the selection of an intake configuration, its position on the fuselage, its cross-section variation and longitudinal shape are not only defined by flow physics requirements.

Aircraft performance strongly influences this selection as well as the internal fuselage structure and the available space inside the fuselage. Additionally, stealth and weight reduction requirements seem to demand short and highly curved intake ducts which are prone to flow separations [18].

Subsequently, the more a new aircraft is trying to fulfill these requirements the more it becomes concerned with the total pressure losses that the engine intake causes. Another source of total pressure distortion is the ground vortex that is created when the engine runs while the aircraft is either parked or taxing (fig.2-12).

Besides the total pressure non-uniformities, variation of total temperature at the AIP may also occur. This inlet temperature distortion is more pronounced for military applications where gun or missile gas ingestion is experienced. Also, carrier airplanes are subjected to steam ingestion from the

catapult system and vertical take-off planes may re-ingest their own exhaust gases [19].

The present study will mainly focus on the effects of the spatial variation of the total pressure (total pressure distortion) on the engine's operation. The magnitude of these steady or unsteady non uniformities depends on the intake/engine mass flow. Today's very stringent cost and weight requirements have led to very compact intake designs exhibiting new risks of possible distortion problems [18].

Figure 2-12 Ground Vortex [21]

Total pressure distortion may be encountered in forms of either radial or circumferential, depending on the pattern of pressure distribution on the AIP with the latter to create great concerns for the mechanical integrity of the FAN. And this because such difference in circumferential pressure distribution introduces vibration issues, as the rotating blades periodically move between high and low pressure areas. The loading cycles that the fan blades experience through that process deplete their fatigue life creating thus great concerns for high cycle fatigue (HCF) blade failures. Also in case the number of total pressure defect areas in conjunction with the engine's rotational speed coincides with the natural frequency of the blades, resonanance issues may arise with catastrophic consequences for the structural integrity of the engine (fan blade-off events).

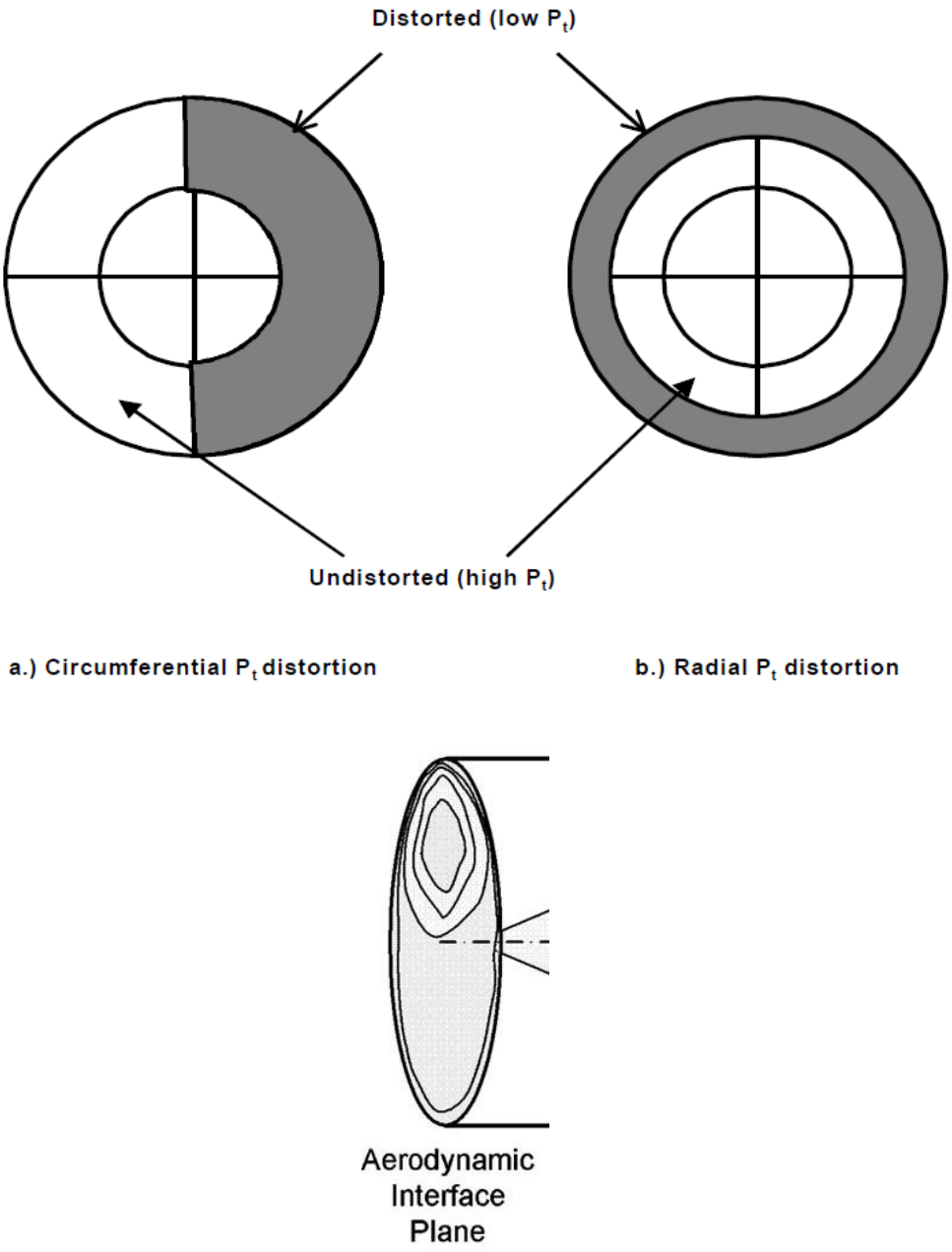

Figure 2-13 Non-Uniform Total Pressure Distribution at the AIP [19]

2.5.2 Distortion Descriptors

Having discussed some aspects of this important phenomenon, it becomes obvious the necessity of having a quantitative measure of distortion by which both the quality of intake flow and the tolerance of an engine to its side effects can be assessed. The parameters that are used to quantify the patterns of total pressure non uniformities at the AIP are called distortion descriptors.

Different approaches have been followed in the establishment of such parameters and distortion coefficients may be defined in various ways [17]. The descriptors discussed in this paragraph are well documented in [10], [20]. The required data for the derivation of them are obtained using arrangements similar to the one shown on figure 2-14. Pressure probes usually arranged in rake and probe arrays are installed at the AIP and provide actual pressure readings throughout the engine operation.

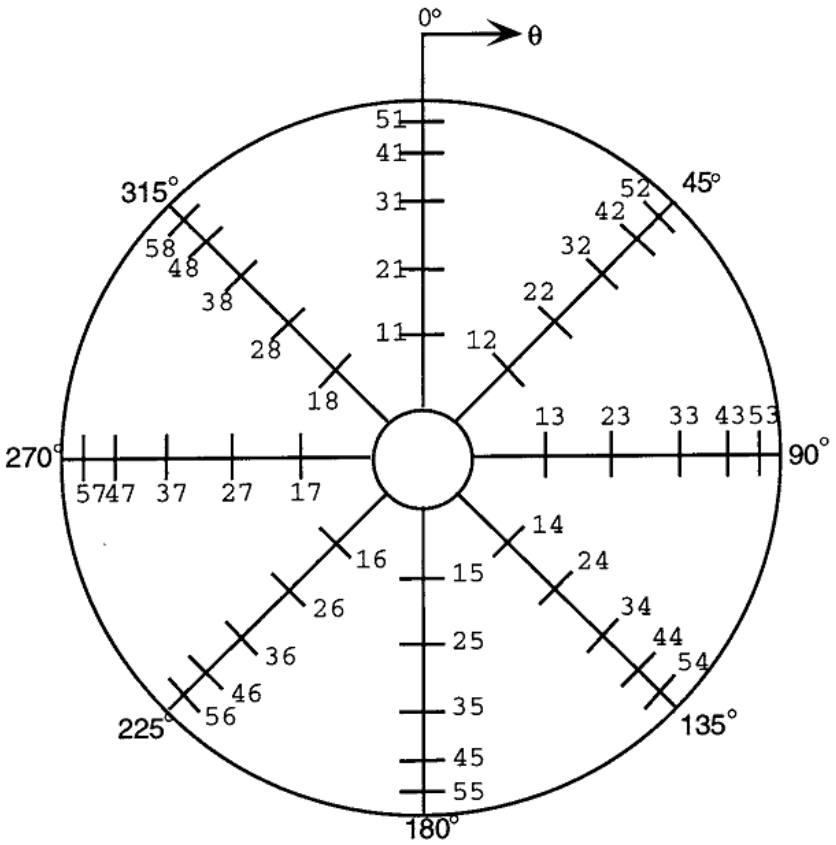

Figure 2-14 Pressure Probe Orientation [20]

The radial and circumferential distortion are described on a ring by ring basis. Circumferential distortion in terms of intensity, extent and multiple per revolution elements and radial in terms of radial distortion intensity element.

The intensity or level of circumferential distortion is a numerical indication of the magnitude of the total pressure non-uniformities [10].

$$Intensity = \left(\frac{\Delta PC}{P} \right)_i = \left(\frac{PAV - PAVLOW}{PAV} \right)_i \quad \text{(eq. 2-8)}$$

Where,

PAV$_i$ is the i$_{th}$ ring average total pressure and

PAVLOW$_i$ is the average total pressure of the low total pressure region for the i$_{th}$ ring.

The extent element is a numerical indication of the circumferential size of the low-pressure (spoiled) region [10].

$$Extent = \theta_i = \theta_{2i} - \theta_{1i} \quad \text{(eq. 2-9)}$$

Where,

θ_i refers to the circumferential location in degrees on the i$_{th}$ ring.

The multiple-per-revolution (MPR) element is a numerical indication of the equivalent number of circumferential regions of low pressure [10].

The radial distortion intensity of a ring is defined as the difference between the face average pressure (PFAV) and the ring average pressure (PAV) divided by the face average pressure (PFAV). Thus [10],

$$Radial\ Intensity = \left(\frac{\Delta PR}{P} \right)_i = \left(\frac{PFAV - PAV}{PFAV} \right)_i \quad \text{(eq. 2-10)}$$

2.5.3 Intake Pressure Recovery and Distortion

Distortion characteristics at the AIP and pressure recovery vary considerably depending on the type of the intake systems, their location on the aircraft and their mode of operation. Intake designs range from conventional configurations with simple round-lip, short and straight duct shapes to complicated ones with sharp-lip, long and curved ducts. The former are suitable for podded

subsonic transport aircrafts whilst the latter are more appropriate for fighter aircrafts.

The more conventional a configuration the more efficient it is, in terms of pressure recovery. Such configurations provide close to 100% pressure recovery [10] and the distortion levels that they experience are remarkably low. Any pressure recovery defects are mainly due to the tip radial and the boundary layer effect, both of which can be considerably predicted during the design and development process. As for the distortion levels they can only reach noticeable levels in cases where adverse environmental conditions such as crosswinds, are present.

On the other hand the complex intake configurations create larger regions of lower pressure at the AIP and subsequently they provide lower pressure recovery values. Distortion patterns contain both radial and circumferential elements. In these cases an assessment of the engine performance changes due to distortion is likely to be necessary. Such a methodology will be studied in the present work.

2.5.4 Distortion and Engine Stability

The effects of distorted inflow to turbomachinery have been a concern since the early days of engine installations [74]. Whether stationary power units or aircraft engines, designs are performed assuming a particular inlet flow characteristic. Variations in the inlet total pressure, total temperature, or flow angle from the design flow characteristic all have an effect on the operation of the gas turbine engine. The characterization of these effects has been a continuous effort for turbomachinery designers since the early days [74].

The first basic work that started to examine compression system stability and dynamics as a function of inlet total pressure variation was that of Pearson and McKenzie [75], who first proposed the parallel compressor theory. This theory proposed that a compression system under the influence of a total pressure distortion could be treated as two compressors operating in parallel (figure 2-15). Each of the “parallel” compressors would operate as if each were under undistorted flow conditions, with one inlet corresponding to the original compressor’s distorted

side and the other corresponding to the original compressor's undistorted side. The two "parallel" compressors are assumed to discharge to the same static pressure. The compressor was considered destabilized whenever the operating point of the distorted sector moved beyond the clean compressor's surge line.

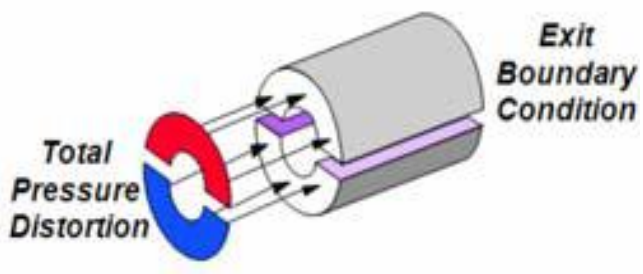

Figure 2-15 Schematic representation of the parallel compressor model concept [74]

This technique of analyzing inlet distortion assumes that the compression system responds to changes in inlet flow conditions in an instantaneous manner. Several years later, Reid [37] showed that for small circumferential extent inlet distortion patterns, the parallel compressor model did not hold true. He concluded that there must be some critical angle of circumferential extent for a compressor to respond in an instantaneous manner.

In 1972, a committee was formed as a working group under the auspices of the Society of Automotive Engineers (SAE), called the S-16 Committee, made up of representatives of the engine manufacturers, airframers, and customers [20]. As a result of the work of this committee, an aerospace recommended practice (ARP) document was developed and given the annotation of ARP-1420 and titled "Gas Turbine Inlet Flow Distortion Guidelines" [20]. In this document the engine's compression system stability assessment was expressed in terms of Surge Pressure Ratio loss (ΔPRS).

In a gas turbine engine the FAN is the most affected by flow distortion component since it is the first engine part that meets the distorted air flow. The distortion that the downstream components experience is significantly attenuated due to the rotating parts of the FAN. As a result it is the fan destabilization due to air flow distortion that is of great concern.

The FAN characteristics are captured in its map, a representation of which is shown in figure 2-16 below [20]. The stability of the FAN is assessed through the Surge or Stability Margin (SM) which is described as the pressure ratio range, at a constant rotational speed or non dimensional mass flow, through which a compressor may be operated without stall [20] (distance between its running point and the surge limit line). Thus,

$$SM = \left(\frac{PR_1 - PR_0}{PR_0} \right) \times 100 \qquad \text{(eq. 2-11)}$$

where,

PR_1 refers to the pressure ratio value that coincides with the undistorted flow stability line and

PR_0 is the pressure ratio at the fan operating point.

It is worthy of mention that in the case presented in fig. 2-16, the SM calculations are made under constant non dimensional (corrected) mass flow.

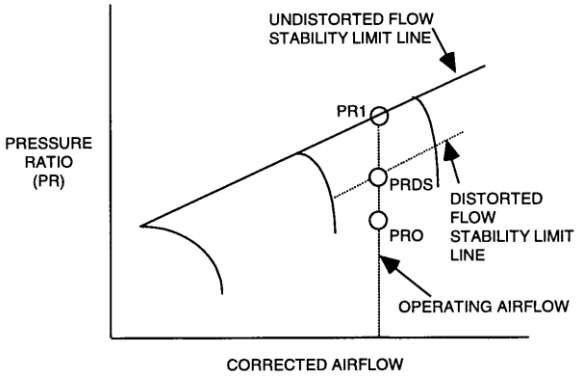

Figure 2-16 Stability Margin Definition [20]

This FAN stability assessment may be expressed in terms of Surge Pressure Ratio loss (ΔPRS) , which is defined as [20]

$$\Delta PRS = \left(\frac{PR_1 - PRDS}{PR_1} \right) \times 100 \qquad \text{(eq. 2-12)}$$

where,

PRDS refers to the value of pressure ratio that coincides with the distorted flow stability line.

In [10] there is a correlation between the stability pressure ratio loss and the flow distortion descriptors. This relationship allows the communication between the distorted flow and its effects on the stable operation of the FAN. So [10],

$$\Delta PRS = \sum_{i=1}^{N} \left[\; KC_i \times \left(\frac{\Delta PC}{P} \right)_i + KR_i \times \left(\frac{\Delta PR}{P} \right)_i + C_i \; \right] \times 100$$

(eq. 2-13)

The sensitivity and offset coefficients, as they are called (KC, KR, and C), are empirically determined parameters that have been derived from wind tunnel experiments during which the specific FAN has been tested under actual distorted conditions (screen induced). These parameters vary with distortion (extent, multiple-per-rev, etc.), compression system design and operating conditions. The sensitivity and offset coefficients should be of sufficient accuracy to correlate the effect of critical distortion patterns to within ±2% stability pressure ratio [20].

2.6 Computational Fluid Dynamics as an Engineering Tool

When dealing with problems related to fluid mechanics there are three different approaches that can lead to a solution, namely experimental, analytical and numerical.

An experimental solution seems to be the most accurate but it is also the most expensive as well. In this approach a model needs to be designed and built and special facilities need to be considered which will be able to accommodate the model and the required instrumentation equipment.

The analytical solution is only possible for simple geometries and physics, limited to cases that can be described using linear partial differential equations

(LPDE) [24]. Although the acquired results can be considered accurate it is a method that can only be applied to simplified cases.

For the numerical approach, some assumptions are made which they help in the transformation of the partial differential equations (PDE) that describe the flow, into algebraic ones. To make this happen the derivatives of the PDE are approximated by discretized differences.

Computational Fluid Dynamics (CFD) is a form of this last approach and enables the computational treatment of complicated fluid problems under a relatively low cost. With the rapid evolution of the computers, which significantly increased the computer processing power and subsequently reduced the processing time, CFD has become a powerful tool which may be used in different engineering applications. New designs are judged based on CFD results and many of the actual tests during the development of a new design have been replaced by CFD simulations.

2.6.1 CFD Solution Procedure

CFD modeling of compressible viscous flow, like the turbomachinery flow, is based on the governing equations of fluid dynamics. These equations represent mathematical statements of the conservation laws of physics [25]:

- The conservation of Mass (continuity equation).
- Newton's 2nd law (momentum equation).
- 1st law of thermodynamics (energy equation).

The equations representing the set of the above laws of physics are usually termed as Navier-Stokes equations. To close these equations it is also necessary to specify an equation of state. In aerodynamics it is safe to assume that the gas behaves as a perfect gas which assumption allows the closure of the partial differential equations (PDE) and the only thing left before one may proceed to solve the equations is the specification of the boundary conditions.

In general, a complete CFD analysis consists of three different elements [25], namely

- The **pre-processor**, which refers to the creation of the flow region's geometry, the definition of the computational domain and the subdivision of it into smaller sub-domains, a process that is termed as meshing.
- The **solver**, where either a commercial or an in-house code is used to run the simulation and solve the case. Computational solutions are obtained through two stages. The first one deals with the transformation of the PDE into algebraic ones, a process that is called discretization, and the second stage deals with the specific technique to solve the algebraic equations.
- The **post-processor,** where the obtained results from the simulation are retrieved and processed in the desired way.

In the context of the present work, as pre-processors were used GAMBIT, at the first steps of the geometry model creation and ANSYS ICEM CFD for the refinement of this geometry and the grid generation. FUENT was used as a solver and post processor.

2.6.2 Turbulence Modeling

Turbulence modeling is the construction and use of a model to predict the effects of turbulence.

All flows become unstable above a critical Reynolds number. At low Reynolds numbers, flows are laminar but in flows where the inertia forces by far dominate the viscous forces, the created eddies are not dissipated smoothly and the motion becomes intrinsically unstable.

Laminar flow problems can be solved using the previously mentioned continuity and momentum equations. In turbulent flow though, the velocity and all other flow properties vary in a random and pattern free way which makes it impossible to solve them following the laminar flow approach. These extra terms make the turbulent flow to need more computational resources compared to laminar flow.

Different approaches have been developed to deal with turbulent flows. The most expensive computationally is the Direct Numerical Simulation (DNS), where all the fluid motions contained in the flow are considered to be resolved [25].

Alternatively, another approach considered is when the turbulent flow is viewed as comprised of large and small eddies. Based on this approach the large eddies are considered to be much more energetic and greater transporters of the conserved properties than the small ones. As such, in this approach which is termed as Large Eddies Simulation (LES), only the large eddies are resolved whereas the small ones are only approximated. LES is less expensive than DNS but its computational cost is still high.

For most engineering applications it is not necessary to resolve the details of the turbulent fluctuations. And this is the point where the turbulence modeling comes into play. In the Reynolds Averaged Navier-Stokes (RANS) equations approach, time averaged properties of the flow are utilized, a simplification that saves much of the computational efforts. In this approach, the chaotically varying properties are decomposed in one time-averaged part, which is independent of time (when the mean flow is steady), and one fluctuating part. Averaging is often used to simplify the solution of the governing equations of turbulence, but models are needed to represent scales of the flow that are not resolved In these cases.

The averaging process has introduced unknown turbulent correlations into the mean-flow equations which represent the turbulent transport of momentum, heat and mass - the Reynolds Stresses and fluxes. A turbulence model can be described as a set of relations and equations needed to determine the unknown turbulent correlations that have arisen from the averaging process.

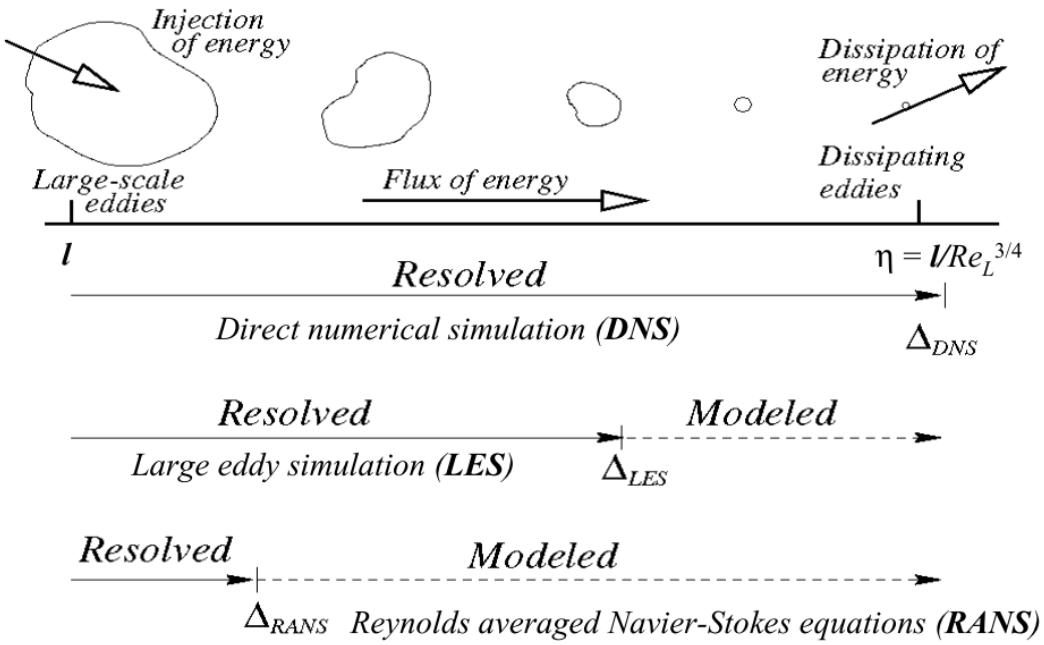

Figure 2-17 Turbulent Flow Solution Approaches [48]

The selection of Turbulence model plays significant role in numerical simulations since the successful modeling of the turbulent flow greatly increases the quality of the acquired solution. And by the term 'successful modeling' is meant the implementation of a simple, accurate and economical to run turbulence model that will better capture the flow phenomena.

In the present study wall turbulence and free turbulence are expected to occur due to the position of the aircraft in the middle of the flow domain and also due to the shear stresses between the flow layers as they move in the free stream region and they interact with the disturbed by the aircraft, flow.

2.6.3 A review of Prior Investigations

Distortion effect has been given a great attention among the aerospace community in the last decades [37], [41], [74], [75]. Whenever the integration between the airframe and the propulsion system has been investigated, one of the prime considerations has been how the first will affect the operability of the latter.

There is no doubt that the successful ''marriage'' between the gas turbine engines and the airframes has remained a major engineering challenge. The external airframes including the inlet systems must capture flow from the free stream and deliver it to the installed engine at Mach numbers that meet the requirements of the fan. There are cases though that due to the shape of the intake systems, the airflow reaches the engine's face and it is not uniform at all in terms of total pressure and total temperature. It is these flow non uniformities that are covered under the term airflow distortion.

The most concentrated work on flow distortion was originally (pre-1960) carried out on the first generation of lift engines and compressors (RB 108 and RB 145) where the V.T.O.L application called for the toleration of extremely high distortion levels [37].

Currently, the airframe-propulsion integration process is handled by an established methodology that has been derived by consensus of industry and government experts over the last 37 years and reported by the Society of Automotive Engineers (SAE) in an Aerospace Recommended Practice namely the ARP-1420 [20]. This document was developed by the SAE Technical Committee, S-16 (Turbine Engine Inlet Flow Distortion), and along with its companion document, AIR 1419 [10] they set the guidelines for the intake/engine compatibility as far as the total pressure distortion is concerned.

In a ground test environment and in the absence of an airframe/inlet system, the engine may be tested against equivalent distorted conditions, similar to those when installed on an airframe, by means of distortion generator methods. The two most widely used such methods are the distortion screens and the air jet distortion generators [36]. In the context of numerical calculations steam injectors have been also tested as distortion generators with promising results [38]. The described methodology in SAE AIR 1419 [10] refers to distortion data obtained from distortion screens.

The general result from experimental testing of engines operating under distorted inflow conditions was that their compression system maps were modified due to distortion by shifting their surge lines towards an unfavourable direction limiting thus their surge margin. An extensive experimental effort has been

carried out at the Lewis Research Centre to establish a data base for evaluating the effect of inlet flow distortion on the performance of gas turbine engine compression systems. The low by-pass turbofan engine PW1128 was tested at altitude conditions with steady state inlet temperature distortion, pressure distortion, and combined temperature and pressure distortion to evaluate the engine's stability when it operates under such conditions. Pressure distortion was created with the aid of screens positioned upstream of the fan [39].

The effect of the inlet's shape on the quality of the airflow reaching the engine's face has been also studied. A 0.15-scale model of an under fuselage engine inlet designed for a single-engine fighter airplane was also tested in the NASA Lewis Research Centre's 8 by 6 ft wind tunnel [40]. The purpose of the test was to obtain the performance of a baseline inlet and the effects of several configuration variations, namely splitter-plate length and included angle, fuselage boundary-layer-diverter height, cowl sidewall cutback, splitter-plate boundary-layer bleed, and vortex generators in the inlet duct [40].

Another wind tunnel investigation was carried out on a scaled intake system of the Eurofighter (Typhoon) aircraft [41] to determine the intake flows at high angles of attack and to specify any design areas that might have been improved. Numerical flow calculations, based merely on the intake geometry, were also performed to support the obtained experimental results.

The effects of high-angle-of-attack flight on aircraft inlet aerodynamic characteristics were investigated at NASA Dryden Flight Research Centre [42]. The highly instrumented F/A-18A High Alpha Research Vehicle was used for this research effort where a newly designed inlet total-pressure rake was installed in front of the F404-GE-400 engine to measure inlet recovery and distortion characteristics [42]. At that study it was found that high AOA flight (>20˚) caused high levels of circumferential and radial distortion and degraded intake pressure recovery [42].

In that continuous effort in the study of distortion, CFD has played a significant role. Wind tunnel tests have been replaced by the much cheaper numerical simulations, at least at the conceptual and preliminary design phases of novel airframe/intake systems which helped significantly in the direction of reducing the respective costs. This approach may give a better insight on the flow

characteristics while the flow travels through the engine's compression system. Voytovych et al [43], studied computationally a single flow passage of an isolated fan blade row in order to evaluate the effects of radial total pressure distortion on performance and stall margin of the fan while also providing insight into this flow structure.

The majority of both experimental and computational research studies on the effects of inlet distortion on gas turbine engine's performance is focused on compression stability. As such, there is relatively limited mention in the open literature of the effects of inlet distortion on overall performance parameters such as thrust. Of course, compressor surge is a much more dangerous event than a limited loss of thrust. Nevertheless, it is of interest how much the performance of an engine is affected by inflow distortion. AIR1419 [10] contains engine performance data from a test in which distortion was simulated by a screen. Also, Williams [44] stated that the effect of distortion on performance is minimal at important aircraft operational conditions. However, performance changes can be large if control system input signals are affected by the distortion. Kurzke [19] describes how changes in performance due to the inlet pressure and temperature distortion can be calculated with an overall engine simulation that employs an integrated parallel compressor model.

The present study provides a holistic methodology for the evaluation of the total pressure distortion effect on the performance of an installed gas turbine engine. Patterns of distortion at the engine's face are obtained through CFD simulations where the flow over a full scale military aircraft with an active intake is numerically resolved. Different flight attitudes are considered by changing accordingly the direction of the incoming flow in the computational domain. The fan stability is assessed following the guidelines of SAE ARP 1420 [20] and AIR 1419 [10]. whereas the engine's performance in terms of resulted net thrust is also estimated in Turbomatch (gas turbine performance simulation software). This methodology enhances the existing engine-inlet compatibility analysis and design methodology (ARP-1420) through the use of modeling and simulation.

3 CFD SIMULATION MODEL

3.1 Selection of a Baseline Airframe-Engine Set

In the context of the present study, for the purpose of the CFD analysis, as a baseline set of airframe and gas turbine engine were selected an airframe inspired by the General Dynamics/Lockheed Martin F-16 fighter aircraft which was supposed to be equipped with a Pratt and Whitney F-100-PW-229-like engine. The reasons behind this specific selection are the following:

- Both of them comprise successful designs where the gas turbine engine is highly integrated with the airframe. The engine is embedded in the structure and it is of great interest to study the interaction of this specific installation.
- The linking component between the engine and the airframe is a fixed geometry intake which gives a maximum speed capability of around Mach 2 without compromising the performance and stability of the engine [26]. So it is quite challenging and interesting at the same time to try to create a geometry that is close to that design given the lack of any details referring to the actual component's configuration.
- Finally, the specific configuration is a well known aircraft with high number of open source documentation [26], [57].

3.2 Airframe Geometry

One of the most challenging parts in the progress of the present work, has been the creation of an accurate and clear geometry, capable of capturing the desired effects. And this because any details referring to the design of the F-16 airframe comprise proprietary information and as such they could hardly be found in the open literature. There were cases though where some information about this specific installation were found but even in these cases the chances were that these information were ''half true'' and the entire picture, as far as the actual installation's design is concerned, remained purposely concealed.

The process of creating such geometry was mainly based on information found freely on line. First a drawing with some cut views at different locations of the aircraft was come across in [27] and the general dimensions of the airframe, like its length, height and span, were located in [28]. Figure 3-1 presents the drawing with these cut views.

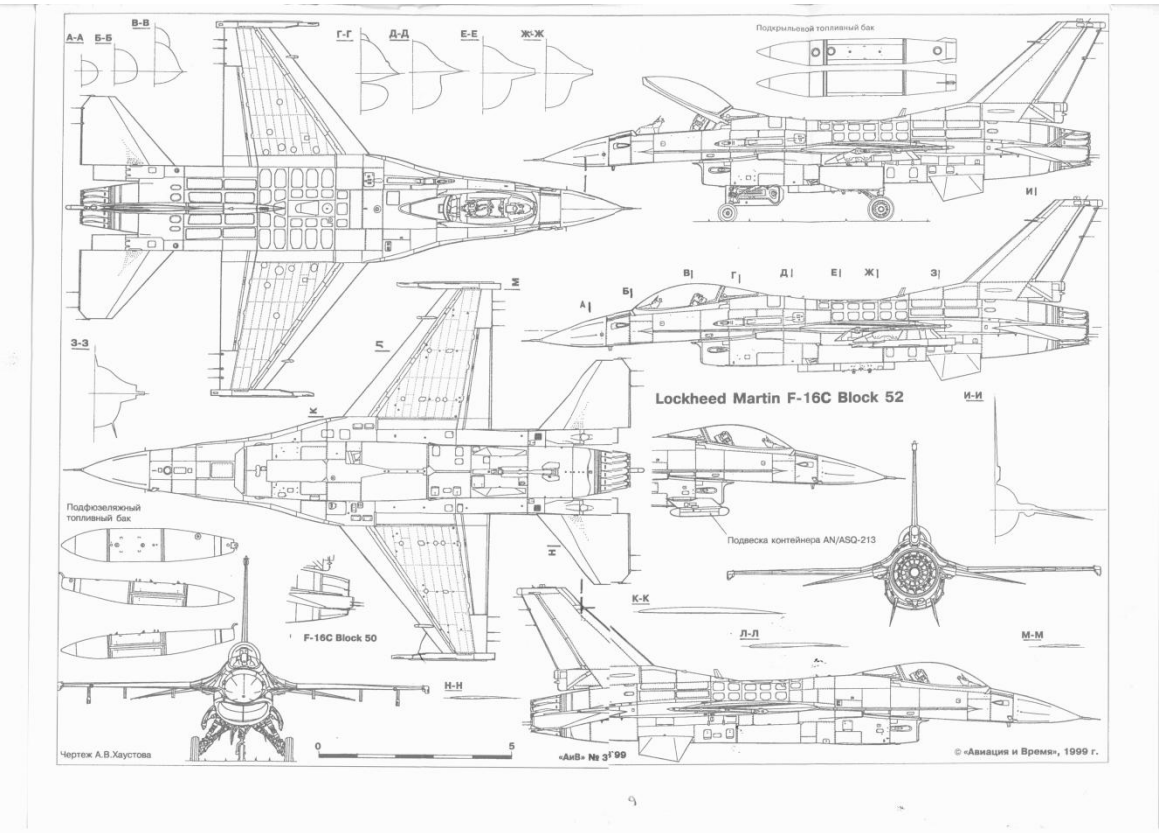

Figure 3-1 Sketch of an F-16 Aircraft with Different Cut Views [27]

Then, with the aid of the XY extract [28], these cut views were translated into vertex coordinates, having always in mind that every cut view through proper scaling should comply with the external dimensions of the aircraft. The acquired vertex data were finally imported in GAMBIT [29] where the capability of importing coordinates in a .txt format was really helpful and saved a lot of routine work.

In the next step the created geometry in GAMBIT, comprising only from points, was exported in an IGES format and imported into ICEM CFD. Lines connecting these points and surfaces oriented by these lines were created. It is worthy of mention that due to the complexity of the geometry many attempts had to be made in order

to end up with ‘’a water tight’’ geometry ready to be meshed. Any voids between the created surfaces needed to be carefully located and treated so that to prevent a possible failure in the creation of the mesh.

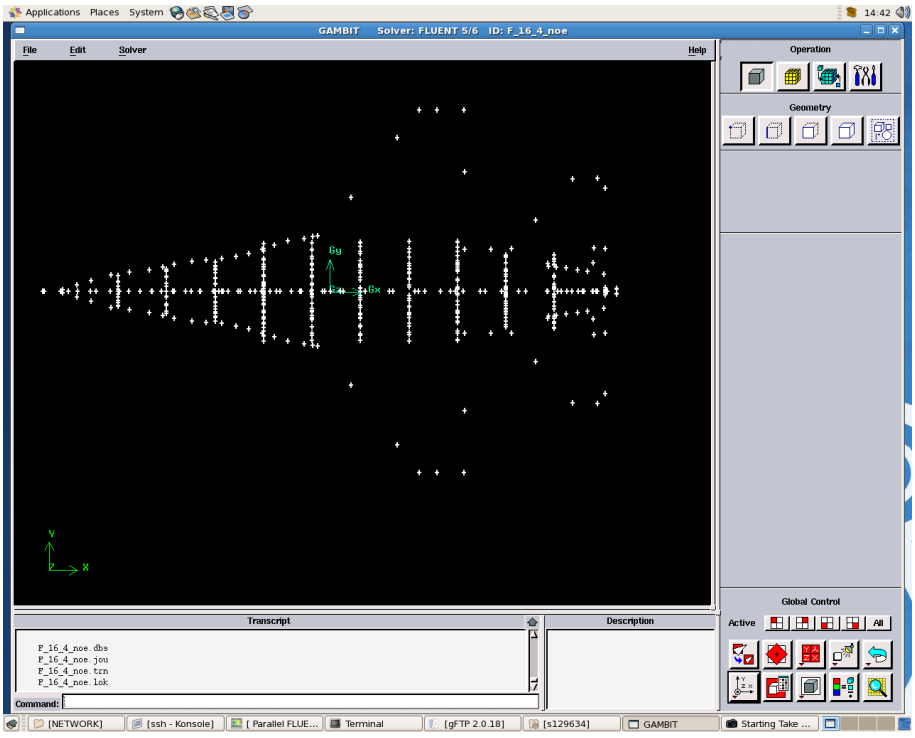

Figure 3-2 Vertex Data Imported into GAMBIT

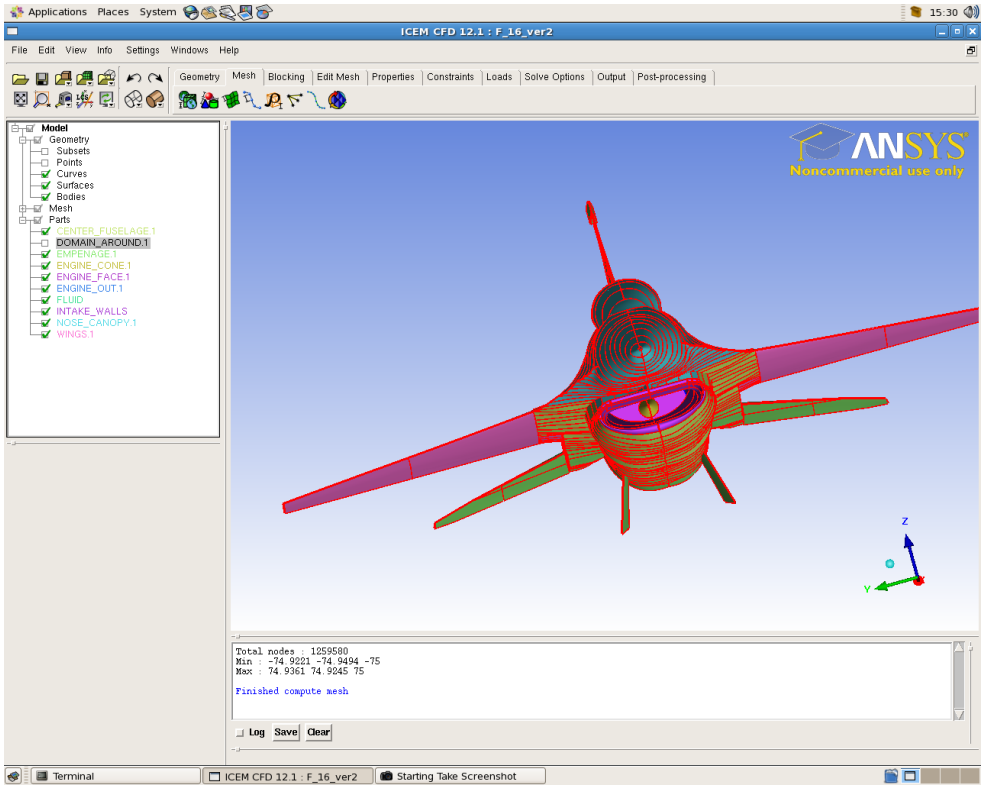

Figure 3-3 Aircraft Model Created in ICEM CFD

3.3 Intake Geometry

In the present study, the air intake system of the created geometry constitutes the point of interest. The reason is because the AIP, where distortion data were collected at, is located at the end of the intake. Some of the geometric features of the intake, as described in [26], are the following:

- Its geometry is fixed without any variable geometry parts.
- Its subsonic part is a diffusive duct with a gradually increasing cross section from the throat to the end.
- At the inlet the lower lip is blunt, while the upper is sharp.
- There is a 10in long splitter plate at the beginning of the intake which extends from the upper lip towards the nose of the aircraft.
- The intake is separated by the fuselage by a 3.3in diverter.

In the context of the present study, the aforementioned features were taken into account in the creation of the intake's geometry.

3.4 Air Intake-Engine Flow Demand Matching Process

Taking into account the great importance of creating a model with a reliable intake design and given the fact that details about its exact shape and size could not be found in the open literature, a preliminary design process needed to be undertaken.

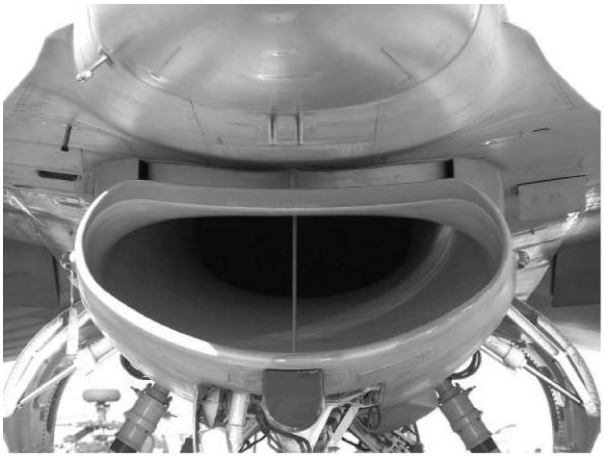

Figure 3-4 Fixed Geometry Intake on the F-16 Aircraft [53]

The position and the basic shape of the intake are both implied and restricted by the surrounding airframe structure. What needed to be considered though were

- the size of the throat area
- the rate of diffusion for the cross sectional areas from the throat to its exit, and
- the size of the outlet area at the engine's face.

These parameters had to be specified in such a way so that the air mass flow allowed to pass through the intake matched the demands of the gas turbine engine at the desired flight conditions.

In cases where the intake geometry is fixed, like the one studied in the present work, this matching process becomes more challenging, because the same geometry needs to provide the engine with the desired mass flow in the entire operating envelope.

The fixed intake throat was sized to accommodate the maximum engine corrected airflow at a throat Mach number of 0.75 [26]. Following the approach described in [17] for the sizing of fixed geometry intakes, this condition was assumed that happens when the aircraft flies at a high subsonic Mach number (≈0.9) and at a high altitude (at the tropopause, around 37,000ft altitude).

Running in Turbomatch a model for the baseline engine at the above conditions, resulted in getting the desired by the engine mass flow. The way this simulation model has been created is described in detail in Appendix B.

When it was taken into account the fact that at the engine's face the flow is subsonic and about 0.48 Mach [26], the sizing of the intake could proceed. The thermodynamic parameters (total and static temperature, total and static pressure) were based on an assumed 0.95 intake pressure recovery, a value that is within the typical range for subsonic flows (54).

Having all these data, the key geometric features of the intake geometry were calculated by using the 'Q-function' [17], which relates the Mach number (M) with the cross sectional area at a specific point, given the mass flow rate (W) and the total pressure (P) and temperature (T) at this point.

$$Q = \frac{W\sqrt{T}}{A \times P} = \sqrt{\frac{\gamma}{R}} \times \frac{M}{\left(1 + \frac{\gamma - 1}{2} M^2\right)^{\frac{\gamma+1}{2\times(\gamma-1)}}} \qquad (3.1)$$

Figure 3-5 below presents an outline of the resulted intake geometry (upper part), as it appears in the ICEM CFD environment. The gradual growth of the intake's cross sectional area from the throat to the exit (outlet), is presented in a graph form in the lower part of the same figure.

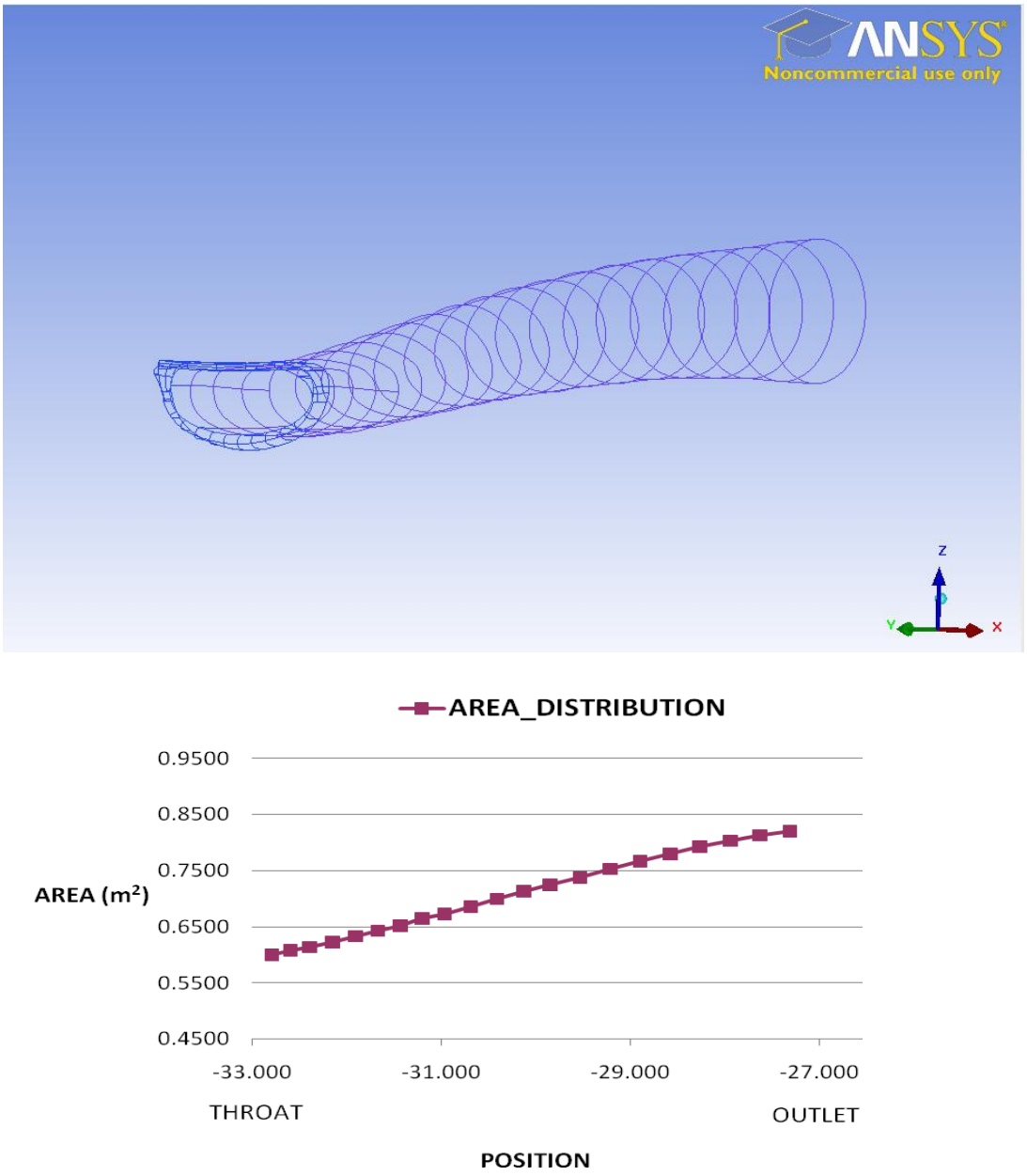

Figure 3-5 Intake Cross Sectional Area Distribution

Many similarities can be observed with the respective area distribution (fig. 3-6) of the F-16's intake [26], giving thus some credibility to the created geometry.

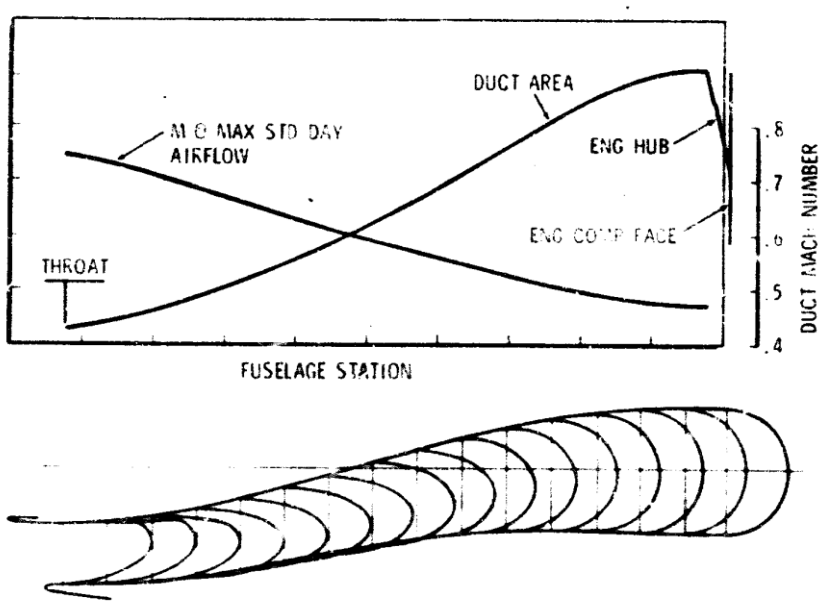

Figure 3-6 YF-16 Subsonic Duct Geometry and Area Distribution [26]

Another important geometric parameter of the intake is the contraction ratio (CR) which is defined as the ratio of major cross-sectional area of the intake (highlight area) divided by its throat area. The specification of this ratio implies the shape of the intake lip. Initially, and given the absence of specific details about this parameter, the intention was to create a visually smooth lip, which satisfies the surrounding geometry, sharper at the upper side blunt at the lower and to gradually optimize the design in case of unsatisfactory results.

3.5 Mesh Generation

Once the geometry was created the next steps in the process of setting up the numerical solution were first the definition and then the meshing of the flow region (computational domain).

The domain selected in the present work had a bullet shape comprising of a hemisphere and a cylinder. The radius of the hemisphere is about 12 times the length of the aircraft (=180m) and the length of the cylinder is more than 15 times the length of the aircraft (=250m). The aircraft model is placed inside the domain closer to its front part (in the hemisphere) leaving enough space for the exhaust

gases to sufficiently adapt with the surrounding undisturbed conditions before they reach the domain's boundary.

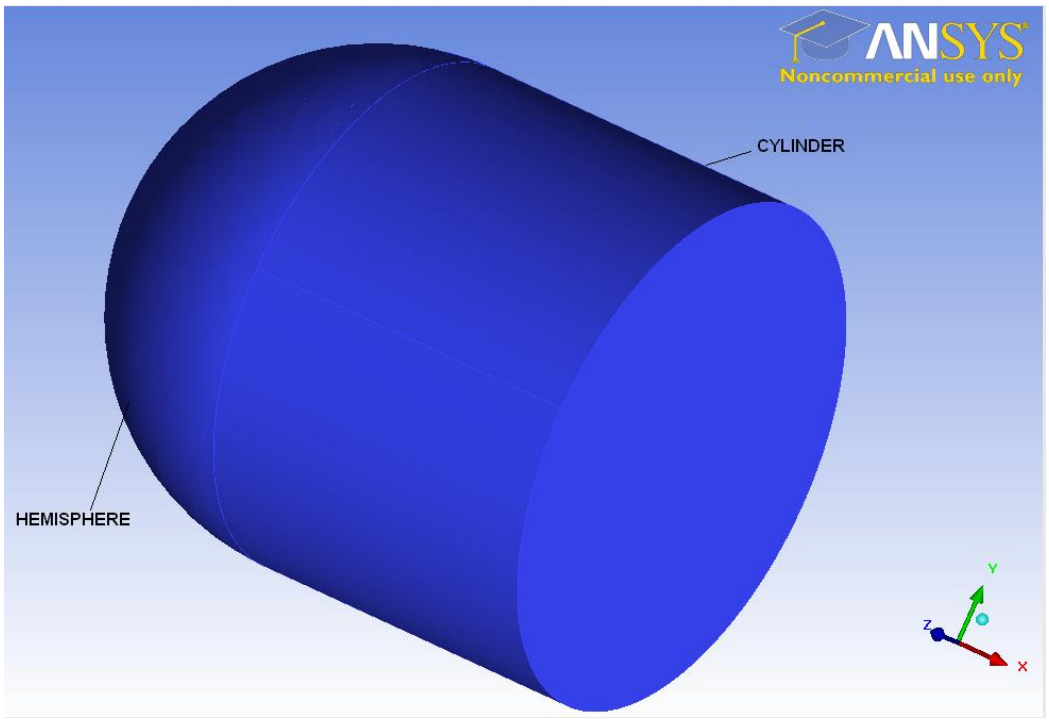

Figure 3-7 Computational Domain

The selected size of the domain was a compromise between computational cost and accuracy. On one hand the computational domain should have been big enough to allow the flow dynamics to be fully developed but on the other hand it should have been kept at a manageable size so that it could have been handled by the capabilities of the solving processor.

For the grid generation the approach of an unstructured mesh was adopted mainly due to the complexity of the model's geometry. The mesh was generated in ICEM CFD following a bottom up approach i.e. starting from a water tight geometry (without any gaps between the surfaces) which is a prerequisite for a successful mesh generation process, a surface mesh consisting of triangle elements was created on the aircraft.

The maximum curve size for each surface line was specified in such a way aiming first to avoid the creation of highly skewed elements and at the same time to generate a more fine mesh at the areas of higher interest (like inside the intake

where the airflow distortion data needed to be collected). For a better control over the created surface mesh the meshing parameters were set individually for each curve. Although it sounds like a time consuming approach, it saves much time by preventing later on mesh adaptations. The created surface mesh is presented in fig. 3-8 below.

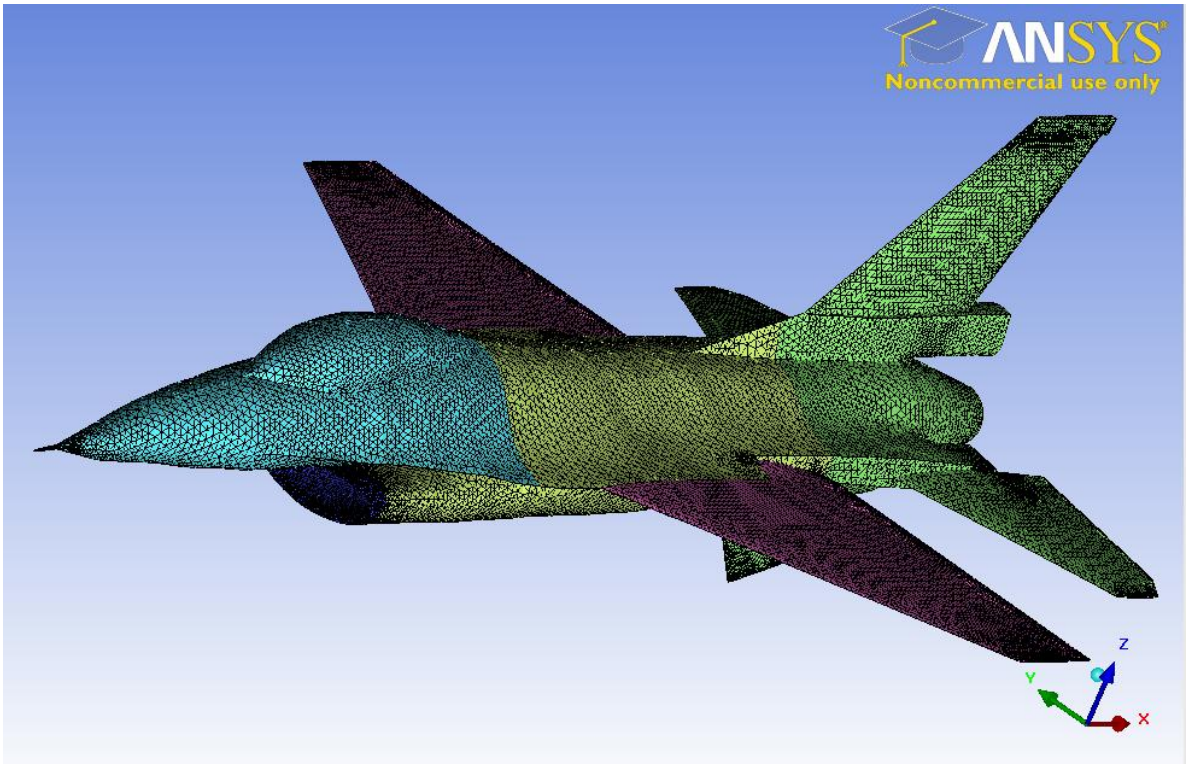

Figure 3-8 Surface Mesh

The volume mesh comprised of tetrahedral elements created following a Delaunay algorithm. In Delaunay meshing the general idea is to form a mesh where each triangle's three points lie on the edge of a circle that doesn't contain any other point [54]. This forces the mesh to have triangles that tend to be as close to evenly spaced as possible which helps to avoid highly skewed elements.

What's more, the Delaunay approach is quick in the creation of the volume grid and helps the grid to be kept in manageable sizes as far as the number of the created tetras is concerned.

The size of the tetra elements created to cover a volume is implied by the mesh settings applied to the surrounding surfaces. Wherever there is a need for extra refinement a grid density can be applied. In the present study such densities

were introduced inside the intake and behind the exhaust nozzle to help the capturing of the severe wakes created at that point.

A cut view of the created volume mesh is presented in fig. 3-9.

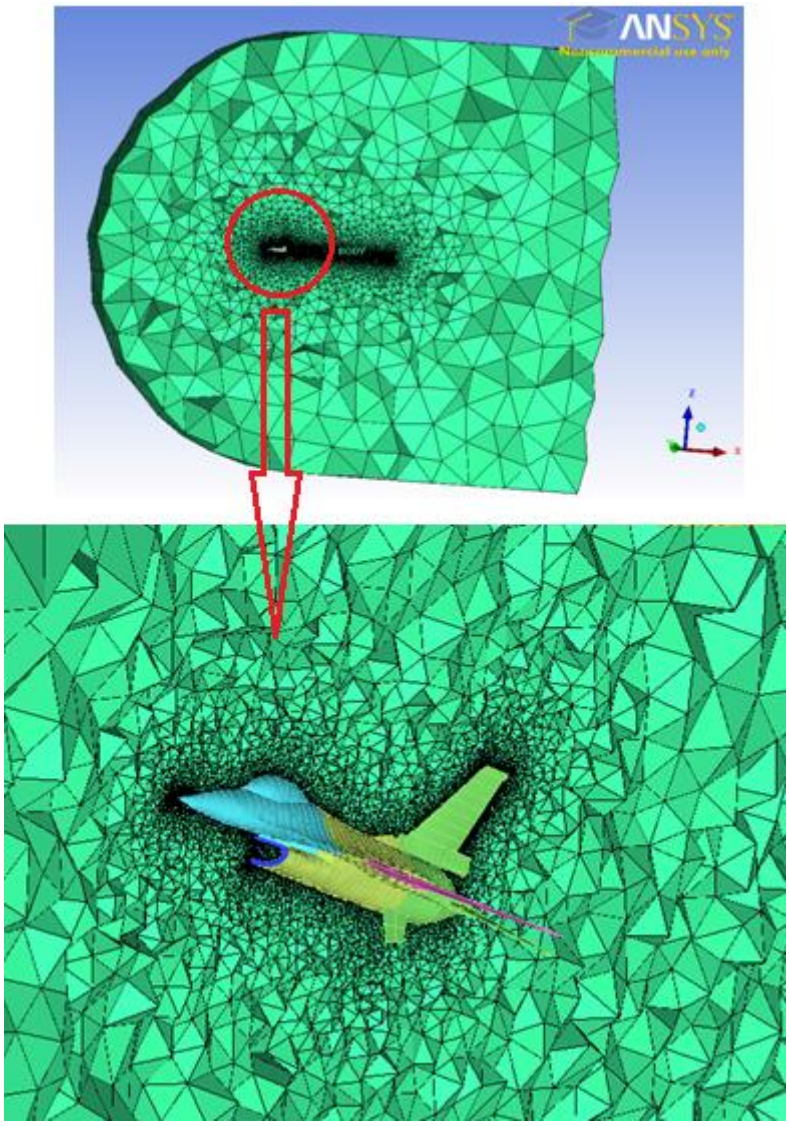

Figure 3-9 Cutview of the Volume Mesh

Finally, 13 prism layers (fig. 3-10) were created adjacent to all the wall surfaces to capture the boundary layer effects. The selected parameters were based on a Y+ value in the log-law region (30-300) and the height of the first node was set to 0.001m from the surface, relying on the wall functions of the chosen turbulence model to capture the space in between. The specific selection was made so that this value would remain the same and provide valid results at different flow conditions.

So, the intention was the created mesh to be used when different flight conditions of the aircraft were studied.

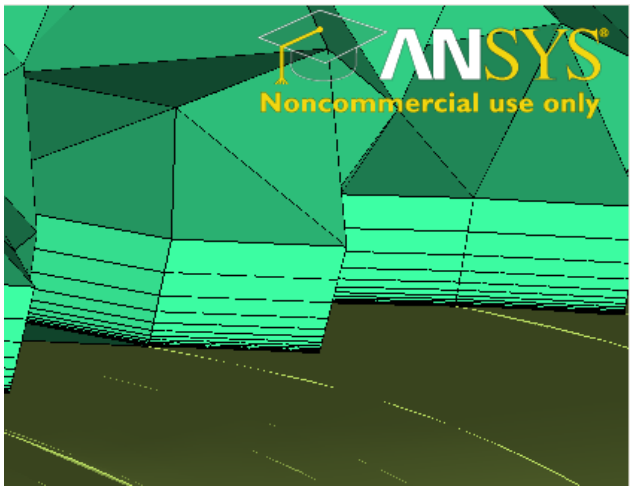

Figure 3-10 Prism Layers

Different cut views of the generated grid which comprises of about 3.5 million cells, are presented in figure 3-11 below.

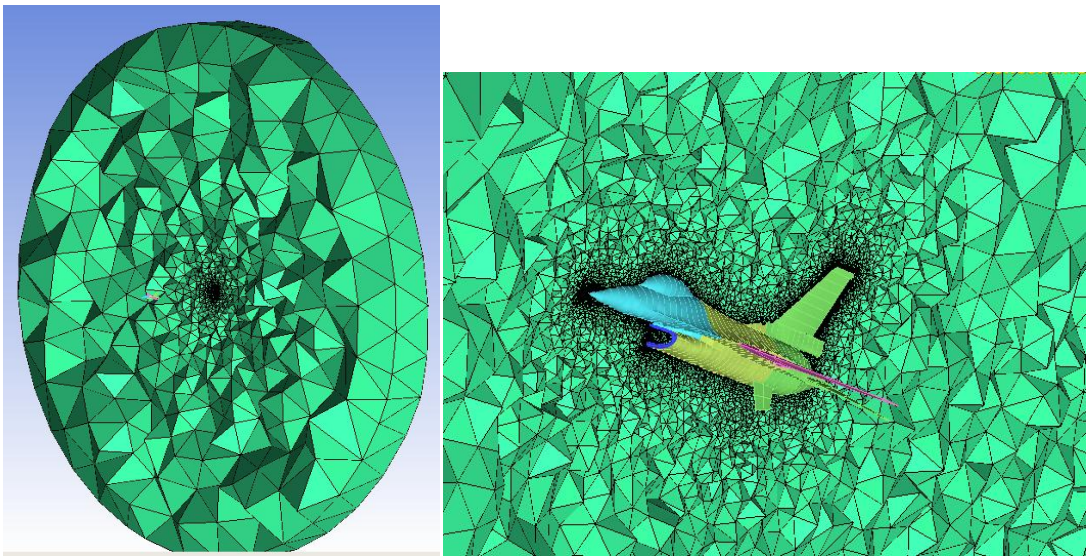

Figure 3-11 Cut Views of the Generated Grid

It worths mentioning that at the early stage of the study one thing that was of great concern was the creation of a manageable model, size wise, i.e. a model with a relatively small number of cells so that the testing of the initial settings on the solver could be achieved effectively and at a reasonable turnaround time. On the other hand this selection was not free from tradeoffs since the not enough resolution of

the domain might have been the culprit for convergence problems in the solving process.

3.6 Specification of Boundary Conditions

The next step of the pre-processing was the specification of the boundary conditions. The boundary conditions describe the physical flow behaviour and flow parameters at specified locations of the computational domain and in that way they augment the differential equations to completely determine the solution.

As it can be seen in fig 3-12, boundary conditions have been set,

- at the boundaries of the entire domain,
- at the intake's exit,
- at the engine's nozzle exit and
- at the solid walls of the geometry (aircraft structure).

Table 3-1 below summarizes the types of the CFD boundaries that have been selected for each one of the above boundaries of the computational model.

Table 3-1 Selected Types of CFD Boundaries

Boundary	Type of CFD Boundary
Domain's outer boundary	Pressure Farfield
Intake's exit	Pressure Outlet
Engine's nozzle exit	Pressure Inlet
Aircraft structure	Walls

The outer boundaries of the entire computational domain were defined as pressure far field and the flight conditions of the aircraft were defined through the settings of Mach number and direction of the incoming flow. At the examined altitude of 20,000ft, the ambient pressure is 46,557 Pa and the temperature is 248.5 K [31].

To complete the boundary condition settings with specifying the transported turbulence quantities, the turbulence intensity was set to 2%, since the flow at this point is expected to be moderately turbulent and the hydraulic diameter was set to 360m. The turbulence intensity, I, is defined as the ratio of the root-mean-square

of the velocity fluctuations, u', to the mean flow velocity u_{aver}. A turbulence intensity of 1% or less is generally considered low and turbulence intensities greater than 10% are considered high [32].

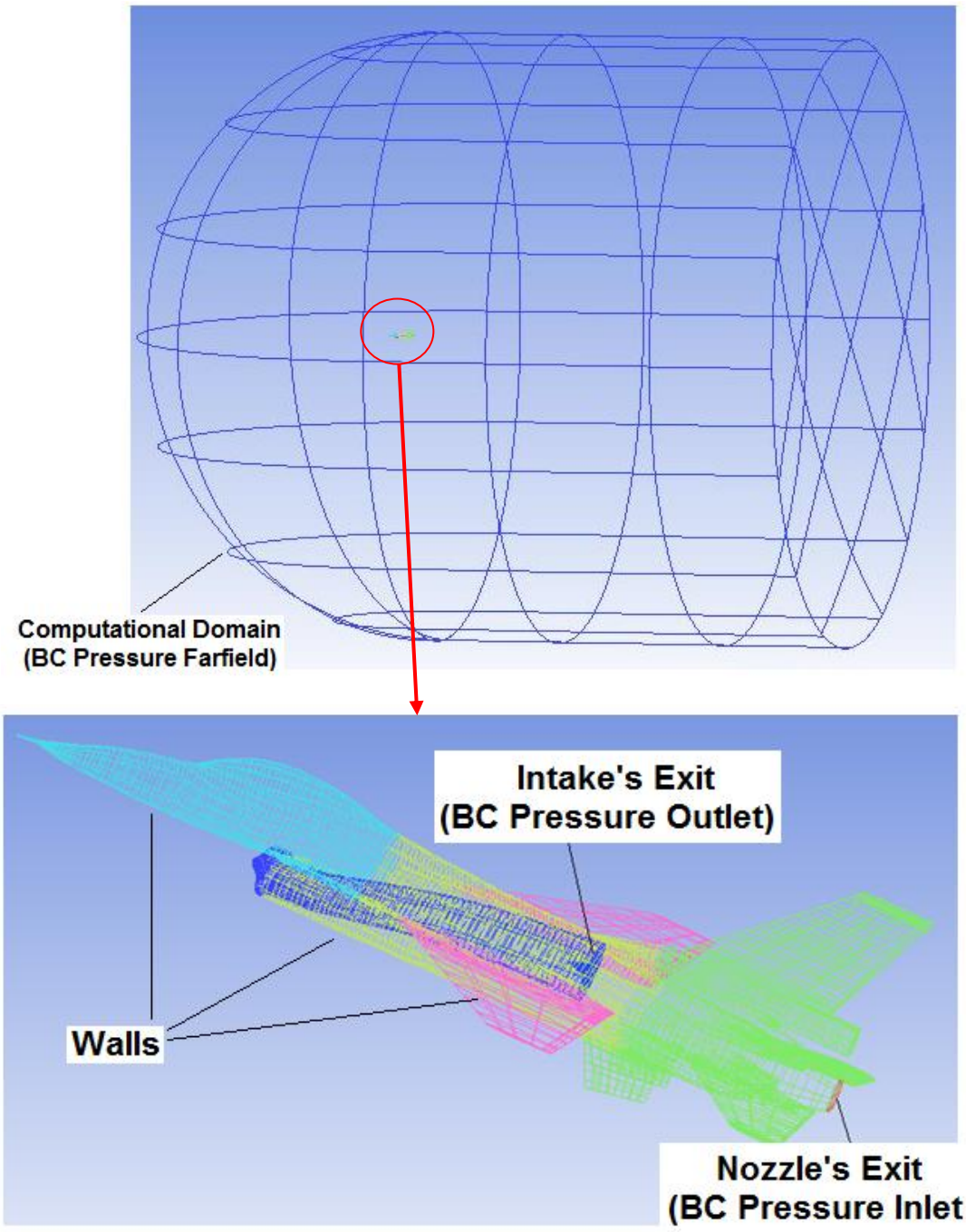

Figure 3-12 Boundaries of the Computational Domain

Inside the Computational Domain, on the aircraft's geometry the intake's exit and the nozzle's exit were respectively outlet and inlet boundaries (fig 3-12) and the

conditions applied at these boundaries denoted the coupling between the airframe and the engine (presence of the gas turbine in the domain). The engine's face which coincides with the exit of the intake was defined as pressure outlet. Since flow results at the intake's exit were of increased importance for the present study it was decided not to impose explicit boundary conditions at that plane. Instead, a simple accelerating duct (with a decreasing cross sectional area to the direction of the flow) was added behind that plane, as shown in fig 3-13. Inside that duct it was assumed that neither pressure losses nor work additions took place. By extending the flow region in such a way the flow was considered to be freely expressed at the plane of interest. The boundary of the domain had been moved downstream and the conditions imposed at that point did not directly interfere with the flow results at the AIP.

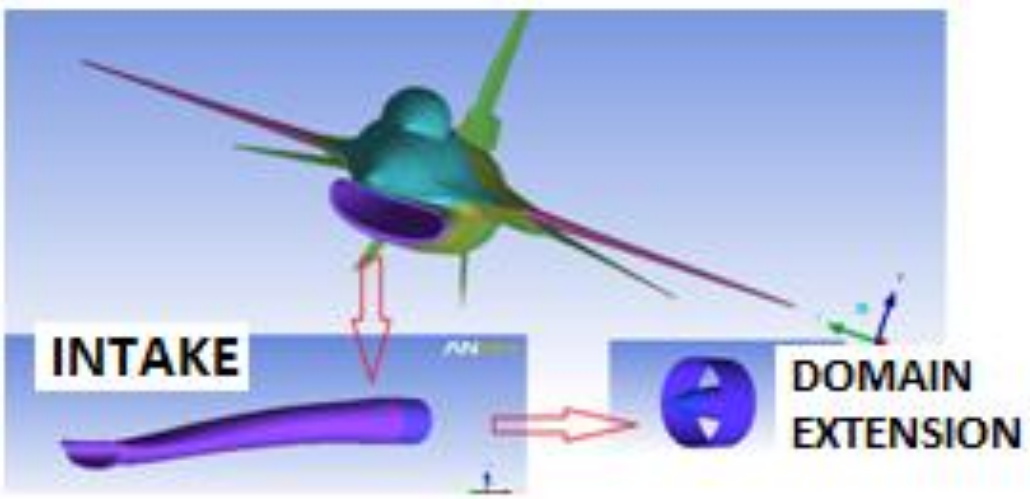

Figure 3-13 Computational Domain's Extension Behind the AIP

The boundary condition at the exit of that duct was set as pressure outlet and the value of Static Pressure needed to be specified at this point. This value in the simulation process creates sufficient ''sucking conditions'' at the intake's exit and in conjunction with the flight Mach number they both define the mass flow rate that will eventually enter the intake.

The required static pressure at this point was the result of an iteration process between TURBOMATCH and CFD. One of the prerequisites for this assessment was to create the baseline engine’s performance simulation model. The model's

parameters, e.g. FAN pressure ratio, overall pressure ratio, bypass ratio, TET, were based on information found in the open literature [52], [56], [57]. As for the important parameters that we did not have any information about, e.g. component effeciencies, pressure losses, cooling flows, these were continously adjusted, through engineering judgments and optimization techniques, in order to match the engine's DP known output (net thrust and SFC). Consequently, an engine with performance closely approximating that of the F100-PW-229 engine was finally modeled. Table 3-1 presents the baseline engine's design point performance data that were used for the validation of the performance simulation model.

Table 3-2 F100-PW-229 Engine Parameters

FPR	3.2
OPR	32.9
Mass Flow Rate (Kg/s)	114.1
TET (K)	1,750
SFC (g/s/KN)	20.96
Dry Fuel Flow (Kg/s)	1.67
Dry Thrust (KN)	79.2

Using the engine's performance simulation model a design point run at Sea Level Static (SLS) conditions was conducted in TURBOMATCH. Then three off design cases were also run simulating the operation of the engine at 0.35M, 0.6M and 0.85M flights at 20,000ft altitude.

In these performance calculations the FAN shaft relative rotational speed (PCN) was used as the driving parameter and its value was progressively adjusted until for each condition the resulted mass flow entering the engine, corresponded to the 100% of the design corrected airflow (CM).

The rationale underlying this selection was to create the same inflow conditions in all cases, for comparison purposes. In that way all the cases were compared on the same basis as far as the incoming flow is concerned. Then, the resulted mass flow rates were used in CFD as target values and the static pressure at the intake's exit was respectively adjusted so as to match the mass flow rate values

resulted from TURBOMATCH. The resulted values of static pressures were the following:

- 40,679 Pa at 0.35M
- 48,000 Pa at 0.6M
- 60,200 Pa at 0.85M

From the TURBOMATCH results the Total Temperatures at the same plane (intake's exit) were the following

- 255K at 0.35M
- 266K at 0.6M
- 284K at 0.85M

These temperature values were also introduced into CFD as temperature boundary condition settings.

To complete the boundary condition settings at the intake's exit the turbulence intensity was set to 7% since the upstream flow is considered quite turbulent and the hydraulic diameter was set to 0.961m taking into consideration the cross sectional area of the intake.

The engine's nozzle exit was defined as pressure inlet. The required Total Pressure and Temperature at this point were resulted from the aforementioned TURBOMATCH simulation runs for the three off design cases (0.35M, 0.6M and 0.85M flights at 20,000ft altitude). The resulted values were the following

- 151,987 Pa and 780K for the 0.35M flight
- 180,359 Pa and 816K for the 0.6M flight
- 225,418 Pa and 869K for the 0.85M flight

As for the static pressure at this point of the engine, its value was derived from the critical ratio of total to static pressure and based on a choked nozzle assumption.

$$\frac{P}{p}=\left(1+\frac{\gamma-1}{2}M^2\right)^{\frac{\gamma}{\gamma-1}}=1.85 \qquad (3.2)$$

The turbulence parameters at the engine outlet were set to 8% and 0.583 for the turbulence intensity and hydraulic diameter respectively.

The whole process of defining the boundary conditions through the interaction between Turbomatch and CFD is summarized in the flow chart presented in fig. 3-14.

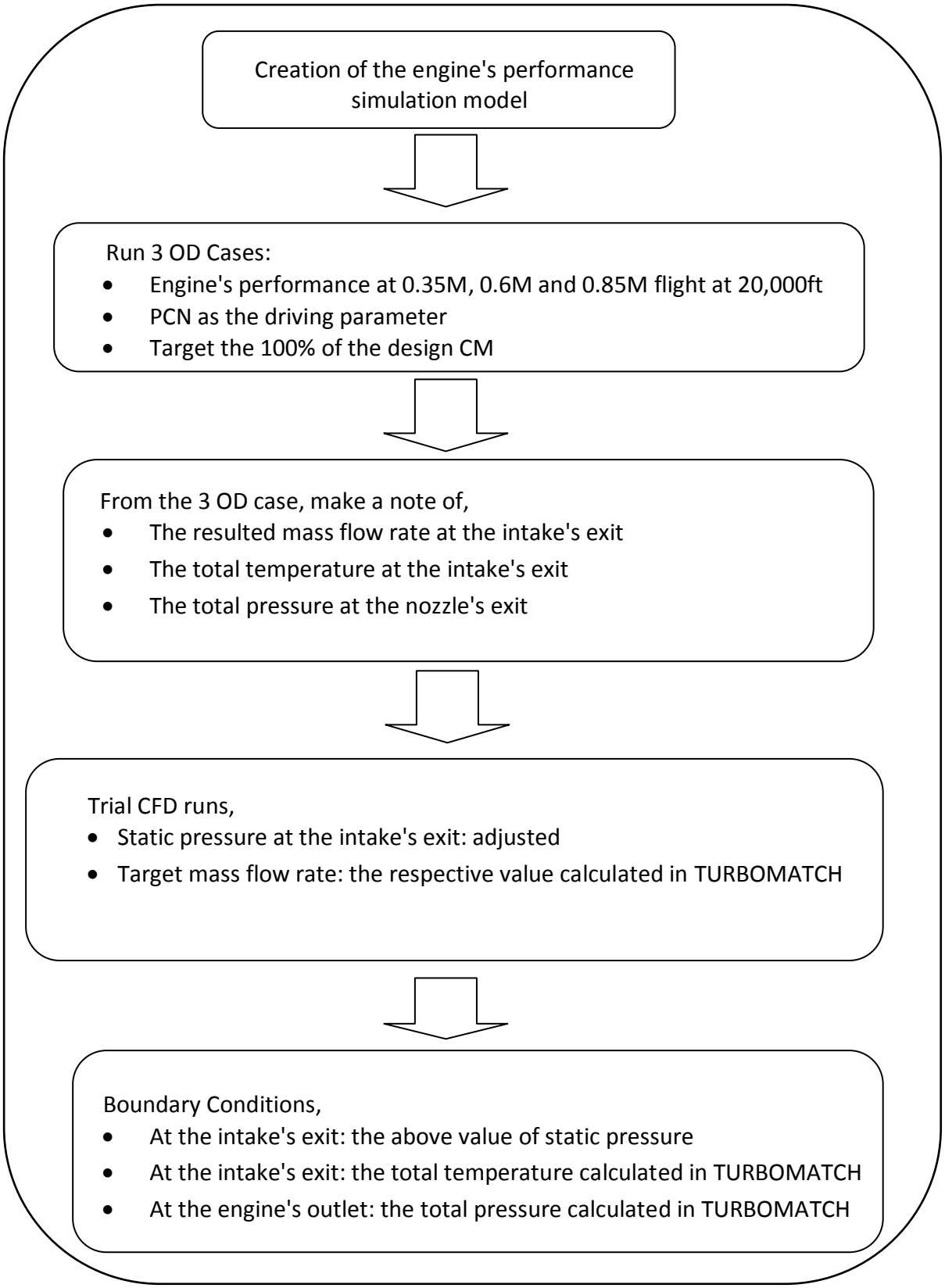

Figure 3-14 The Process of Defining the Static Pressure at the Intake's Exit

Finally, all the solid surfaces were defined as stationary walls with no slip as shear condition.

3.7 Solver Settings

Before the case was ready to run in the solver's environment, some final settings needed to be applied. The density based solver was selected which solves the governing equations of continuity, momentum and energy simultaneously i.e. coupled together [32]. Although this type of solver may require more computational time it was realized that it was more stable comparing to the pressure based solver where the adjustment of the under relaxation factors was necessary to start the calculation.

The energy model was enabled and the ideal gas was selected under the air material option. In setting the solution method, the implicit formulation and the 1^{st} order upwind discretization scheme were initially selected. Although the choice of 1^{st} order upwind discretization scheme has been also made in some other similar studies, like the swirl flow analysis of the port side F-5E intake using CFD [33], after 1000 iterations the solution was switched to the 2nd order discretization scheme aiming to more accurate results.

After having set all the above, the solution was ready for initialization where a first guess of the parameters, based on the boundary conditions set, would provide a good start for the solution.

3.8 Convergence Monitoring

The convergence of the solution was assessed in two different ways. The first one was by progressively tracking the imbalances (residuals) of the algebraic equations. The solution was considered converged when the residuals reached and stabilized at a low value in the order of 10^{-4}.

Along with examining the residuals two flow parameters were also monitored in the progress of the solution namely the mass flow rate at the intake's exit and the flow velocity magnitude at the same plane. Solution was not considered converged

not until these variables had been stabilized at a certain value that stayed unchanged in the progress of the solution.

3.9 Grid Dependency Study

Mesh structures of different sizes were developed to eradicate mesh dependency of the solution. The aim was the created mesh to be at a size that would neither compromise the finite computing resource nor incur large computational expense. The grid refinement strategies that were considered in the present work included global refinement of the entire model and local refinements at specific parts of the domain. The strategy of local refinements was finally adopted instead of the global one since the size and complexity of the geometry called for refinements applied locally at specific areas of the geometry and not globally since such an action would result in an unmanageable mesh. The difficulty in applying a constant grid refinement ratio globally in the computational domain boils down to the fact that the resulting size of the mesh would make the computational cost of the solution unaffordable. On the other hand, a too coarse mesh plays an intrusive role on the solution, which might lead to flow details not being captured.

To examine mesh influences, four different grids were utilized to simulate a 0˚ AOA and 0˚ AOSS flight scenario at 0.6M flight speed. In all cases the computational solutions were obtained with the code FLUENT by solving the Reynolds Averaged Navier–Stokes equations amended by those implied by the standard k–ε turbulence model with standard wall functions. The methodology followed aimed to quantify the mesh dependencies by monitoring some basic flow parameters, like the mass flow rate at the intake's exit and the area weighted flow velocity magnitude at the same plane.

At the first steps of the project, the size of the initially created mesh, was kept at a very coarse level since there was a need for quick feedback from any applied changes to the solver's settings. And a coarse mesh although it may intrude the solution it is not computationally expensive and it needs less time to give results. The size of that mesh was about 3.5 million cells and although it helped the process

of finding the proper solver settings it caused the solution to diverge when the second order differentiating scheme was selected.

After changing the meshing parameters for all the curves of the geometry to make them more 'node-populated' a more refined mesh of about 6 million cells was created. The refined mesh, a mid-Y cut plane of which is shown in figure 3-15, was imported into the solver and the solution was considered converged when the residuals were stabilized at the order of 10^{-3} (except continuity which stayed at the order of 10^{-2}) and the monitored parameters of mass flow rate and flow velocity magnitude at the intake's exit remained unchanged at certain values.

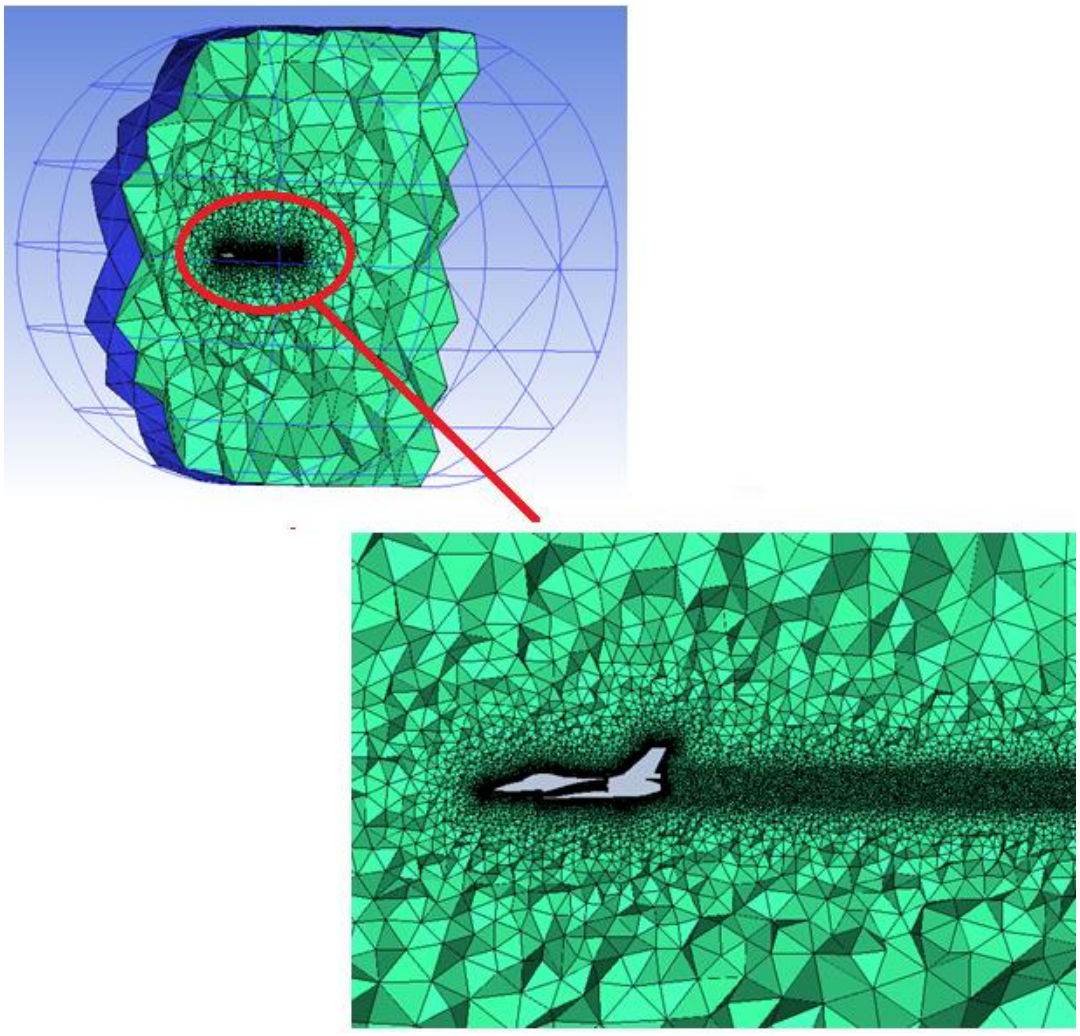

Figure 3-15 Mid-Y Cut Plane View-6 Million Cell Mesh

Figure 3-16 presents the plot of the residuals whereas in figure 3-17 the static pressure contours on the mid-Y plane of the domain are shown.

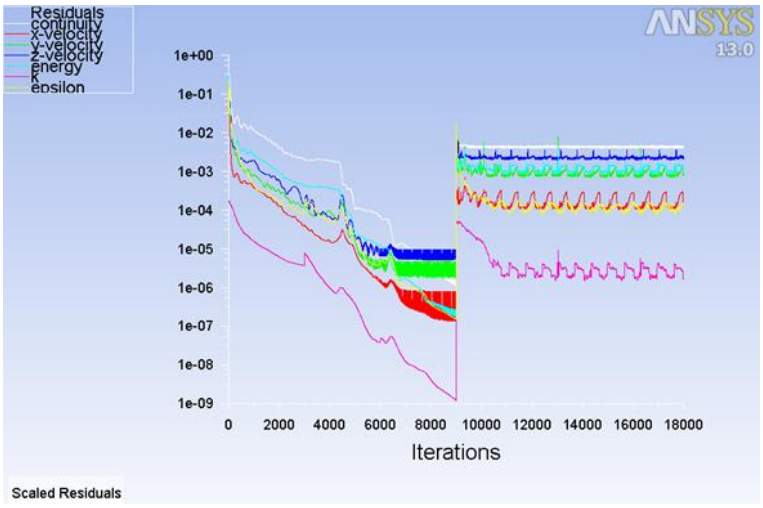

Figure 3-16 Residuals Plot - 6 Million Cell Mesh

The kick in the residuals' progress occured exactly at the point where the switch to the 2nd order discretization scheme took place.

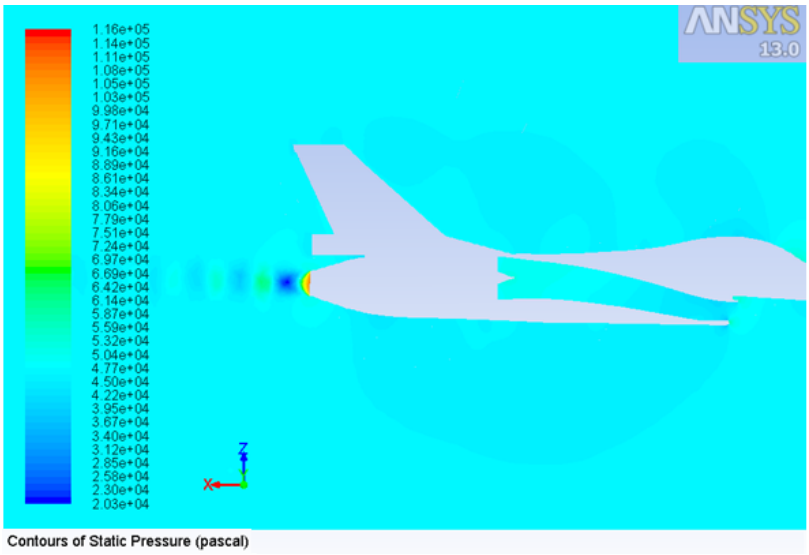

Figure 3-17 Static Pressure Contours - 6 Million Cell Mesh

By subsequently applying greater densities at specific areas of the domain, like inside the intake, behind the aircraft and behind the wings and horizontal stabilizers, three other grids were constructed. The sizes of them were at the order

of 8, 10 and 12 million cells respectively and figures 3-18, 3-19 and 3-20 show respectively the resulted static pressure contours.

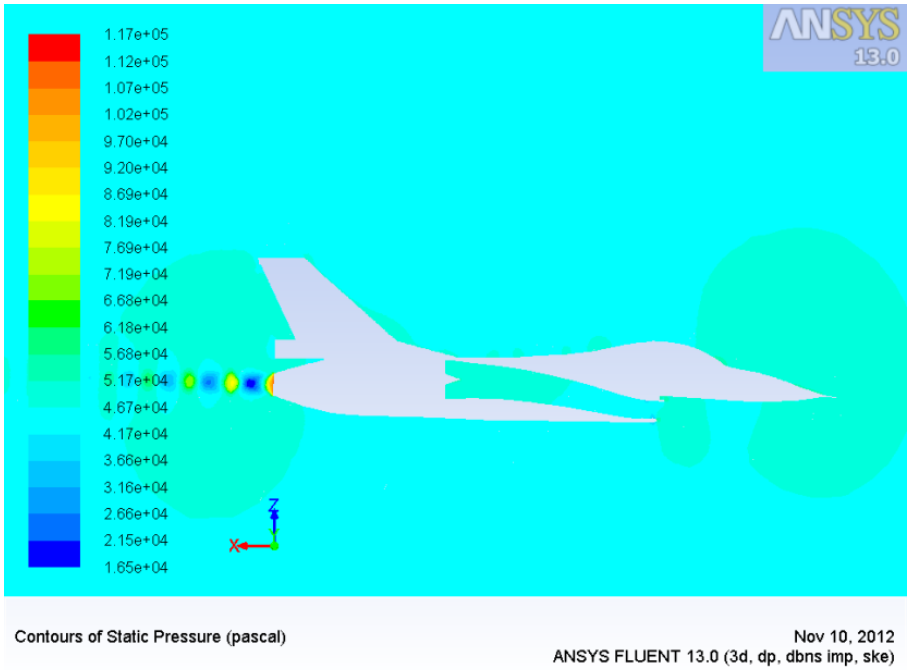

Figure 3-18 Static Pressure Contours - 8 Million Cell Mesh

Figure 3-19 Static Pressure Contours - 10 Million Cell Mesh

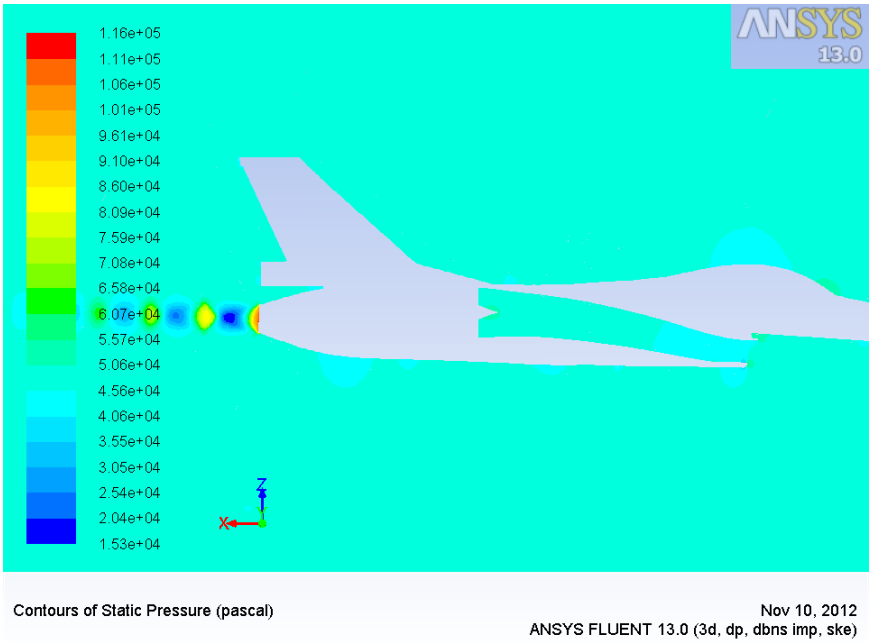

Figure 3-20 Static Pressure Contours - 12 Million Cell Mesh

To quantify the mesh dependency, the predicted by the CFD simulations parameters of area weighted average flow velocity magnitude and mass flow rate at the engine's face were graphed against the number of the cells of each of the above tested grids. The resulted graphs are presented on figures 3-21 and 3-22 respectively.

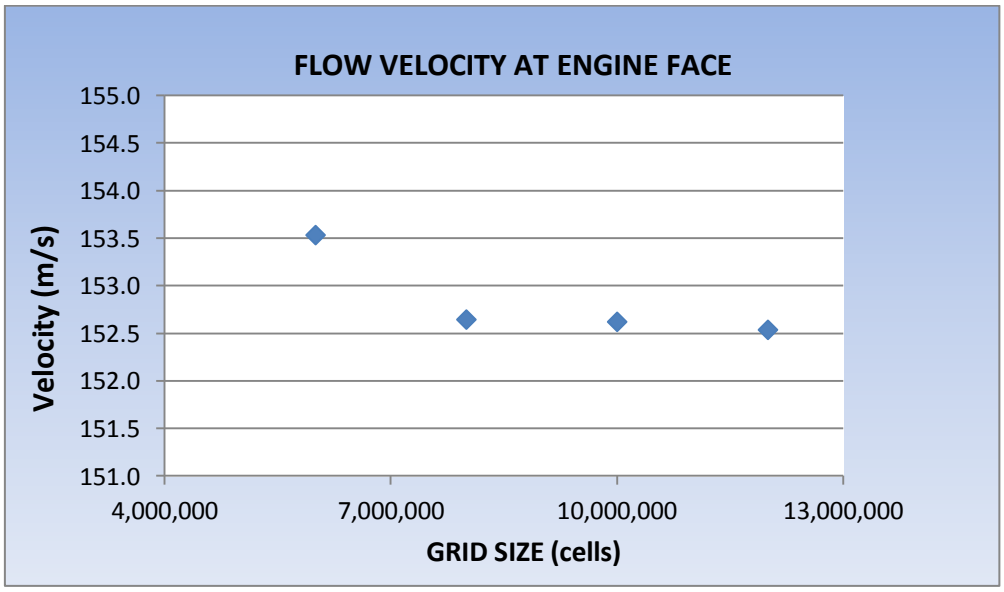

Figure 3-21 Influence of Grid Size on Monitored Flow Velocity at Engine Face

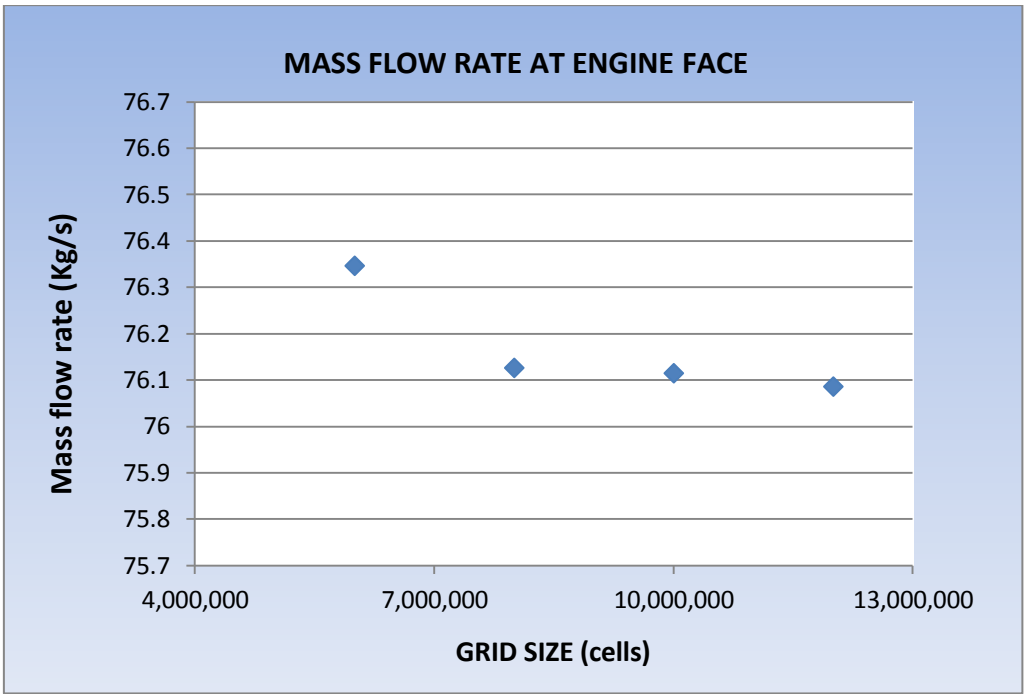

Figure 3-22 *Influence of Grid Size on Monitored Mass Flow Rate at Engine Face*

Looking at the above figures it is clearly revealed that grids consisting of more than 8 million cells are in the asymptotic region. As such, the usage of grids of that size is a good compromise between affordable computational cost and acceptable numerical uncertainty. Based on that, the simulations required by the present study were run utilizing 10 million cell models.

3.10 Model Geometry Dependency Study

In CFD, the set of basic equations that govern fluid flow are discretized and solved numerically within a finite computational domain. In the present study, the flow domain inside the aircraft's intake, was initially terminated at the engine's face where a boundary condition of pressure outlet was imposed. The fact that explicit boundary conditions were imposed at that point added an extra constraint to the flow, because instead of being fully expressed it (the flow) was trying to match the boundary conditions imposed by the user.

Given the fact that the plane of interest for the present study was exactly at that point (engine's face) it was decided to extend the computational domain beyond that point. In that way, the flow would be less manipulatively expressed at the plane of interest and the boundary conditions would be imposed at a point which was downstream of it.

An ideal way to do that would have been to add the exact geometry of the FAN including the three stages of blades and vanes of the baseline engine. But the geometries of these items are proprietary information and no data about their design could have been found in the open literature. Adding to that, the size of the model would have been so much increased that no computational resources, at least not at the author's disposal, would sustain such a simulation.

Instead of that a more simplified and viable idea was implemented. A simple accelerating duct (cross sectional area decreasing to the direction of the flow) was added behind the engine's face (figure 3-23). With the addition of that duct, the flow was fully expressed at the plane of interest and the boundary conditions were imposed at a point which was downstream of it.

Inside the duct which was added to the geometry, it was assumed that neither pressure losses nor work additions take place. As such, the total pressure and total temperature of the airflow remained unchanged.

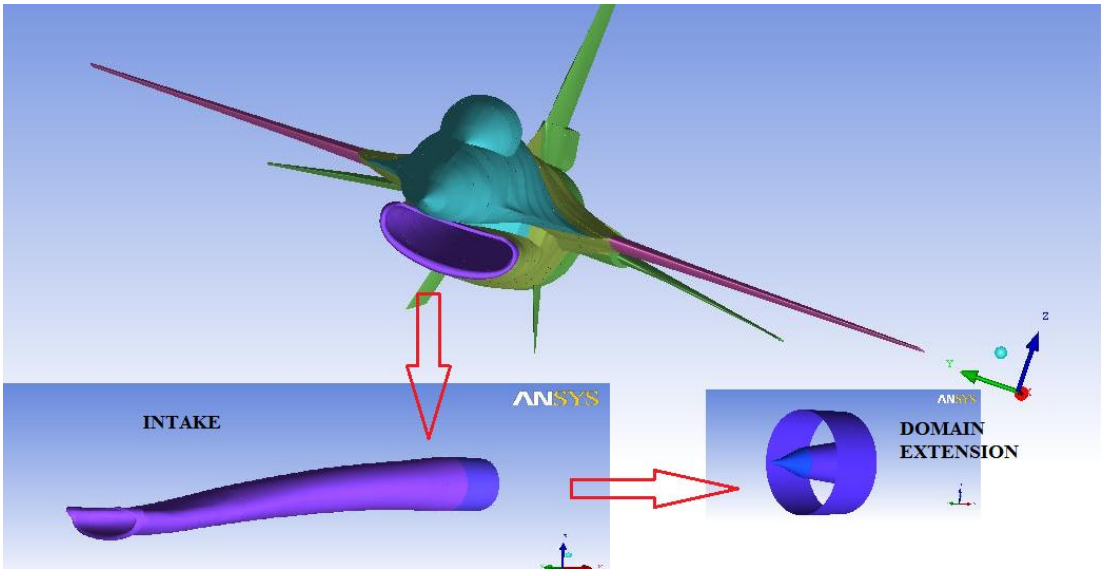

Figure 3-23 Model Geometry and Computational Domain Extension

To investigate how the extension of the computational domain would affect the solution, three different grid configurations were examined. In the first one the length of the extension was 0.53m, which is the length of the FAN module of the baseline engine (F100-PW-229) [56]. In the second and third grid configurations the length of that domain was doubled and tripled respectively (figure 3-24). In the three grid configurations the exit area was kept unchanged. Only the length of the added volume varied to match once, twice and three times respectively the actual length of the F100-PW-229's FAN module.

Figure 3-24 Computational Domain Extension Variable Length

The three resulted meshes, the size of which was about 10 million cells, were imported into the FLUENT solver to examine the influence of the domain extension on the solution. The case chosen to test this influence was a flight scenario with AOA and AOSS namely, flight with 0.6M at 20000ft altitude with 16 degrees of AOA and 16 degrees of AOSS. The turbulence model selected was the k-ε standard with standard wall functions.

Figure 3-25 below presents the resulted total pressure contours at the plane of interest for the three different configurations. It is clearly revealed that the profiles are identical giving credits to the independency of the solution on the domain extension's length.

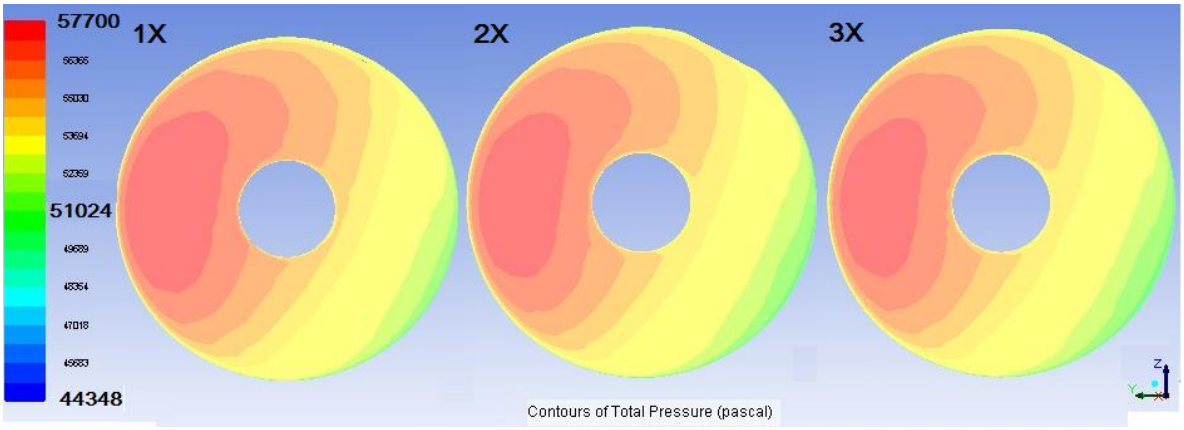

Figure 3-25 *Total Pressure Contours at the Engine's Face with Varying the Domain Extension's Length*

To further elaborate this statement, the data shown in Table 3-3 were collected during the post processing of the three different cases. These data refer to the area weighted average total Pressure at the engine's face and the mass flow rate at the engine's face. Again the results, although not identical, they were close to each other (the difference is in the range of 1%) allowing us to consider that the length of that extension added to the computational domain did not affect the solution. For computational economy reasons for the rest of the tested cases, it was chosen to use the grid configuration with the single length extension.

Table 3-3 Engine Face Results with Varying the Domain Extension's Length

	Engine Face			
Domain Extension	Area Weighted Average Total Pressure (Pa)	% Variation	Mass Flow Rate (Kg/s)	% Variation
1X	55,248.3	-	73.2	-
2X	55,020.5	-0.412	73.8	0.820
3X	54,952.5	-0.535	74.0	1.093

3.11 Selection of Turbulence Model

The selection of Turbulence model plays significant role in numerical simulations since the successful modeling of the turbulent flow greatly increases the

quality of the acquired solution. The term 'successful modeling' implies the implementation of a turbulence model that will better capture the flow phenomena.

In the present study wall turbulence and free turbulence are expected due to the position of the aircraft in the middle of the flow field and also due to the different velocities that the flow layers may have while moving in the free stream region and interacting with the disturbed by the aircraft, flow. The prism layers of the created mesh, for capturing the boundary layer effect, were built based on a Y+ value greater than 30. That means that the first node of the grid, next to the walls, was placed in a considerable distance from them (log-law layer) and as such a turbulence model with wall functions needed to bridge the flow results with the solution variables in the viscosity-affected area [58].

In order to examine any influence on the solution that the selection of the turbulence model may had, three variants of the k-ε turbulence model were tested namely the standard version, the k-ε RNG and the k-ε Realizable.

The RNG k-ε model was derived using a statistical technique called renormalization group theory, to the instantaneous Navier-Stokes equations. It is similar in form to the standard k-ε model, however includes some refinements in that it has correction terms for swirling flow, low Reynolds number flow, and flow with high velocity gradients [5]. The realizable *k*- ε model contains a new formulation for the turbulent viscosity. Also, a new transport equation for the dissipation rate, ε, has been derived [4].

All three models were tested in two different flight conditions in order to duplicate any potential findings. Flight at 0.35M with 8^0 AOA and 8^0 AOSS was the first one, whereas flight at 0.85M with 8^0 AOA and 16^0 AOSS was the second one. The results obtained with the above referenced Turbulence Models are resumed in the following figures, where the total pressure distribution at the engine's face is shown.

Figure 3-26 reveals that the total pressure distribution differs depending on the utilized Turbulence Model. The high total pressure area depicted with the red colour on the AIP plane differs in size between the three tested cases. Based on this observation, it can be safely assumed that the three tested turbulence models provide different results.

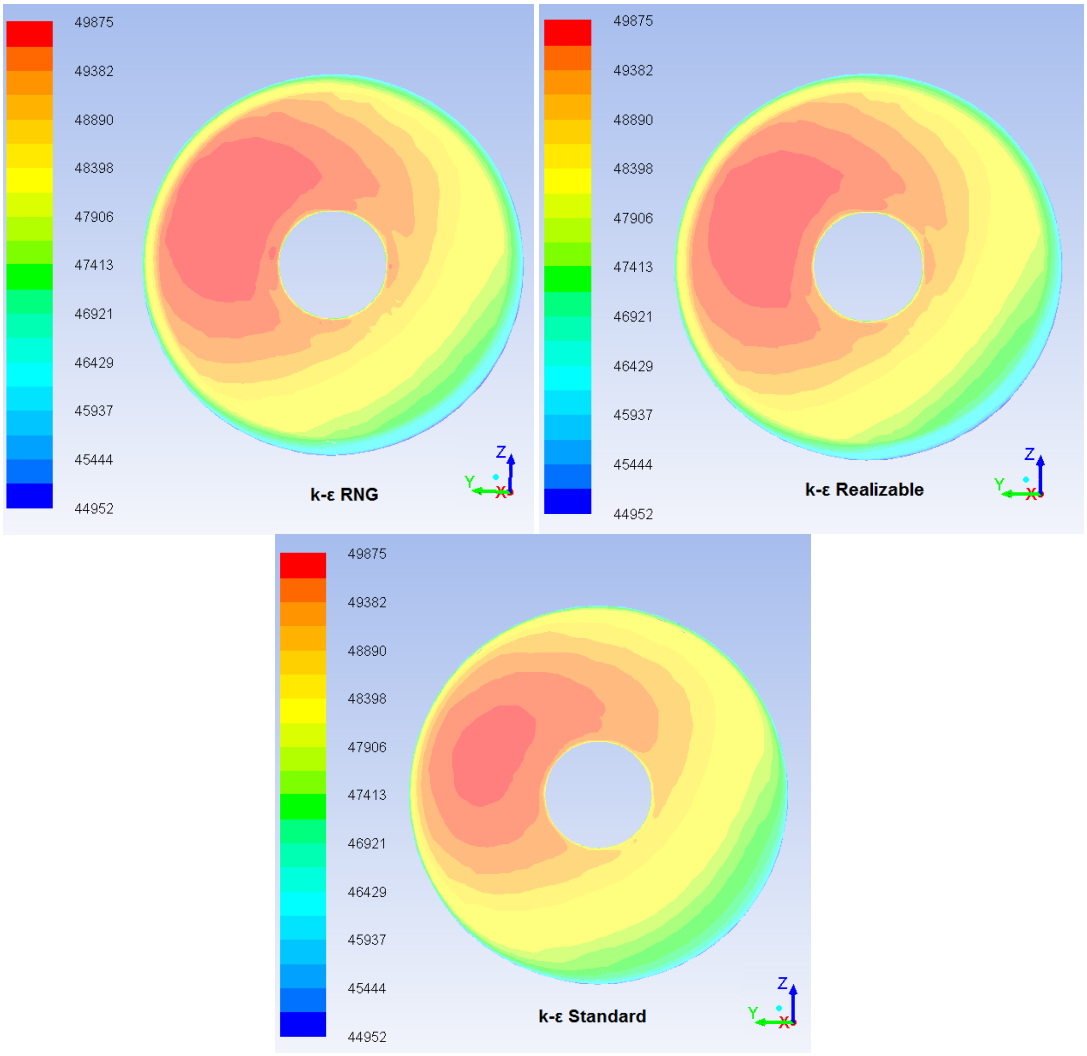

Figure 3-26 Total Pressure(Pa) Contours at the Engine's Face with Varying the Turbulence Model-Flight at 0.35 with 8° AOA and 8° AOSS

This statement duplicates its truth looking at figure 3-27, where again the k-ε Realizable's visualized results show that the total pressure distribution differs between the three selected turbulence models. In that figure it can be observed that both the RNG and the realizable variants of the k-ε turbulence model predict a low pressure area of about the same size at the 3 o'clock area of the engine's face plane. It is highly likely this low pressure area to occur at that location due to the increased value of the AOSS. The k-ε standard turbulence model though predicts a smoother variation of the total pressure at that area.

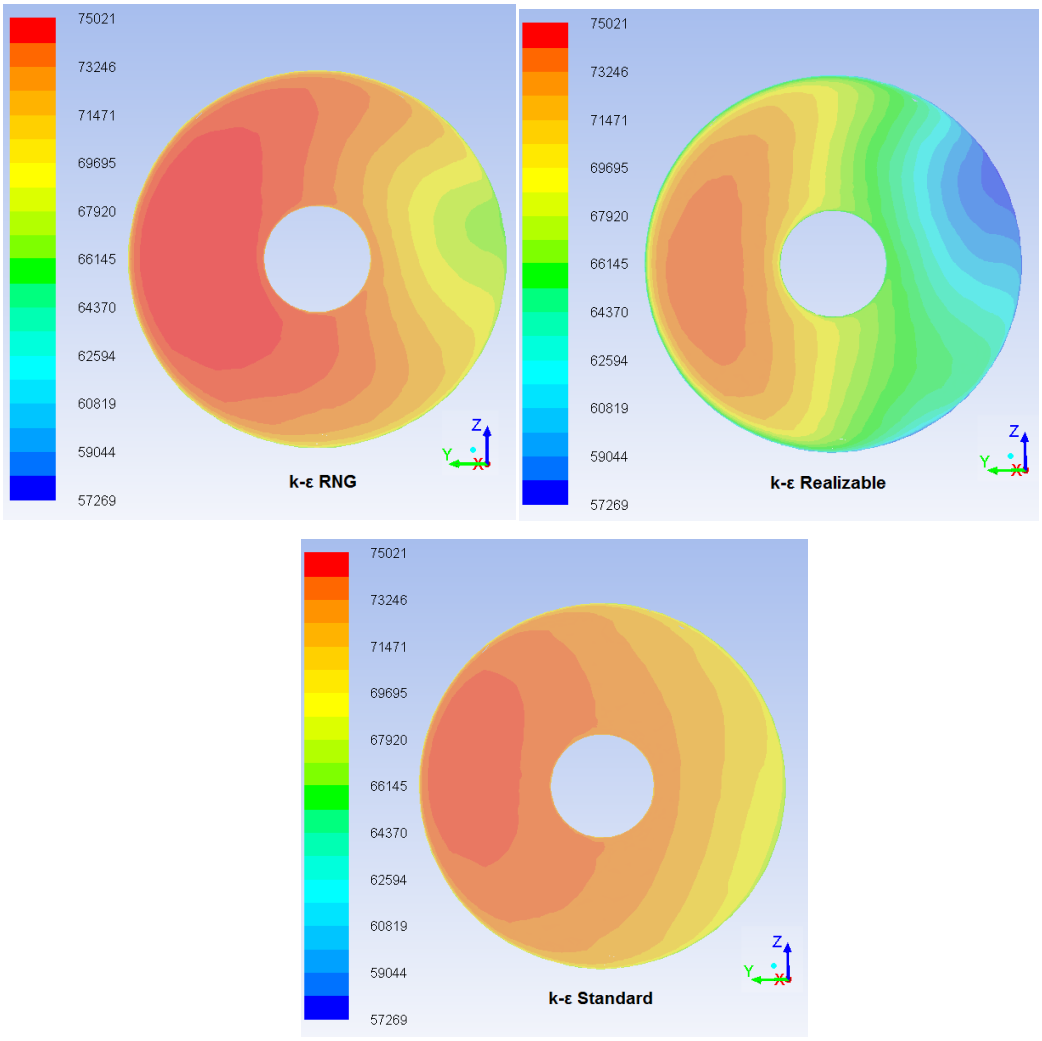

Figure 3-27 Total Pressure(Pa) Contours at the Engine's Face with Varying the Turbulence Model-Flight at 0.85 with 8° AOA and 16° AOSS

More quantitative difference among the examined models is observed when comparing predicted information (Area weighted average Total Pressure and Mass flow rate) at the engine's face plane for the above referenced flight conditions. The results are shown in Table 3-3 below. The results, although they differ they are really close to each other.

Table 3-4 Engine Face Results with Varying Turbulence Models

	Engine Face							
	0.35M, 8^0 AOA and 8^0 AOSS				**0.85M, 8^0 AOA and 16^0 AOSS**			
Turbulence Model	**Area Weighted Average Total Pressure (Pa)**	% Variation	**Mass Flow Rate (Kg/s)**	% Variation	**Area Weighted Average Total Pressure (Pa)**	% Variation	**Mass Flow Rate (Kg/s)**	% Variation
k-ε standard	48,613.68	-0.70	56.67	1.12	71,788.64	0.16	78.53	-0.20
k-ε RNG	48,677.46	0.05	56.14	0.18	72,324.39	0.91	80.69	2.54
k-ε Realizable	48,651.95	-	56.04	-	71,670.71	-	78.69	-

Based on the above findings and having no other experimental data to validate the obtained results and to clearly reject or support one of the three Turbulence Models, it was decided to use the k-ε Realizable variant since:

- it neither overestimates nor underestimates the flow phenomena taking place in the present study,
- it seems to be more accurate than the k-ε standard model since it predicted the low pressure area at 3 o'clock on the engine's face plane, for the flight attitude of 0.85M with 8˚ AOA and 16˚ AOSS which is highly likely to occur due to the increased AOSS,
- its usage is suggested by the ANSYS FLUENT when the case is finally checked before start iterating, and it is recommended for better prediction of the turbulent viscosity [6].
- this model is also likely to provide superior performance for flows involving rotation, boundary layers under strong adverse pressure gradients, separation, and recirculation [32], like the flow field inside the intake.

Another turbulence model considered was the k-omega SST one, which predicts with better accuracy flow cases where flow separations may occur (59). This model though does not provide standard wall functions in FLUENT [32] and it uses enhanced wall functions as the near-wall treatment [35] . As such it needs the mesh to be fully refined near the walls (y+≈1). The complexity of the geometry in the present study though did not allow the usage of this model since such an action

would have increased the already big size of the mesh and it would have made its solution unaffordable.

Among the default turbulence models of FLUENT, only the k-epsilon and the Reynolds Stresses Model (RSM) incorporate wall functions. The RSM, which is a 7-equation advanced model was tested on two flight conditions

- 0.35M with 0˚ AOA and 8˚ AOSS
- 0.85M with 8˚ AOA and 16˚ AOSS

During the solution of both cases instabilities were noticed. The residuals did not fall below 10 as it can be observed in fig. 3-28 and reverse flows were also noticed . The 2nd case actually diverged from the beginning of the solving process. To help the convergence of the solution, the .inp files in both cases were set in such a way so that the case ran for a while in 1st order differentiation scheme and after stabilization had occurred it was switched to 2nd order. But the results were unsatisfactory. One possible explanation of this behaviour may stem from the fact that in this model the momentum and turbulence equations are tightly coupled and they may demand a better refinement of the mesh to help the convergence of the solution.

Taking into consideration the results from these attempts, the selection of the k-epsilon realizable turbulence model was more sustained.

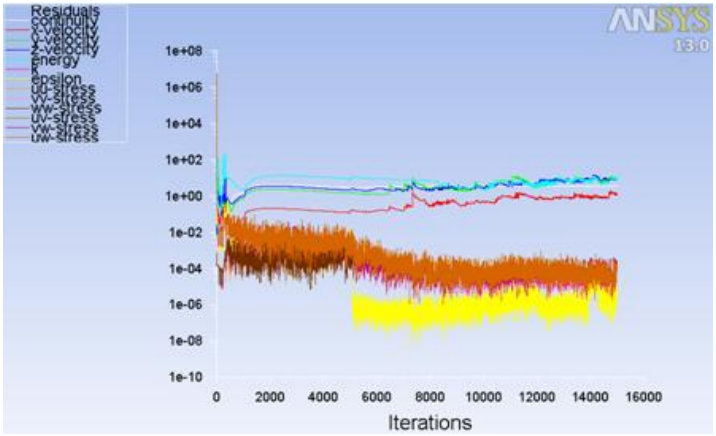

Figure 3-28 Residuals Plot for the 0.35M Flight with 0˚ AOA and 8˚ AOSS and the RSM Turbulence Model Selected.

4 FULL SCALE AIRCRAFT FLOW RESULTS

4.1 Selection of Flight Conditions to be Tested

The next step in the progress of the present work was to define the flight conditions that were to be tested in order to examine the influence of the aircraft's attitude onto the engine's performance.

In all tested flight attitudes, it was chosen the flight altitude to remain unchanged at 20,000ft. In that way only the aircraft's attitude changes would affect the engine's performance the study of which was one of the objectives of the present study.

The variation of aircraft's attitude was expressed by altering the AOA and AOSS. The same attitude conditions were tested at three different flight speeds, namely 0.35M, 0.6M and 0.85M flights. Based on that, the 27 resulted conditions that were studied are presented in Table 4-1 below. The selected flight attitudes comprise a rather mild sample from this aircraft flight envelope which was considered suitable for the testing of a newly developed model.

Table 4- 1 Tested Flight Conditions

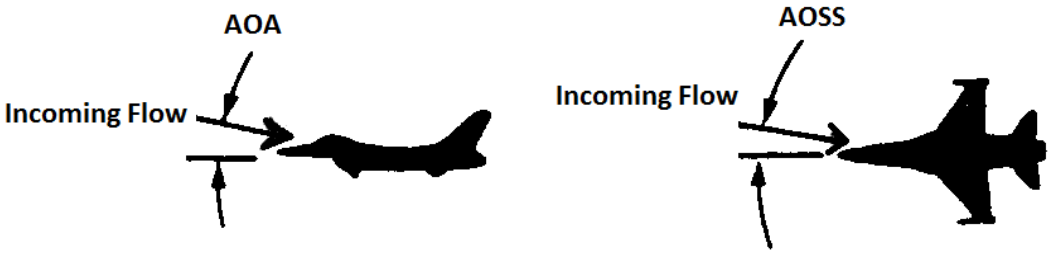

	Altitude (ft)	Flight Speed (M)	AOA (deg)	AOSS (deg)
1	20,000	0.35	0	0
2			8	0
3			16	0
4			0	8
5			0	16
6			8	8
7			8	16
8			16	8
9			16	16
10		0.6	0	0
11			8	0
12			16	0
13			0	8
14			0	16
15			8	8
16			8	16
17			16	8
18			16	16
19		0.85	0	0
20			8	0
21			16	0
22			0	8
23			0	16
24			8	8
25			8	16
26			16	8
27			16	16

4.2 Flow Field Around the Airframe's Geometry

The finalized simulation model was tested in the previously mentioned 27 different flight conditions. Three different flight Mach numbers with 9 different flight attitudes each. The change from one condition to the other was communicated into the solver's settings by changing the boundary conditions imposed on the outer boundaries of the Computational Domain. So, the flight Mach number and the attitude of the Aircraft (AOA and AOSS) were all defined by setting accordingly the Mach number and the direction, in reference to the X, Y and Z axis, of the flow entering the computational domain.

Figure 4-1 below presents the predicted contours of total and static temperature for the flight condition of 0.6M with 0˚ AOA and 0˚ AOSS.

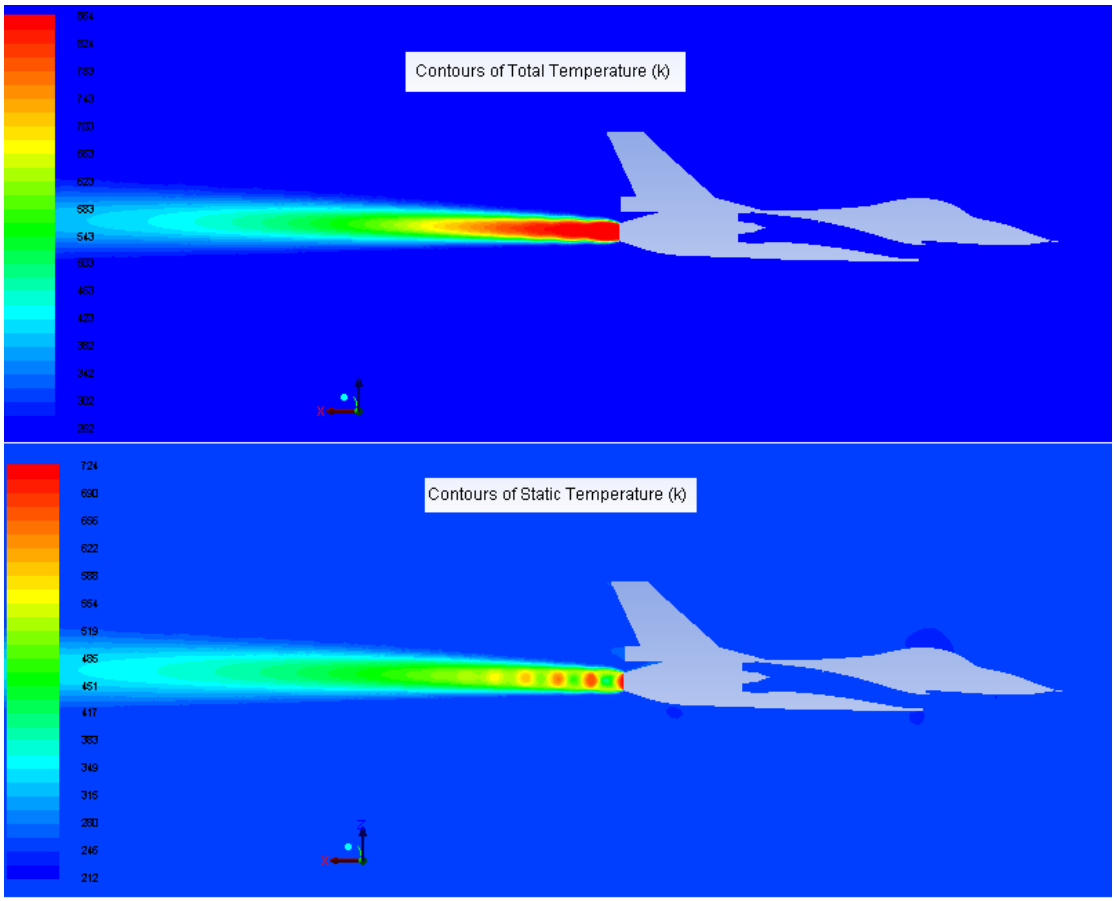

Figure 4-1 Total (upper part) and Static (lower part) Temperature Contours on a Centre Plane for the 0.6M Flight with 0˚ AOA and 0˚ AOSS

Around the airframe the total temperature presents no great variations except from the area behind the nozzle's exit. In areas just after points where the flow stagnates, e.g. at the canopy or at the lower lip of the intake, the static temperature decreases due to the velocity of the accelerated flow.

What prevails behind the nozzle's exit is the dissipation of the exhaust gases' increased temperature. In that area, the leaving gas stream is deformed and gradually mixes with the surrounding gas. The temperature of the leaving gas will be the same as that of the surrounding gas at some distance from the exit of the nozzle and exactly at the point where the leaving gas reaches a thermodynamic balance with the surrounding gas.

Figure 4-2 presents the contours of static and total pressure at a center plane of the computational domain for the same flight attitude (0.6M with 0° AOA and 0° AOSS). The lowest total pressure values are observed in the washed out flow areas, e.g. behind the aircraft's wings and vertical stabilizer, and adjacent to the intake walls. This low total pressure area denotes the losses that the flow experiences while traveling at these areas.

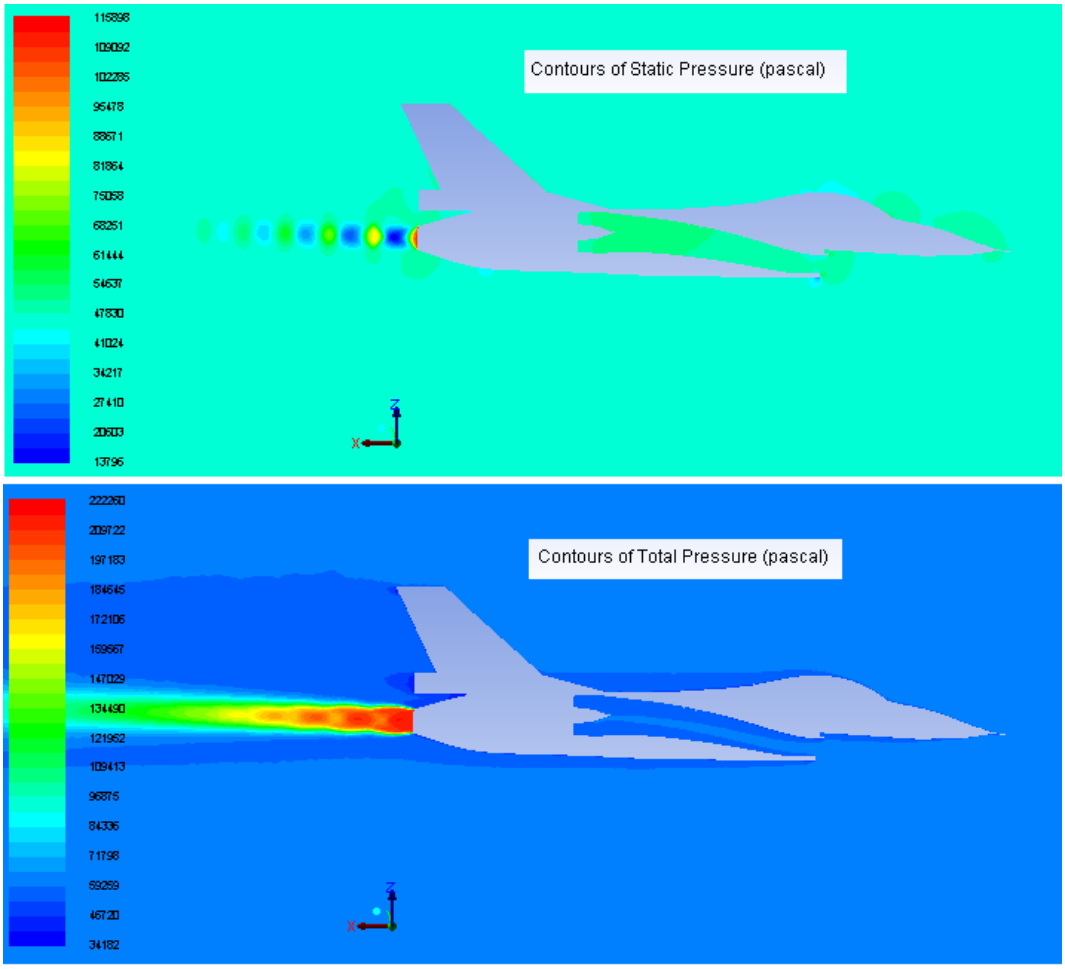

Figure 4-2 Total (lower part) and Static (upper part) Pressure Contours on a Centre Plane for the 0.6M Flight with 0˚ AOA and 0˚ AOSS

At the exhaust plume, the repeated expansion and compression of the flow is accompanied by the formation of shock waves that result in the static pressure and Mach number variations presented in figs 4-2 (upper part) and 4-3. In the latter figure what can be also noticed is the gradual diffusion of the flow inside the intake duct with the Mach number decreasing as the flow travels towards the engine's face.

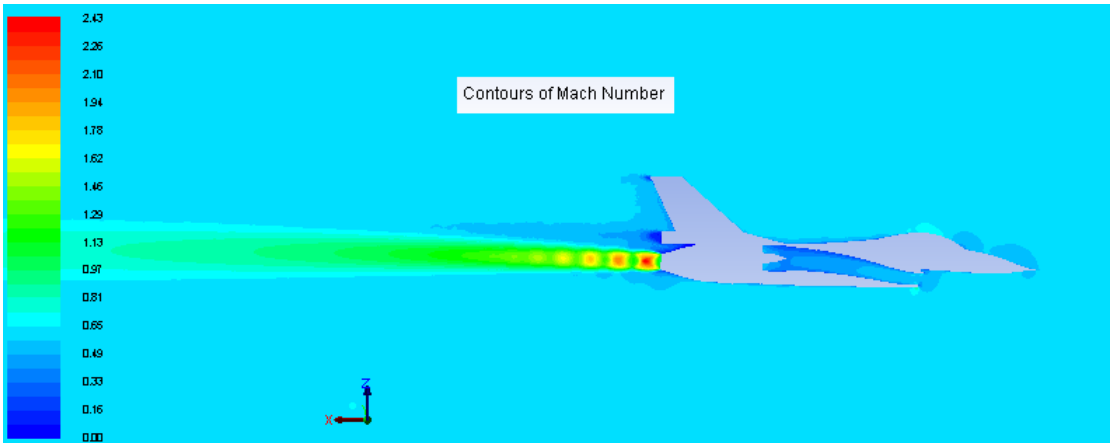

Figure 4-3 Predicted Mach Number Results on a Centre Plane for the 0.6M Flight with 0˚ AOA and 0˚ AOSS

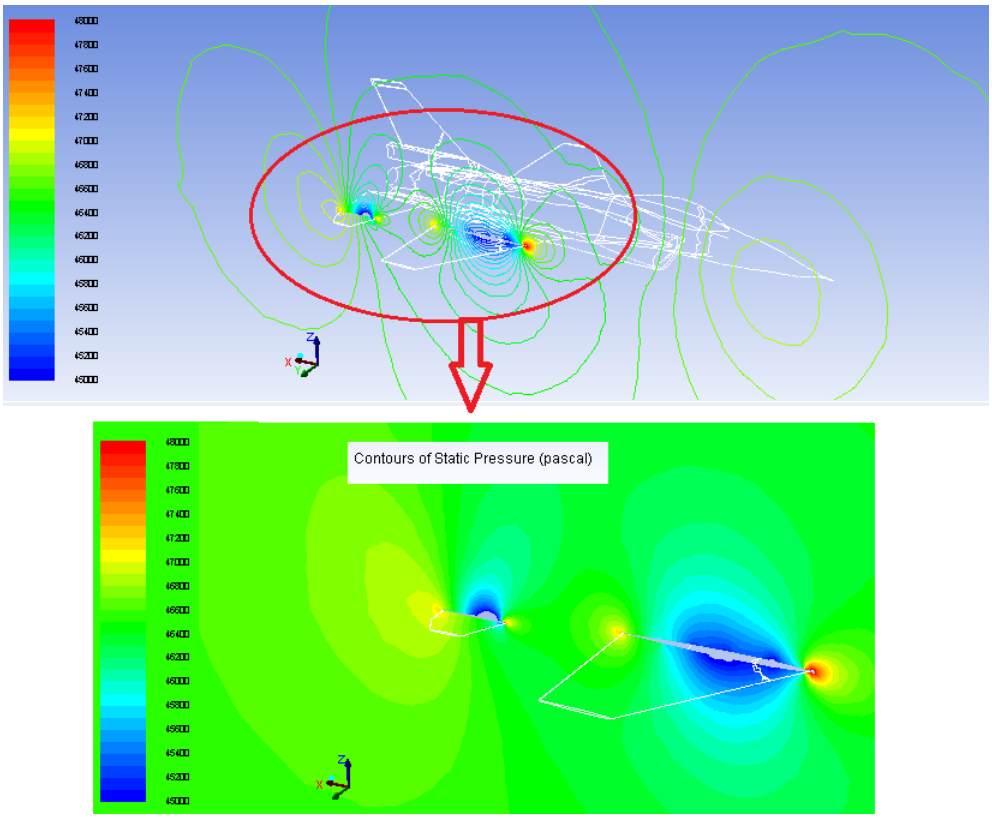

Figure 4-4 Static Pressure Contours on a Wing Cross Plane for the Flight Attitude of 0.6M with 0˚ AOA and 0˚ AOSS

Figure 4-4 above is a contour plot that shows what the static pressure is doing in the vicinity of the wing. The static pressure is almost equally distributed at the pressure and suction sides of the wing and there is almost no high pressure on the bottom of the wing. This is due to the shape of the airfoil in conjunction with the fact that the incoming flow meets the wing at 0˚ AOA.

As the AOA increases the static pressure difference between the pressure and suction sides of the wing increases and the produced lift is obviously greater. This static pressure distribution for the flight attitude of 0.6M with 8˚ AOA and 0˚ AOSS is shown in fig. 4-5 below. At the lower side of the wing the static pressure is obviously greater comparing to the upper side creating thus a lift force. Also the stagnation point at the leading edge has moved towards the pressure side of the wing.

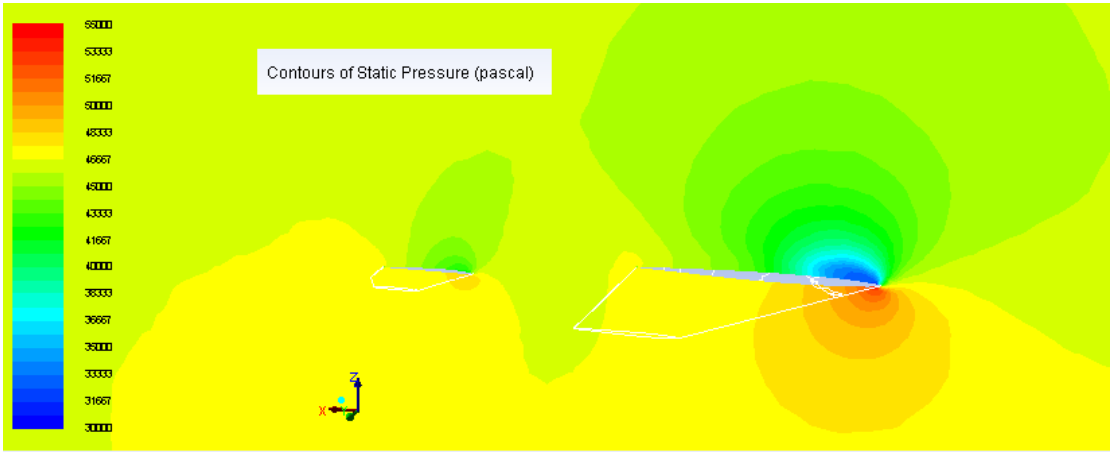

Figure 4-5 Static Pressure Contours on a Wing Cross Plane for the Flight Attitude of 0.6M with 8˚ AOA and 0˚ AOSS

4.3 Validation of the External Flow Results

The numerical results referring to the external flowfield (around the entire aircraft) were validated through a comparison with [60] and [61]. The former describes a numerical solution based on a scaled F-16A model flying at 0.85M with 16.04˚ AOA whereas the latter gives out some experimental results from the same model exposed to the same flying conditions in a wind tunnel environment.

Figure 4-6 below compares the Static Pressure contours obtained numerically in the present study for the flight scenario of 0.85M with 16˚ AOA and 0˚ AOSS and the respective one described in [60].

As it can be clearly seen the contours present many similarities. In both cases the lowest pressure areas are predicted to occur at the wing roots and at the leading edges of the horizontal stabilizers. Looking closer at the values of Static pressure at

these areas it can be clearly seen that they are very close to each other. For instance, the Static pressure at the wing root in the present study is predicted to be in the range of 9420 Pa which is really close to the 200 psf static pressure that was predicted in [60] for the same area.

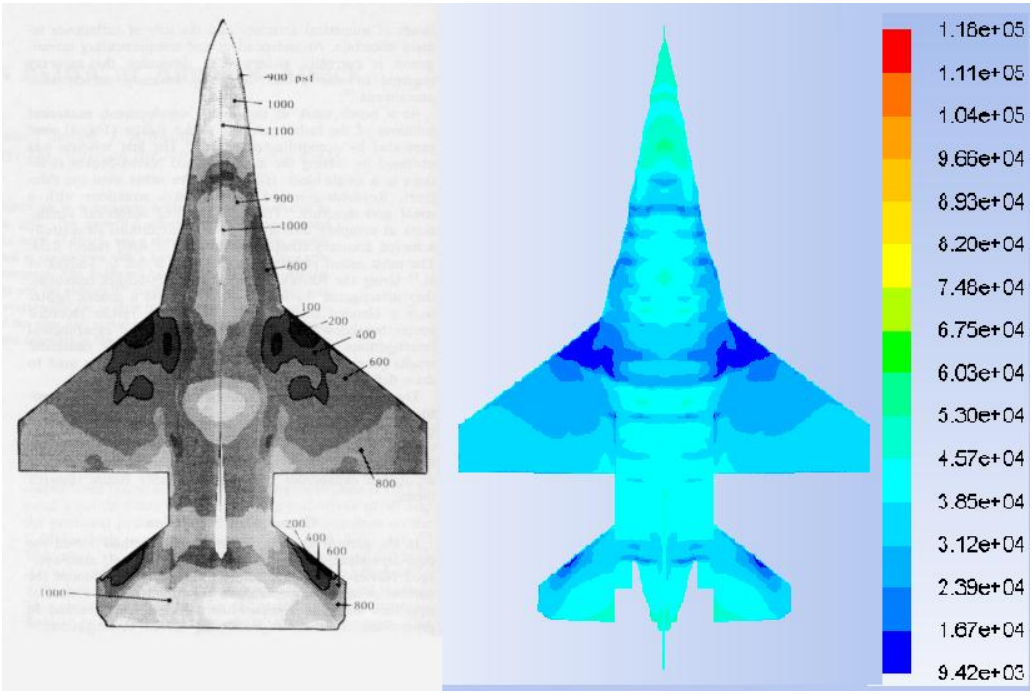

Figure 4-6 Comparison of the Static Pressure Contours Obtained in my Case (in Pa) (on the Right) with those (in psf) Quoted in [60] (on the Left) for the Flight Scenario of 0.85M with 16˚ AOA.

Specific values of pressure coefficients are stated in [61] which were based on actual measurements taken circumferentially at the planes 1, 2 and 3 depicted in fig 4-7. A direct comparison of these results with the respective ones calculated in the present study is presented in figs 4-8, 4-9 and 4-10. The compared results are again in a good agreement. A possible explanation for the fact that the compared lines in the presented graphs do not coincide is because the geometry models at the examined areas are not exactly the same.

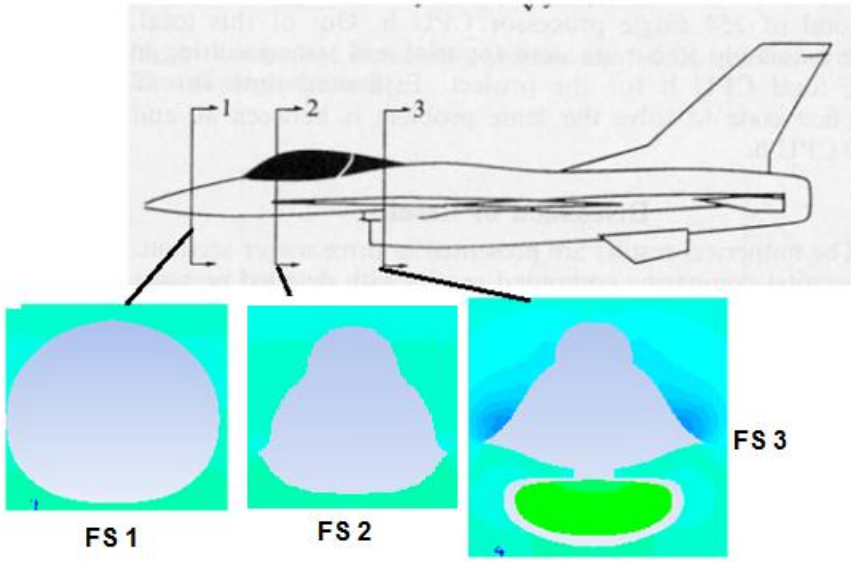

Figure 4-7 *Location of the Pressure Measurement Planes in Relation to the Entire Geometry*

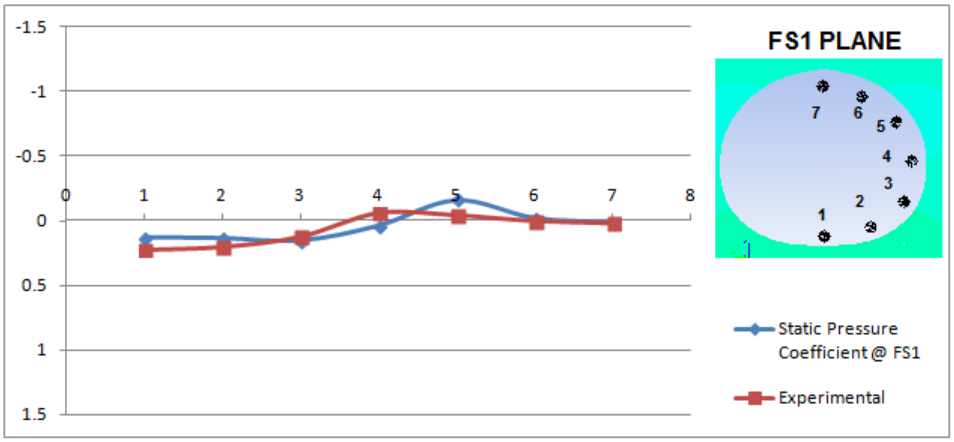

Figure 4-8 *Comparison with experimental Results [61] of the Static Pressure Coefficient at the Plane FS1 for 0.85M Flight and 16˚ AOA*

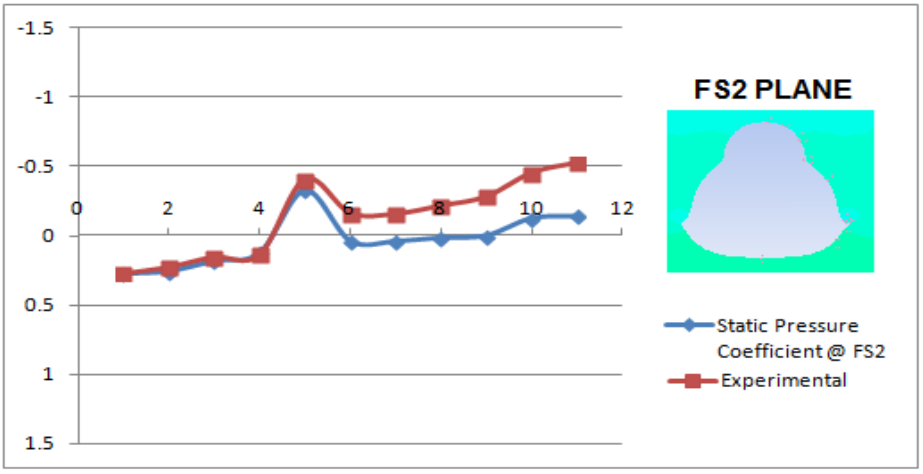

Figure 4-9 *Comparison with experimental Results [61] of the Static Pressure Coefficient at the Plane FS2 for 0.85M Flight and 16˚ AOA*

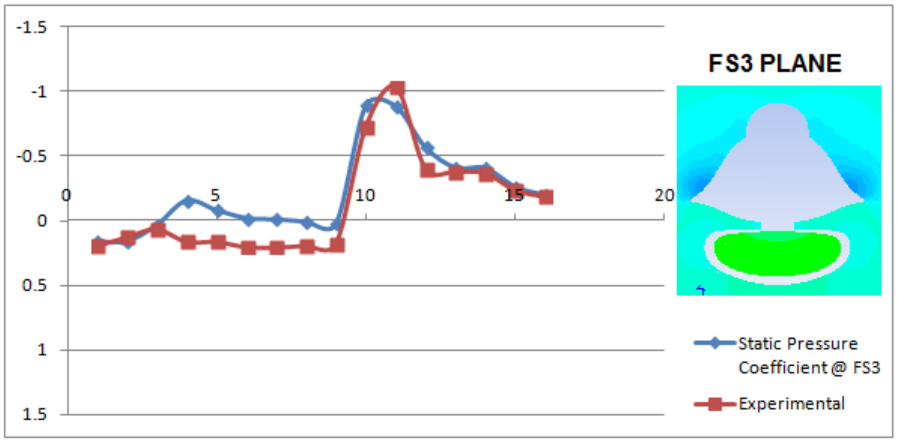

Figure 4-10 Comparison with Experimental Results [61] of the Static Pressure Coefficient at the Plane FS 3 for 0.85M Flight and 16˚ AOA

4.4 Aircraft Intake Flow Results

The area of interest in the present work was the aircraft's intake and more specifically the Aerodynamic Interface Plane (AIP) which comprises the analytical boundary between the airframe and the power plant. The condition of the airflow, in terms of total pressure distribution, when it reaches that plane defines the level of total pressure distortion.

4.4.1 Propagation of Air Flow Inside the Aircraft's Intake

In fig. 4-11 which presents the velocity contours for the flight attitude of 0.6M with 0˚ AOA and 0˚ AOSS, on a center cross plane of the computational domain, parallel to the longitudinal axis of the aircraft, it can be clearly observed that the flow diffuses while it propagates towards the AIP. On this figure what can be also seen is the extension of the domain behind the AIP, an approach that as it has been already explained, was adopted in the present study so that the flow results at the plane of interest were not affected explicitly by the boundary conditions.

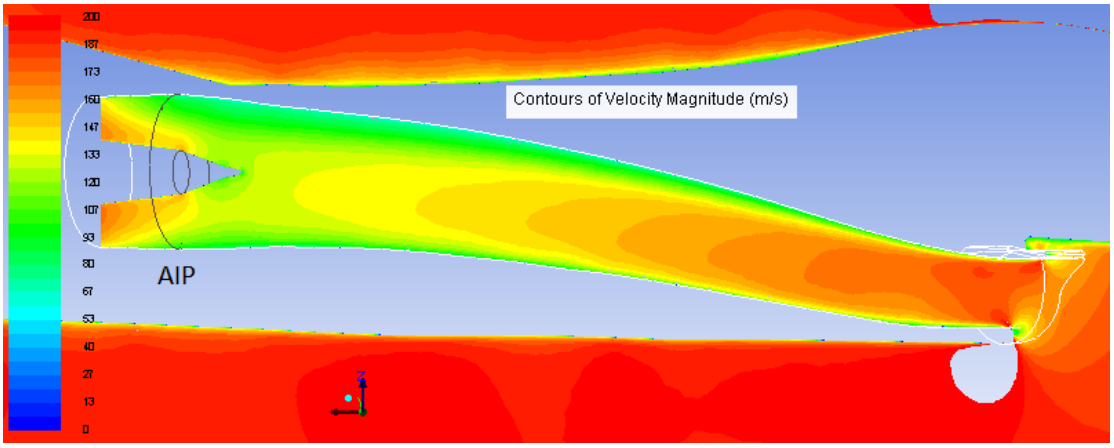

Figure 4-11 Contours of Velocity Magnitude on a Centre Cross Plane for the 0.6M Flight with 0˚ AOA and 0˚ AOSS

Figures 4-12 and 4-13 present in terms of flow pathlines and velocity vectors respectively, a visualization of the flow inside the intake at this flight condition. The predicted flow for this specific flight attitude propagates smoothly through the duct without any flow reversals. Also the flow enters the intake around its lip without any separations.

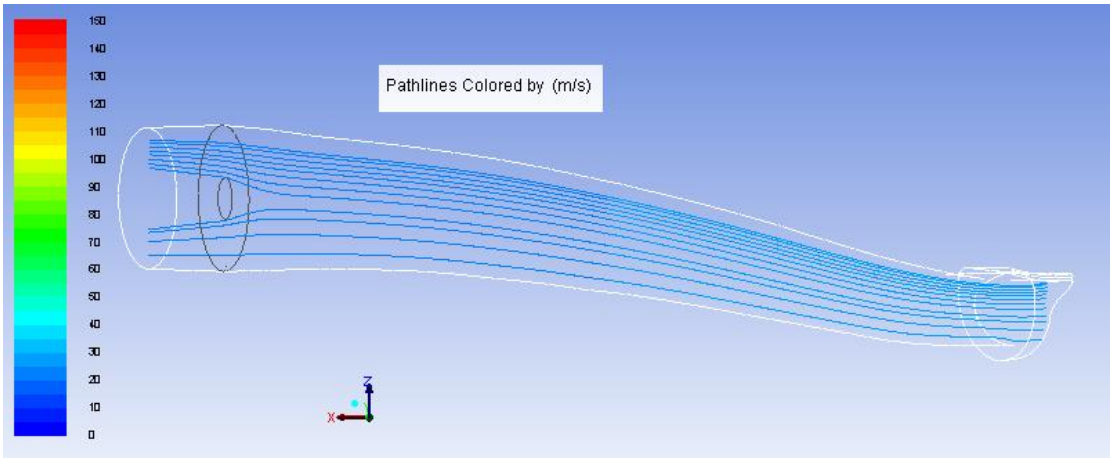

Figure 4-12 Flow Pathlines Inside the Intake on a Centre Cross Plane for the 0.6M Flight with 0˚ AOA and 0˚ AOSS

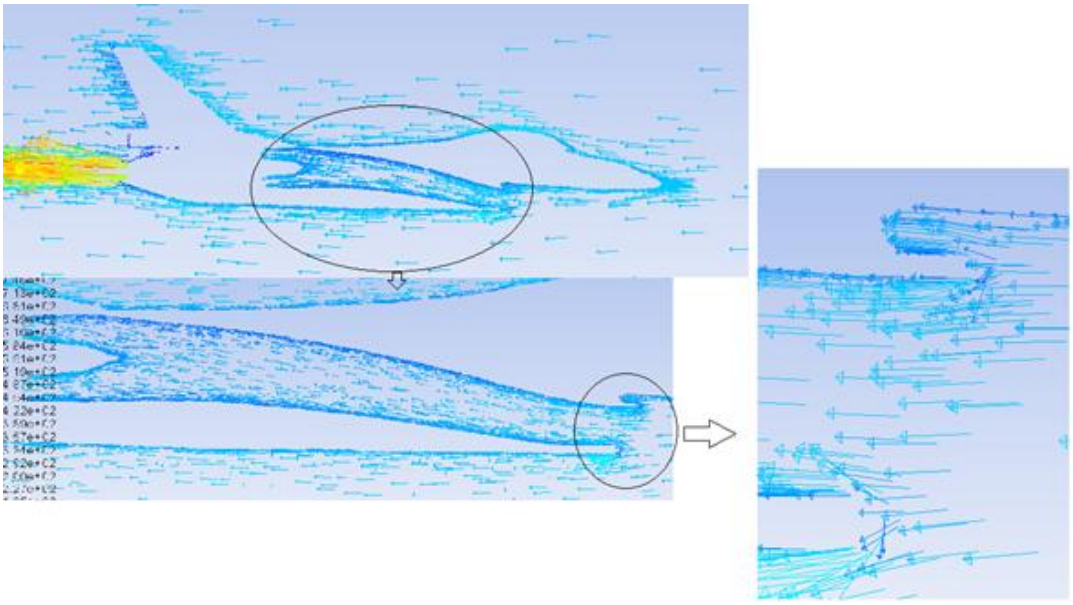

Figure 4-13 Visualization of the Flow Inside the Intake in Terms of Velocity Vectors on a Centre Cross Plane for the 0.6M Flight with 0˚ AOA and 0˚ AOSS

There is a flight attitude though, that of 0.35M flight with 16˚ AOA and 0˚ AOSS, in which a small region of streamwise flow reversal was noticed at the lower side of the intake near to its entrance. At this specific flight attitude the lower side of the intake becomes "shielded" to the incoming flow, due to the increased AOA. As a result the flow has a lower velocity at this point comparing to the rest of the intake.

The low velocity in conjunction with the low flight Mach number make the flow incapable of both following the intake's curvature and overcoming the adverse pressure gradient due to the flow diffusion that occurs after the throat of the intake and the flow eventually reverses.

This reversed flow area which does not exist at the higher flight Mach number attitudes, is presented in fig. 4-14.

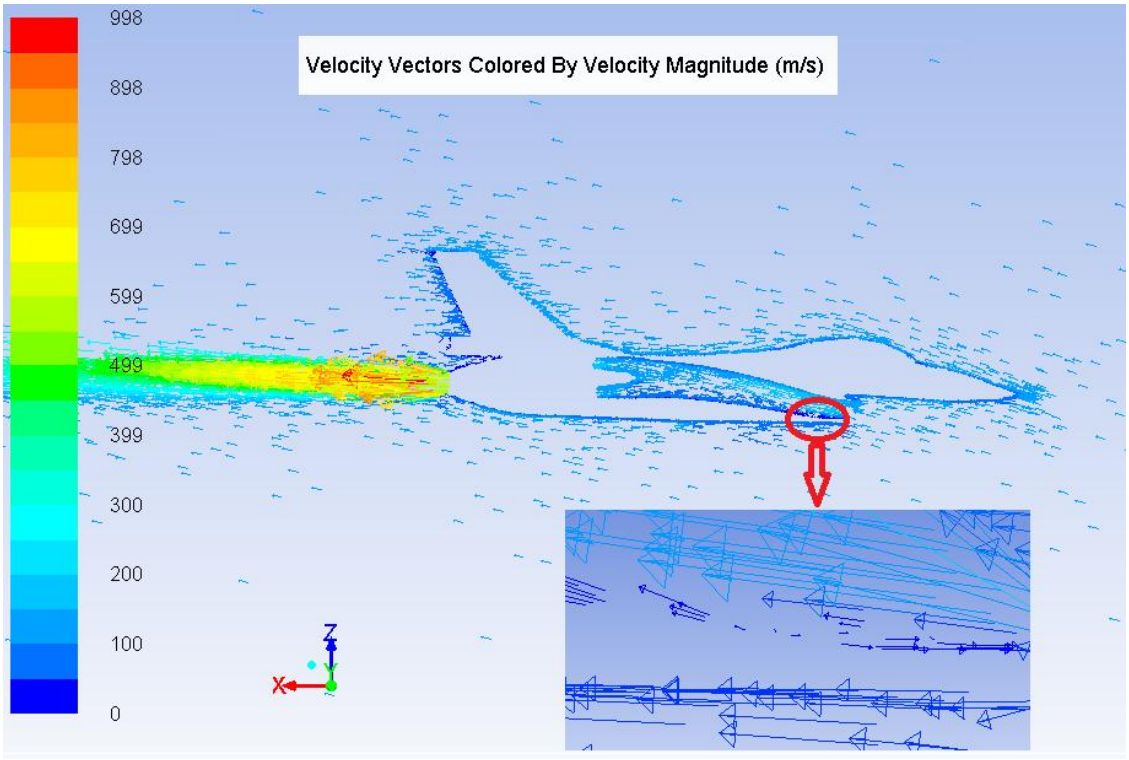

Figure 4-14 Reversed Flow Area at the Flight Attitude of 0.35M with 16˚ AOA and 0˚ AOSS

Figure 4-15 below presents the total pressure distribution at the AIP for the flight attitudes of 0.35M, 0.6M and 0.85M with 0˚ AOA and 0˚ AOSS. What can be observed in this figure is that as the flight Mach number increases the high pressure area resembles the shape of the intake's ''mouth'' and it migrates towards the lower part of the AIP.

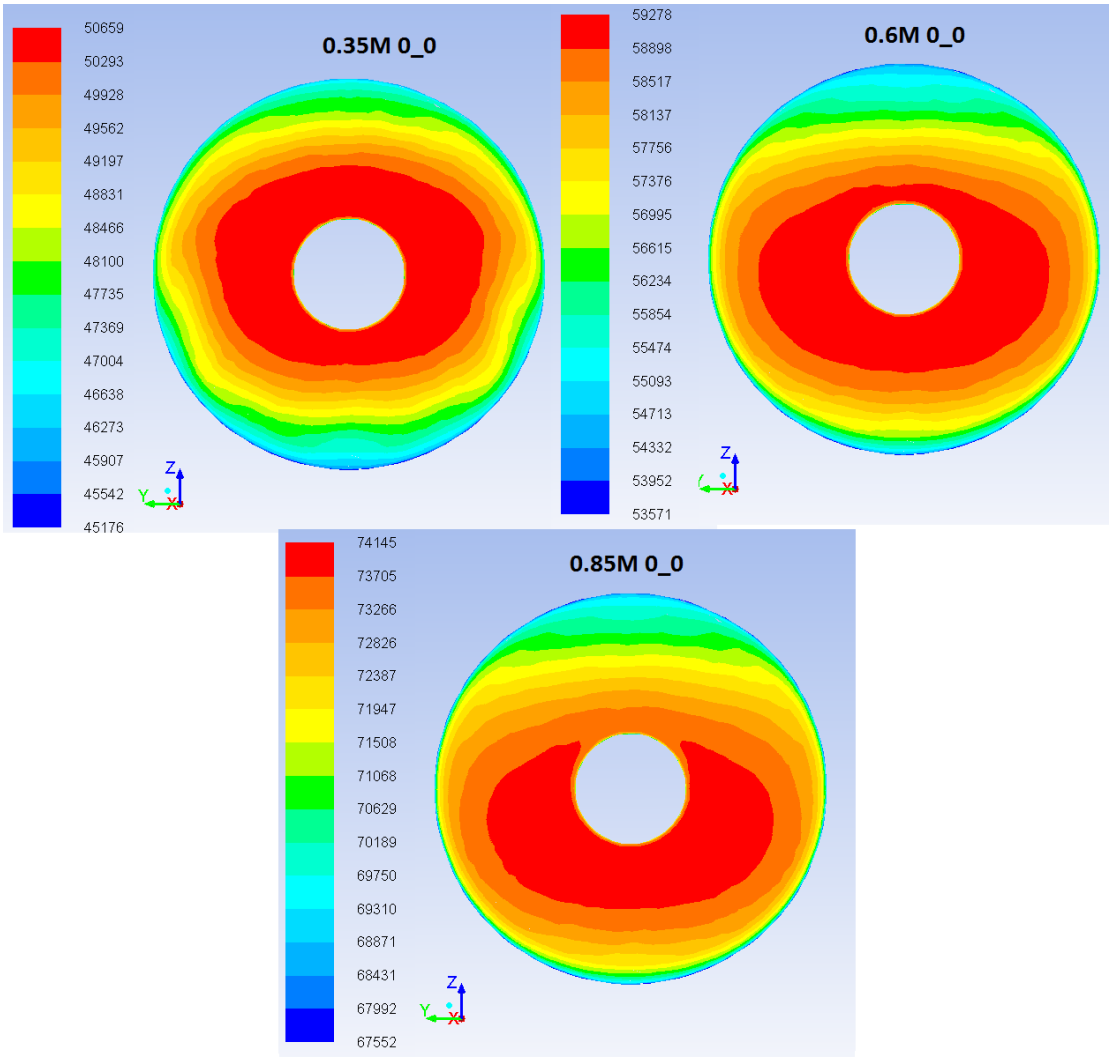

Figure 4-15 Total Pressure Profiles at the AIP for the 0.35M, 0.6M and 0.85M Flights with 0˚ AOA and 0˚ AOSS

4.4.2 Investigation of the Airflow inside the Aircraft's Intake

To better investigate the airflow in the intake duct, four cross stream planes were created across the intake and with the aid of these planes the propagation of different flow parameters was observed. On each plane, four measurements of total and static pressures were taken, three circumferentially of each plane, at the top, the bottom and the side points (at 90 degrees) and one at the centerline (see fig. 4-16).

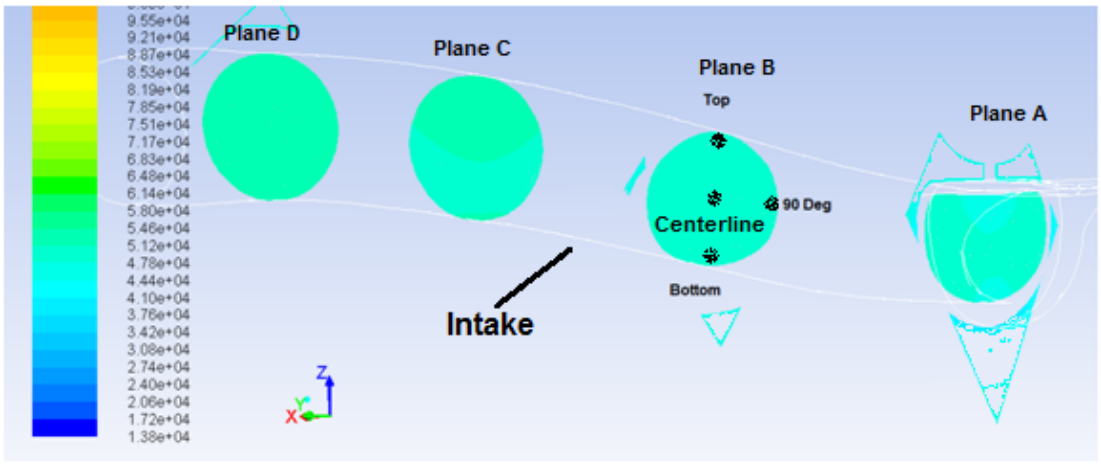

Figure 4-16 Location of Measurement Planes

Based on these measurements and having as a reference the free flow conditions, the Static (Cp) and Total (CP) Pressure coefficients were calculated,

$$C_p = \frac{p - p_{ref}}{P_{ref} - p_{ref}} \qquad (\text{eq. } 4-1)$$

$$CP = \frac{P - P_{ref}}{P_{ref} - p_{ref}} \qquad (\text{eq. } 4-2)$$

where **P** and **p** are the Total and Static pressures respectively at the points of interest and the suffix 'ref' refers to the free flow conditions measured upstream of the geometry.

The variation of these calculated coefficients across the length of the duct is presented in fig. 4-17. The absence of any flow separations is again confirmed, since the static pressure keeps rising streamwise. On the other hand, the total pressure keeps falling, denoting the losses that the flow experiences while travelling through the duct. The numbers on the abscissa represent the x coordinate of that specific plane location that the taken values refer to. It is reminded that the results refer to the flight attitude of 0.6M flight with 0˚ AOA and 0˚ AOSS.

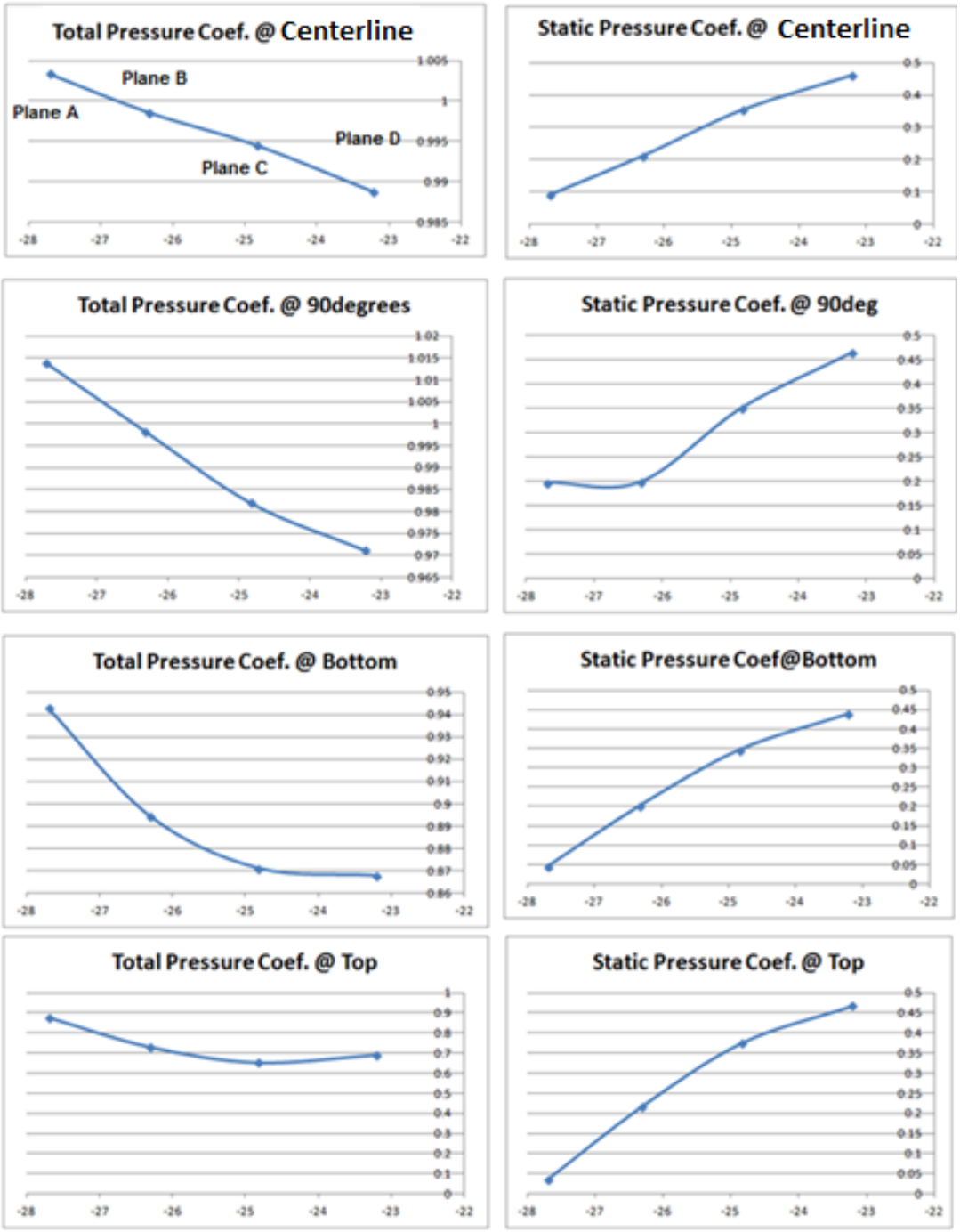

Figure 4-17 Variation of Total and Static Pressure Coefficients Across the Intake for the 0.6M flight with 0˚ AOA and 0˚ AOSS

4.4.3 Development of Secondary Flow

Figure 4-18 presents the progress of total pressure across the intake at 0.35M, 0.6M and 0.85M for the flight attitude of 0˚ AOA and 0˚ AOSS. As can be seen on this figure the low total pressure flow develops from top to the center and

in the last plane, the one that is closer to the AIP, the high total pressure is around the center. As the flight Mach number increases the high total pressure area becomes smaller and it migrates towards the lower part of the AIP.

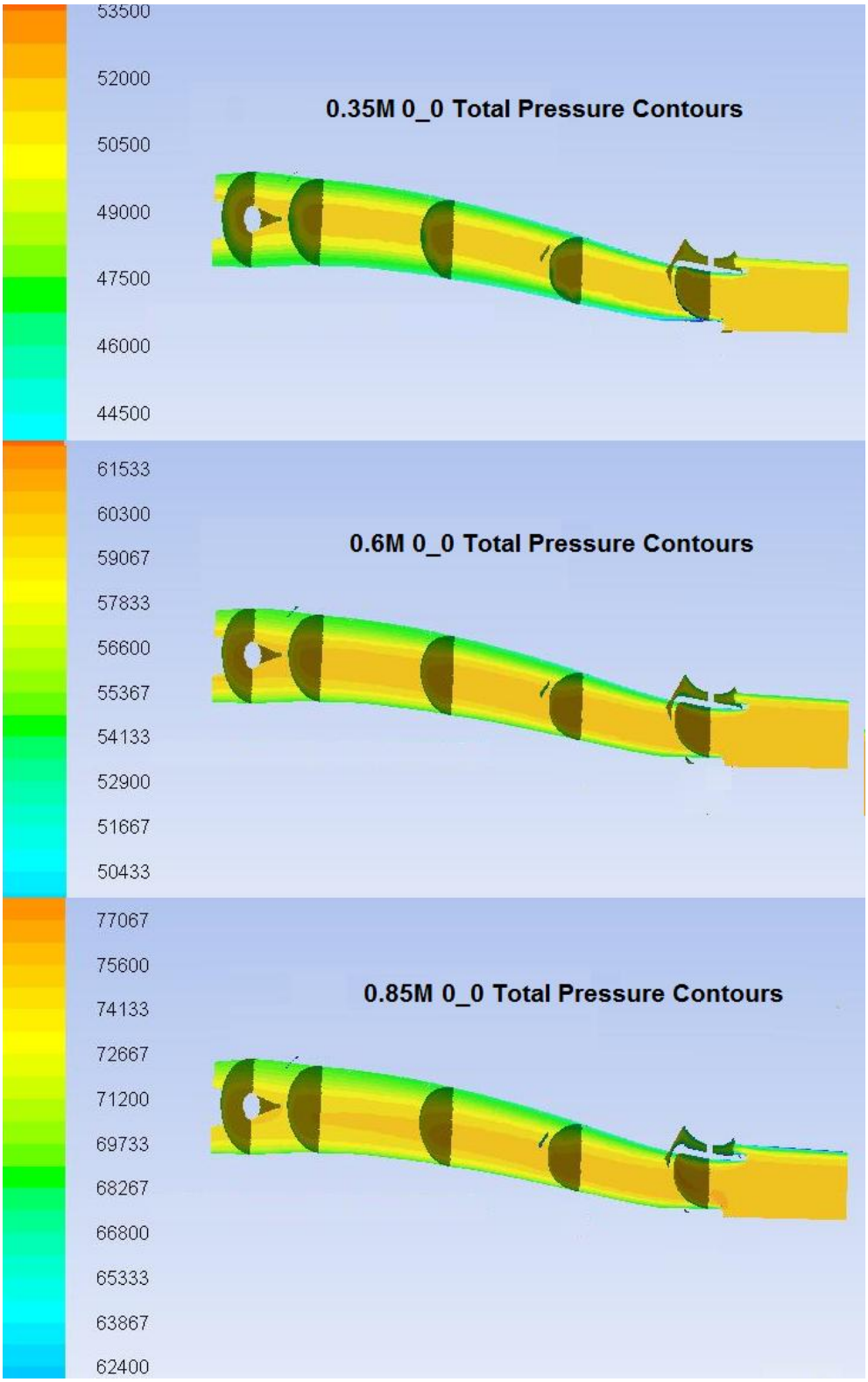

Figure 4-18 Total Pressure Contours Across the Intake for the 0.35M, 0.6M and 0.85M Flights with 0˚ AOA and 0˚ AOSS

One of the reasons inducing the change of the total pressure is the development of secondary flow which is created due to the curvature of the intake. As soon as the airflow enters the intake it is diverted upwards due to the curvature of the intake creating thus secondary flow. Figure 4-19 presents this flow in the four cross stream planes for the flight attitude of 0.85M flight with 0˚ AOA and 0˚ AOSS. This figure, accompanied with fig. 4-20 which presents the propagation of the static pressure across the intake cross stream planes, provides an explanation on the direction and the magnitude of the secondary flow.

In Plane A, the static pressure is higher at the sides, due to the intake's shape at that plane in conjunction with the fact that this shape gradually changes to a circular one downstream. A pressure gradient is created which gives rise to a flow motion towards the centerline of the plane. In plane B the secondary flow has become more severe since up to that plane the flow has gone through the first bend of the intake and it has been diverted towards its upper part.

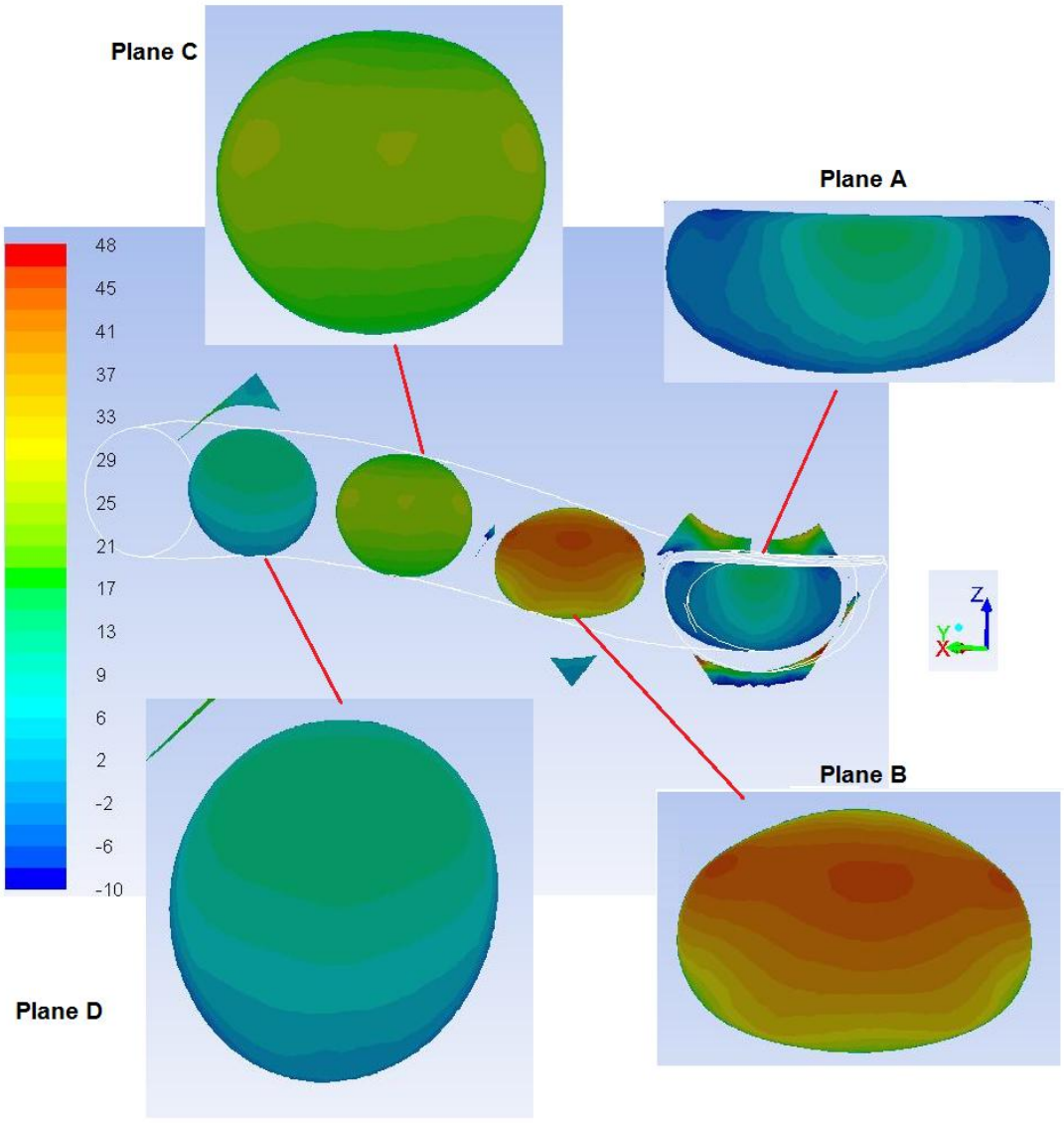

Figure 4-19 Secondary Flow in Terms of z Velocity Contours on the Cross Stream Planes Across the Intake for the 0.85M Flight with 0˚ AOA and 0˚ AOSS

The secondary flow at that plane is slightly mitigated by the pressure gradient that has been created, with higher static pressure at the top than at the lower part of the intake, as it can be observed in fig. 4-20. As the flow propagates furthermore and it passes through the second bend of the intake which is in the opposite direction, the secondary flow alleviates even more and in plane D is at a much lower level than it was in the previous ones.

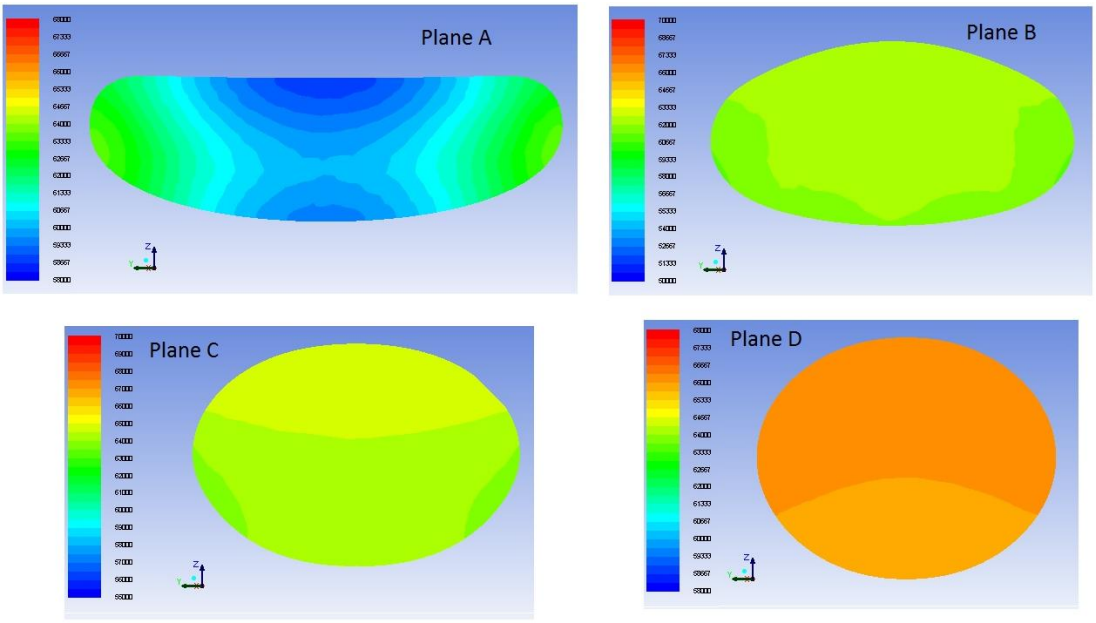

Figure 4-20 Static Pressure Contours at the Cross Stream Planes Across the Intake for the 0.85M Flight with 0˚ AOA and 0˚ AOSS

In lower Mach number flights the core flow has more time to interact with the low momentum boundary layer flow and to finally increase its low velocity. As a result in lower Mach number flights the high total pressure area in plane D is greater comparing to a high Mach number flight.

4.4.4 Effect of AOA

When the incoming flow enters the intake at an AOA it ends up on the AIP having the total pressure distributed in the way presented in figures 4-21 and 4-22. The former presents the total pressure distribution on the AIP when the airframe is exposed to an incoming flow with an AOA of 8˚ whereas the latter presents the same results for the 16˚ AOA. As it can be observed in these figures the high pressure area is again confined in the centre and migrates towards the lower side of the AIP as the flight Mach number increases. The low pressure area though, located at the lower part of the AIP, becomes more pronounced. Also, the lower the flight Mach number the more severe this low total pressure area seems to be.

At these flight attitudes the lower side of the intake becomes shielded to the incoming flow. As a result the flow moving adjacent to that wall has a lower velocity. This lower momentum flow is more sensitive to the pressure gradient due

to the boundary layer build up as the flow propagates inside the intake. At higher flight Mach numbers the velocity of the flow near the wall is higher which is translated in a less severe low total pressure area on the AIP.

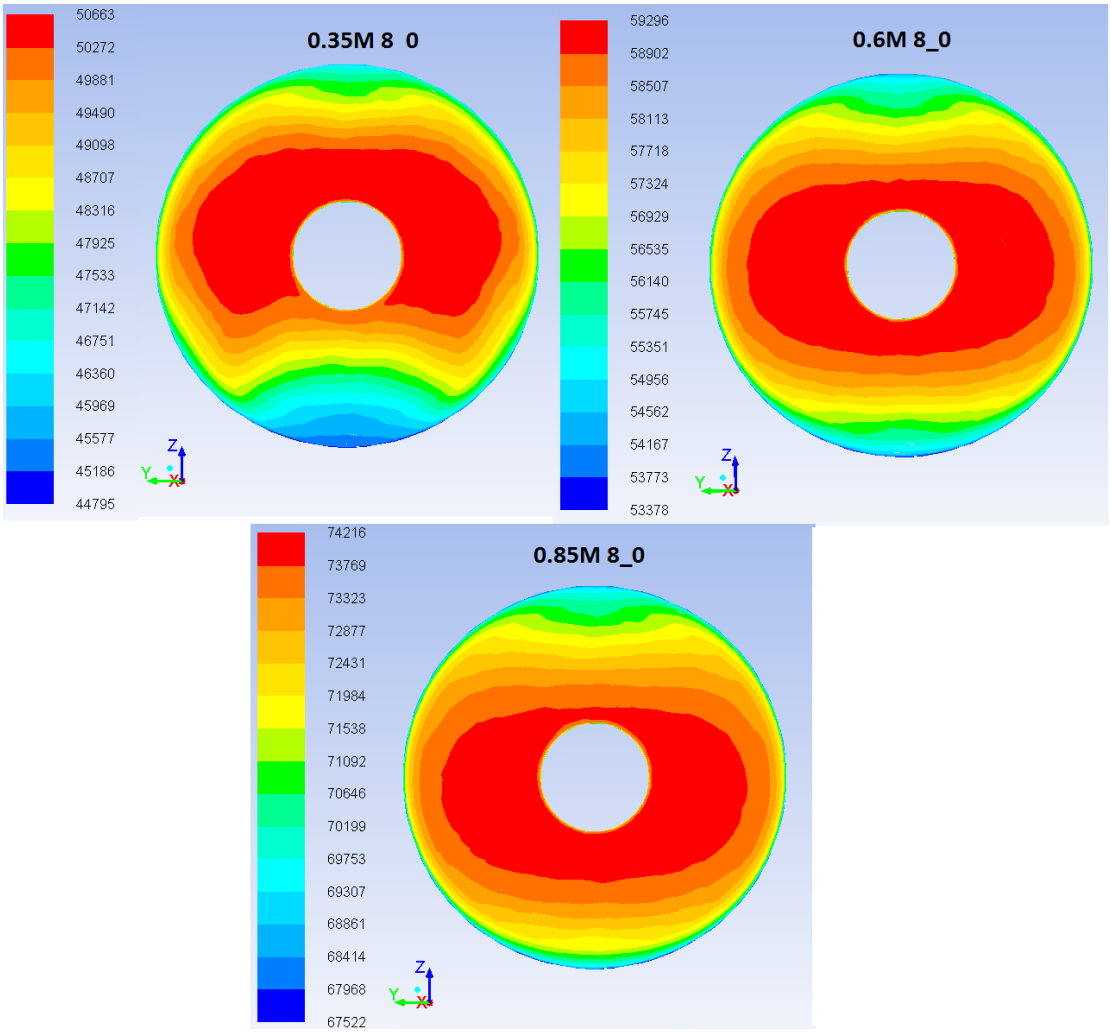

Figure 4-21 Total Pressure Profiles at the AIP for the 0.35M, 0.6M and 0.85M Flights with 8˚ AOA and 0˚ AOSS

When the AOA increases, the flow neighboring the lower side of the intake moves with an even lower velocity. This lower velocity flow is translated into a more intense low pressure area at the lower side of the AIP. This can be visualized in fig. 4-22 that presents the total pressure distribution at the AIP for the flight attitudes with 16˚ AOA and 0˚ AOSS.

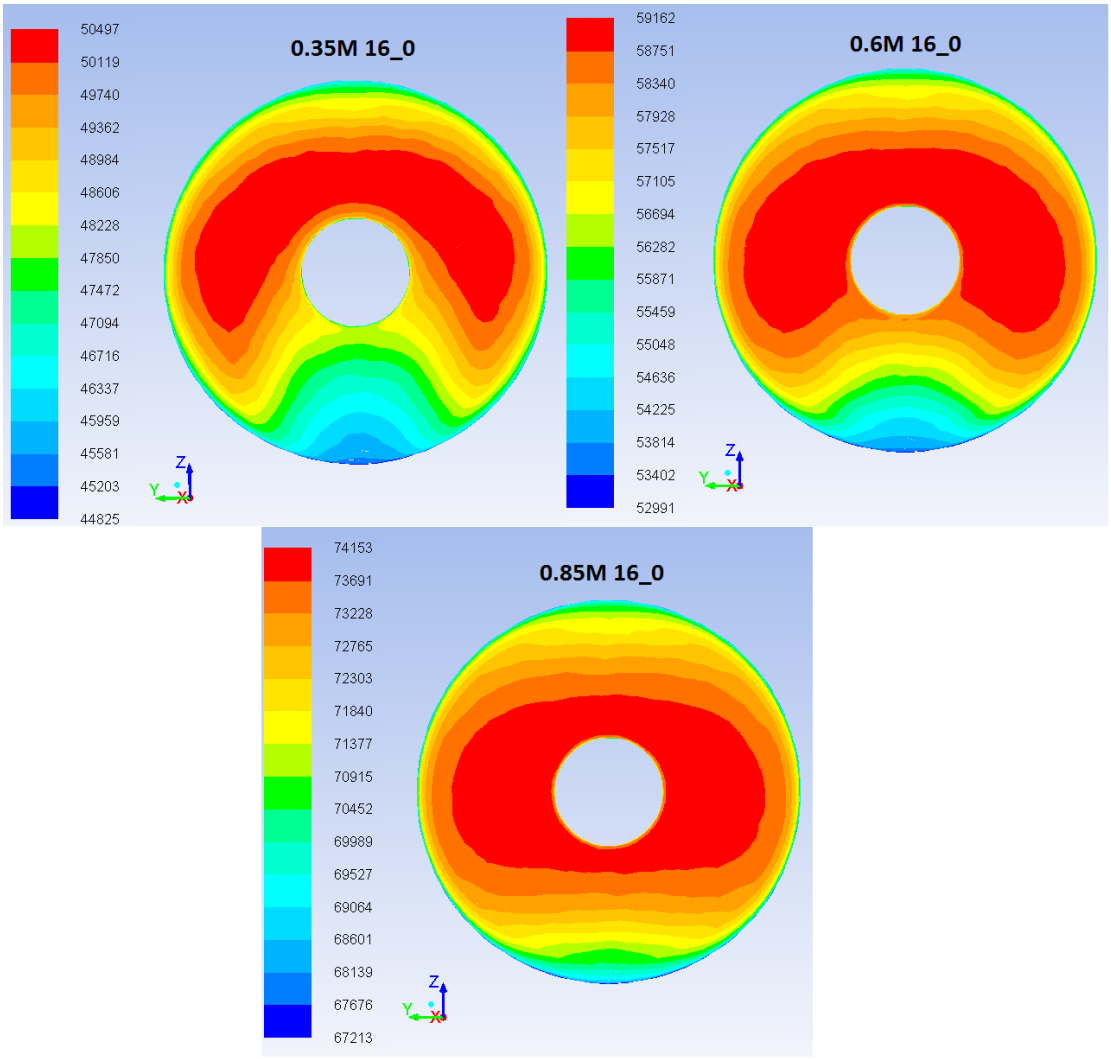

Figure 4-22 Total Pressure Profiles at the AIP for the 0.35M, 0.6M and 0.85M Flights with 16˚ AOA and 0˚ AOSS

4.4.5 Effect of AOSS

In the case of an incoming flow at an AOSS the low pressure area on the AIP migrates to the side at ''3 o'clock'' as it can be observed in figures 4-23 and 4-24 in which the total pressure distribution on the AIP for the AOSS of 8˚ and 16˚ are presented respectively. It is this part of the intake that becomes shielded to the incoming flow and consequently has lower flow velocity. This low pressure area becomes more pronounced at higher AOSS.

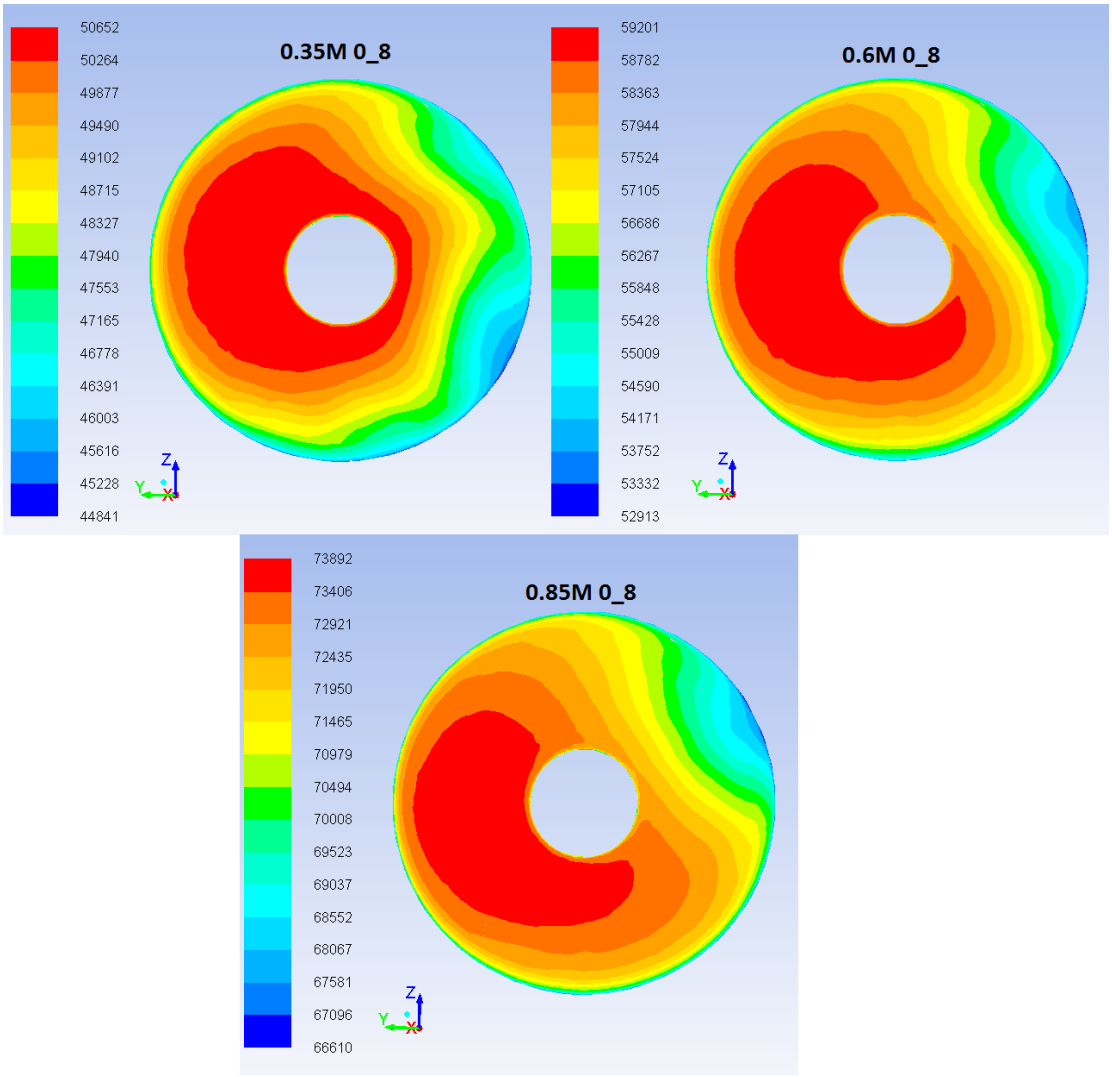

Figure 4-23 Total Pressure Profiles at the AIP for the 0.35M, 0.6M and 0.85M Flights with 0˚ AOA and 8˚ AOSS

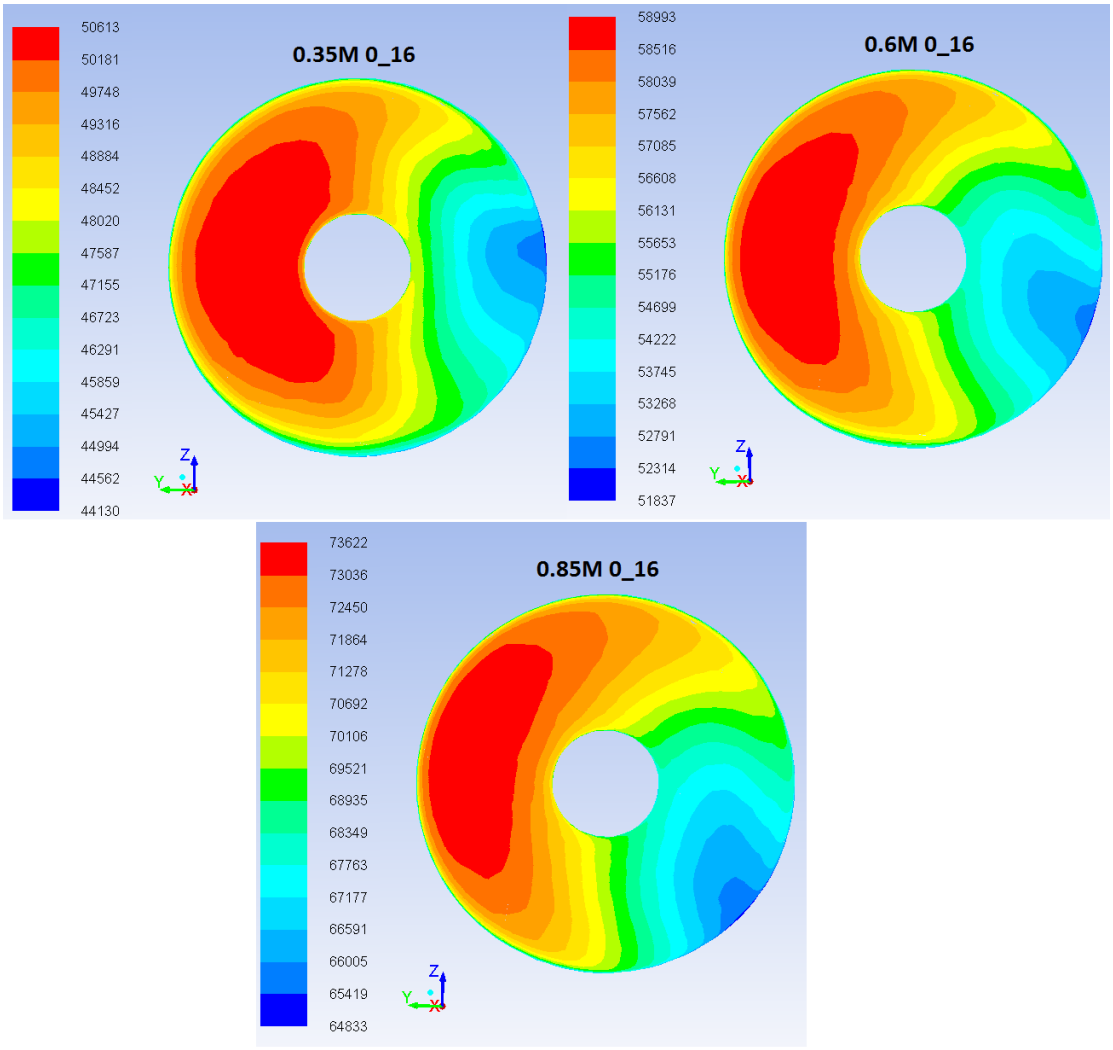

Figure 4-24 Total Pressure Profiles at the AIP for the 0.35M, 0.6M and 0.85M Flights with 0˚ AOA and 16˚ AOSS

4.5 Total Pressure Profiles at the Engine's Face

In the context of the present work, the 27 flight conditions that are quoted in table 4-1 above, were simulated and for each case the total pressure distribution at the **Engine's Face** plane was obtained. These specific conditions were selected to cover a wide area of the aircraft's operating envelope.

As it has already been mentioned, the change from one condition to the other was communicated into the solver's settings by changing the boundary conditions imposed on the **Domain_Outer** zone which comprises the boundary of the whole computational domain. So, the flight Mach number and the attitude of the Aircraft (AOA and AOSS) were all defined by setting properly the Mach number and

the direction, in reference to the X, Y and Z axis, of the flow entering the computational domain.

In the post processing of each case, for each flight attitude the distribution of the total pressure at the engine's face was obtained. The location of that plane inside the computational domain is presented in fig. 4-25 below. This plane coincides with the Aerodynamic Interface Plane and comprises the boundary between the airframe and the engine.

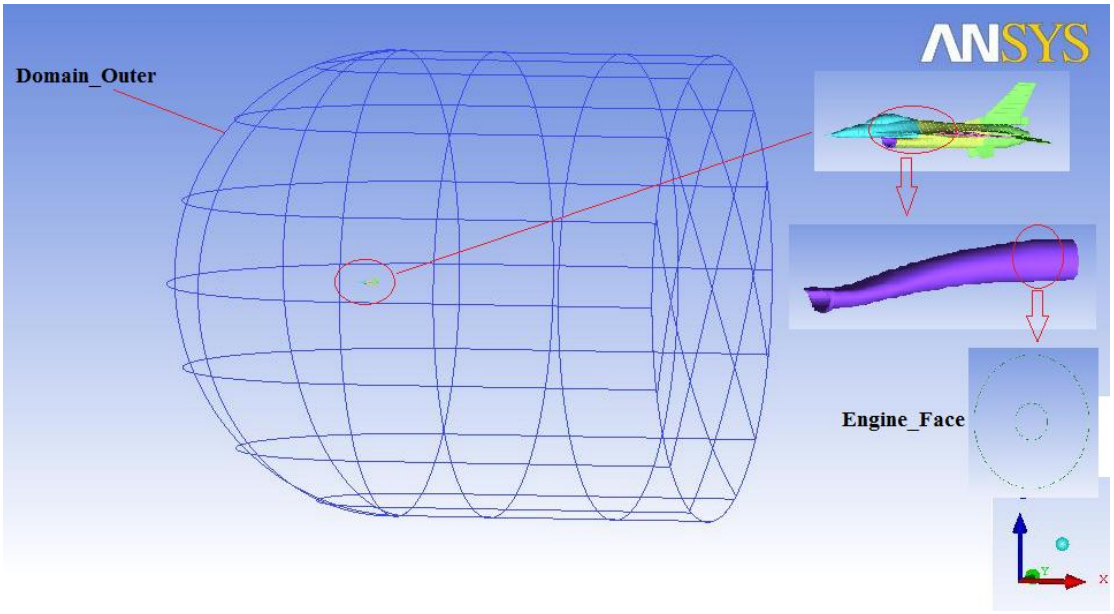

Figure 4-25 Location of the Engine's Face (AIP) in the Computational Domain

Figures 4-26, 4-27 and 4-28 show respectively the numerically predicted total pressure profiles at the AIP for the 0.35M, 0.6M and 0.85M flight attitudes. As can be observed at a glance, through the colour variations, in flight attitudes with an AOSS, the total pressure non uniformities are more obvious.

As a first guide in translating these patterns what can be noted is that the bluish coloured areas refer to low total pressure regions and the red ones denote the areas where higher pressure prevails.

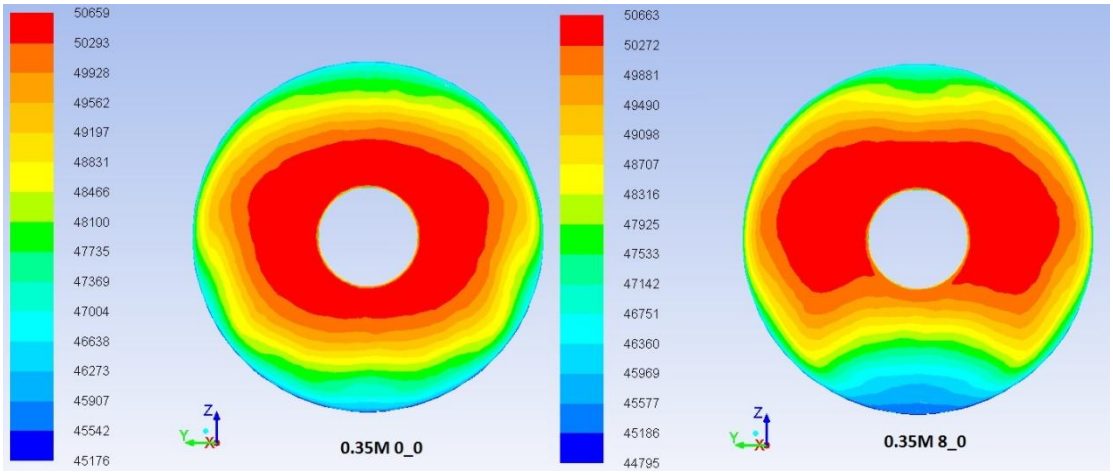

(a) (b)

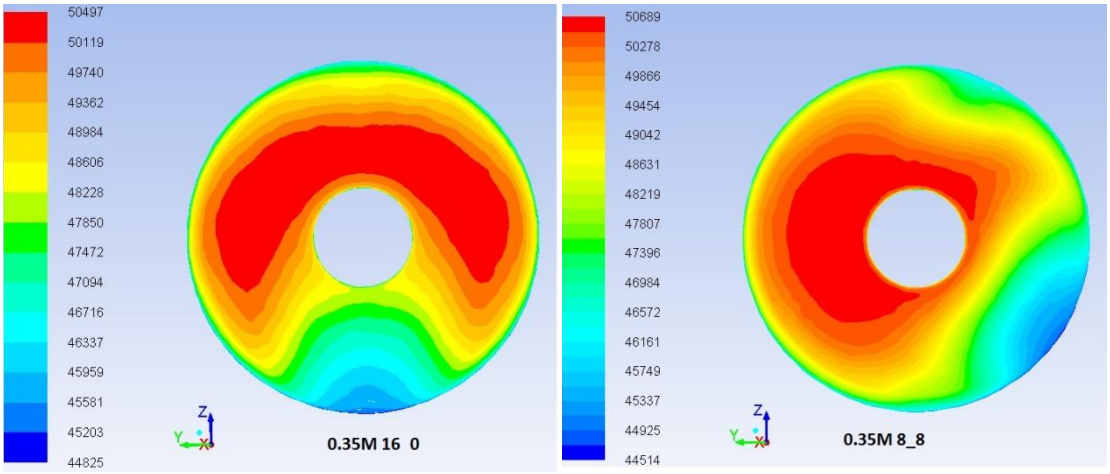

(c) (d)

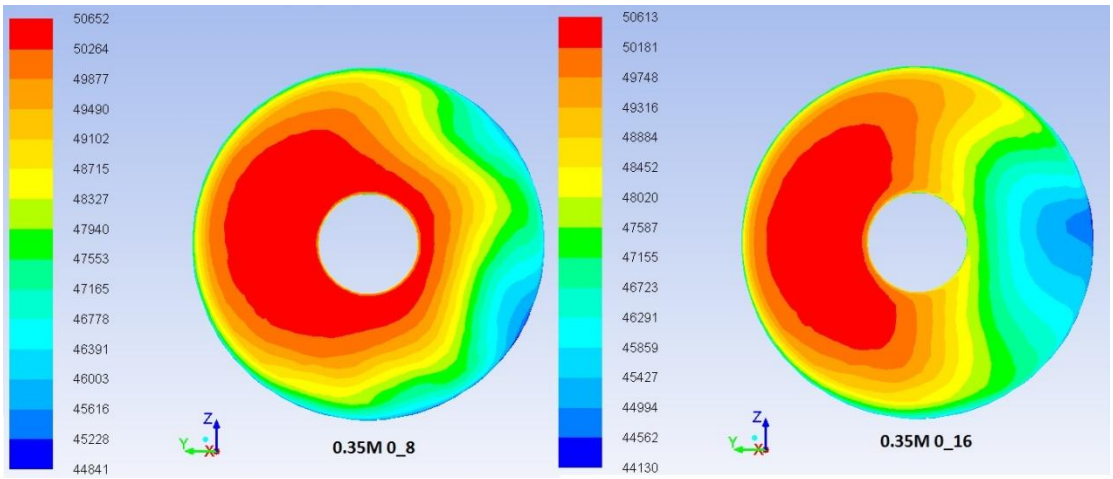

(e) (f)

Figure 4-26 Total Pressure Contours at the AIP for the 0.35M Flight Attitudes (continued)

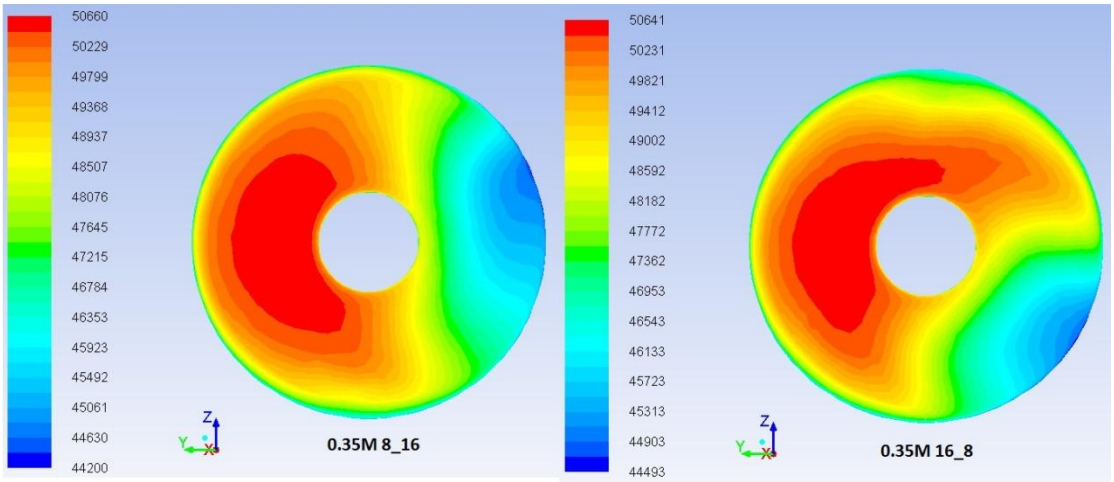

(g) (h)

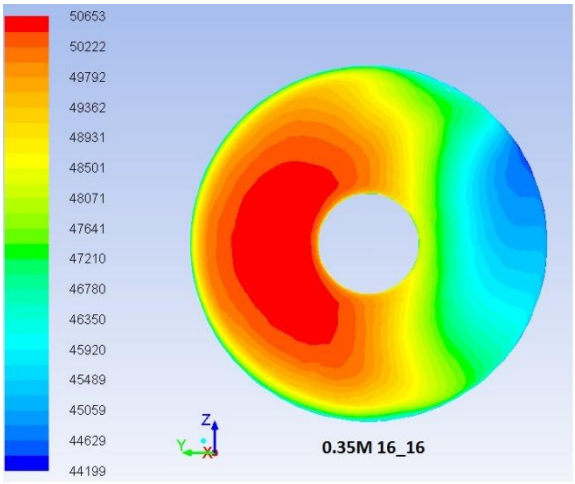

(i)

Figure 4-27 Total Pressure Contours at the AIP for the 0.35M Flight Attitudes

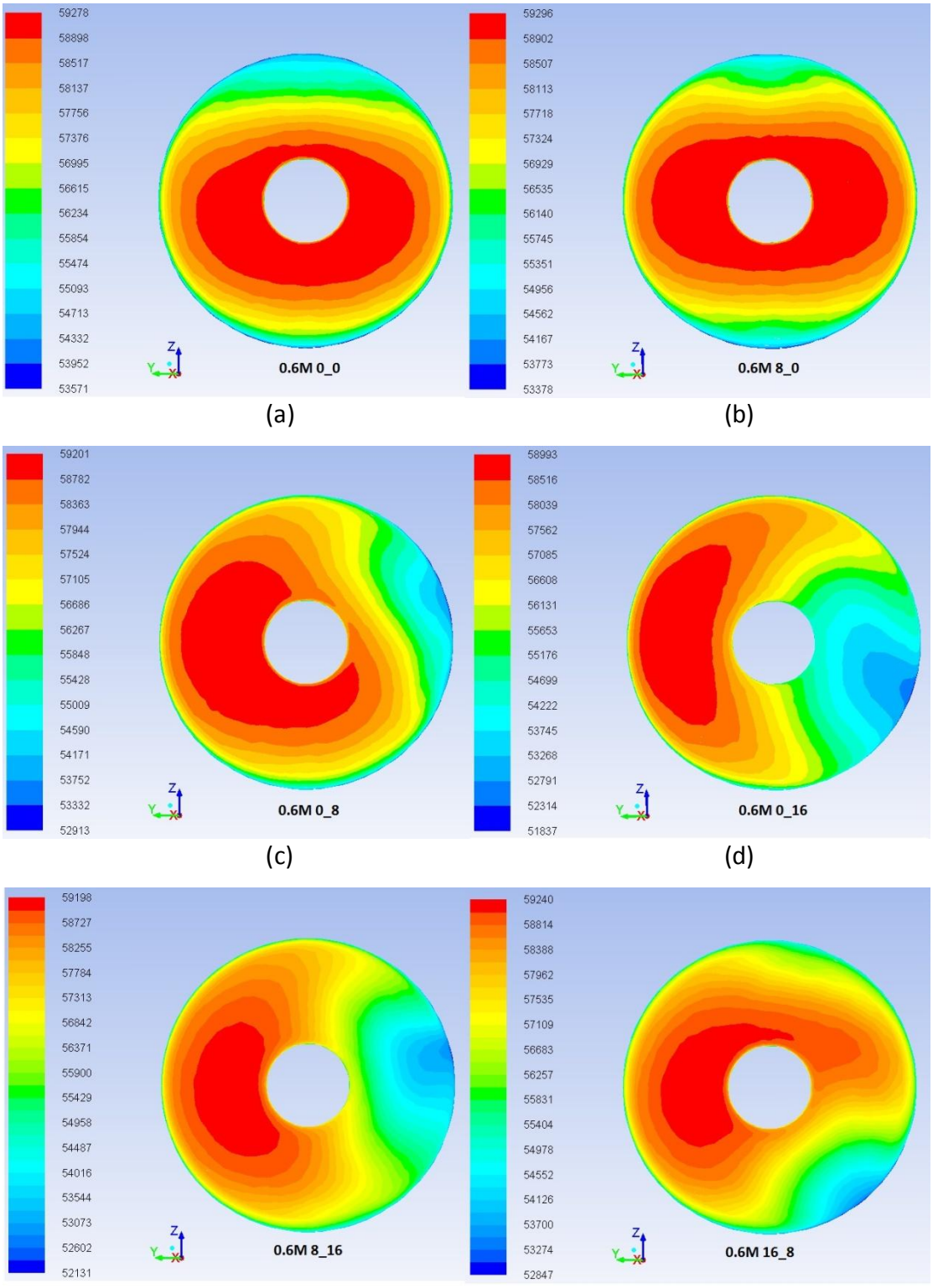

Figure 4-28 Total Pressure Contours at the AIP for the 0.6M Flight Attitudes (continued)

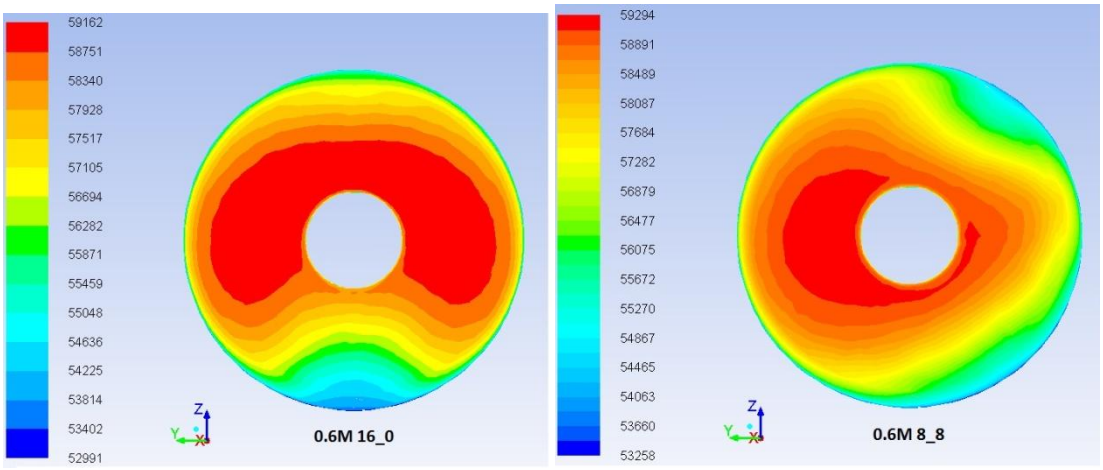

(g) (h)

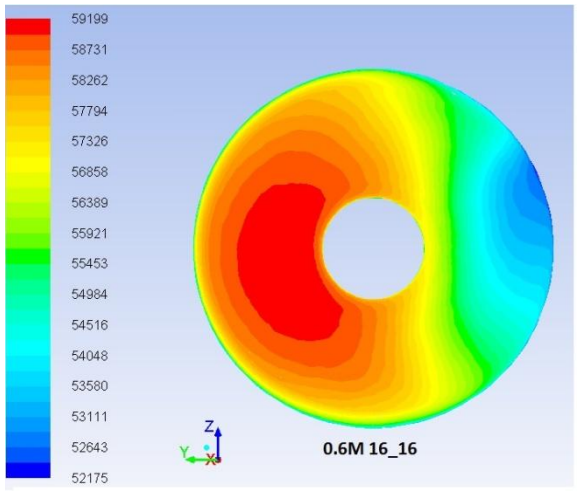

(i)

Figure 4-29 Total Pressure Contours at the AIP for the 0.6M Flight Attitudes

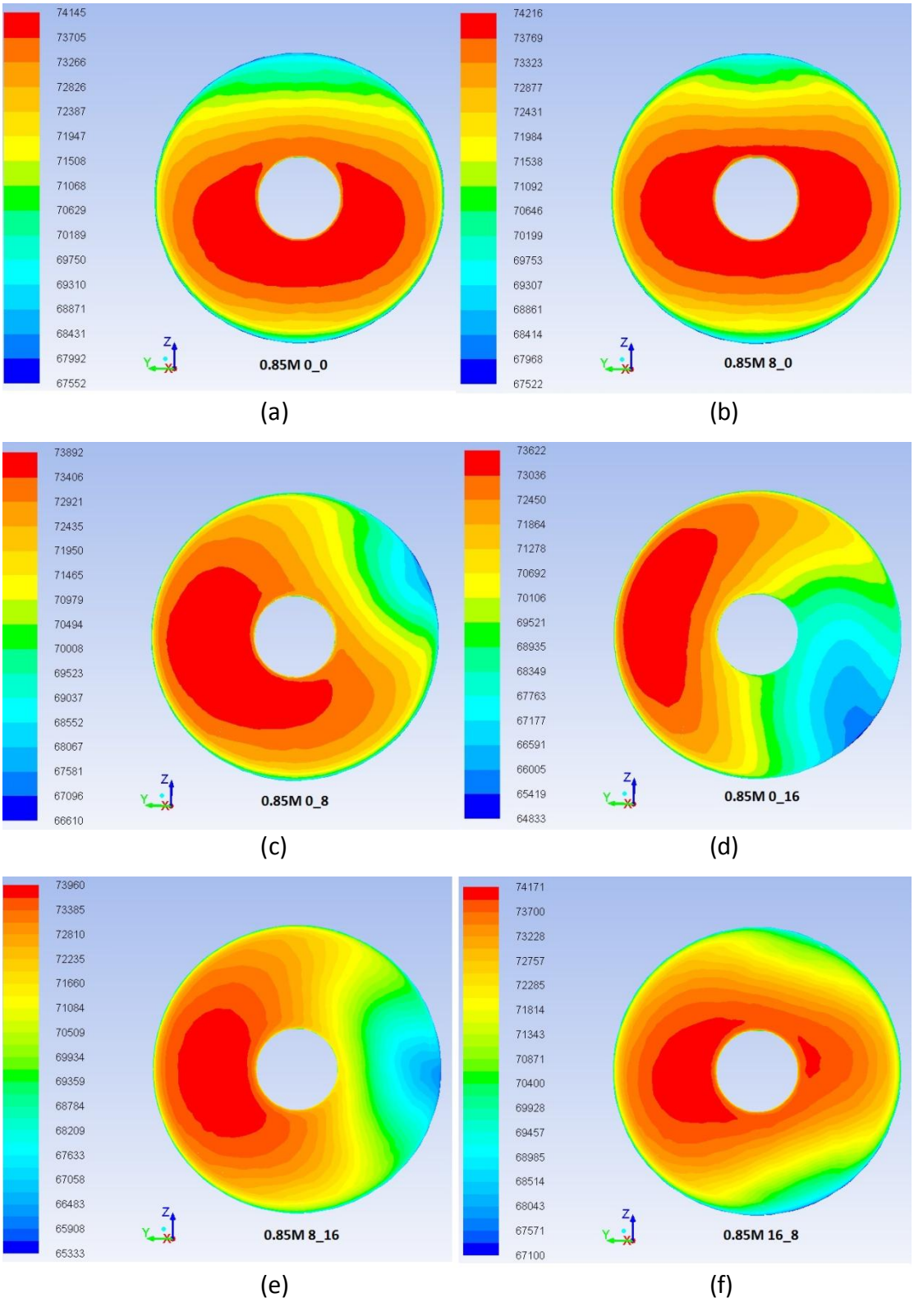

Figure 4-30 Total Pressure Contours at the AIP for the 0.85M Flight Attitudes (continued)

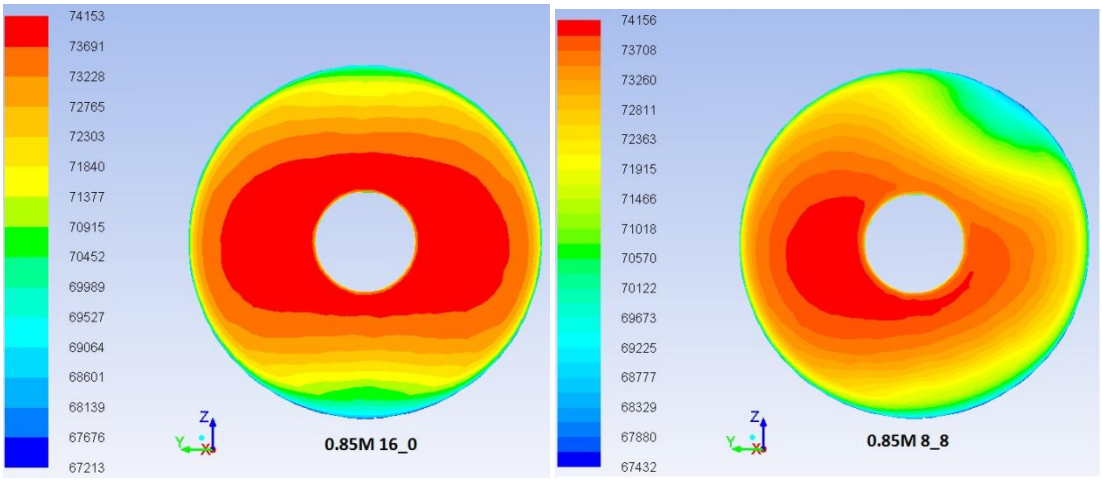

(g) (h)

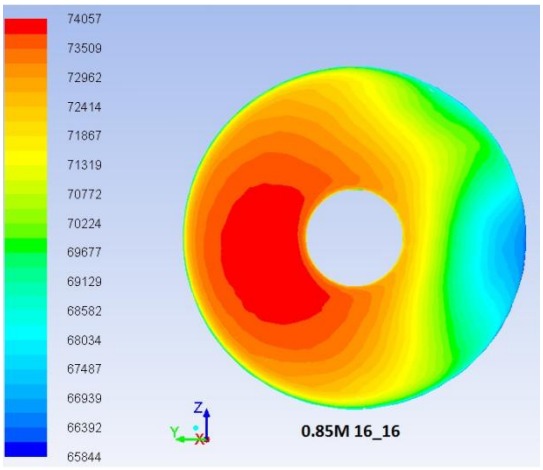

(i)

Figure 4-31 Total Pressure Contours at the AIP for the 0.85M Flight Attitudes

4.6 Chapter Summary

In this chapter, the flight conditions that were to be tested in order to examine the infuence of the aircraft's attitude onto the engine's performance were defined. The selected flight attitudes comprise a rather mild sample from the flight envelope of this aircraft (AOA and AOSS values within the aircraft's normal controllable range[76]) which was considered suitable for the testing of a newly developed model like the one described herein.

The variation of the aircraft's flight attitude was expressed by altering the angle of the incoming flow into the computational domain in CFD.

The novelty in the created model is the presence of the intake that allows the airflow to travel all the way up to the engine's face. Since no similar experimental work referring to the entire model was found in the open literature the validation of the present CFD model was accomplished through the comparison of the flow results around the aircraft geometry with similar ones [60], [61] and through the examination of the flow characteristics inside the aircraft intake.

Satisfactory results were obtained from that indirect validation process which gave credits to the accuracy of the CFD model and thus confidence for its usage in the progress of the current research work.

The finalized CFD model was tested in 27 flight conditions and the total pressure distribution at the engine's face was CFD calculated for each one of them.

5 DISTORTION RESULTS

5.1 Distortion Patterns

The total pressure profiles presented in Figures 4-26, 4-27 and 4-28 are representative of the level of total pressure distortion that the engine experiences due to the changes in the aircraft's flight attitude. As can be observed the total pressure is not uniform at all on the AIP area and great variations exist. The severity of these variations depends on the AOA and the AOSS values.

These profiles comprise the distortion patterns the effect of which on the engine's performance will be estimated later on.

5.2 Distortion Quantification Process

In order to communicate the level of distortion into the engine's operation, the distortion patterns, presented before, needed to be quantified. In other words the colourful images representing the variation of total pressure needed to be translated into numbers representing the amount of distortion due to the changes in the aircraft's flight attitude. These numbers were the distortion descriptors.

The distortion descriptor elements provide means of identifying critical distorted inlet-flow conditions. Also they help airframe and propulsion designers to communicate in common terminology during the conceptual design and integration of novel airframe and engine systems.

Distortion descriptors are based on total pressure readings at specific points on the AIP. In the present study, 40 points were alocated on this plane, configured in a five-ring arrangement, similar to that presented in Figure 2-14. Figure 5-1 presents the arrangement of these measurement points on the AIP. Ring number 1 is near to the hub whereas ring no 5 is closer to the tip. Each ring covers equally spaced areas of the whole plane and comprises 8 measuring points (i.e. one point per 45° circumference).

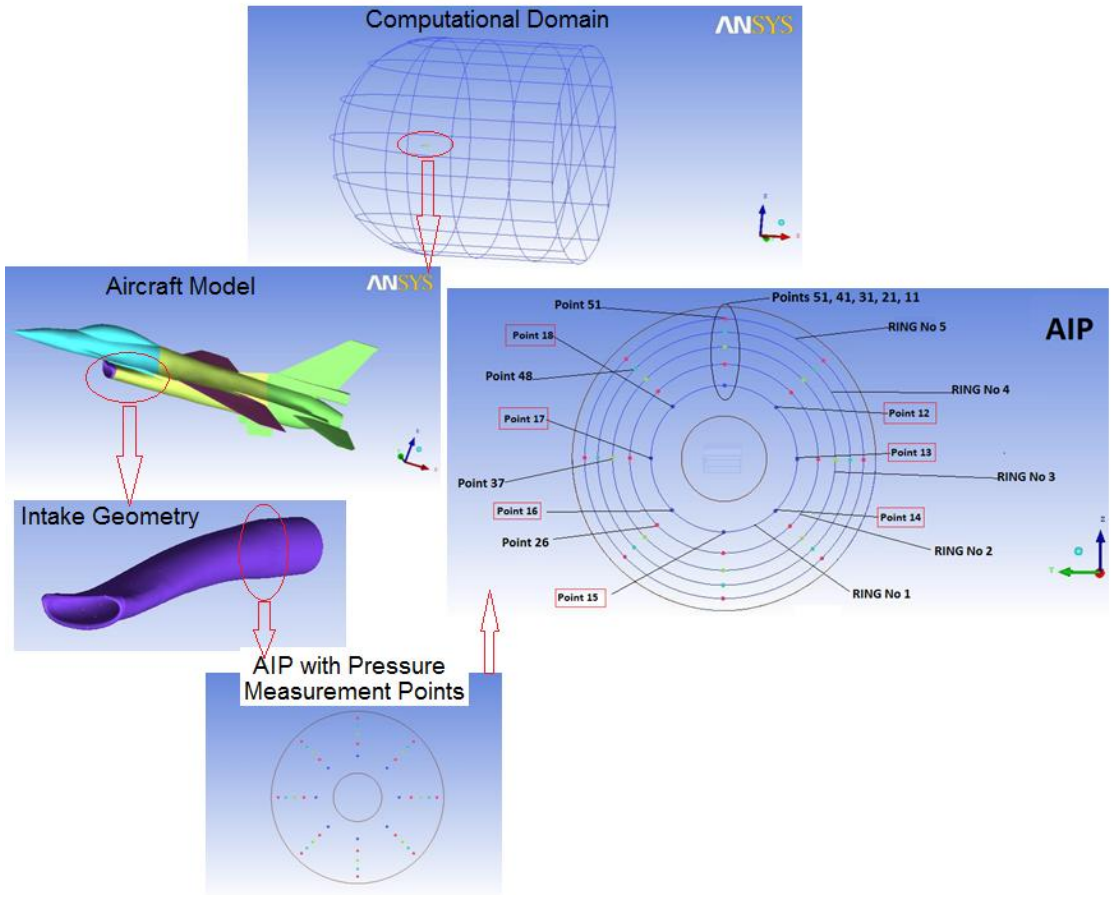

Figure 5-1 Position of AIP and Location of Total Pressure Measurement Rings and Points on the AIP

Through the CFD model the values of total pressure at these points for each one of the examined flight attitudes were calculated. Based on these values the distortion descriptors were derived.

The number of 40 total pressure measurement points has been adopted since it has been experimentally proved that provides suficiently accurate results[(62), (63), (64)]. Consequently, it was selected not to allocate more measuring points on the AIP since the difference in the obtained results would have been negligible.

The distortion has been quantified on a ring by ring basis. At first, the total pressure results predicted for each point on the ring were collected. These total pressure values were then linearly interpolated and plotted against the angular location of the measuring point that they were taken at.

In order for the low total pressure region to be clearly defined the ring average total pressure (PAV) was also fitted on the same graph. The total pressure results on the 1st ring were averaged through the integral of the function P(θ), which represents the linear fit between the pressure data points. Thus [10], [20],

$$(PAV)_1 = \frac{1}{360}\int_0^{360} P(\theta)_1 \, d\theta \qquad (eq.5-1)$$

Based on the way it is generally approached, distortion can be described through its circumferential and radial components both of which are studied on a ring by ring basis.

5.2.1 Circumferential Distortion

The descriptors that refer to the circumferential distortion are the following:[10]

- The **multiple per revolution** (MPR) is a numerical indication of the number of low-pressure regions for each ring. The value this parameter may take, depends on the number of the ring low pressure regions comparing to the ring average value and on the circumferential angle that separates them from each other. In the quantification process two main categories of pressure distribution were encountered. Profiles with pressure measurement rings with one multiple per revolution (MPR=1), in which only one low pressure region was noticed. In this case the quantification was quite straight forward. Apart from that, there were profiles with more than one low pressure regions encountered on the pressure measurement rings. In these cases it was important to find out how far away from each other the low pressure regions were. If they were less than 25 degrees apart, then their effect was considered to be the result of their summation. In cases where the low pressure regions were more than 25 degrees [10] apart from each other, only the greatest one was considered to have affected the operation of the engine. The distortion descriptors were calculated for both low pressure regions and only the greatest of them was adopted for the next calculations. In the present work the values that were collected for this parameter ranged from 1, at the majority of the tested cases, to 1.99 at ring No 5 of 0.6M with 8˚ AOA and 0˚ AOSS flight attitude.

Figure 5-2 provides a visualization of the resulted total pressure distribution at the engine's face for this flight attitude, presenting two clearly distinguished low pressure areas one at the upper part of the AIP and another one at its lower part.

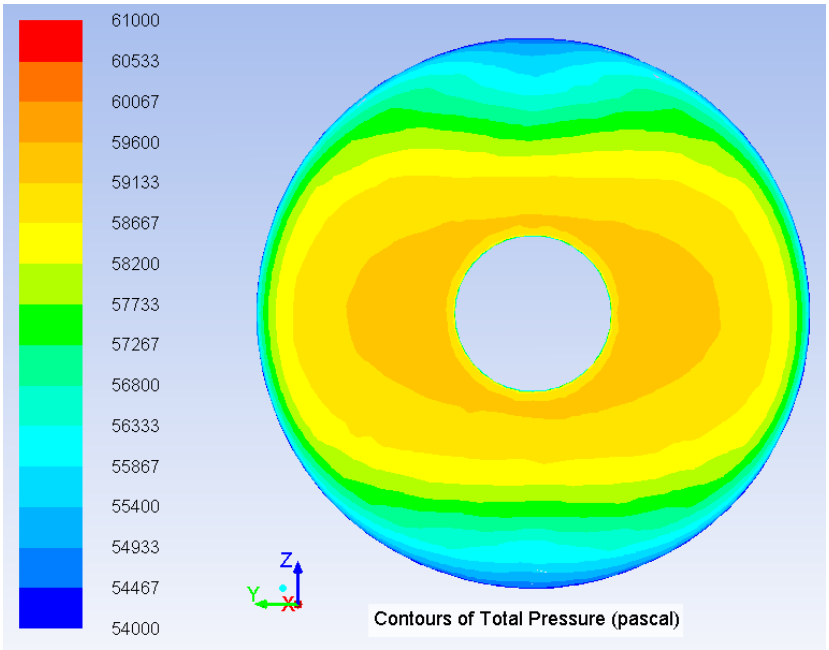

Figure 5-2 Profile of Total Pressure at the AIP for the 0.6M Flight with 8˚ AOA and 0˚ AOSS

- The **extent** element is the angular region in degrees in which the pressure is below the ring average pressure. The higher this value the more extended the low pressure region is. In the present study the highest value which was 189˚, occurred at the flight attitude of 0.6M with 8˚AOA and 8˚AOSS. Figure 5-3 below (upper part) presents the numerically calculated total pressure distribution at the AIP for this specific flight attitude. The bluish coloured area represents the low pressure area which as it can be seen in the figure, near the tip extends to that angular region (189˚).

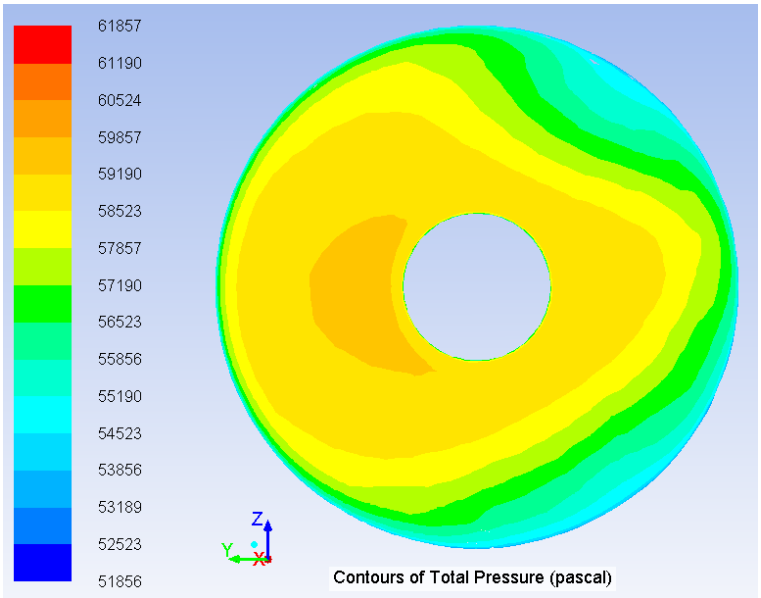

Figure 5-3 Profile of Total Pressure at the AIP for the 0.6M Flight with 8˚ AOA and 8˚ AOSS

The **intensity element** which is a numerical indication of the magnitude of the pressure defect for each ring. Pressure defect refers to the areas with lower pressure than the ring average value. The intensity value is given by equation 2-8 and it may range from 0 to 1 with the higher values to denote more severe pressure variations. The highest value for this parameter in the present study was 0.05 and occurred at the flight attitude of 0.6M flight with 8˚ AOA and 8˚ AOSS.

5.2.2 Radial Distortion

Radial distortion is described in terms of the **radial distortion intensity.** This element indicates the difference between the ring average total pressure (PAV) and the face average total pressure (PFAV) normalized with the face average value [10], [20].

Each ring on the same total pressure profile has its own value of radial distortion intensity. This parameter may take negative values as well when the ring average total pressure happens to be greater than the face average one.

5.3 Distortion Quantification Results

The steps of the distortion quantification process will be demonstrated on two flight attitudes that were representative of all in terms of MPR. The first flight attitude is the one of 0.6M with 8˚ AOA and 16˚ AOSS which is representative of the flight attitudes with MPR=1. The second flight attitude which is representative of the cases where MPR>1 is that of 0.6M with 8˚ AOA and 0˚ AOSS.

These two methodologies have been followed for the rest of the tested cases, the results of which are quoted in Appendix A. Based on these results:

- The values of MPR that were collected ranged from 1, at the majority of the tested cases, to 1.99 at ring No 5 of the resulted total pressure profile from the flight attitude of 0.6M with 8 AOA and 0 AOSS (fig. 5-2). The other distortion descriptors though (circumferential intensity and extent) for this specific flight attitude, as shown in table A-2, are at their lowest values. As a result this maximum MPR in conjunction with the low values of circumferential intensity and extent does not render this flight attitude a severe one in terms of total pressure distortion.
- The greatest calculated circumferential extent was 189˚, and occurred at the flight attitude of 0.6M with 8˚AOA and 8˚AOSS. The total pressure profile for this flight attitude is presented in fig. 5-3.
- The highest circumferential intensity found to be 0.050 again at the flight attitude of 0.6M flight with 8˚ AOA and 8˚ AOSS (fig. 5-3).
- The highest radial distortion (0.026) was calculated for the flight attitude of 0.35M flight with 0˚ AOA and 0˚ AOSS.

5.3.1 Results for the 0.6M Flight Attitude with 8˚ AOA and 16˚ AOSS

The CFD predicted total pressure profile at the AIP for this specific aircraft flight attitude is presented in fig. 5-4 and the CFD predicted values of total pressure at the 8 points of the 1st ring (near to the hub), are shown in table 5-1.

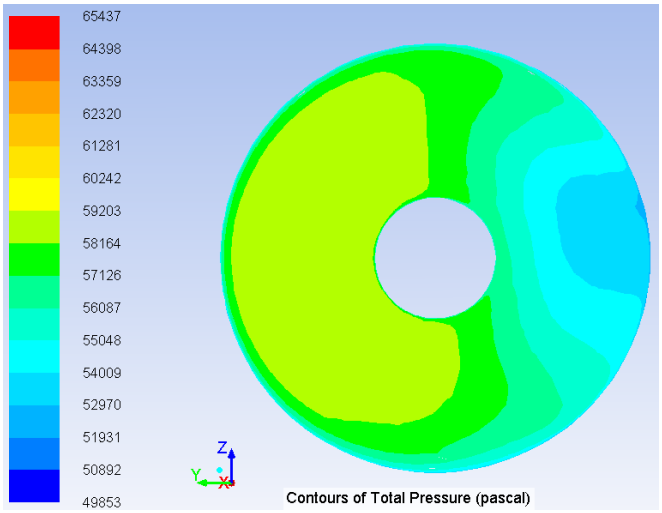

Figure 5-4 Profile of Total Pressure at the AIP for the 0.6M Flight with 8˚ AOA and 16˚ AOSS

Table 5- 1 CFD Predicted Values of Total Pressure at the 1st Ring for the Flight attitude of 0.6M with 8˚ AOA and 16˚ AOSS

RING No	Point Name (fig. 5-6)	Angle (°)	P (Pa)
1	11	0	58,029.48
	12	45	55,560.68
	13	90	54,755.64
	14	135	56,723.66
	15	180	58,536.45
	16	225	59,079.98
	17	270	59,194.46
	18	315	59,028.90

These total pressure values were then linearly interpolated for every degree of angle which resulted in the graph shown in fig. *5-5*. In order for the low total pressure region to be clearly defined, the ring average total pressure (PAV) was also plotted on the same graph.

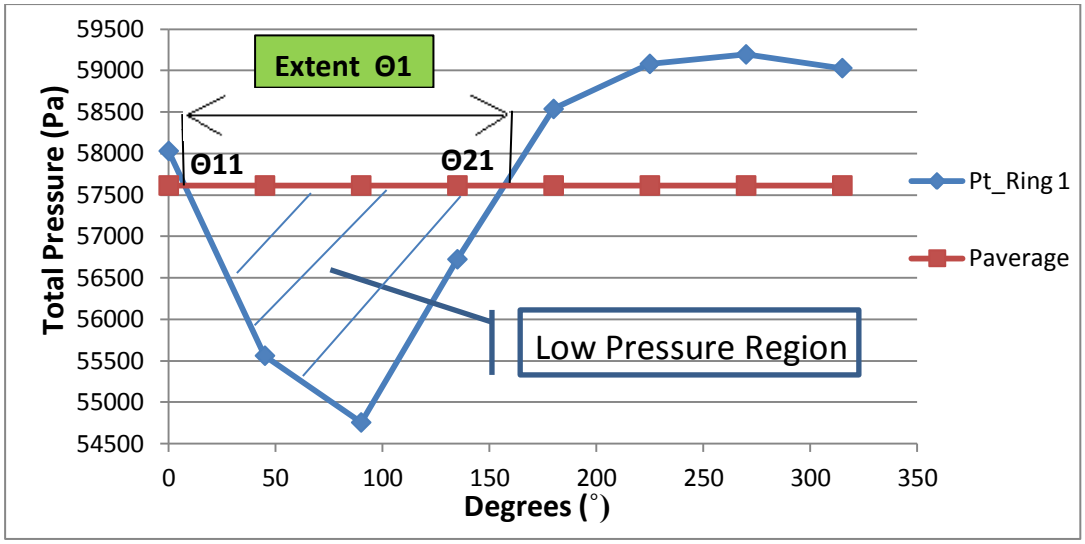

Figure 5-5 *Linear Interpolation of the CFD Predicted Values of Total Pressure at the 1st Ring for the Flight Attitude of 0.6M with 8˚ AOA and 16˚ AOSS. Line of Average Total Pressure and Circumferential Extent of Low Pressure region also Shown.*

Applying the eq. 5-1 resulted in,

$$(PAV)_1 = 57{,}613.66 \text{ Pa} \qquad (eq. 5-2)$$

For the distortion pattern of the flight attitude of 0.6M with 8 degrees AOA and 16 degrees AOSS the MPR for Ring No1 is equal to unity since the linear interpolation of the total pressure results for this ring revealed that there was only one low total pressure region.

$$MPR = 1 \qquad (eq.5\text{-}3)$$

The circumferential extent (Θ_1 in fig. 5-5) of that low Pressure region is defined as,

$$Extent = \theta_1 = \theta_{21} - \theta_{11} = 157.09 - 7.58 = 149.51^\circ \qquad (eq.5\text{-}4)$$

where **θ21** and **θ11** were the angles on the linear interpolation graph (fig. 5-5) at which the pressure data line intersected with the total pressure ring average line.

Before the calculation of the intensity of the circumferential distortion, the average total pressure of the low pressure region (PAVLOW) needed first to be found. The low pressure region of the 1st ring was averaged through the integral of the function P(θ) between the boundaries of that region. Thus,

$$(PAVLOW)_1 = \frac{1}{\Theta_1}\int_{\Theta_{11}}^{\Theta_{21}} P(\theta)_\iota \, d\theta = 55987.91\ Pa \qquad \textit{(eq. 5-5)}$$

And then from eq. 2-8 it was obtained that the circumferential intensity element for that ring was

$$Intensity = \left(\frac{PAV - PAVLOW}{PAV}\right)_1 = 0.028 \qquad \textit{(eq.5- 6)}$$

The AIP face average total pressure (PFAV) for the examined flight attitude was CFD predicted at,

$$PFAV = 57{,}102.91\ Pa \qquad \textit{(eq. 5-7)}$$

And then for the No 1 ring,

$$Radial\ \ Intensity = \left(\frac{PFAV - PAV}{PFAV}\right)_1 = -0.007 \qquad \textit{(eq.5- 8)}$$

Negative values for radial intensity mean that the ring average total pressure is greater than the face average one.

Up to now we have seen the distortion results based only on the 1st measurement ring. Exactly in the same way the results for the other 4 rings, allocated on the profile of figure 5-4, were obtained. Table 5-2 below contains all the data related to the Distortion Descriptor Elements referring to the 0.6M flight with 8˚ AOA and 16˚ AOSS distortion pattern.

The first column refers to the rings' location on the AIP, with the ring number 1 to be closer to the centre of the AIP. The next column contains the names

of the measuring points (just for reference) and the third one specifies the circumference distance in degrees from the vertical line at which each point was located at.

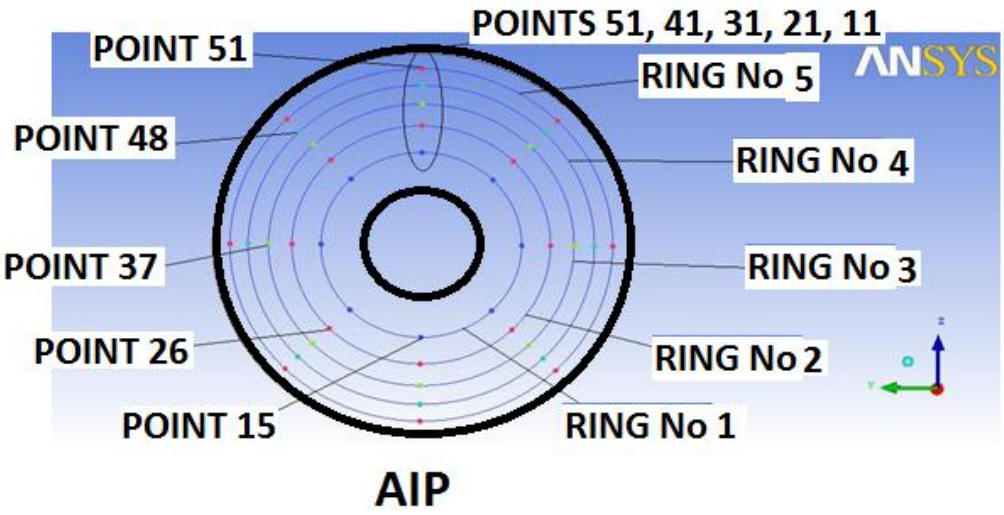

Figure 5-6 Measuring Point Location on the AIP

In the next column the Total Pressures measured at each point are quoted. These values were linearly interpolated for each ring and from the resulted graphs the respective average values for the Total Pressure were obtained which were also fitted on the same graphs. Finally, in the last columns of table 6, the distortion descriptor elements are quoted.

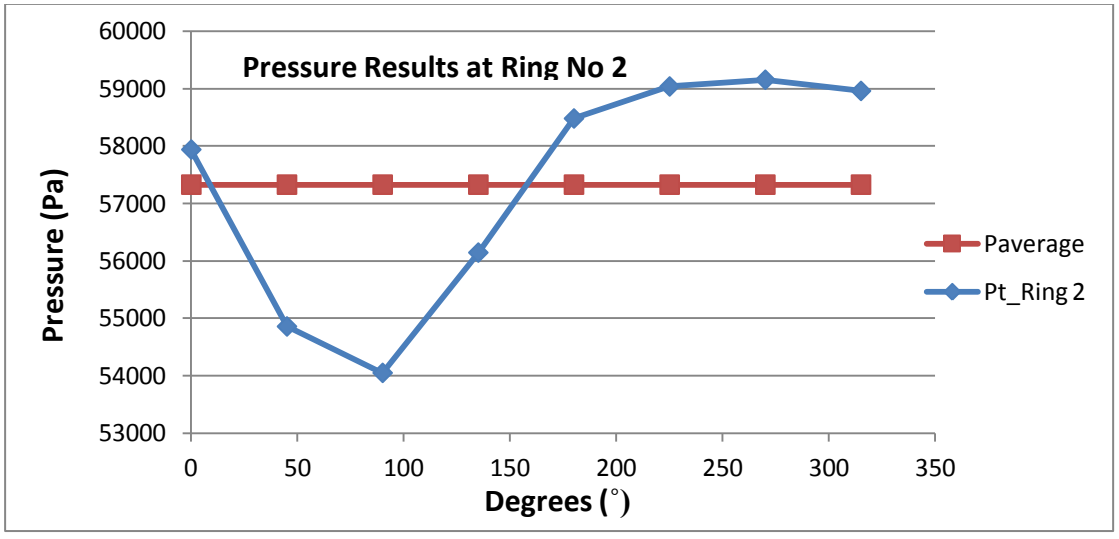

Figure 5-7 2nd Ring- Total Pressure Results

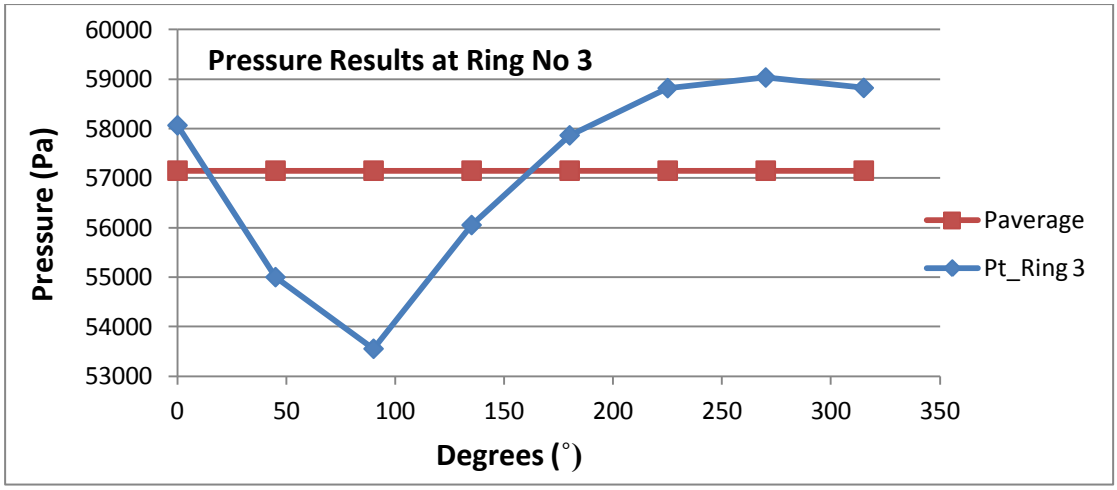

Figure 5-8 3rd Ring- Total Pressure Results

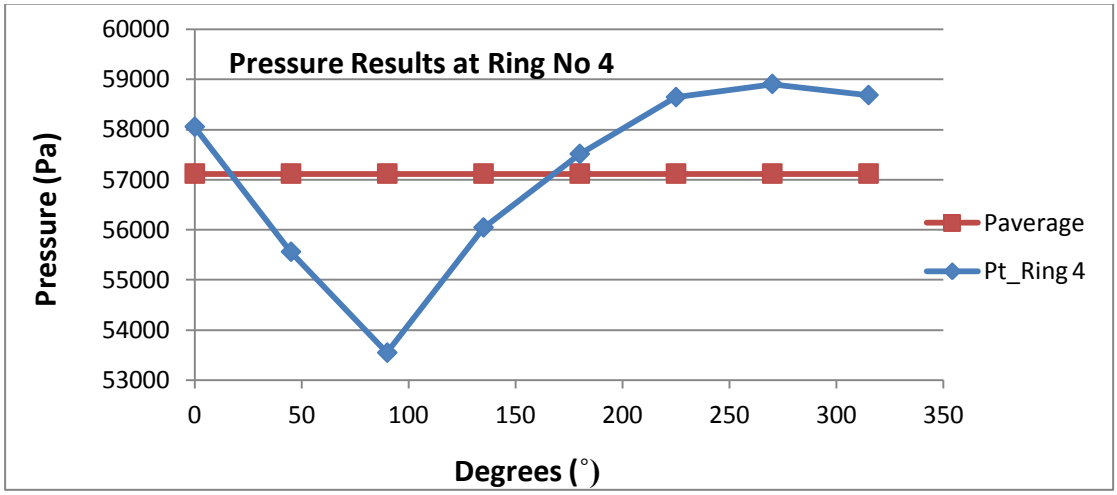

Figure 5-9 4th Ring- Total Pressure Results

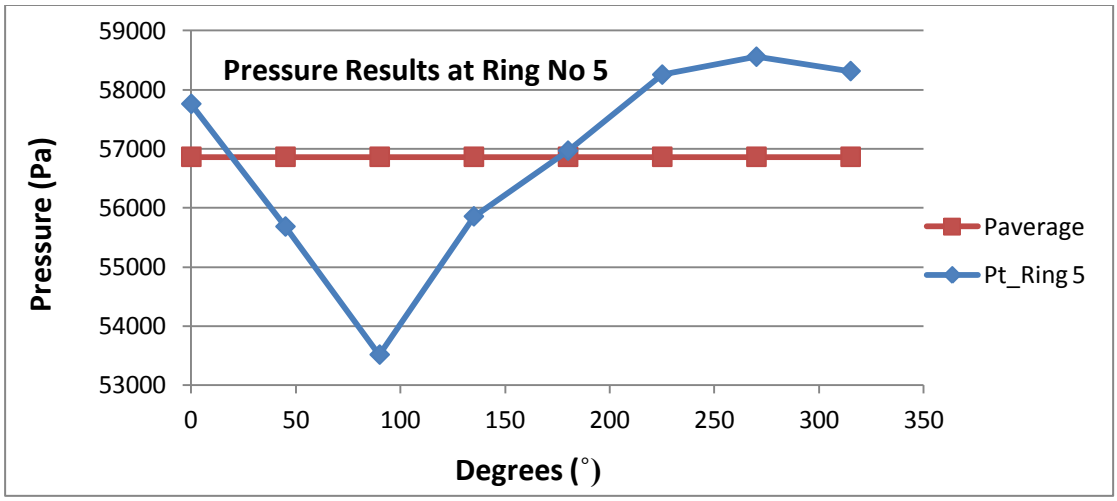

Figure 5-10 5th Ring- Total Pressure Results

Table 5- 2 Distortion Descriptor Elements Data for 0.6M Flight with 8˚ AOA and 16˚ AOSS (continued)

			PFAV=57102.91 Pa		Distortion					
						Circumferential				Radial
RING	Point Name	Angle (˚)	Pt (Pa)	PAV (Pa)	Intersects at (˚)	Extent (˚)	PAVLOW (Pa)	MPR	Intensity	Intensity
1_hub	11	0	58029.48	57613.66	7.58	149.51	55987.91	1	0.028	-0.007
	12	45	55560.68							
	13	90	54755.64							
	14	135	56723.66		157.09					
	15	180	58536.45							
	16	225	59079.98							
	17	270	59194.46							
	18	315	59028.90							
2	21	0	57936.48	57325.35	8.93	148.87	55392.18	1	0.034	-0.002
	22	45	54855.27							
	23	90	54046.45							
	24	135	56141.94		157.8					
	25	180	58477.69							
	26	225	59035.04							
	27	270	59152.30							
	28	315	58957.61							
3	31	0	58065.93	57151.09	13.43	148.86	55243.06	1	0.033	0.001
	32	45	54999.57							
	33	90	53552.54							
	34	135	56052.20		162.28					
	35	180	57864.58							
	36	225	58818.18							
	37	270	59033.04							
	38	315	58822.71							

Table 5-2 Distortion Descriptor Elements Data for 0.6M Flight with 8˚ AOA and 16˚ AOSS										
						Circumferential				**Radial**
RING	**Point Name**	**Radius (˚)**	**Pt (Pa)**	**PAV (Pa)**	**Intersects at (˚)**	**Extent (˚)**	**PAVLOW (Pa)**	**MPR**	**Intensity**	**Intensity**
4	41	0	58052.97	57117.42	16.86	151.10	55397.40	1	0.030	0.002
	42	45	55556.29							
	43	90	53542.33		167.97					
	44	135	56041.73							
	45	180	57510.11							
	46	225	58644.64							
	47	270	58906.38							
	48	315	58684.90							
5_tip	51	0	57760.32	56864.22	19.43	156.37	55358.19	1	0.026	0.006
	52	45	55684.59							
	53	90	53516.52		175.8					
	54	135	55856.52							
	55	180	56968.01							
	56	225	58255.24							
	57	270	58557.74							
	58	315	58314.84							

All distortion elements for each ring of this pattern are summarized and illustrated using a bar graph display, as shown in figs 5-11, 5-12 and 5-13, where circumferential extent, circumferential intensity and radial intensity are displayed respectively. Similar graphs for all the tested flight attitudes are quoted in Appendix D.

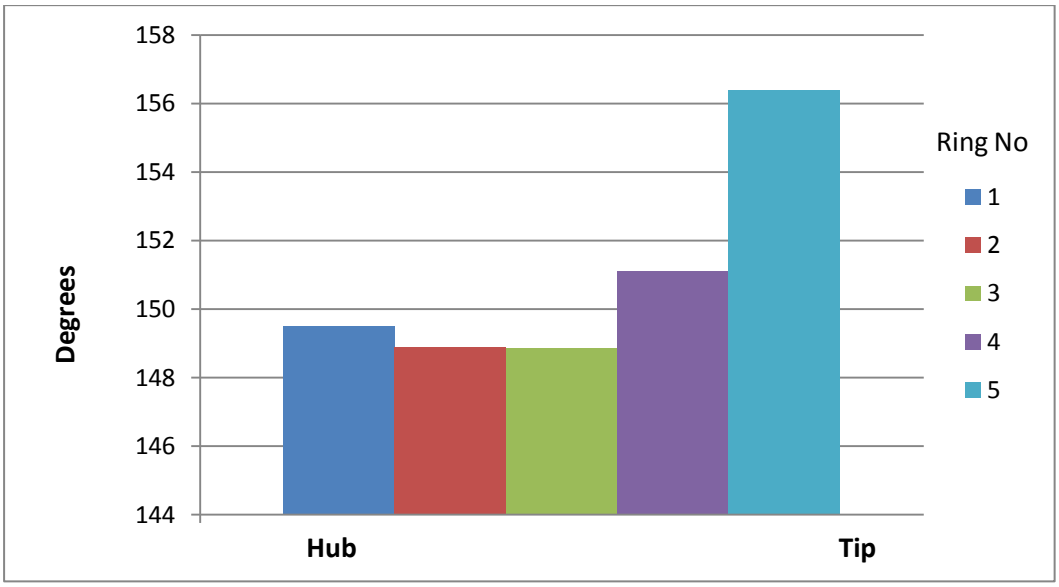

Figure 5-11 Circumferential Extent at Each Ring on the Total Pressure Profile for the Flight Attitude of 0.6M with 8˚ AOA and 16˚ AOSS

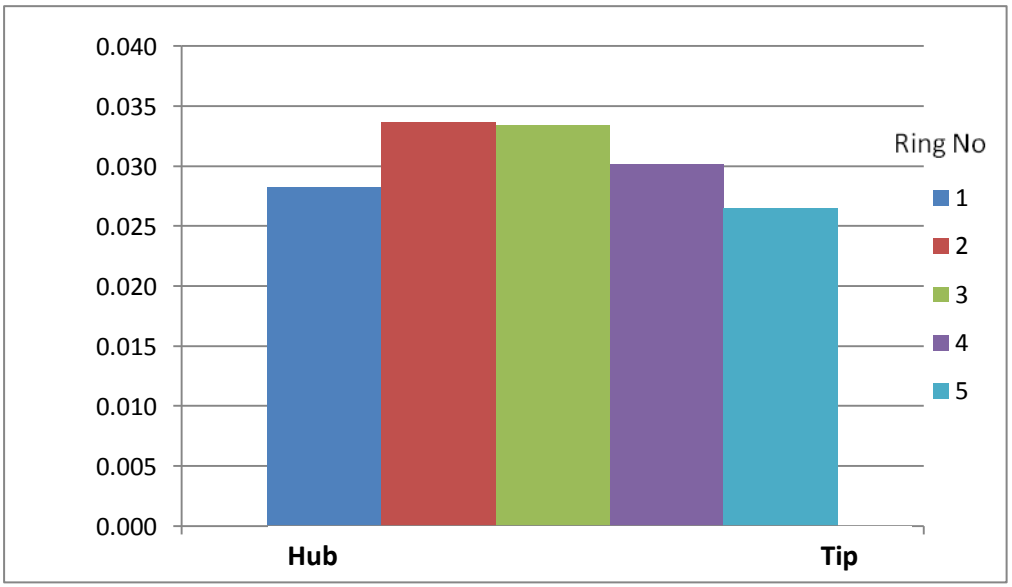

Figure 5-12 Circumferential Intensity at Each Ring on the Total Pressure Profile for the Flight Attitude of 0.6M with 8˚ AOA and 16˚ AOSS

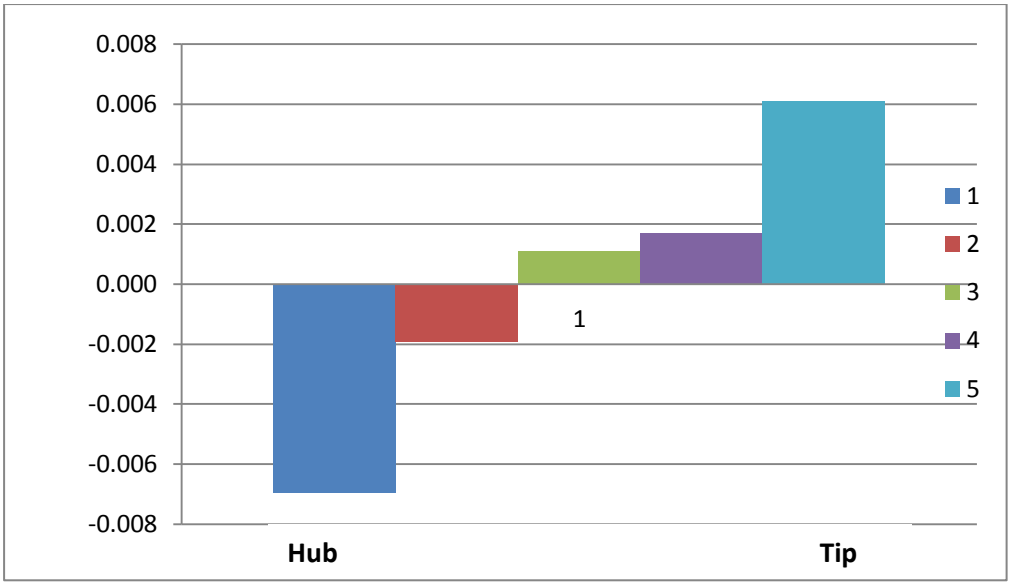

Figure 5-13 Radial Intensity at Each Ring on the Total Pressure Profile for the Flight Attitude of 0.6M with 8˚ AOA and 16˚ AOSS

This type of representation makes it easier to conclude on the following characteristics of this distortion pattern, namely:

- The greatest circumferential intensity is noted at ring No2, (fig. 5-12). Considering eq. 5-4, this means that the difference between PAV and PAVLOW becomes greatest at that region. So, for this specific flight attitude the magnitude of the total pressure defect is greatest at the area between hub and tip.
- The greatest circumferential extent is noted closer to the tip (ring No 5), as it can be seen on fig. 5-11. At that area the total pressure defect extends to the highest circumference comparing to the other rings.
- The greatest radial intensity occurs at ring No 5, (fig. 5-13). Considering eq. 5-8, the average total pressure at that ring presents the greatest deviation from the face average total pressure as the latter was numerically calculated from CFD.

The above observations can be visualized in fig. 5-14 below where the total pressure contours obtained from the simulation model when it is exposed to these specific flight conditions, are presented. When focusing inside the intake, it can be observed that the lowest pressure area is located at one side of the AIP. This was expected to happen as due to the AOSS and the position of the airframe in relation to the incoming airflow one part

of the intake becomes shielded to this incoming flow. This is translated into a pressure defect at the AIP with the characteristics already described above.

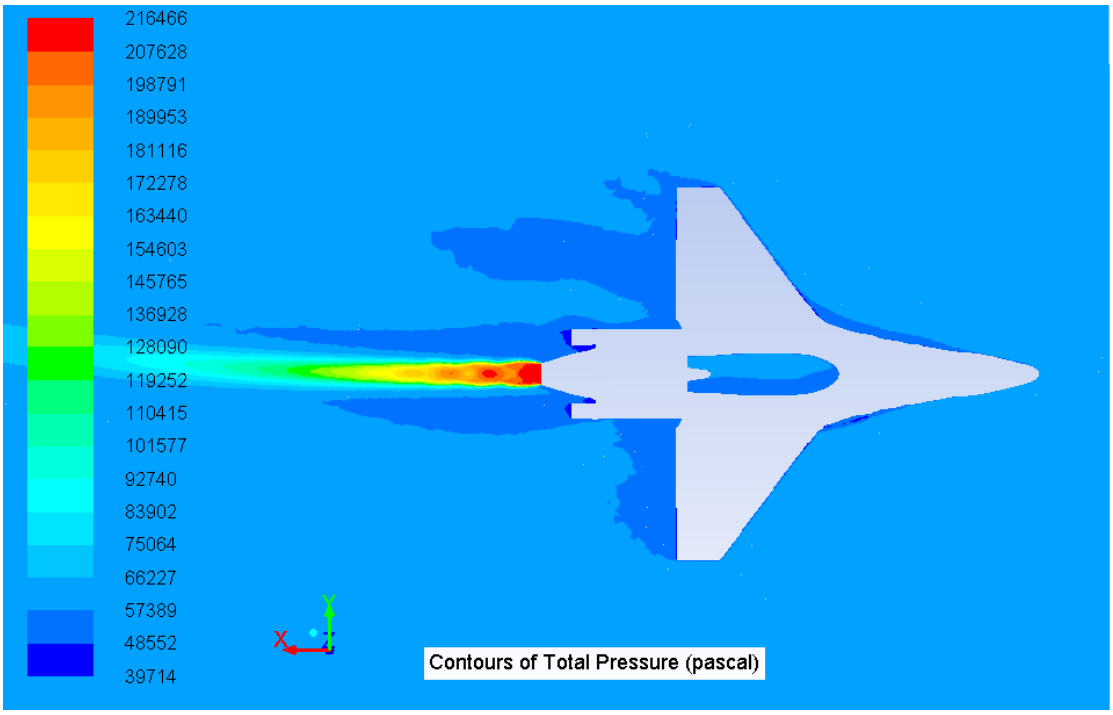

Figure 5-14 Contours of Total Pressure for the Flight Attitude of 0.6M with 8˚ AOA and 16˚ AOSS

5.3.2 Results for the 0.6M Flight Attitude with 8˚ AOA and 0˚ AOSS

The total pressure distribution at the engine's face for this flight attitude is presented in fig. 5-15 below.

As can be observed on this figure, at the outer circumference of the AIP there are two low pressure areas that are circumferentially separated from each other. One low pressure area is formed at the upper part of the AIP and another low pressure area is formed at the lower part of it at an angular distance of about 180˚. Based on this observation and considering the definition of the MPR, given in par. 5.2.1 above, it was expected this distortion descriptor (MPR) for this case to be greater than unity.

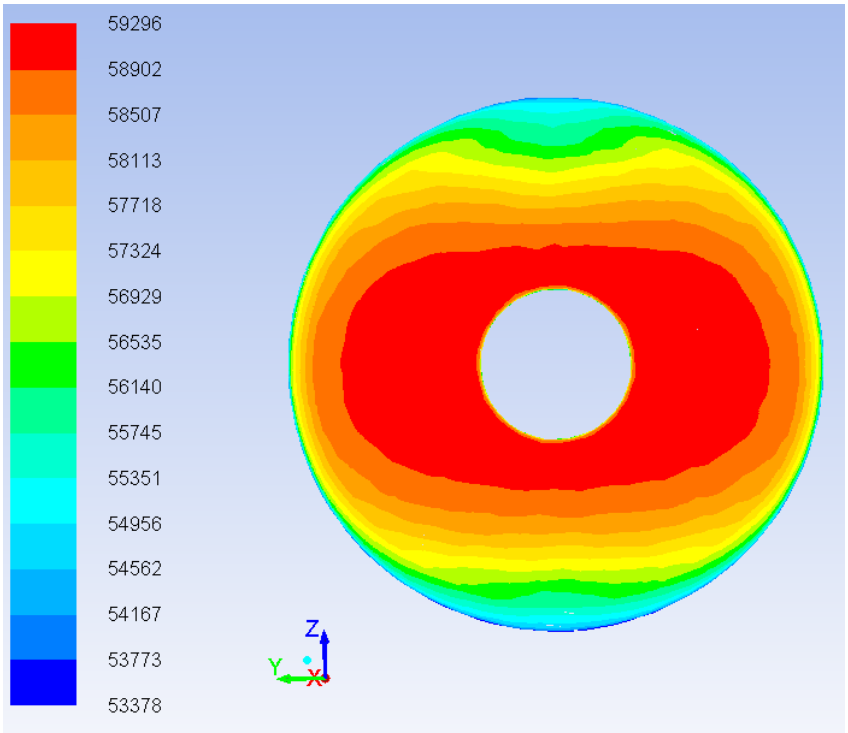

Figure 5-15 *Contours of Total Pressure (Pascal) on the AIP for the Flight Attitude of 0.6M flight with 8˚ AOA and 0˚ AOSS*

The CFD calculated values of total pressure at the 8 points of the 1st ring (close to the hub), are shown in table 5-3.

Table 5- 3 CFD Predicted Values of Total Pressure at the 1st Ring for the Flight attitude of 0.6M with 8˚ AOA and 0˚ AOSS

RING No	Point Name (fig. 5-6)	Angle (°)	P (Pa)
1	11	0	58,658.77
	12	45	59,118.83
	13	90	59,267.97
	14	135	59,114.78
	15	180	58,819.00
	16	225	59,037.56
	17	270	59,262.63
	18	315	59,124.59

Applying eq. 5-1 to these data results in,

$$(PAV)_1 = 59{,}050.52 \text{ Pa} \qquad (eq. 5-9)$$

The linear interpolation of the total pressure data quoted in table 5-3 resulted in the graph shown in fig. 5-16. In order for the low total pressure regions to be clearly defined, the line representing the ring average total pressure (PAV) was also plotted on the same graph.

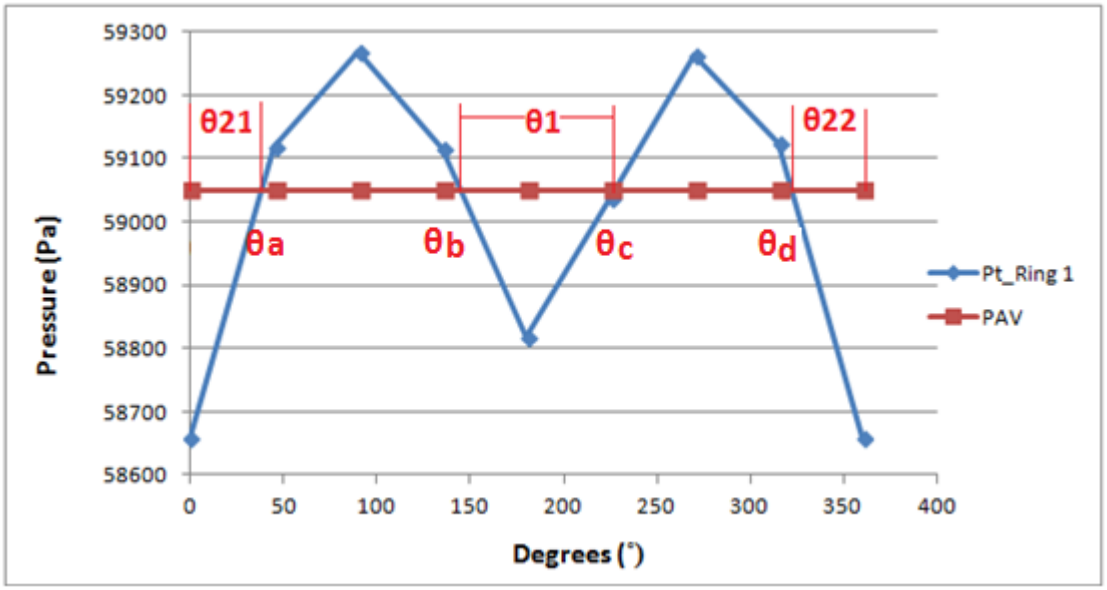

Figure 5-16 *Linear Interpolation of the CFD Predicted Values of Total Pressure (Pascal) at the 1st Ring for the Flight Attitude of 0.6M with 8˚ AOA and 0˚ AOSS. Line of Average Total Pressure is also Shown.*

The circumferential extent of each low pressure region (in degrees) was defined as (fig. 5-16),

$$Extent_1 = \theta_1 = 227.59 - 144.78 = 82.81 \qquad (eq.5\text{-}10)$$

and

$$Extent_2 = \theta_2 = \theta_{22} + \theta_{21} = (360 - 322.16) + 38.32 = 76.16 \qquad (eq.5\text{-}11)$$

where **θ22** and **θ21** are the sub-extents on the linear interpolation graph (fig. 5-16) of the second low pressure region of the 1st ring.

The circumferential angular distance between the two low pressure regions was obviously more than 25 degrees and as such the extent (distortion descriptor) which can be considered representative for the first ring, was the one corresponding to the maximum value between the two low pressure regions [10]. Thus,

$$Extent = \max(Extent_1, Extent_2) = Extent_1 = 82.81° \qquad (eq.5\text{-}12)$$

The average total pressure for each low pressure region (PAVLOW) was then calculated and this parameters was used in the calculation of the circumferential intensity.

The low pressure regions of the 1st ring were averaged through the integral of the function P(θ) between the boundaries of these regions. Thus (fig.5-16),

$$(PAVLOW)_1 = \frac{1}{\Theta_1}\int_{\theta b}^{\theta c} P(\theta 1)_1 \, d\theta = 58934.66 \, Pa \qquad (eq.\ 5\text{-}13)$$

and

$$(PAVLOW)_2 = \frac{1}{\Theta_2}\int_{\theta d}^{\theta a} P(\theta 2)_2 \, d\theta = 58{,}854.64 \, Pa \qquad (eq.\ 5\text{-}14)$$

And then from eq. 2-8 and for each low pressure region it was obtained that the circumferential intensity element was

$$Intensity_1 = \left(\frac{PAV - PAVLOW_1}{PAV}\right)_1 = 0.002 \qquad (eq.5\text{-}15)$$

and

$$Intensity_2 = \left(\frac{PAV - PAVLOW_2}{PAV}\right)_2 = 0.003 \qquad (eq.5\text{-}16)$$

The circumferential intensity, representative for the first ring, is the maximum between those two intensities [10]. As such,

$$Intensity = \max(Intensity_1, Intensity_2) = 0.003$$

The MPR term is defined as the number of equivalent low pressure regions, the equivalence being based on the ratio of the total integrated area beneath the PAV line in fig. 5-16. This is given by the following equation [10],

$$MPR = \frac{[(\frac{\Delta PC}{P})_1 \times \theta_1] + [(\frac{\Delta PC}{P})_2 \times \theta_2]}{\max[[(\frac{\Delta PC}{P})_1 \times \theta_1], [(\frac{\Delta PC}{P})_2 \times \theta_2]]} =$$

$$= \frac{(0.002 \times 82.81°) + (0.003 \times 76.16°)}{(0.003 \times 76.16°)} = 1.64 \qquad \textit{(eq.5-17)}$$

The AIP face average Total Pressure (PFAV) for the examined flight attitude was CFD calculated at,

$$PFAV = 58108.99\ Pa \qquad \textit{(eq. 5-18)}$$

And then for the No 1 ring and as far as the radial intensity distortion descriptor was concerned [10],

$$Radial\ \ Intensity = \left(\frac{PFAV - PAV}{PFAV} \right)_1 = -0.014 \qquad \textit{(eq.5-19)}$$

It is reminded that negative values for radial intensity mean that the ring average total pressure is greater than the face average one.

In the same way the results for the other 4 rings allocated on the profile of fig. 5-15 were obtained. The linear interpolation of the total pressure results on each ring are presented in the following graphs (figs 5-17, 5-18, 5-19, 5-20).

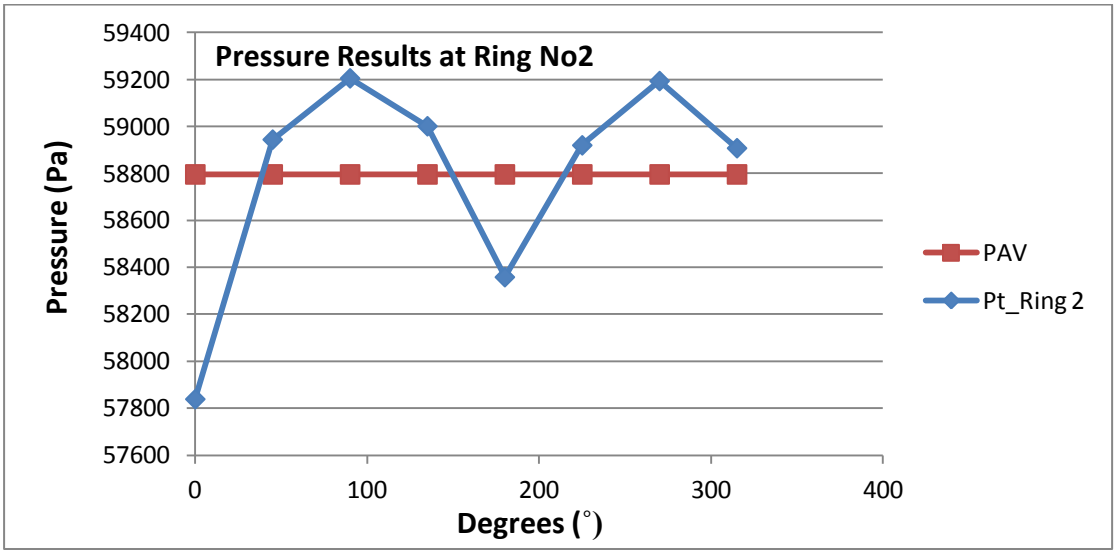

Figure 5-17 2nd Ring- Total Pressure Results

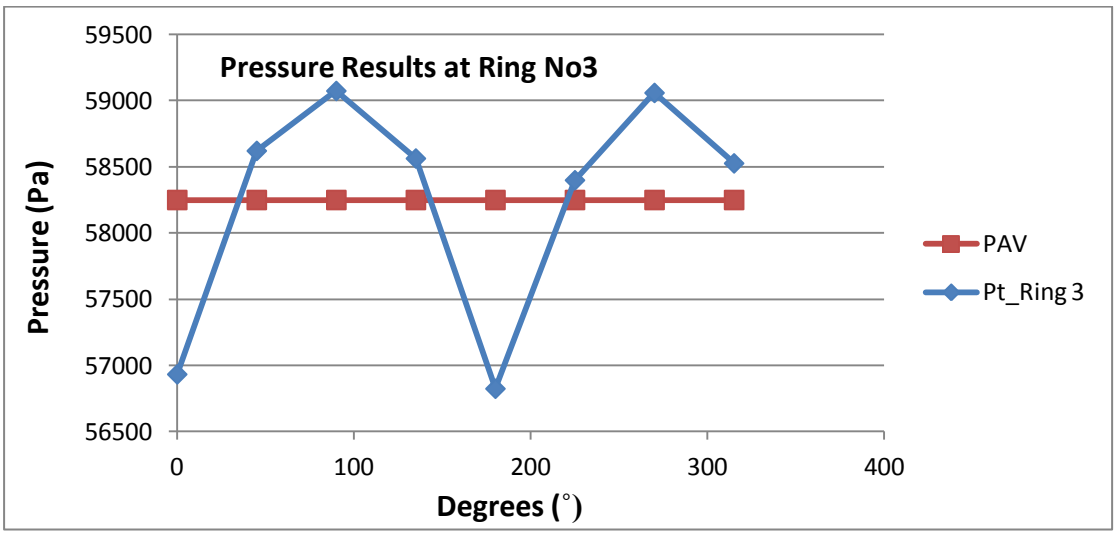

Figure 5-18 3rd Ring- Total Pressure Results

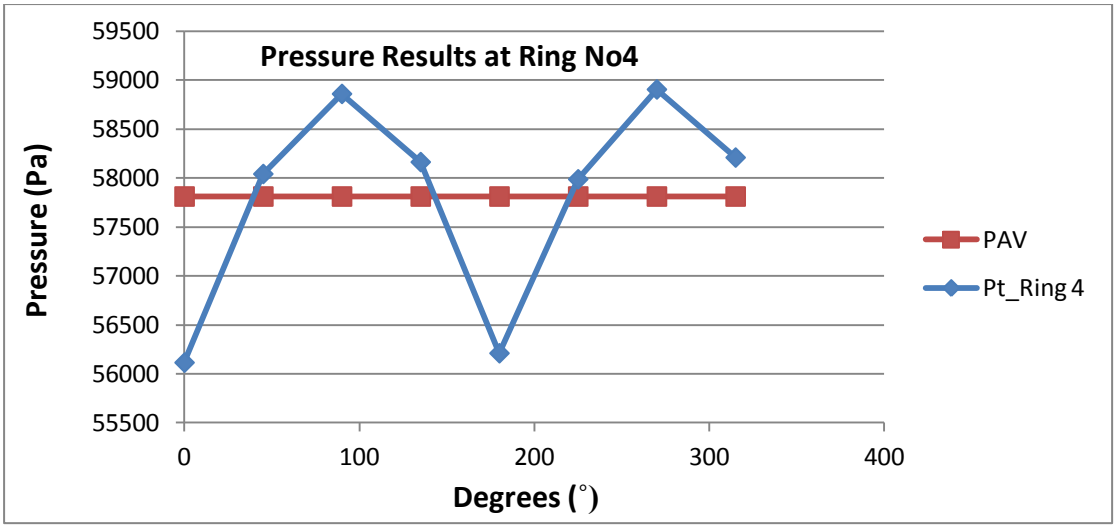

Figure 5-19 4th Ring- Total Pressure Results

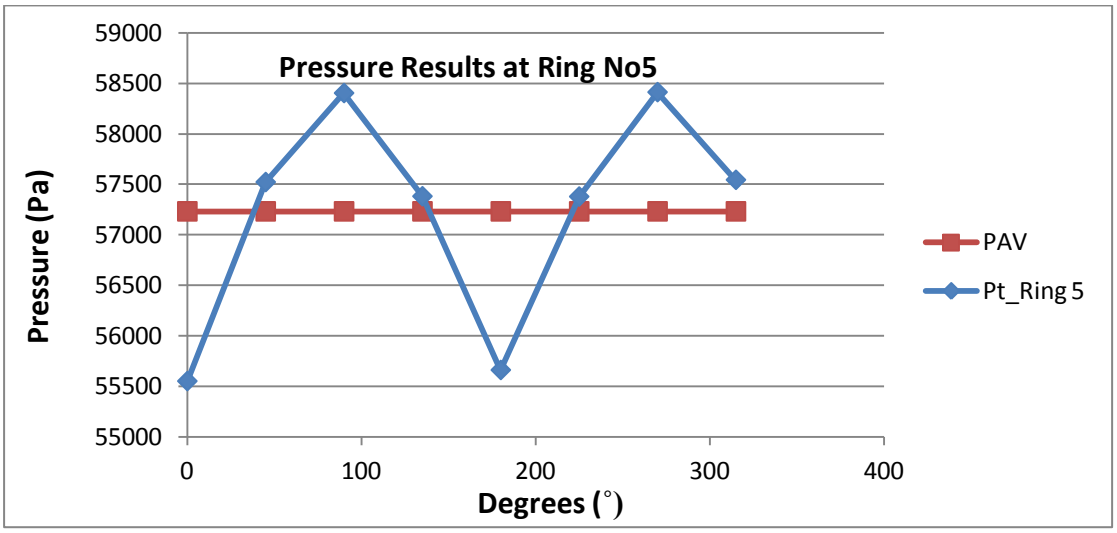

Figure 5-20 5th Ring- Total Pressure Results

Table 5-4 below contains all the calculated data related to the distortion descriptor elements referring to the 0.6M flight with 8˚ AOA and 0˚ AOSS distortion pattern.

Table 5- 4 Distortion Descriptor Elements Data for 0.6M Flight with 8˚ AOA and 16˚ AOSS

0.6M 8_0					
	RING_1	**RING_2**	**RING_3**	**RING_4**	**RING_5**
CIRCUMFERENTIAL_EXTENT	76.16	79.27	77.63	76.08	82.24
CIRCUMFERENTIAL INTENSITY	0.003	0.008	0.012	0.015	0.014
RADIAL INTENSITY	-0.014	-0.009	0.000	0.007	0.017
MPR	1.64	1.38	1.86	1.96	1.99

All distortion elements for each ring of this pattern are summarized and illustrated using a bar graph display, as shown in figs 5-21, 5-22 and 5-23, where circumferential extent, circumferential intensity and radial intensity are displayed respectively.

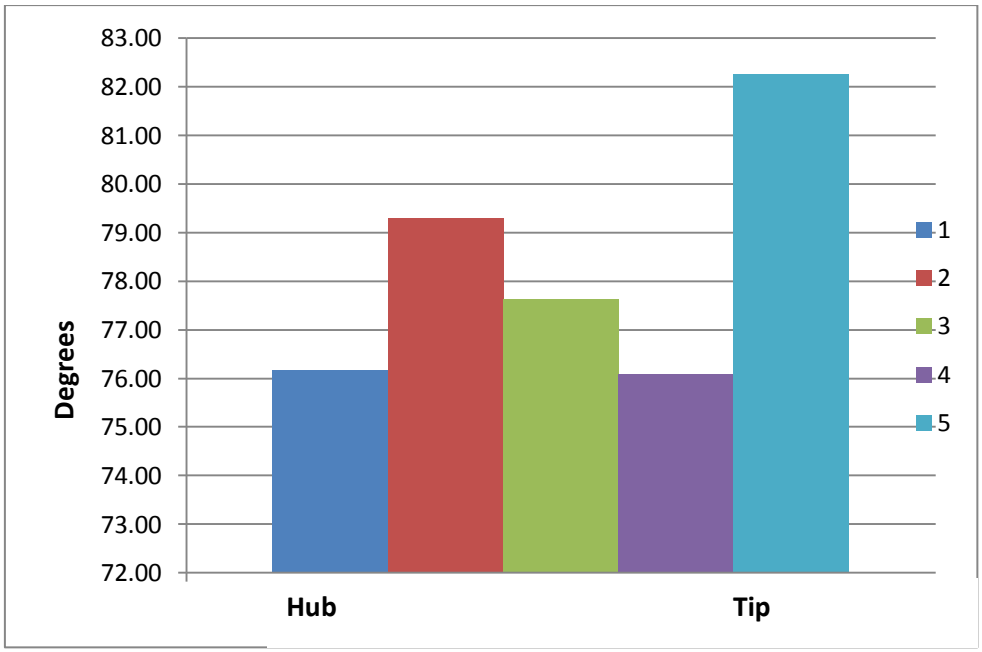

Figure 5-21 Circumferential Extent at Each Ring on the Total Pressure Profile for the Flight Attitude of 0.6M with 8˚ AOA and 0˚ AOSS

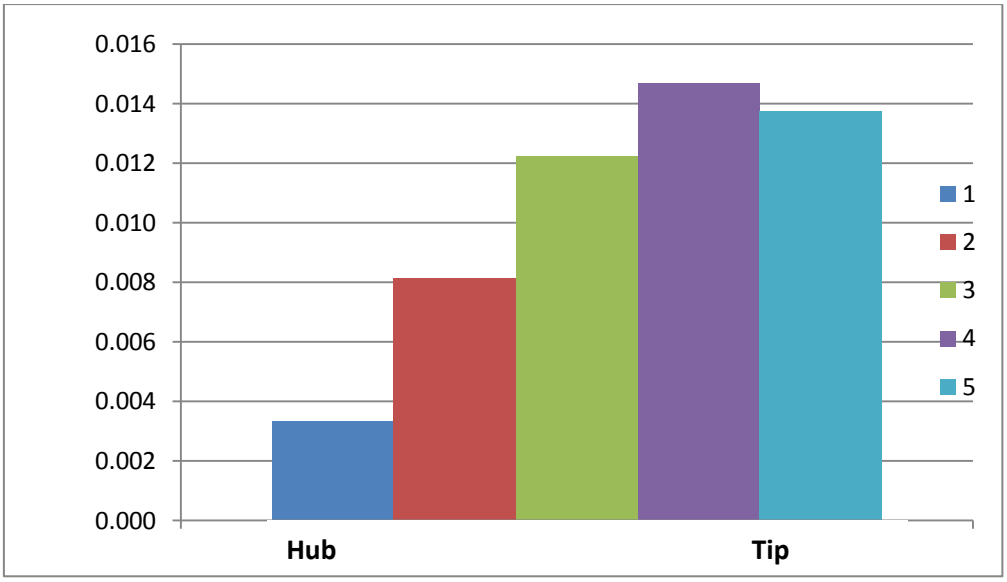

Figure 5-22 Circumferential Intensity at Each Ring on the Total Pressure Profile for the Flight Attitude of 0.6M with 8˚ AOA and 0˚ AOSS

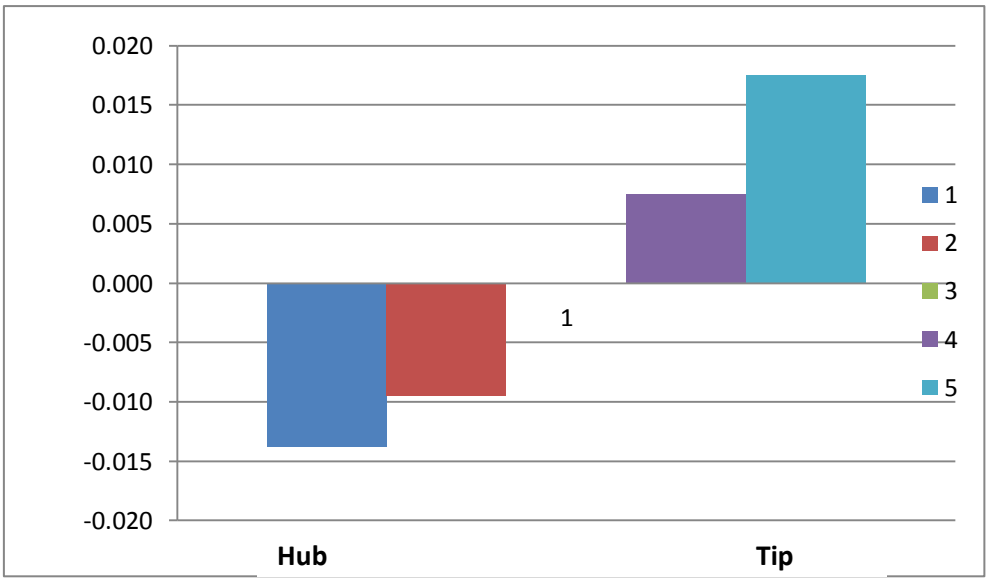

Figure 5-23 Radial Intensity at Each Ring on the Total Pressure Profile for the Flight Attitude of 0.6M with 8˚ AOA and 0˚ AOSS

Based on the above graphical representations:

- The greatest circumferential intensity is noted at ring No4, (fig 5-22). Considering eq. 5-15, 5-16, this means that the difference between PAV and PAVLOW becomes greatest at that region. So, for this specific flight attitude the magnitude of the total pressure defect is greatest at the area between hub and tip.

- The greatest circumferential extent is noted closer to the tip (ring No 5), as it can be seen on fig. 5-21. At that area the total pressure defect extends to the highest circumference comparing to the other rings. Actually, as it was mentioned before, there are two low pressure regions on this profile which are circumferentially separated from each other.
- The greatest radial intensity occurs at ring No 5, (fig. 5-23). Considering eq. 5-19, the average total pressure at that ring presents the greatest deviation from the face average total pressure as the latter was numerically calculated from CFD.

5.4 Effect of AOA and AOSS on Average Circumferential Intensity

For each one of the tested flight attitudes a total pressure profile representing the distribution of the total pressure at the AIP has been obtained. These profiles were then quantified in terms of distortion in the way it was described in paragraph 5.3 above.

Table 5-5 below presents the five ring (as shown in fig. 5-6) average values of circumferential intensity for each tested flight attitude. The first column on this table presents the flight attitudes in terms of AOA_AOSS whereas the three other columns show the resulted five ring averaged circumferential intensity for each flight attitude.

Table 5- 5 Results of Average Circumferential Intensity

	AVERAGE CIRCUMFERENTIAL INTENSITY		
AOA_AOSS	**0.35M**	**0.6M**	**0.85M**
0_0	0.0103	0.0122	0.0115
0_8	0.0152	0.0178	0.0165
0_16	0.0344	0.0335	0.0328
8_8	0.0252	0.0180	0.0108
8_16	0.0352	0.0304	0.0273
16_8	0.0288	0.0214	0.0093
8_0	0.0280	0.0103	0.0100
16_0	0.0281	0.0225	0.0098
16_16	0.0362	0.0311	0.0231
27_0	0.0264	0.0204	0.0211
35_0	0.0247	0.0180	0.0175

In order to investigate the effect of the AOA on the five ring averaged circumferential intensity, the results from the flight attitudes that only included AOA variation and 0° AOSS were examined and plotted on a graph. The graph in fig. 5-24 presents the variation of the five ring averaged circumferential intensity in relation to the AOA for the tested flight Mach numbers.

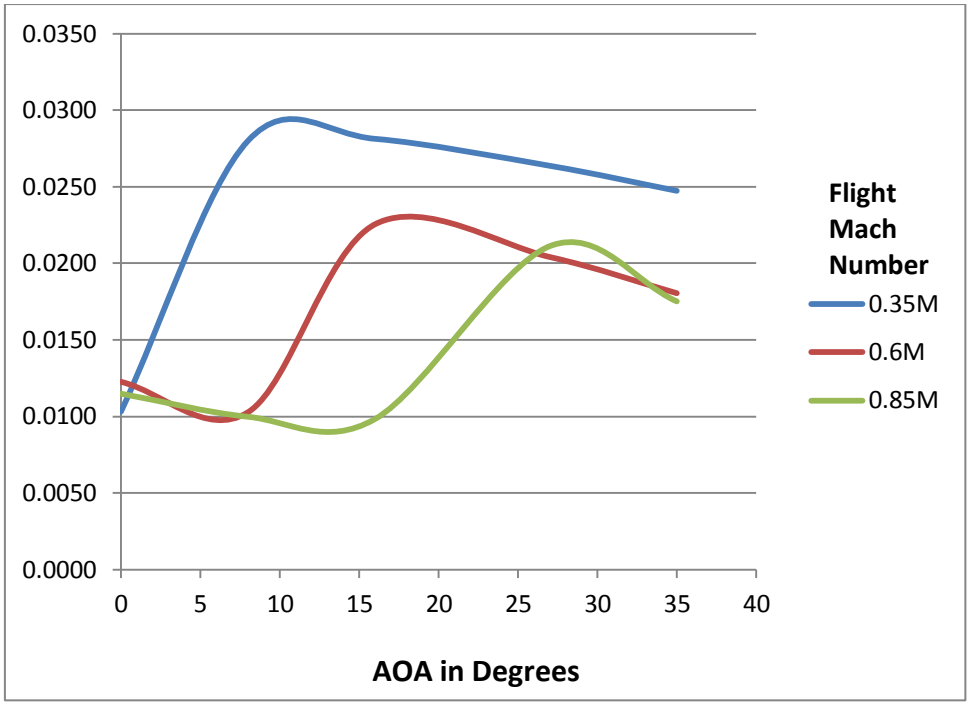

Figure 5-24 Effect of AOA on Average Circumferential Intensity (AOSS=0)

Looking into this graph the following conclusions may be drawn

- The variation of the average circumferential intensity with the AOA presents similar behaviour in all tested flight Mach numbers, in that each curve has a peak at a specific value of AOA.
- As the flight Mach number increases, the peak value of the average circumferential intensity occurs at higher AOA.
- Also as the flight Mach number increases, the variation of the average circumferential intensity presents a slower response to the changes in AOA (the line has lower slope).
- For 0.35M flight attitudes the circumferential intensity starts increasing from low AOA values and this is in contrast with the trends for 0.6M and 0.85M i.e. there is a reduction in circumferential intensity for low AOA values (0 to 15° depending on flight Mach number). For this point, it is worth noting that the reduction is lower for lower Mach number (0.85M to 0.6M) i.e. the reduction in circumferential intensity at low AOA diminishes when the flight Mach number reduces (0.85M to 0.6M) and for 0.35M the curve has changed slope.

- For each flight Mach number there is a certain value of AOA for which the average circumferential intensity gets its minimum value. Also this minimum average circumferential intensity occurs at higher AOA when the flight Mach number increases.

Putting all the above together makes it clear that as this specific airframe configuration flies at a low Mach number, the magnitude of the subsequent pressure defect at the AIP becomes greatest at relatively low AOA. In higher flight Mach numbers, the most severe total pressure defect at the AIP occurs at higher AOA and its value is lower than what it was in lower Mach flights.

Also, at low flight Mach numbers (0.35M) the average circumferential intensity increases with AOA and it gets its minimum value when AOA=0˚. As the flight Mach number increases the AOA starts working to the benefit of the pressure uniformity at the engine's face and the higher the flight Mach number the higher the AOA in which the circumferential intensity gets its minimum value.

The effect of varying the AOSS is demonstrated in fig. 5-25, based on the results presented on Table 5-5. By choosing different flight attitudes at AOA=0, the variation of AOSS shows that the average circumferential intensity presents an almost linear relation with the AOSS. When the AOSS increases the average circumferential intensity increases as well. The effect is quite alleviated though when the flight Mach number increases.

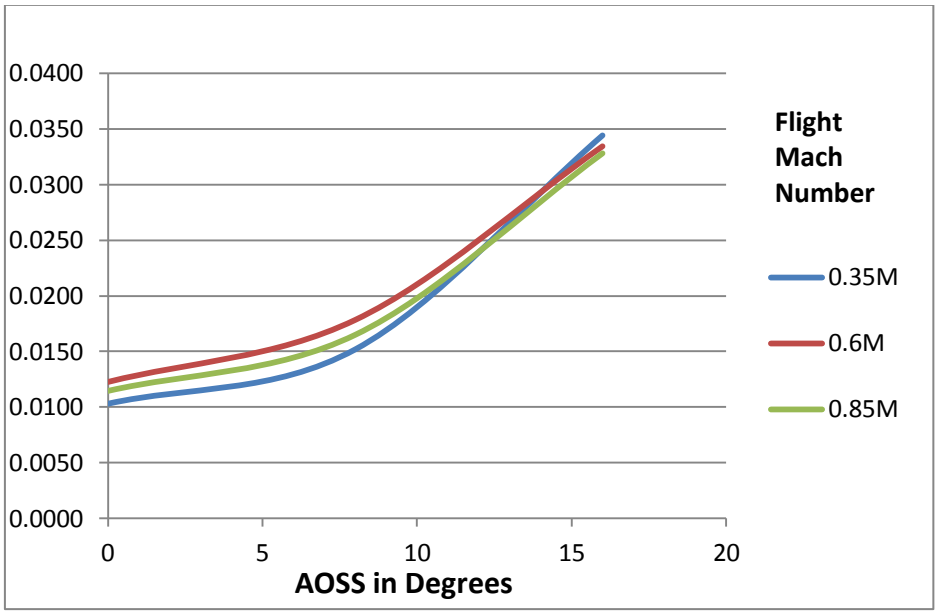

Figure 5-25 Effect of AOSS on Average Circumferential Intensity (AOA=0)

5.5 Effect of AOA and AOSS on Average Circumferential Extent

The five ring averaged values of circumferential extent for each tested flight attitude are presented in table 5-6. The highest value appears at the flight attitude of 0.35M with 0˚ AOA and 8˚ AOSS whereas the lowest is noted at the flight attitude of 0.6M with 8˚ AOA and 0˚ AOSS. The total pressure profiles at the AIP for these flight attitudes are presented in figs 5-26 and 5-27 respectively. The profile shown on the right hand side of both figures has been derived after the total pressure values at the AIP have been normalized against the total pressure at the intake's entry. In that way an indication of the pressure recovery can be given.

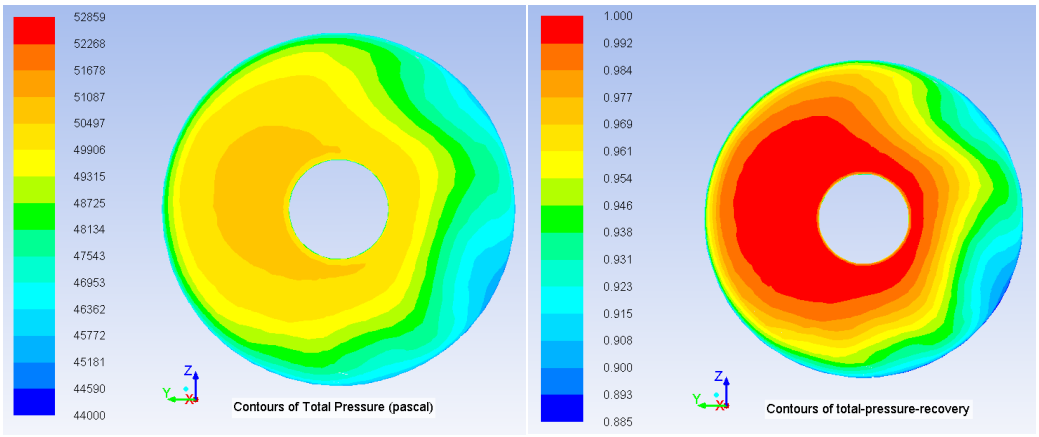

Figure 5-26 Profiles of Total Pressure (left) and Total Pressure Recovery (right) at the AIP for the 0.35M Flight with 0˚ AOA and 8˚ AOSS

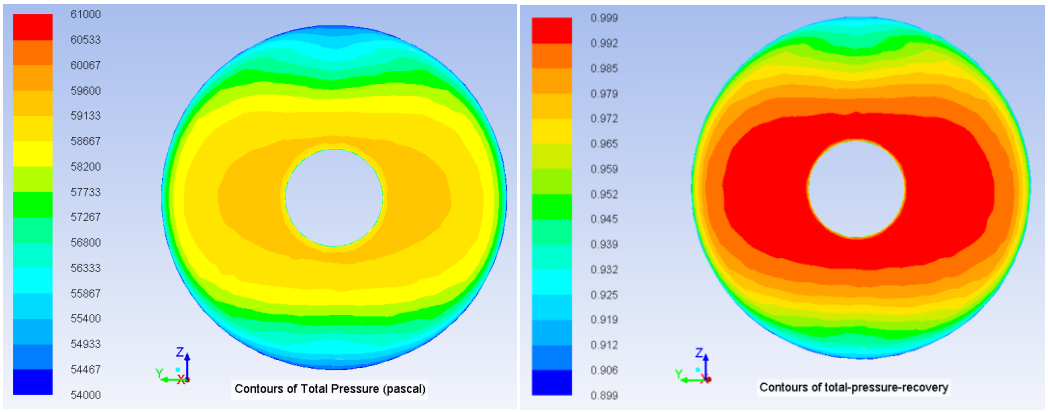

Figure 5-27 Profiles of Total Pressure (left) and Total Pressure Recovery (right) at the AIP for the 0.6M Flight with 8˚ AOA and 0˚ AOSS

As it can be seen the former presents a circumferentially wide area of blue which represents the low pressure area with considerable variation in the value of total pressure (more than 50 %). On the other hand, in fig. 5-27 the total pressure variation is less than 20% which denotes a more uniform total pressure distribution. The blue area is considerably smaller as well.

So, among the tested flight conditions, this specific airframe – intake configuration presents the widest area of pressure defect at the AIP when the incoming flow conditions are 0.35M with 0˚ AOA and 8˚ AOSS.

Table 5- 6 Results of Average Circumferential Extent

	AVERAGE CIRCUMFERENTIAL EXTENT		
AOA_AOSS	**0.35M**	**0.6M**	**0.85M**
0_0	101	119	132
0_8	178	140	137
0_16	152	154	159
8_8	131	137	109
8_16	152	151	149
16_8	130	110	103
8_0	100	80	99
16_0	114	96	87
16_16	152	151	155
27_0	122	116	109
35_0	128	114	111

Figure 5-28 shows how the average circumferential extent varies with the AOA for the three tested flight Mach numbers. As it can be seen for each flight Mach number there is an AOA value for which the five ring averaged circumferential extent takes its minimum value. This lowest value of circumferential extent seems to occur at higher AOA as the flight Mach number increases.

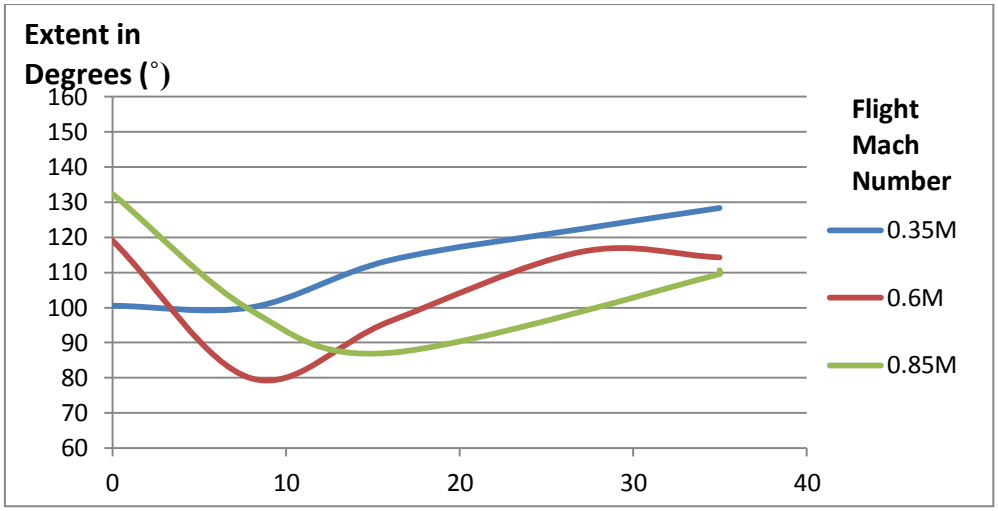

Figure 5-28 Effect of AOA on Average Circumferential Extent (AOSS=0)

Based on these results it can be concluded that for this specific airframe-intake system there is an optimum combination of flight Mach number and AOA for which the extent of the total pressure defect at the AIP gets its minimum value. And this is the flight attitude of 0.6M with 8˚ AOA.

Figure 5-29, on the other hand, presents how the AOSS affects the five ring averaged circumferential extent. Here the AOSS has an opposite effect on the circumferential extent comparing to that of the AOA. In all tested flight Mach numbers there is an AOSS for which the circumferential extent takes its maximum value. This specific AOSS becomes higher as the flight Mach number increases.

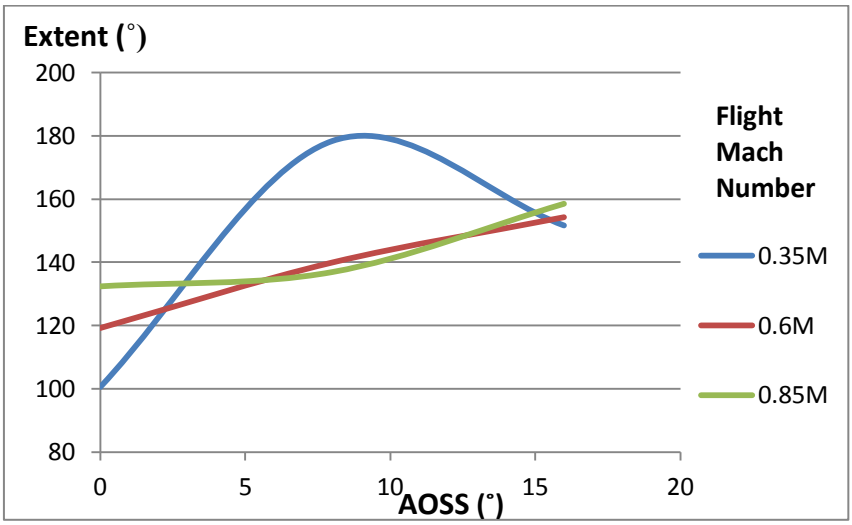

Figure 5-29 Effect of AOSS on Average Circumferential Extent (AOA=0)

5.6 Effect of AOA and AOSS on Maximum Radial Intensity

Table 5-7 presents the calculated values of maximum radial intensity among the five rings for each one of the tested flight attitudes. The five ring maximum value was selected over the respective average one, for the study of the radial intensity variation in relation to AOA and AOSS, since based on its definition (eq. 5-10) the five ring average radial intensity is equal to 0.

The variation of the maximum radial intensity with the AOA and AOSS respectively is demonstrated in figs 5-30 and 5-31. The maximum radial intensity decreases as the AOA and AOSS increases. But the falling of the maximum radial intensity is steeper (higher slope) when the AOSS increases comparing to the falling of the maximum radial intensity when the AOA increases.

Table 5- 7 Results of Maximum Radial Intensity

	MAXIMUM RADIAL INTENSITY		
AOA_AOSS	**0.35M**	**0.6M**	**0.85M**
0_0	0.0256	0.0180	0.0124
0_8	0.0201	0.0139	0.0091
0_16	0.0086	0.0021	0.0027
8_8	0.0198	0.0167	0.0122
8_16	0.0116	0.0061	0.0075
16_8	0.0146	0.0138	0.0125
8_0	0.0200	0.0171	0.0121
16_0	0.0134	0.0140	0.0119
16_16	0.0121	0.0094	0.0108
27_0	0.0061	0.0049	0.0054
35_0	0.0100	0.0093	0.0066

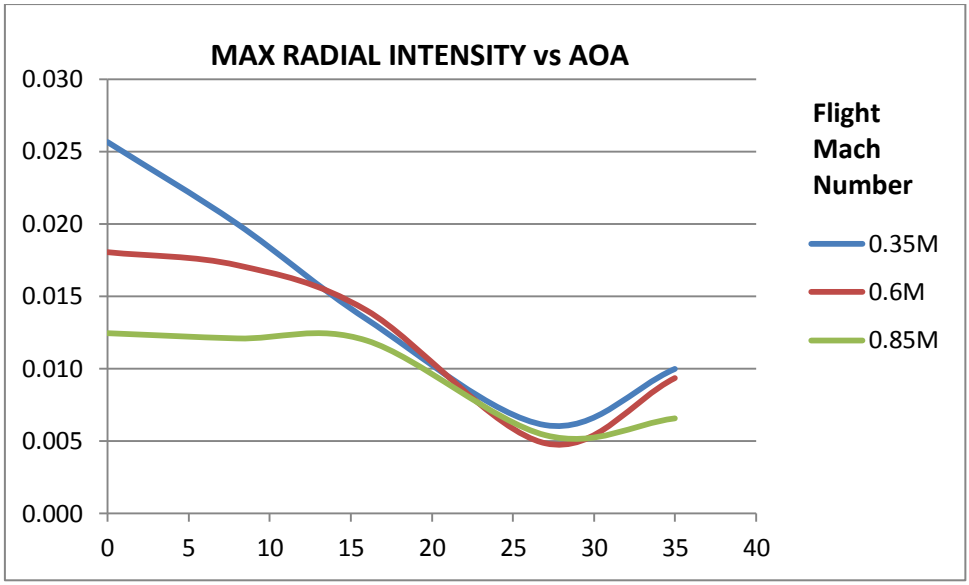

Figure 5-30 Effect of AOA on Maximum Radial Intensity (AOSS=0)

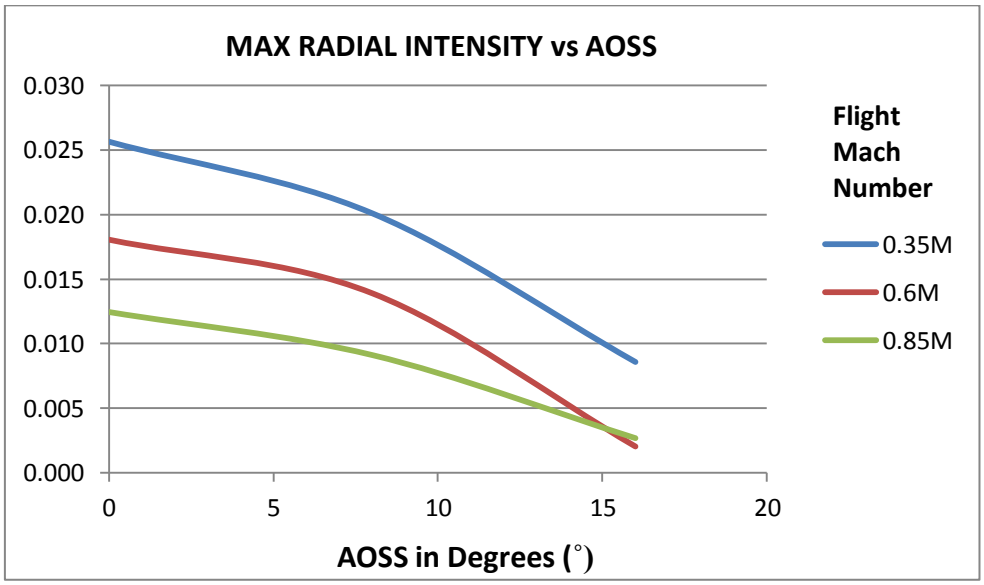

Figure 5-31 Effect of AOSS on Maximum Radial Intensity (AOA=0)

5.7 Chapter Summary

In this chapter the total pressure profiles at the engine's face that were calculated in CFD for each one of the tested flight attitudes were quantified in terms of distortion descriptors. This quantification process was accomplished following the guidelines of SAE AIR 1419.

The novelty though in the present research work was that the total pressure distribution at the engine's face which is representative of the total pressure distortion was calculated in CFD instead of actual screen tests and total pressure measurement rakes that were used in the SAE AIR 1419. This approach is considerably less expensive than conducting actual tests.

Another novelty was that distortion descriptor values were calculated for specific flight attitudes of the F-16 aircraft using only CFD. These values as it will be demonstrated in the next chapter are used to evaluate whether the respective flight attitudes may destabilize the fan operation or not. This process may be followed to establish the operating envelope of this aircraft's fan.

Based on the distortion quantification results it was then examined how the AOA and the AOSS affect the resulted distortion descriptor values and respective graphs were created. These graphs may be used to establish an optimum combination of AOA and AOSS for each flight Mach number of this aircraft in order to minimize the distortion effect.

For example in fig. 5.24 is captured that for each flight Mach number there is a certain value of AOA for which the ring average circumferential intensity gets its minimum value. This practically means that for each flight Mach number there is an optimum AOA for which the magnitude of the pressure defect at the engine's face becomes minimum and as such this flight attitude should be preferred when practical.

Similar conclusions were drawn based on the rest of the created graphs.

6 FAN STABILITY ASSESSMENT

The first engine's component that experiences the distorted airflow is the FAN. Depending on the severity of these distorted conditions the stability of the FAN may be threatened i.e. its operating point may move beyond the surge line on its characteristics map.

In the present study before the engine's performance was assessed, it was first investigated whether any of the tested aircraft's flight attitudes provoked the surge of the FAN.

In the previous section it was presented how the AIP total pressure profiles, obtained from CFD, were quantified in terms of distortion descriptors. In this section these distortion parameters will be correlated to the engine's fan surge margin and in that way a fan stability assessment will be accomplished.

6.1 Estimation of Fan Map

FAN ’s stability was assessed having as frame of reference one of the automatically scaled default compressor maps from Turbomatch database. The reason this selection was made was basically the fact that no data on the actual engine’s FAN map were accessible. Actual compressor maps are Original Equipment Manufacturers' (OEM) proprietary information arising from costly rig tests and they can hardly be located in the open literature.

Figure 6-1 presents the resulted map that was assumed to cover the operation of the under examination FAN with the design point (DP) located on it. The design point is assumed to be at T/O – SLS (sea level static conditions). Figure 6-2 presents the map of the efficiency lines where it can be seen how close to the maximum efficiency the DP is located at.

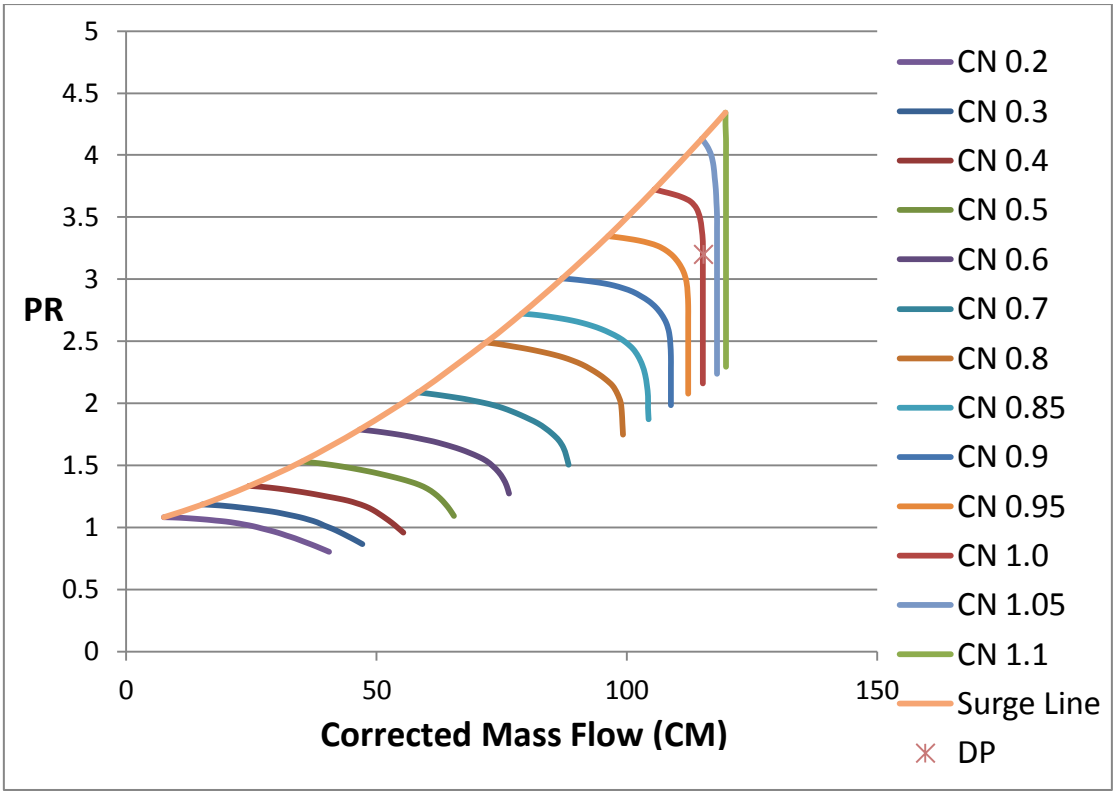

Figure 6-1 FAN Map with the Design Point

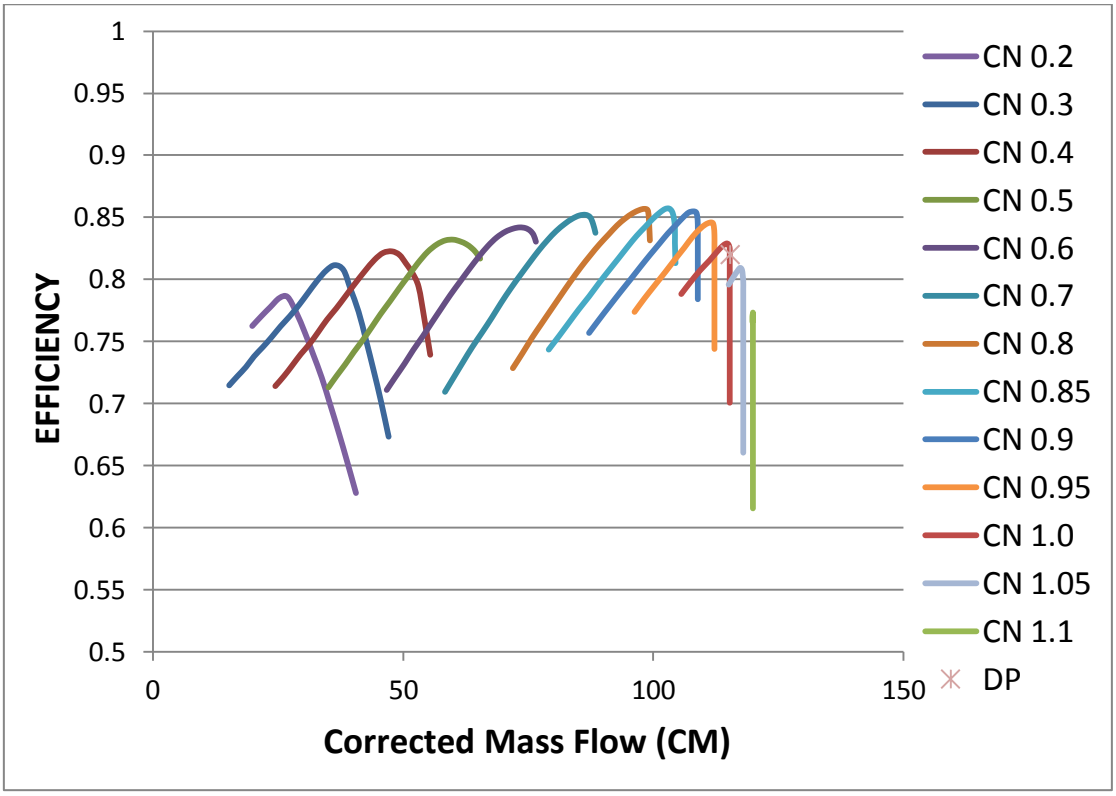

Figure 6-2 FAN Map Effeciency Lines with the Design Point

6.2 Baseline Conditions

After the design point was defined on the FAN map, three off design (OD) cases were run simulating the performance of the engine as it operated at an altitude of 20,000ft and while flying at 0.35M, 0.6M and 0.85M conditions respectively. At these OD calculations a rather high intake pressure recovery was chosen (0.99) denoting the uninstalled status of the engine i.e. at this point of the calculations the effect of the intake on the engine's performance was not taken into consideration.

In these three baseline cases, the FAN rotational speed (PCN) was used as the driving parameter and its value was progressively adjusted until for each one of them, the resulted mass flow entering the engine, corresponded to the 100% of the design corrected airflow (CM).

The rationale underlying this selection was twofold:

- To create the same inflow conditions in all cases, for comparison purposes.
- To control one of the engine's basic performance parameters simulating thus the action of a control system that monitors the FAN rotational speed.

Table 6-1 presents the FAN PCN values that resulted in the same corrected mass flow (CM) entering the engine for the three OD cases.

Table 6-1. Turbomatch Results Showing the Constant CM

Mach	CM	PCN	NET THRUST (KN)
0.00 (DP)	115.28	1.0	79.3
0.35 (OD)	115.28	0.940	33.8
0.60 (OD)	115.28	0.961	36.6
0.85 (OD)	115.28	0.993	43.1

These conditions were the baseline for the FAN stability assessment and the Surge Margin (SM) was defined for each one of them following the guidelines of SAE ARP 1420[20]. So with reference to fig. 6-3,

$$\mathrm{SM} = \frac{\mathrm{PR}_1 - \mathrm{PR}_0}{\mathrm{PR}_0} \times 100 \qquad \text{(eq. 6-1)}$$

When eq. 6-1 was applied to the baseline conditions, the SM results presented in table 6-2 were obtained.

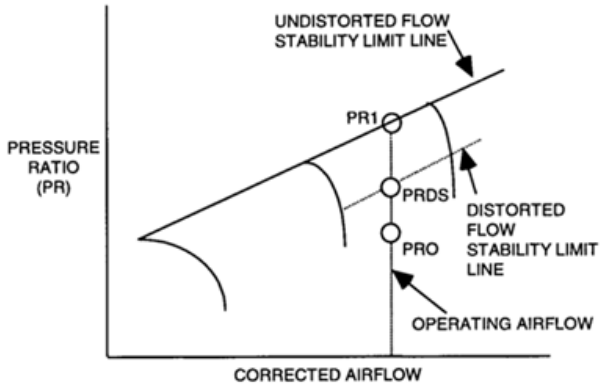

Figure 6-3 Definition of Surge Margin [20]

Table 6-2. FAN Surge Margin for the Baseline Conditions

Baseline Points (Flight Mach)	**see Figure 6-2**			
	PR0	**CM**	**PR1**	**SM**
DP (SLS)	3.200	115.28	4.148	29.62
0.35M	3.192	115.28	4.148	29.95
0.6M	3.195	115.28	4.148	29.82
0.85M	3.199	115.28	4.148	29.66

For the calculation of the baseline conditions the engine was considered uninstalled and as such the airflow that reached the engine's face was rather uniform. In case of an installed engine though the airframe interacts with it and this interaction affects the quality of the airflow that the engine experiences.

6.3 Loss in Surge Pressure Ratio (ΔPRS)

Distortion descriptors provide means of identifying the critical distorted inlet-flow conditions because they can be correlated to the loss of FAN surge Pressure Ratio (ΔPRS) caused by the distorted airflow [10]. This loss of surge pressure ratio is an indication of how the compressor's surge line will be shifted because of the distorted airflow it experiences. It is a combined effect caused by both the circumferential (ΔPRSc) and radial (ΔPRSr) components of distortion.

$$\Delta PRS = \Delta PRS_c + \Delta PRS_r \qquad \text{(eq. 6-2)}$$

The circumferential component can be correlated to the distortion descriptors shown in eq. 6-3 [10],

$$\Delta PRS_c = \left[\sum_{i=1}^{N} \alpha_i K_c \left(\frac{\Delta PC}{P} \right)_i \left(\frac{\bar{e}_i}{180} \right) \left(\frac{1}{MPR} \right)_i \right] \times 100 \qquad \text{(eq. 6-3)}$$

where, **N** is the number of the pressure measurement rings on the engine's face plane,

$\mathbf{a_i}$ is the weighting factor for ring i,

$\mathbf{K_c}$ is the average circumferential sensitivity, determined empirically from tests with 180 degrees classical inlet distortion screens.

$(\frac{\Delta Pc}{P})_i$ is the circumferential distortion intensity of ring i,

$\boldsymbol{\theta_i}$ is the circumferential extent of distortion in ring i in degrees,

$\mathbf{MPR_i}$ is the multiple per revolution element for ring i.

The loss in surge pressure ratio because of radial distortion is the highest among the losses evaluated for the hub and tip regions [10].

$$\Delta PRS_r = \text{larger of } \Delta PRS_h \text{ or } \Delta PRS_t \qquad \text{(eq. 6-4)}$$

Equation 6-5 presents the loss in surge pressure ratio in the hub region which consists of rings 1 and 2 weighted equally [10].

$$\Delta PRS_h = \left\{ \left[\sum_{i=1}^{2} 1/2 \, K_r \left(\frac{\Delta PR}{P} \right)_i \right] + C_h \right\} \times 100 \qquad \text{(eq. 6-5)}$$

where, $\mathbf{K_r}$ is the average radial sensitivity, determined empirically,

$\left(\frac{\Delta PR}{P}\right)_i$ is the radial distortion intensity of ring i,

$\mathbf{C_h}$ is the radial offset term for the hub.

Equation 6-6 describes the loss in surge pressure ratio in the tip region which consists of rings 4 and 5 weighted equally [10].

$$\Delta PRS_t = \left\{ \left[\sum_{i=N-1}^{N} 1/2 \, K_r \left(\frac{\Delta PR}{P} \right)_i \right] + C_t \right\} \times 100 \qquad \text{(eq. 6-6)}$$

where, $\mathbf{C_t}$ is the radial offset term for the tip.

Typical variations of circumferential sensitivity, radial sensitivity, hub and tip radial offsets with corrected airflow are given in figures 6-4 through 6-7 [10].

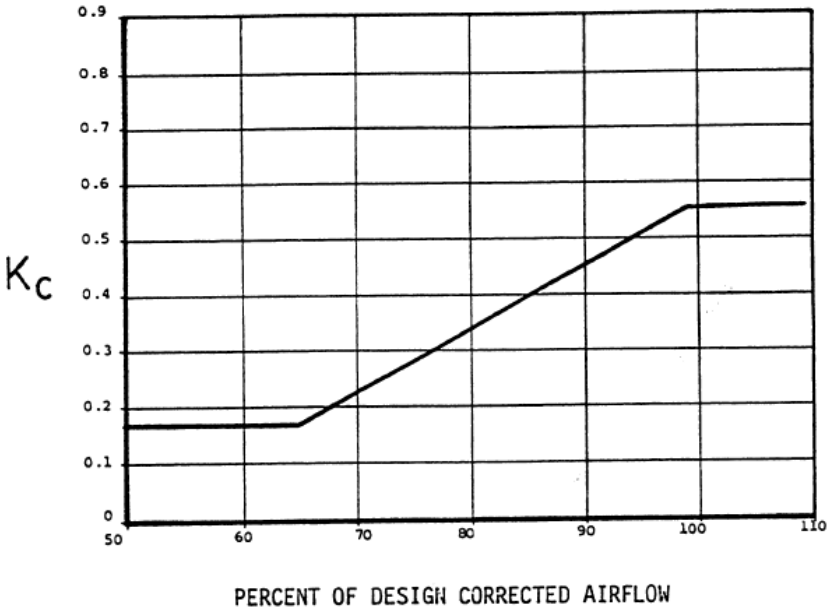

Figure 6-4 Circumferential Sensitivity (Kc) Variation with Corrected Airflow [10]

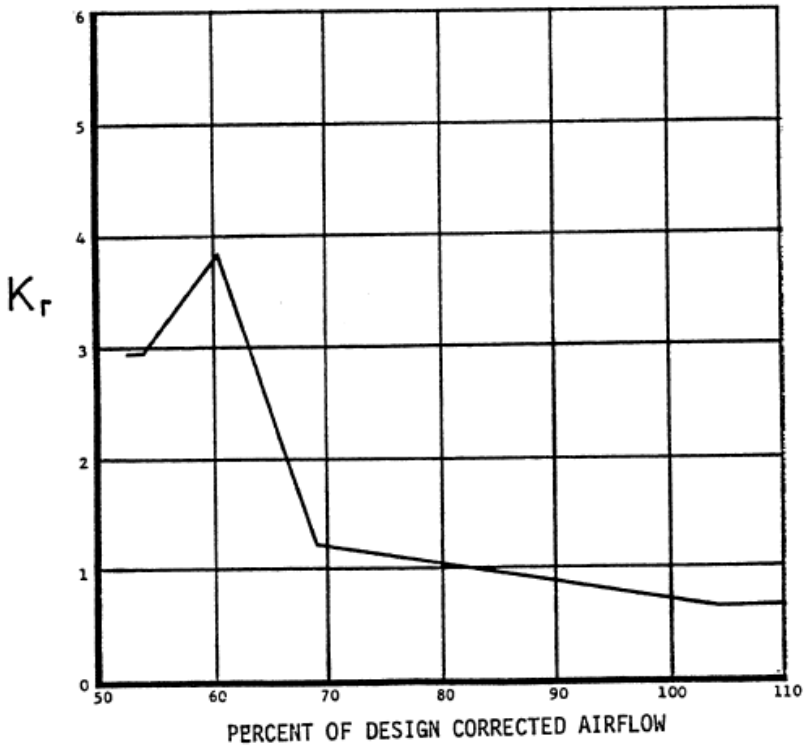

Figure 6-5 Radial Sensitivity (Kr) Variation with Corrected Airflow [10]

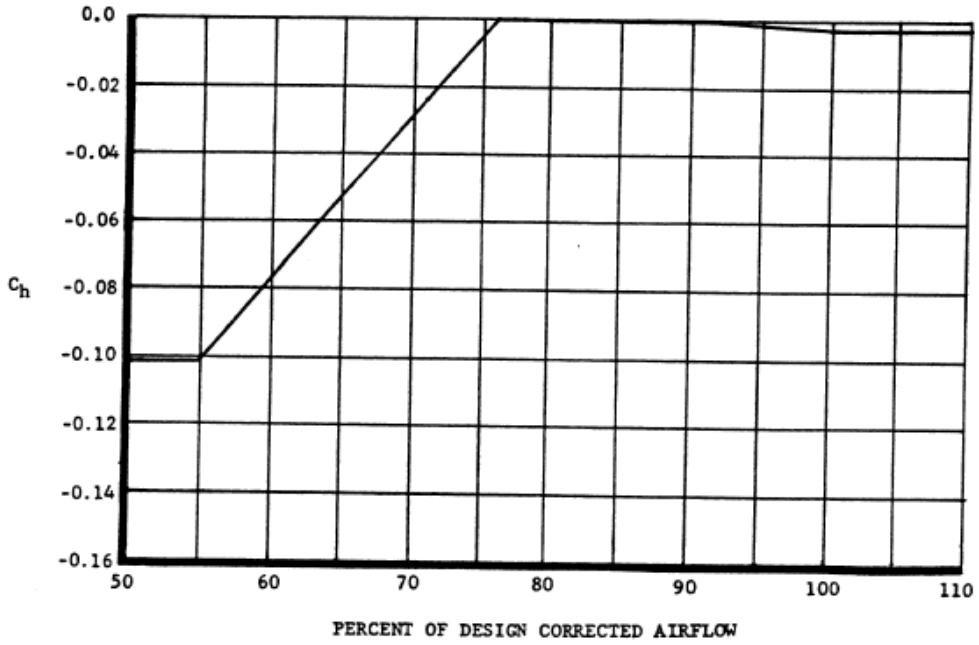

Figure 6-6 Hub Radial Offset (Ch) Variation with Corrected Airflow [10]

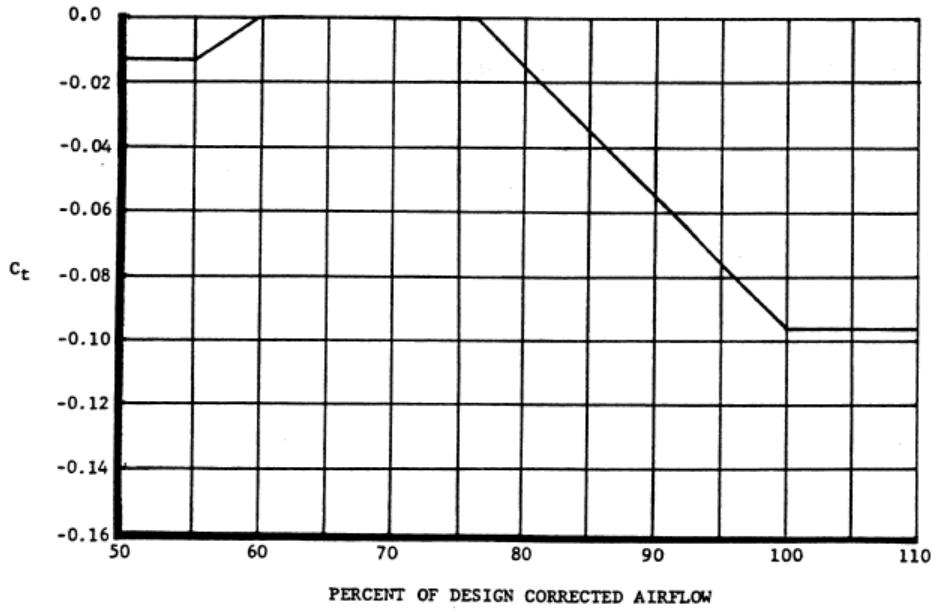

Figure 6-7 Tip Radial Offset (Ct) Variation with Corrected Airflow [10]

The loss in surge pressure ratio (ΔPRS) results for the examined flight attitudes are presented in table 6-3. It is clarified that the flight attitudes with negative values of ΔPRS resulted in an increase in surge pressure ratio (relative to the uninstalled engine) because in accordance with eq. 6-2 above, in these cases the absolute value of the radial distortion

component was greater than that of the circumferential distortion and since the reasulted radial distortion was negative in these cases the outcome of eq. 6-2 was also negative. This practically means that in the cases which resulted in negative values of ΔPRS the gain in surge margin due to radial distortion more than offsets the loss in surge margin due to circumferential distortion.

All in all, the total pressure distortion causes a shift to the baseline FAN surge line and its new position for each flight attitude can be estimated by taking into account the ΔPRS that was calculated in eq. 6-2.

So, the distorted surge PR (PRDS) for each tested flight attitude, was calculated from the eq. 6-7 below [10],

$$PRDS = PR_1 - \frac{PR_1 \times \Delta PRS}{100} \qquad \text{(eq.6- 7)}$$

where, PR1 is the undistorted Surge PR of the baseline condition.

Then, with reference to fig. 6-3 [20], the distorted Surge Margin (SM_{dist}) for each case could have been also defined.

$$SM_{dist} = \frac{PRDS - PR_0}{PR_0} \qquad \text{(eq. 6-8)}$$

where, PR_0 is the operating PR of the baseline condition.

Table 6-3 presents the estimated SM_{dist} results for each tested case. Looking at these results it becomes obvious that none of the examined flight conditions threatens the stability of the FAN i.e. the $SM_{dist} > 0$ in all cases.

The most severe attitude in the three examined flight Mach numbers, in terms of loss in surge pressure ratio (ΔPRS), was the one with 0˚ AOA and 16˚ AOSS, but even this attitude was far away from the stability limit line of the FAN.

Figure 6-7 presents the engine's FAN map with the distorted surge line that refers to the flight attitude of 0.85M with 0˚ AOA and 16˚ AOSS. This specific flight attitude based on the results quoted in table 6-3 is the worst one in terms of Loss in surge pressure ratio (ΔPRS). Comparing to the undistorted surge line, the distorted one is shifted towards the

direction of SM depletion. The amount of shift reflects how the surge line is affected when the FAN operates under these distorted conditions.

Table 6-3. FAN Stability Assessment Results

0.35M FLIGHT ATTITUDES									
AOA_AOSS	**0_0**	**0_8**	**0_16**	**8_8**	**8_16**	**16_8**	**8_0**	**16_0**	**16_16**
PRS (NDMF constant in fig. 6-3)					4.148				
ΔPRS	-1.421	-0.663	0.937	-0.596	0.567	0.263	-0.571	0.310	0.806
PRDS	4.207	4.176	4.109	4.173	4.124	4.137	4.172	4.135	4.115
SMdist	31.797	30.811	28.733	30.724	29.213	29.608	30.692	29.548	28.902
0.6M FLIGHT ATTITUDES									
AOA_AOSS	**0_0**	**0_8**	**0_16**	**8_8**	**8_16**	**16_8**	**8_0**	**16_0**	**16_16**
PRS (NDMF constant in fig. 6-3)					4.148				
ΔPRS	-0.791	-0.274	1.520	-0.477	0.764	-0.325	-1.015	-0.308	0.639
PRDS	4.181	4.159	4.085	4.168	4.116	4.161	4.190	4.161	4.122
SMdist	30.854	30.184	27.855	30.447	28.836	30.250	31.145	30.228	28.999
0.85M FLIGHT ATTITUDES									
AOA_AOSS	**0_0**	**0_8**	**0_16**	**8_8**	**8_16**	**16_8**	**8_0**	**16_0**	**16_16**
PRS (NDMF constant in fig. 6-3)					4.148				
ΔPRS	-0.491	-0.036	1.544	-0.596	0.550	-0.731	-0.658	-0.731	0.159
PRDS	4.168	4.150	4.084	4.173	4.125	4.178	4.175	4.178	4.141
SMdist	30.302	29.713	27.664	30.438	28.952	30.613	30.519	30.613	29.459

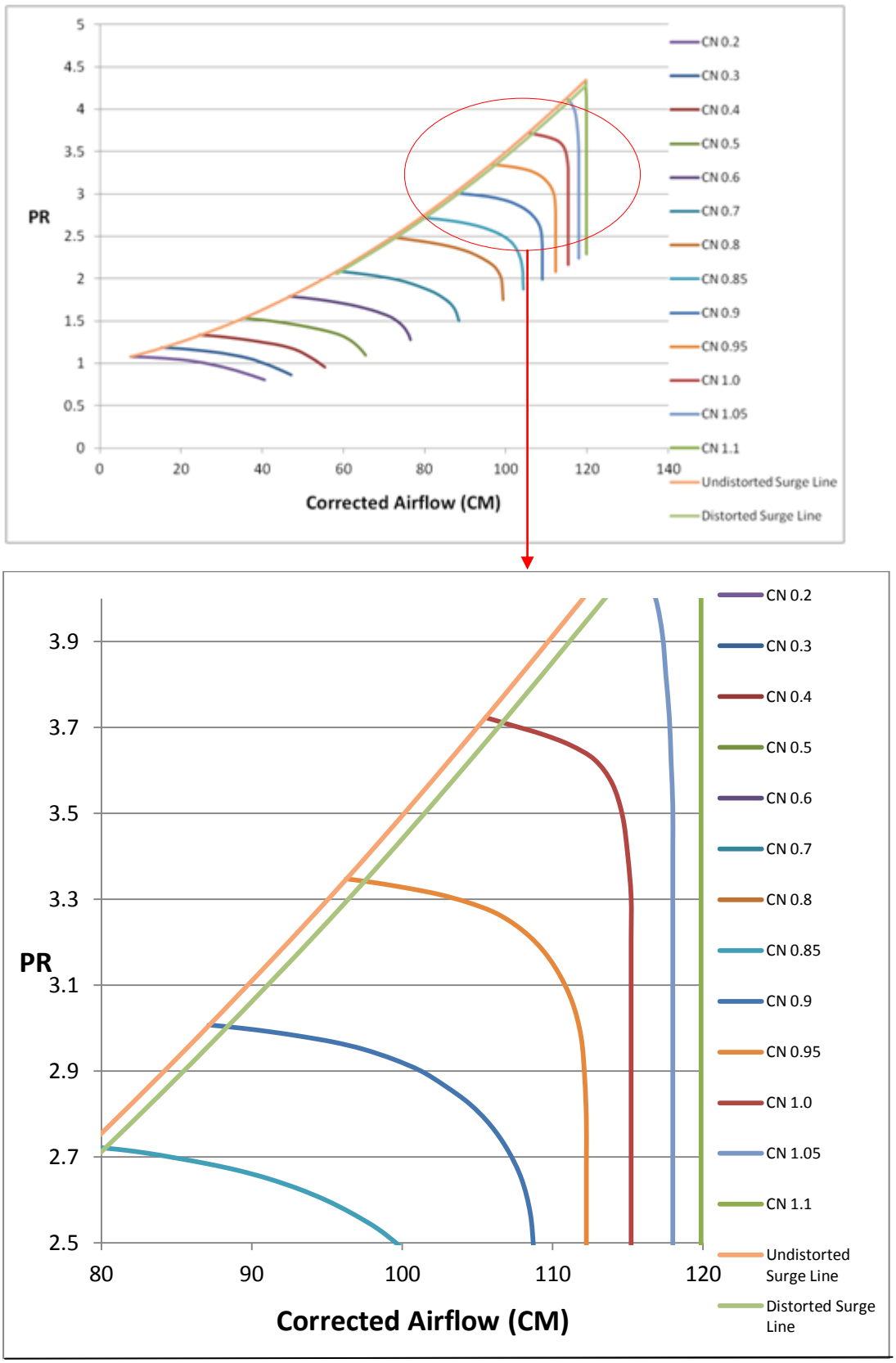

Figure 6-8 FAN Map Showing the Distorted Surge Line for the 0.85M 0_16 Flight Attitude

6.4 Chapter Summary

In this chapter the distortion descriptor values that were calculated for each tested flight attitude were correlated to the surge margin of the engine's fan through the loss in surge pressure ratio (ΔPRS) parameter.

Fan ’s stability was assessed having as frame of reference one of the automatically scaled default compressor maps from Turbomatch database. Firstly, the design point was defined on this map and then three off design (OD) cases were run simulating the operation of the engine at an altitude of 20,000ft and while flying at 0.35M, 0.6M and 0.85M conditions respectively. These three OD cases were considered as the baseline ones and the parameters selected in their simulation implied an uninstalled condition of the engine (high intake pressure recovery and uniform total pressure at the engine's face).

The loss in surge pressure ratio calculated for each tested flight attitude was then applied to the respective baseline condition's surge margin. The fan stability was assessed through the evaluation of the remaining surge margin of the fan for each tested condition.

Following the above methodology it was concluded that none of the tested flight attitudes threatened the stability of the engine's fan. The most severe attitude in the three examined flight Mach numbers, in terms of loss in surge pressure ratio (ΔPRS), was the one with 0˚ AOA and 16˚ AOSS, but even this attitude was far away from the stability limit line of the fan.

The novelty in this methodology is that it can be used to evaluate whether a specific flight attitude may threaten the stable operation of the fan. This methodology is very important from an operational point of view since without having design details from the airframe-engine manufacturers it may help to troubleshoot an engine's in-flight strange behaviour and whether it may be related to the flight attitude of the aircraft.

7 ENGINE PERFORMANCE ASSESSMENT

As it was concluded after the FAN stability assessment, none of the 27 examined flight conditions was found to threaten the stability of the FAN i.e. the distortion levels due to the tested flight attitudes did not cause the depletion of the FAN surge margin.

The next step was to estimate how the engine's performance in terms of produced thrust was affected due to the distorted airflow as a result of these flight attitudes. The basic tool used in that process was Turbomatch. The tested flight scenarios were grouped in three major categories under the three flight mach numbers 0.35M, 0.6M and 0.85M.

7.1 Engine Performance Parameters Varying with Distortion

The changes in the aircraft's flight attitude caused some of the engine's performance parameters to vary as well. These parameters were the mass flow rate and the intake's pressure recovery. So, if for each flight attitude these parameters were calculated and their respective values were entered into the Turbomatch simulation model then the engine's performance could have been estimated for that specific flight attitude.

In these performance calculations, the rotational speed of the FAN (PCN) was selected to be the driving parameter. The FAN PCN value was the same as in the respective baseline condition i.e. in the engine's performance simulation for the flight attitude of 0.35M with 8˚ AOA and 16˚ AOSS the FAN PCN from the 0.35M baseline condition was used, and in that way both the installation and the distortion effects expressed in terms of intake pressure recovery and mass flow rate could have been realized.

The way the mass flow rate and the intake pressure recovery have been calculated is discussed below.

7.1.1 Mass Flow Rate

The mass flow rate at the engine's face for each one of the examined flight attitudes was CFD numerically predicted. In the post processing phase of the CFD results, an extra surface was created at the plane where the engine's face is supposed to be located at and the predicted value of mass flow rate at that plane was obtained. These CFD mass flow rate results are shown in table 7-1 below.

Table 7-1 CFD Predicted Values of Mass Flow Rates

	MASS FLOW RATE (Kg/s)		
AOA_AOSS	**0.35M**	**0.6M**	**0.85M**
0_0	59.40	67.85	82.29
0_8	58.74	66.80	80.76
0_16	56.78	62.64	74.59
8_8	58.57	67.59	82.34
8_16	56.94	64.71	78.69
16_8	57.97	67.04	82.48
8_0	59.09	68.20	83.05
16_0	58.34	67.53	82.98
16_16	56.67	64.57	79.34

The lowest value of mass flow rate among the tested conditions was predicted at 0.35M flight with 16˚ AOA and 16˚ AOSS whereas the highest value was predicted for the flight attitude of 0.85M with 8˚ AOA and 0˚ AOSS. As can be observed in fig. 7-1 below which presents the velocity magnitude contours referring to the former flight attitude, a part of the intake becomes ''shielded'' to the incoming flow, due to the position of the aircraft. This part experiences a lower velocity air flow resulting in a low total value of mass flow rate for this specific flight attitude.

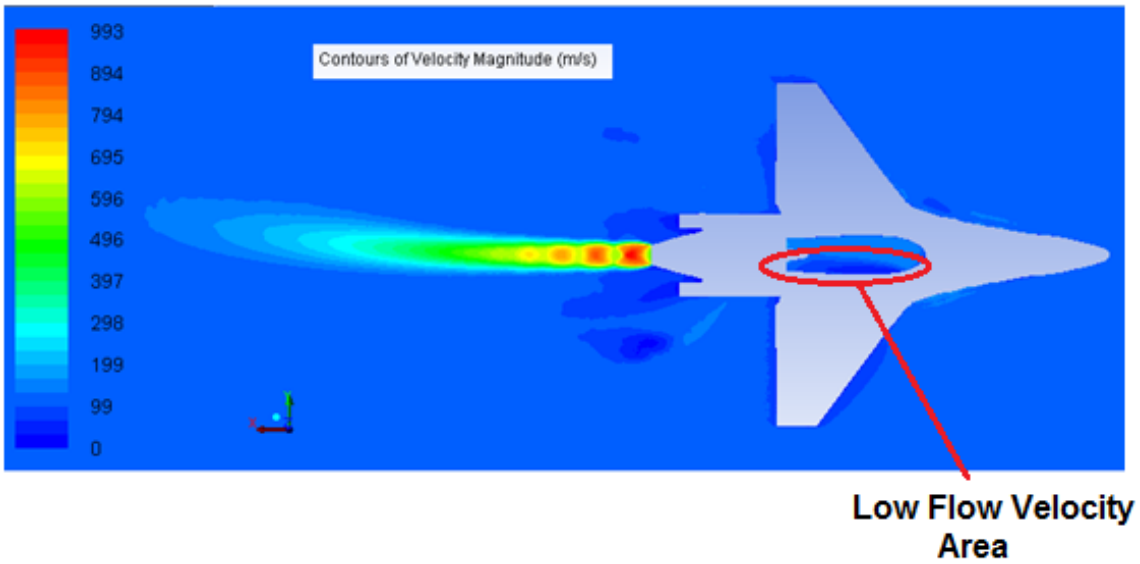

Figure 7-1 *Contours of Velocity Magnitude for the Flight Attitude of 0.35M with 16˚ AOA and 16˚ AOSS*

Figure 7-2 presents the mass flow rate results in a graphical form where the RAM effect can be clearly observed i.e. the mass flow rate increases with Mach number [77].

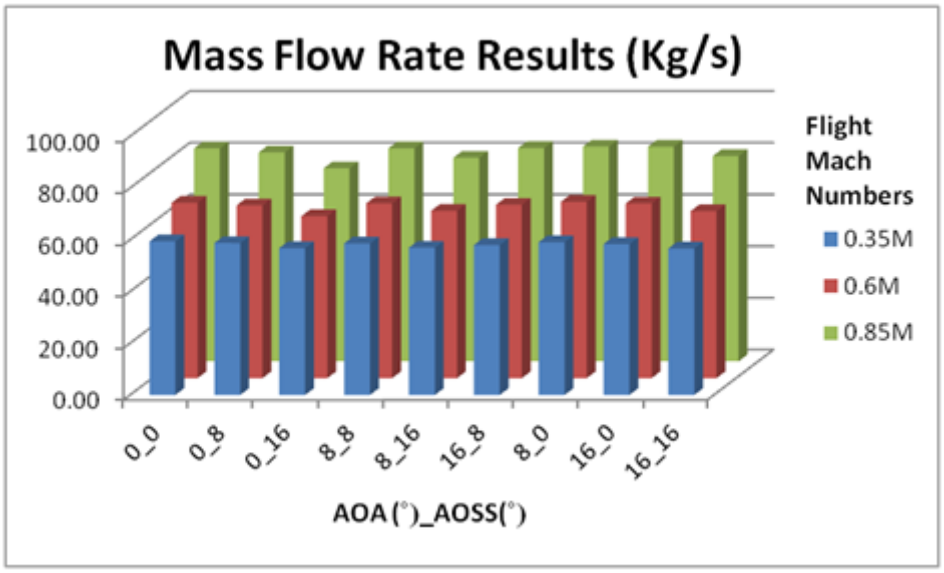

Figure 7-2 Mass Flow Rate Results

When the flight attitudes of 0˚ AOA and 0˚ AOSS (0_0) are considered as the baseline conditions in the three tested flight Mach numbers and all the other tested flight conditions are compared to them in terms of the resulted mass flow rate entering the aircraft's intake, it results to the % changes presented in Table 7-2 below.

As can be clearly observed from these results as the flight Mach number increases in the 0˚ AOSS flight attitudes, the AOA has a positive impact to the amount of mass flow that reaches the engine's face. Respectively in the 0˚ AOA flight attitudes, the AOSS reduces the amount of the airflow that enters the intake as the flight Mach number increases.

Table 7-2 Mass Flow Rate % Changes Results

Mass Flow Rate % Change from baseline (0_0)			
AOA_AOSS	**0.35M**	**0.6M**	**0.85M**
0_0	0.00%	0.00%	0.00%
0_8	-1.11%	-1.55%	-1.86%
0_16	-4.41%	-7.68%	-9.36%
8_8	-1.40%	-0.38%	0.06%
8_16	-4.13%	-4.63%	-4.37%
16_8	-2.41%	-1.19%	0.23%
8_0	-0.52%	0.52%	0.92%
16_0	-1.79%	-0.47%	0.84%
16_16	-4.60%	-4.83%	-3.58%

7.1.2 Intake Pressure Recovery

The intake pressure recovery is the ratio of the area weighted average total pressure at the engine's face to the total pressure at the entry of the intake [15]. In the present work the former was CFD predicted for each tested flight attitude whereas the calculation of the latter was based on the altitude, the static pressure at that altitude (standard atmosphere data) and the flight Mach number. The results are shown in table 7-3.

Table 7-3 Intake Pressure Recovery Results

	INTAKE PRESSURE RECOVERY		
AOA_AOSS	**0.35M**	**0.6M**	**0.85M**
0_0	0.973	0.977	0.974
0_8	0.970	0.972	0.968
0_16	0.959	0.953	0.945
8_8	0.968	0.975	0.975
8_16	0.959	0.962	0.960
16_8	0.965	0.973	0.975
8_0	0.971	0.979	0.978
16_0	0.968	0.975	0.977
16_16	0.958	0.961	0.962

Figure 7-3 presents the intake pressure recovery results in a graphical form. The lowest value was predicted for the flight attitude of 0.85M flight with 0˚ AOA and 16˚ AOSS. On the other hand the highest value was predicted for the flight attitude of 0.85M with 8˚ AOA and 0˚AOSS.

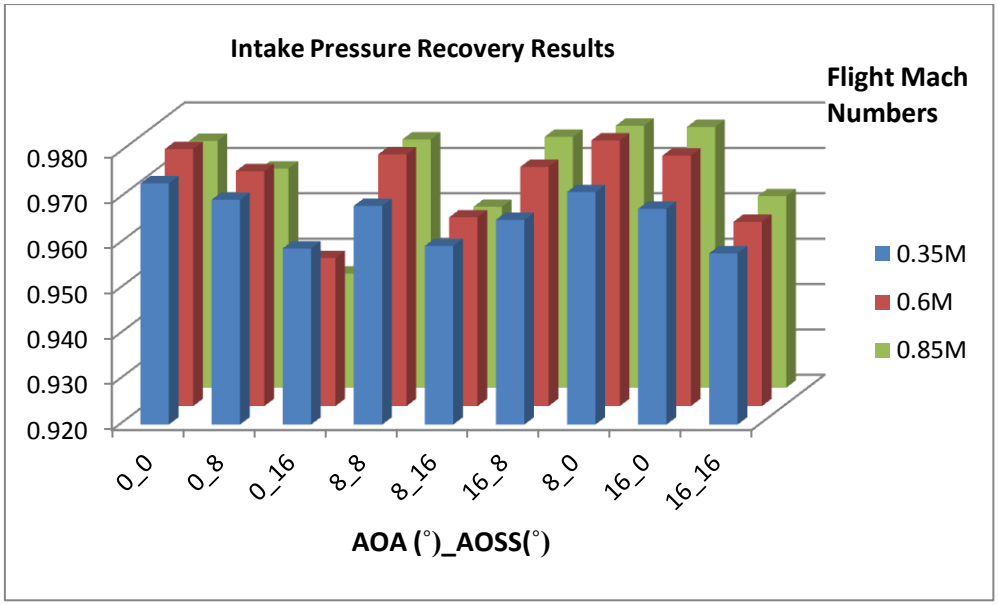

Figure 7-3 Intake Pressure Recovery Results

7.2 Calculation of Engine's Thrust

In the three baseline condition calculations the engine was considered uninstalled and with a uniformly distributed airflow at its AIP. Then, in each one of the 27 tested flight attitudes the same PCN value was used, as in the respective baseline condition and the calculated values of intake pressure recovery and mass flow rate were also applied to represent the installation and distortion effects respectively on the engine's performance.

So, to study the effect of distortion on the installed engine's performance, the two above mentioned parameters e.g. intake pressure recovery and mass flow rate, were entered into the engine's performance simulation model.

The intake pressure recovery was in a form that could have been directly input into the simulation model (as brick data for the intake). However, values of mass flow needed to be entered in a mass flow degradation form [70].

For that purpose, a degradation factor was added in the simulation model as a brick data. The target was this degradation factor when applied as a brick data in the engine's performance simulation model to cause the resulted mass flow rate to match that of the CFD predicted value for that specific flight attitude. Table 7-4 below presents the resulted degradation factors for each flight attitude.

Table 7-4 Mass flow Rate Degradation Factors

	MASS FLOW RATE DEGRADATION FACTORS		
AOA_AOSS	**0.35M**	**0.6M**	**0.85M**
0_0	0.997	0.992	0.994
0_8	0.989	0.981	0.982
0_16	0.967	0.939	0.929
8_8	0.988	0.990	0.994
8_16	0.969	0.961	0.964
16_8	0.981	0.984	0.995
8_0	0.994	0.995	0.999
16_0	0.984	0.989	0.999
16_16	0.966	0.959	0.970

In all performance calculations, as it has already been stated, FAN PCN was used as the driving parameter (handle) and its value was selected to be the same as in the respective baseline condition i.e. all the 0.35M flight attitudes were simulated having the same FAN PCN as in the 0.35M baseline condition. Similar methodology was applied for 0.6M and 0.85M flight attitudes. This methodology was based on the objective to study the effect of airflow distortion on the engine's performance due to merely the changes in the aircraft's flight attitude and not due to changes in any of the engine's power settings.

Also, the efficiency of the FAN was assumed to remain constant in all the examined cases since we had no information about the efficiency variations due to the distorted airflow.

The calculated values of intake pressure recovery (table 7-3) and mass flow rate were entered into the engine's performance simulation model. These two parameters represent:

- The installation effect, since they are highly related to the presence of the intake upstream of the engine.
- The distortion effect, since they are representative of the flow non uniformities at the engine's face due to the aircraft's flight attitude.

The engine's performance simulation model used in the calculation of the engine's thrust after the two parameters mentioned above have been introduced, is quoted in Appendix C.

Tables 7-5, 7-6 and 7-7 below present some of the resulted performance data (Net Thrust) for the 0.35M, 0.6M and 0.85M flight attitudes respectively. The green highlighted areas refer to the highest net thrust attitudes whereas the red ones point the flight attitudes which resulted to the least net thrust.

Figures 7-4, 7-5 and 7-6 present the same results in a graphical form where it can be observed how the changes in the aircraft's flight attitude affect the output of the engine in terms of net thrust. As it can be clearly noticed the minimum values of net thrust occur when the aircraft is supposed to be exposed to an incoming flow with high AOSS.

Table 7-5 Performance Results for the 0.35M Flight Attitudes

0.35M FLIGHT ATTITUDES	
AOA_AOSS	**Net Thrust (N)**
0_0	**32829**
0_8	32295
0_16	30711
8_8	32159
8_16	30842
16_8	31675
8_0	32580
16_0	31972
16_16	30620

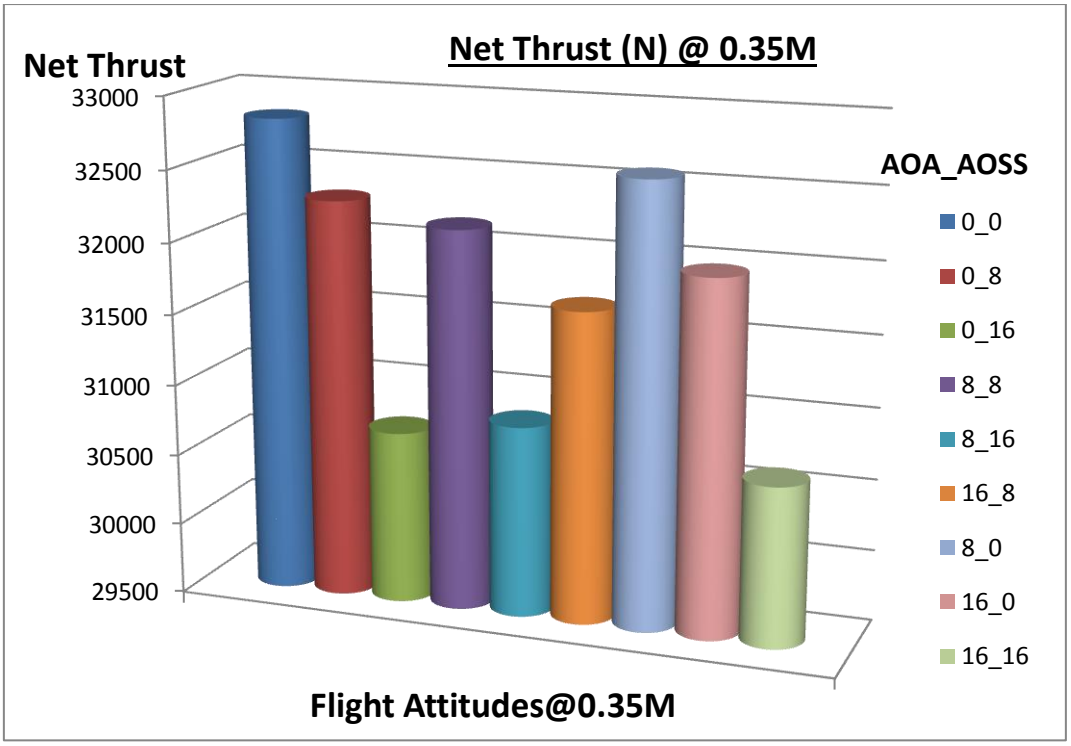

Figure 7-4 Net Thrust at 0.35M Flight Attitudes

The best flight attitude among the tested ones for the 0.35M flight in terms of resulted net thrust is the one with 0˚ AOA and 0˚ AOSS.

On the other hand the worst flight attitude is that with 16˚ AOA and 16˚ AOSS. Based on the results shown in tables 6-3, 7-1, 7-3 and 7-4 this specific flight attitude presents:

- The lowest CFD predicted mass flow rate entering the intake.
- The lowest intake pressure recovery.
- The second highest value of loss in surge pressure ratio.
- The worst mass flow degradation factor.

Table 7-6 Performance Results for the 0.6M Flight Attitudes

0.6M FLIGHT ATTITUDES	
AOA_AOSS	**Net Thrust (N)**
0_0	35533
0_8	34763
0_16	31722
8_8	35343
8_16	33230
16_8	34937
8_0	35791
16_0	35292
16_16	33130

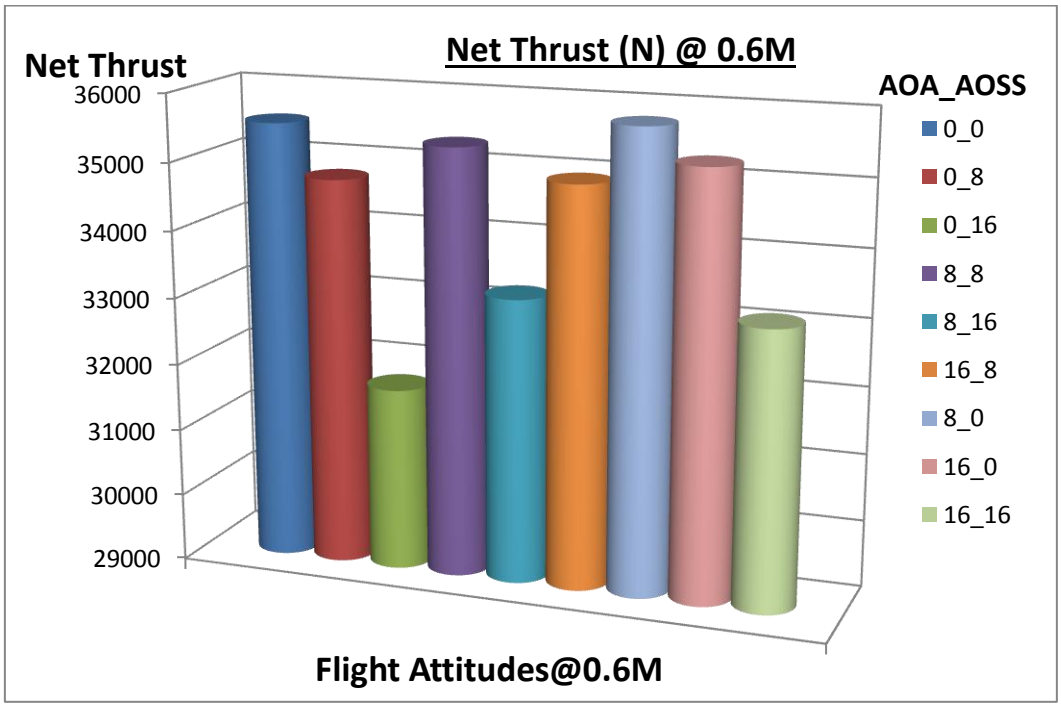

Figure 7-5 Net Thrust at 0.6M Flight Attitudes

For the 0.6M flight attitudes the one with the highest net thrust was that with 8˚ AOA and 0˚ AOSS and the attitude with the lowest net thrust was that with 0˚ AOA and 16˚ AOSS.

Table 7-7 Performance Results for the 0.85M Flight Attitudes

0.85M FLIGHT ATTITUDES	
AOA_AOSS	**Net Thrust (N)**
0_0	41826
0_8	40814
0_16	36716
8_8	41873
8_16	39430
16_8	41963
8_0	42344
16_0	42301
16_16	39863

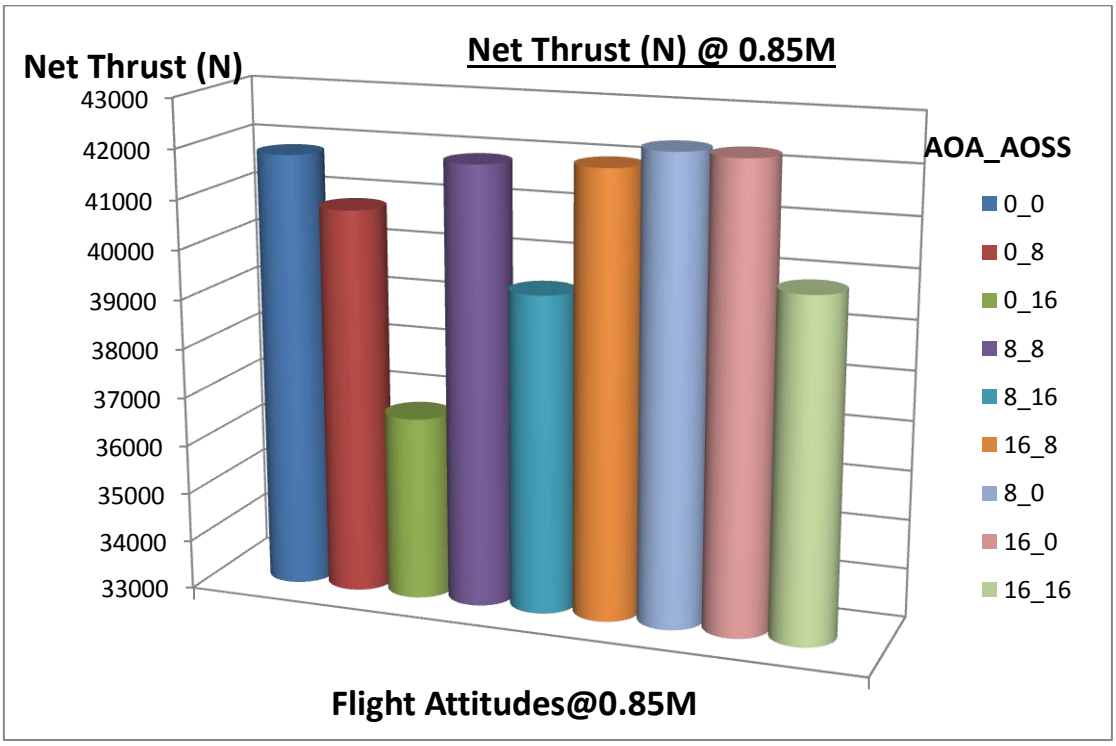

Figure 7-6 Net Thrust at 0.85M Flight Attitudes

For the 0.85M flight attitudes, the attitude with the highest net thrust was again that with 8˚ AOA and 0˚ AOSS and the attitude with the lowest net thrust was, like in the previous flight Mach number, that with 0˚ AOA and 16˚ AOSS.

7.3 Net Thrust Percentage Changes

Table 7-8 below presents the resulted percentage changes comparing to the respective baseline value for all the tested flight attitudes. The green highlighted areas point out the flight attitudes with the least difference comparing to the respective baseline thrust whereas the red ones refer to the flight attitudes with the greatest difference. All tested flight attitudes resulted to less thrust comparing to the respective baseline condition and the amount of difference gives an idea about the installation and the distortion effects on the net thrust.

Table 7-8 Net Thrust Percentage Changes from the Baseline Conditions for the 0.35M, 0.6M and 0.85M Flight Attitudes

	NET THRUST (% CHANGE FROM BASELINE)		
AOA_AOSS	**0.35M**	**0.6M**	**0.85M**
0_0	-3.16	-3.47	-3.33
0_8	-5.29	-6.37	-6.64
0_16	-12.04	-19.59	-22.56
8_8	-5.77	-4.11	-3.22
8_16	-11.40	-12.70	-11.59
16_8	-7.79	-5.68	-2.89
8_0	-4.10	-2.56	-1.76
16_0	-6.62	-4.31	-1.84
16_16	-12.41	-13.11	-9.99

Figures 7-7, 7-8 and 7-9 present the same results in a graphical form where it can be implied how the changes in the aircraft's flight attitude affect the output of the engine in terms of net thrust. As it can be clearly observed the minimum values of net thrust occur when the aircraft is supposed to fly with high AOSS. What's more, as the flight Mach number increases

- The high values of AOSS cause a greater thrust percentage change in relation to the respective baseline condition.
- The difference between the best flight attitude in terms of resulted net thrust and the worst one becomes greater.

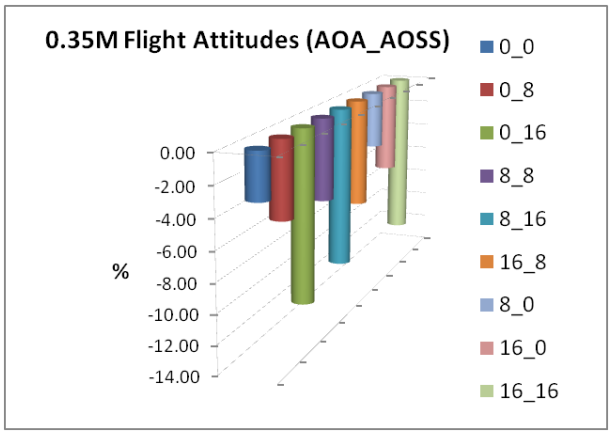

Figure 7-7 *Net Thrust Percentage Change from the Baseline Conditions for the 0.35M Flight Attitudes*

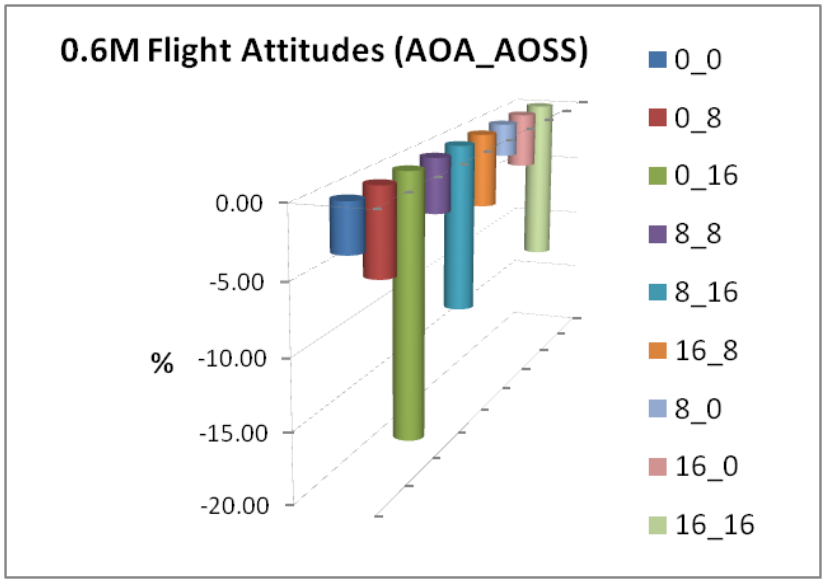

Figure 7-8 *Net Thrust Percentage Change from the Baseline Conditions for the 0.6M Flight Attitudes*

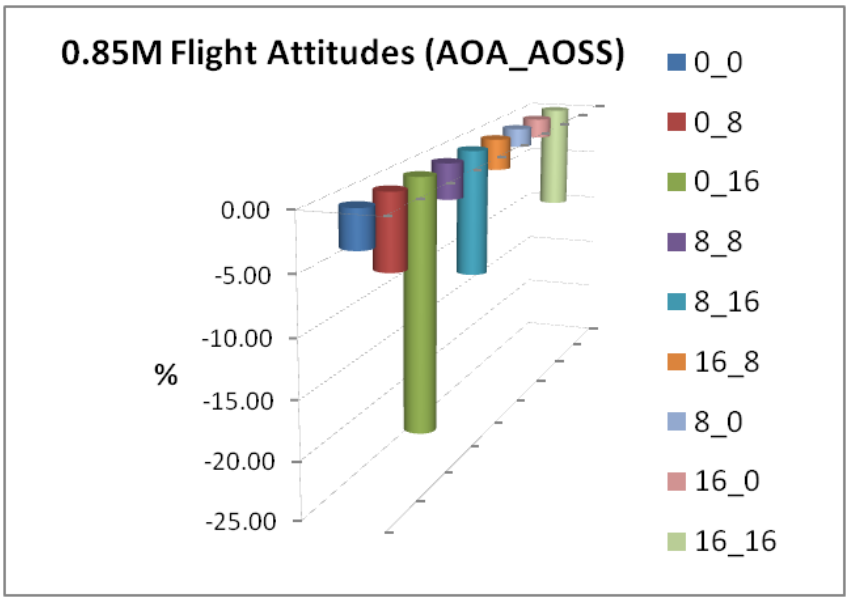

Figure 7-9 Net Thrust Percentage Change from the Baseline Conditions for the 0.85M Flight Attitudes

The best flight attitude among the tested ones for the 0.35M flight in terms of resulted net thrust was the one with 0˚ AOA and 0˚ AOSS. This specific flight attitude presents a net thrust percentage change of -3.16% comparing to the 0.35M baseline condition. On the other hand the worst flight attitude was that with 16˚ AOA and 16˚ AOSS for which the net thrust percentage change is about -12%. This can be justified by considering the low values of mass flow rate and intake pressure recovery presented in Tables 7-1 and 7-3.

As it was noted in the previous paragraph, among the 0.6M flight attitudes the one with the highest net thrust was that with 8˚ AOA and 0˚ AOSS and the attitude with the lowest net thrust was that with 0˚ AOA and 16˚ AOSS. The net thrust percentage change between highest and lowest values varies between -2.56% to -19.59%.

For the 0.85M flight attitudes the attitude with the highest net thrust was once again that with 8˚ AOA and 0˚ AOSS and the attitude with the lowest net thrust is like in the previous flight Mach number that with 0˚ AOA and 16˚ AOSS. The net thrust percentage change comparing to the baseline condition for the 0.85M flight attitudes varies between -1.76% to -22.56% .

7.4 Surge margin depletion

The distorted inflow conditions due to the aircraft's flight attitude cause the variation of the intake pressure recovery and the mass flow rate that the engine experiences. Subsequently, the performance of the engine follows these variations in terms of the resulted net thrust.

Figure 7-10 presents the engine's FAN map with two running lines that refer to the operation of the engine under the flight conditions of 0.85M with 8˚ AOA and 0˚ AOSS and 0.85M with 0˚ AOA and 16˚ AOSS. These two specific flight attitudes, as can be seen in table 7-8, present respectively the lowest and highest net thrust percentage changes comparing to the baseline condition among the tested flight attitudes.

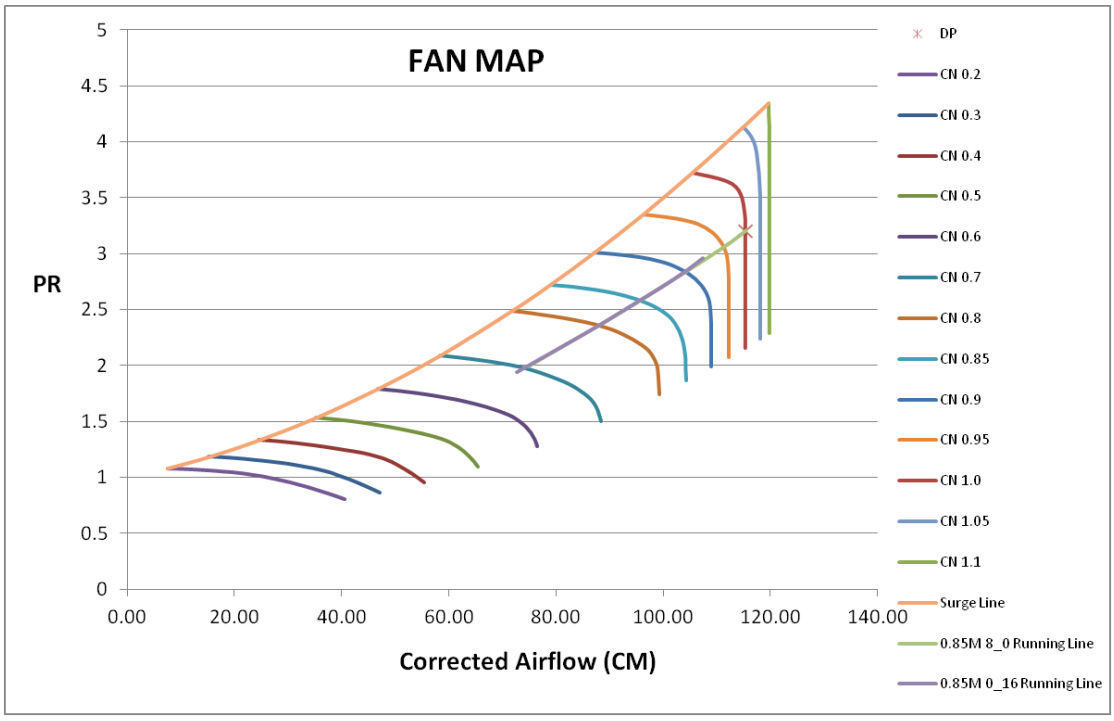

Figure 7-10 FAN Map Showing the 0.85M 8_0 and 0.85M 0_16 Running Lines

As can be observed in this figure the engine's running line moves to the left side of the map and slightly towards to the surge line as the distortion level increases. As a result the surge margin decreases to that direction.

When fig. 7-10 that presents the shift of the running line when the engine operates under the distorted conditions induced by the flight attitude of 0.85M with 0˚ AOA and 16˚ AOSS is combined with fig. 6-7 that presents the respective shift of the surge line under the

same distorted conditions a total view of the distortion effect on the FAN stability can be obtained. This view is depicted in fig. 7-11 where it can be clearly seen that the most distorted condition i.e. the flight attitude that resulted to the greatest loss in surge pressure ratio (ΔPRS) was not detrimental to the FAN stability since the SM was not depleted.

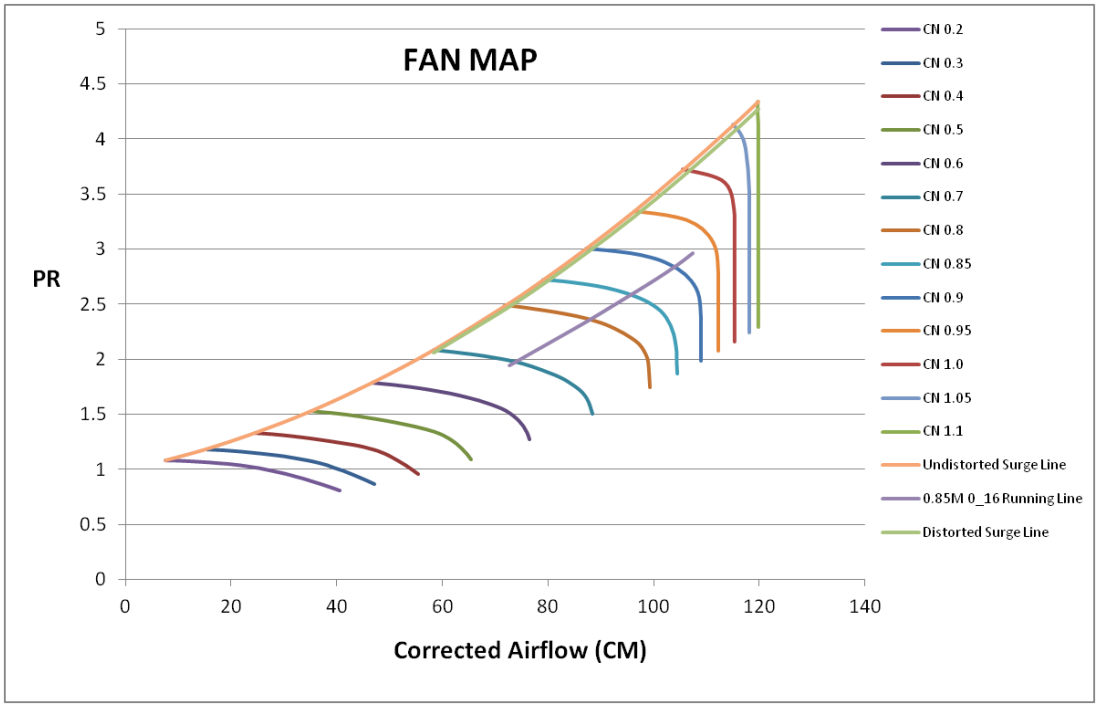

Figure 7-11 FAN Map Showing the Running Line and the Distorted Surge Line for the 0.85M 0_16 Flight Attitude

7.5 Maps of Engine's performance

As it has already been discussed, for each flight Mach number 9 different flight attitudes have been tested. When the distortion results from these flight attitudes are combined in one graph, then the surface graphs presented in figs 7-12 through 7-14 are obtained, one per flight Mach number.

These graphs give an estimation of the distortion levels, in terms of Loss in Surge Pressure Ratio (ΔPRS), for all the aircraft's flight attitudes (with combined AOA and AOSS values in the tested range), even for those that they were not actually tested.

For example, if the distortion levels when the aircraft flies at 0.35M with 10˚ AOA and 10˚ AOSS needed to be estimated (an attitude that was not CFD tested) from fig. 7-12

can be obtained that for this specific flight attitude the resulted ΔPRS would have been in the range of -0.5 to 0.

Figures 7-15 and 7-16 present two graphs which correlate the loss in surge pressure ratio with the Mass flow rate and the Intake Pressure Recovery results respectively. These graphs present in a graphical format the results presented in tables 7-1 and 7-3. Using all the above graphs, the engine's performance parameters can be estimated for each flight attitude that has characteristics in the tested range of flight Mach number, AOA and AOSS.

For example, as it was demonstrated above for the flight attitude of 0.35M with 10˚ AOA and 10˚ AOSS the estimated range of ΔPRS is -0.5 to 0. From graphs in figs 7-15 and 7-16 this specific value is correlated respectively to:

- about 58 Kg/s of mass flow rate
- about 0.968 intake pressure recovery

These values may be entered then into the engine's performance simulation model and in that way an estimation of the resulted net thrust for this specific flight attitude may be obtained.

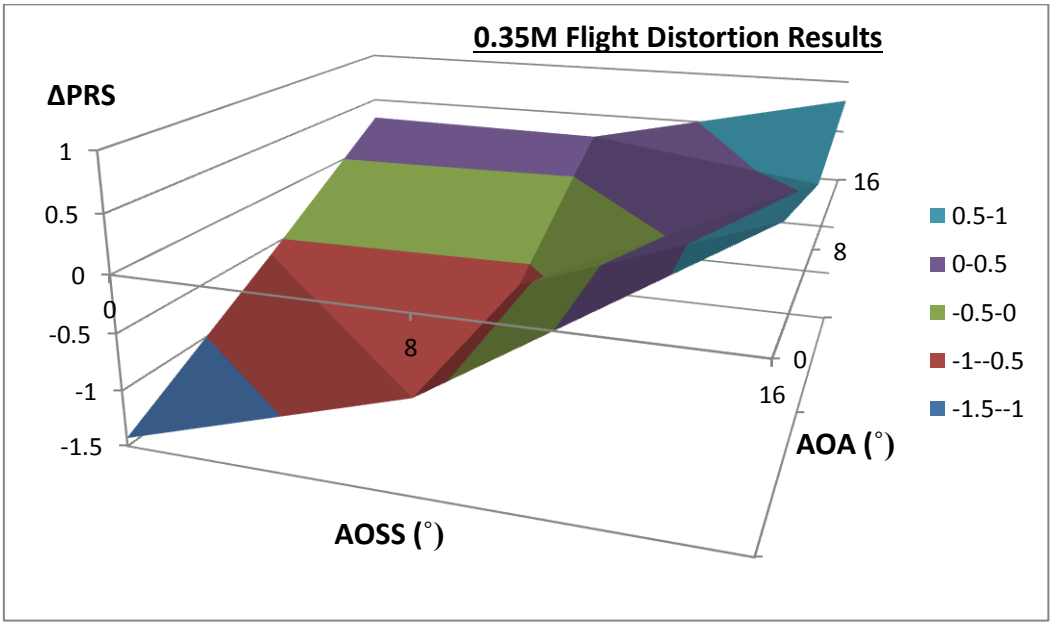

Figure 7-12 0.35M Flight Distortion Results

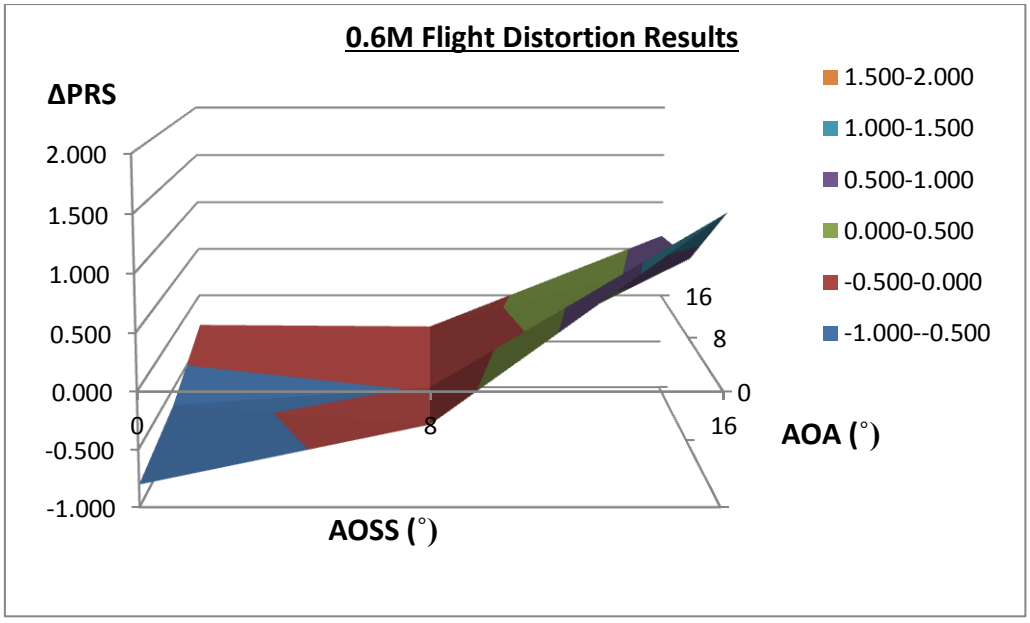

Figure 7-13 0.6M Flight Distortion Results

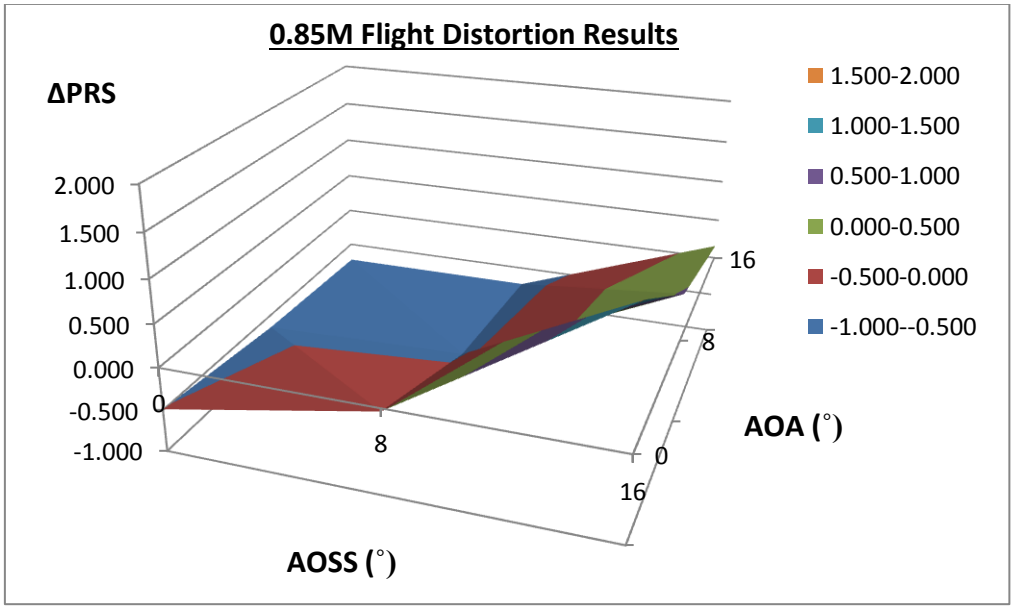

Figure 7-14 0.85M Flight Distortion Results

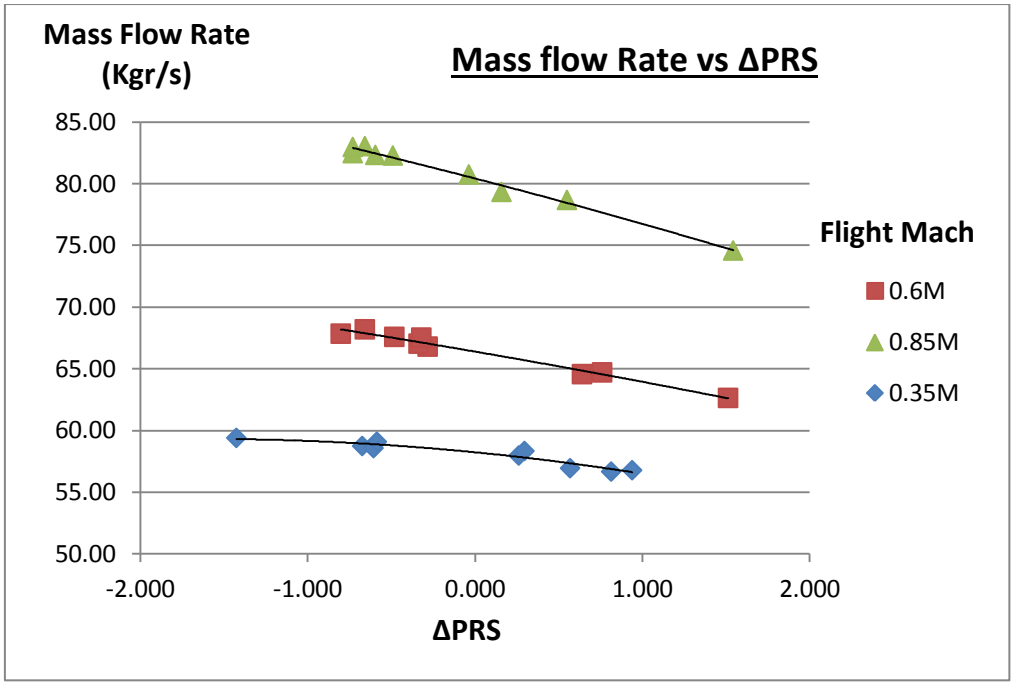

Figure 7-15 Effect of Loss in Surge Pressure Ratio (ΔPRS) on Mass Flow Rate

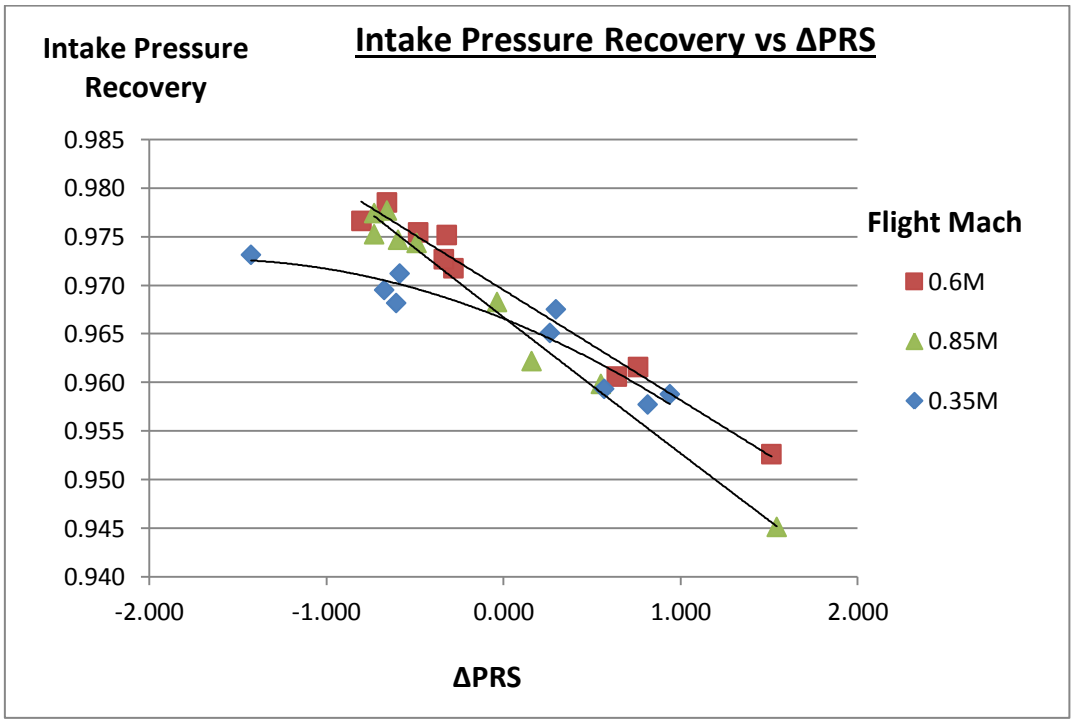

Figure 7-16 Effect of Loss in Surge Pressure Ratio (ΔPRS) on the Intake's Pressure Recovery

7.6 Chapter Summary

As was presented in the previous chapter none of the 27 tested flight attitudes threatened the stable operation of the engine's fan in that the operating point of the fan for each tested attitude was not moved beyond its surge line.

In this chapter it was estimated how the engine's performance is affected, in terms of resulted net thrust, by the distorted conditions. The engine's performance parameters that vary with distortion are the mass flow rate that the engine experiences and the intake pressure recovery. These two parameters were CFD calculated and the resulted values were entered into the engine's performance simulation model in Turbomatch. In that way the net thrust for each tested flight attitude was calculated.

In the next step all the obtained results were combined to create performance maps of this specific airframe-engine configuration. In these maps the flight attitude of the aircraft was correlated to a loss in surge pressure ratio value and then to respective values of mass flow rate and intake pressure recovery. These last parameters when entered in Turbomatch they provide the resulted net thrust of the engine for the under examination flight attitude.

The creation of these performance maps is a novelty of the present work and comprise a means of direct assessment of the resulted net thrust of the engine given the flight attitude of the aircraft.

8 CONCLUSIONS

8.1 Summary of the research project

The present study provides a methodology for the evaluation of the total pressure distortion effect on the performance of an installed gas turbine engine. Patterns of distortion at the engine's face were obtained through CFD simulations where the flow over a full scale military aircraft with an active intake was numerically resolved. The term active intake refers to its capability to allow the airflow to reach the engine's face. Different flight attitudes have been considered by changing accordingly the direction of the incoming flow in the computational domain.

The engine's fan stability is an issue that needs to be firstly considered since the first engine's component that experiences the distorted conditions is the fan and depending on the level of distortion, the operating point of the fan on its characteristics map may be moved to the surge area. In the present study the fan stability was assessed following the guidelines of SAE ARP 1420 [20] and AIR 1419 [10].

Then, the engine's performance in terms of resulted net thrust was estimated in TURBOMATCH, a gas turbine performance simulation tool developed at Cranfield University. This methodology enhances the existing engine-inlet compatibility analysis and design methodology (ARP-1420) through the use of modeling and simulation.

For the purpose of this study, as a baseline set of airframe-engine, were chosen a military aircraft, inspired by the General-Dynamics/LMAERO F-16 airframe, which is assumed to be equipped with a Pratt and Whitney F100-PW-229 equivalent gas turbine engine.

In the first part of this work a numerical simulation of the airflow over a military aircraft was accomplished. The tested conditions referred to 27 different aircraft flight scenarios:

- three different flight Mach numbers -0.35M, 0.6M and 0.85M- at 20000ft altitude;
- nine combinations of Angles of Attack (AOA) and Angles of Sideslip (AOSS) at each one of the above tested flight Mach numbers (AOA and AOSS varied in the range of 0 to 16 degrees).

The obtained results were focused on the distribution of the total pressure at the Aerodynamic Interface Plane (AIP). These results were in the form of total pressure contours.

In the second part these total pressure profiles were quantified in terms of distortion descriptors, following the guidelines of SAE AIR 1419 [10] and SAE ARP 1420 [20]. The distortion descriptors were then correlated to the loss in surge pressure ratio (ΔPRS) and through that process it was determined which ones of the tested flight attitudes threatened the stability of the fan in terms of surge margin depletion. Also in the same part it was presented how the distortion descriptors varied with the aircraft's flight attitude.

None of the tested flight attitudes were found to threaten the fan stability and in the last part, the engine's performance was evaluated, in terms of net thrust, for each one of them. This performance assessment was accomplished with the aid of Turbomatch.

8.2 Research Conclusions

As it can be seen from the resulted total pressure profiles at the intake's exit, the airflow reaching the engine's face is not uniform at all. Depending on the aircraft's flight attitude the quality of the airflow in terms of total pressure that enters the engine, varies significantly. The predicted profiles present a variation in total pressure which becomes more prominent at the flight attitudes that an AOSS has been induced.

The intake's Pressure Recovery which is a performance parameter of the intake, as it was expected, follows these variations and its minimum values occur at the attitudes with the greatest AOSS.

As far as the distortion descriptors are concerned which comprise the means of distortion quantification, among the calculated values of MPR, circumferential extent and circumferential intensity in the 27 different flight attitudes that have been tested,

- The values of MPR that were collected, ranged from 1, at the majority of the tested cases, to 1.99 at ring No 5 of the resulted total pressure profile from the flight attitude of 0.6M with 8 AOA and 0 AOSS. The other distortion descriptors though (circumferential intensity and extent) for this specific flight attitude were at their lowest values. As a result this maximum MPR in conjunction with the low values of circumferential

intensity and extent did not render this flight attitude a severe one in terms of total pressure distortion.

- The greatest calculated circumferential extent was 178˚, and occurred at the flight attitude of 0.35M with 0˚AOA and 8˚AOSS.
- The highest circumferential intensity found to be 0.0362 at the flight attitude of 0.35M flight with 16˚ AOA and 16˚ AOSS .

Figures 5-24, 5-25, 5-28 and 5-29 present the effect of AOA and AOSS on the five ring average values of circumferential intensity and extent. Also figs 5-30 and 5-31 present the effect of AOA and AOSS respectively on the five ring maximum value of radial intensity. All the obtained results present trends that refer to this specific intake-engine system. Based on the resulted graphs and for the flight attitudes with 0˚ AOSS:

- At a 0.35M flight the magnitude of the subsequent pressure defect at the AIP becomes greatest at around 8˚AOA. In higher flight Mach numbers though, the most severe total pressure defect at the AIP occurs at higher AOA and it is milder (the pressure defect) than what it was in the 0.35M flight.
- There is an optimum combination of flight Mach number and AOA for which the extent of the total pressure defect at the AIP gets its minimum value. This is 0.6M flight with 8˚ AOA.
- Generally, the maximum radial intensity decreases as the AOA increases.

As for the flight attitudes with 0˚ AOA, it can be concluded that:

- When the AOSS increases, the maximum circumferential intensity increases as well and this is common for all the tested flight Mach numbers.
- For each flight Mach number, there is an AOSS for which the circumferential extent takes its maximum value. As the flight Mach number increases the maximum circumferential extent occurs at higher AOSS.
- The maximum radial intensity decreases as the AOSS increases.

All in all, among the tested flight attitudes in the context of the present research the two worst ones in terms of distorted airflow at the AIP were the following,

- 0.35M flight with 0˚ AOA and 8˚ AOSS and
- 0.35M flight with 16˚ AOA and 16˚ AOSS.

The total pressure distortion parameters in the AIP for these flight conditions were respectively 0.0344 and 0.0362 for the circumferential intensity and 178˚ and 152˚ for the circumferential extent.

It worths mentioning that the validation of the obtained numerical results could only be made through the validation of the simulation model as described in detail in [67]. The main reason behind that decision was the absence of similar experimental data referring to this specific airframe-engine configuration. CFD technology though has been successfully used elsewhere [68], [69] in the simulation of distorted airflow conditions entering intake ducts. The numerical results obtained in these cases were really close to experimental ones which gives confidence, in a roundabout way, to similar suggested methodologies like the one described herein.

As far as the engine's performance is concerned, the work presented herein has shown that:

- The engine's mass flow rate increased with Mach number in alignment with the RAM effect.
- Also, when considering the results referring to the same flight Mach number it becomes obvious that the AOSS had in general a negative effect on the mass flow rate entering the engine whereas in the flight attitudes with AOA the resulted mass flow was rather increased.
- None of the 27 examined flight attitudes threatened the stability of the FAN i.e. the surge margin was not depleted as a result of the airflow distortion due to these aircraft flight attitudes.
- The stability of the FAN seems to be quite immune to the distorted inflow conditions caused by these specific flight attitudes i.e. in all examined flight attitudes the resulted total pressure distortion level was not even close to the point where it may cause the destabilization of the FAN.
- Total pressure distortion causes the shift of the FAN surge line and the engine’s running line both towards the direction of surge margin depletion.
- The flight attitudes of 0.6M and 0.85M flights with 8 ˚AOA and 0˚ AOSS resulted to a maximum net thrust (lowest net thrust percentage changes comparing to the

respective baseline conditions) indicating that at these flight Mach numbers AOA up to a certain value works to the benefit of the engine's performance.

- On the other hand, the resulted net thrust of the engine is at its minimum values when the aircraft flies with 16˚ AOSS in all three tested flight Mach numbers.
- The net thrust percentage change comparing to the respective baseline condition for the 0.35M, 0.6M and 0.85M flights varies between -3.16 to -12.41%, -2.56 to -19.59% and -1.76 to -22.56% respectively.
- As the flight Mach number increases the difference between the best and the worst flight attitudes in terms of net thrust percentage change comparing to the baseline condition, becomes greater.
- When it comes to the difference between uninstalled and installed engine's performance for the 0.35M, 0.6M and 0.85M flights it was shown (table 7-7) that the presence of the intake causes a thrust loss of at least 3.16%, 2.56% and 1.76 % respectively.

8.3 Sources of Uncertainty

Besides the discretization and truncation errors that are almost inevitable in a CFD approach, there are some points in the course of the entire project that comprise sources of uncertainty for the obtained results.

The geometry model was created based on information found in the open literature. These information provide a part and not the whole picture as far as the under consideration engine's and airframe's designs are concerned. The detailed information comprise proprietary information of the original manufacturers and as such they can hardly be released. Based on that it becomes obvious that the geometry model itself is a source of uncertainty for the obtained results (modeling error).

Also, the selected Turbulence model in the CFD calculations comprises a source of possible uncertainty in the predicted results. The standard wall functions selected may have left unpredicted the occurrence of flow separations inside the intake at specific flight attitudes. However, the absence of wall functions along with a fully refined mesh up to the actual wall boundaries would have rendered the solution of the present flow case computationally unaffordable due to the domain's big size.

Another source of possible uncertainty is the extension of the flow domain behind the intake's exit with the addition of a simple accelerating duct and not with the FAN component itself. However as it has been already explained in detail the complexity of the geometry left no other choices than the selected approaches.

In the distortion quantification process two constant parameters that were used were the circumferential and radial sensitivities (Kc and Kr respectively). These parameters were used in the correlation of the distortion descriptors with the loss in surge pressure ratio in the fan stability assessment. Their values were based on empirical calculations from tests with 180 degrees classical inlet distortion screens [10]. This specific method renders the calculated values of Kc and Kr parameters more applicable to the tested compressors. In case these values are used in other compressors as well, an uncertainty is also introduced, the amount of which is proportional to the difference between the tested compressor and the one under consideration.

Finally, in the fan stability assessment the fan characteristics were visualized using a scaled map from the Turbomatch database and not the actual fan map from the under consideration engine. The reason behind that specific selection was that there was no access to the actual fan map of the baseline engine which comprise proprietary information of the original equipment manufacturer.

8.4 Future Work

There is certainly a great field of potential future work that can be initiated out of this project which continuation would be a validation of the numerical study. This continuation may take place either in the direction of minimizing the sources of uncertainty mentioned above or in the direction of widening the aspects that have already been covered in the present research work.

Some suggestions are given below which could help to further continue the present study:

- Geometry model:

The created geometry model may be used in the study of the flow field not only inside the intake but also around the airframe as well. For example with the same geometry model the after body effect may be also studied focusing this time at the flow field around

the exit nozzle. Also the same model with the addition of an intake screen may be used to predict the flowfield at the engine's face when inside the intake of a flying aircraft has been added a screen. This configuration is quite interesting if someone considers that the specific airframe-engine configuration is susceptible to FOD failures and the addition of such a screen could alleviate the problem.

- CFD model:

The CFD model may be improved in that a turbulence model without wall functions may be used in conjunction with a fully refined mesh near the wall boundaries ($1<Y^{+}<5$). Another improvement would have been to use a structured mesh instead of the unstructured one used herein. These improvements though call for greater computational resources than those that were at the author's disposal during the progress of the present research study.

- Fan component geometry:

The addition of the geometry of the actual engine's fan component behind the intake's exit would have greatly improved the quality of the obtained results especially in the part of the fan stability assessment.

- Validation of a CFD model:

A validation comprises the air flow fields as well as the fluid parameters and distributions. It is crucial to validate numerical studies with experimental data. Despite the fact that full-scale test have so far been beyond the financial limits, steps should be taken in this direction. This may include flow field investigations of scaled intake models or full-scale tests of a reduced area of consideration.

- Tested flight attitudes

The flight attitudes that were tested in the context of the present study comprise rather mild flight attitudes for the specific airframe-engine configuration. It would have been really interesting the CFD model to be tested in more severe flight attitudes in terms of AOA and AOSS. The more severe flight attitudes along with a turbulence model that uses no wall functions would propably reveal areas of flow separation inside the intake causing the operation of the engine under highly distorted conditions.

- Intake geometry

The conclusions drawn from this numerical study refer to the reference airframe-engine installation. The direct application of the findings to different intake engine configurations is limited. The flow fields that develop in different intake geometries may result in different levels of airflow distortion. The intake geometry used in the present study resembles that of an S-duct. It would have been really interesting to see how the engine's performance reacts to any intake's geometry changes for the same flight attitudes.

8.5 Achievements and Contribution to Knowledge

The work presented herein investigated the effect of airflow distortion, in terms of total pressure nonuniformities at the AIP, on a military gas turbine engine's performance. The source of the airflow distortion was considered to be the aircraft's flight attitude in conjunction with the fact that the intake is a curved duct, highly embedded into the airframe. This section outlines the achievements and the contribution to knowledge from the present PhD research project.

First of all a detailed literature review of prior investigations related to airflow distortion in gas turbine engines has been contacted which revealed the aspects that needed some light to be shed on.

Then, the great achievement of this research effort was the creation of a full scale 3D geometry model representing a military aircraft inspired by the multi-role General Dynamics/LMAERO F-16 fighter aircraft. The geometry model was created from scratch in ICEM CFD and comprised all the basic features of the airframe along with an active intake in that the airflow may enter the intake and travel all the way up to the engine's face. This model, similar to which was not found during the literature review process, may be used in many cases where the flow around a military aircraft needs to be simulated and resolved. It can be also used as a design tool to verify and refine the outcome of a preliminary design analysis refering to such geometry.

Another achievement was the CFD steady state solution of the flow field around the created geometry model. The complexity of the geometry along with the size of the computational domain made the generation of the required mesh not free from difficulties. Hopefully, all of them were overcome and a converged solution of the flow field was achieved. The selection of an unstructured mesh and a turbulence model with wall functions

were two approaches that were adopted in the present study as means to overcome the previously mentioned difficulties.

From an operational point of view, this model may be used to investigate the interaction between the airframe and an attached external load, like a missile or bomb, in case it is required to include it in the aircraft's external loads inventory. Another usage of this model may be to calculate, for specific flight conditions, the aerodynamic loads that are induced to a certain structural area of this aircraft and to investigate in that way the structural integrity of the materials used in a possible repair in that area.

The presence of the engine in the CFD model was declared through the boundary condition settings at the intake's exit. By setting this boundary as pressure outlet and by defining the proper static pressure value at this plane, sufficient sucking conditions are created which resemble the engine's operation. The required static pressure at this point was the result of an iteration process between TURBOMATCH and CFD. This kind of coupling between the CFD model and the engine comprises another contribution to knowledge of the present study.

The establishment of a method that when followed it could provide performance correction factors due to airflow distortion was another important contribution of the present study. This method which comprise a significantly less expensive alternative to the actual full scale testing in a wind tunnel environment is based on Computational Fluid Dynamics and provides a means to assess the compatibility of an airframe-engine set, given the geometry of the upstream intake and the simulation model of the under examination gas turbine engine. The steps of this method include

- The creation of a data base of aircraft flight conditions (altitude, speed and attitude) tied together with the resulted total pressure profiles at the AIP representing the level of flow distortion.
- The quantification first and then the communication of this flow distortion downstream to the engine's fan compression system.
- The estimation of the change in engine’s performance in terms of resulted net thrust, due to this aforementioned distortion.

This method comprise a means to assess from an operational point of view whether a specific flight attitude of this aircraft may be responsible for an abnormal operation of the engine. The author as an active member of the Hellenic Air Force has experienced many

cases in which aircraft returned from flight and the aircrew reported unusual engine's malfunctions accompanied by strange ''bang'' noises. These engine's write-ups required the maintenance personnel to accomplish an extended troubleshooting which in most of the times ended up with an engine entirely disassembled with no actual findings. This process increases the time that the engine is grounded for unscheduled maintenance and subsequently reduces its operational usage.

The method described herein may contribute in limiting these undesired phenomena since in case an aircraft returns from a flight and reports a similar behaviour of the engine before any actual maintenance action is taken, the flight attitude of the aircraft may be examined in the model described herein to assess whether it may destabilize the operation of the fan. So, in this way the strange noise reported by the air-crew may be attributed to a fan destabilized operation by the distorted conditions that the engine experienced due to the flight attitude of the aircraft. And the maintenance actions may be thus limited and focused just to the fan component.

Of course these data are well known to the manufacturers and they are implicitly transferred to the operational environment of the aircraft through the Technical Orders which include detailed troubleshooting information for most of the reported malfunctions. But, there are cases, like the ones described before that they are not covered by the Technical Orders and these are the cases that the present work may contribute to troubleshoot.

The refinement of the baseline engine's performance simulation model was another achievement in the context of the present work. This performance simulation model of the F100-PW-229 engine was tested in the latest version of Turbomatch and the results are presented in chapter 7.

Finaly another achievement was the creation of performance maps for the baseline airframe-engine configuration that corelate the airframe's flight attitude with the resulted gas turbine engine's net thrust.

9 REFERENCES

[1] Hoheisel H., 1997, Aerodynamic Aspects of Engine-Aircraft Integration of Transport Aircraft, *Aerospace Science and Technology*, 7, pp 475-487.

[2] Palmer J. R., 1990, The TURBOMATCH Scheme For Aero/Industrial Gas Turbine Engine Design Point/Off Design Performance Calculation, *SME,* Thermal Power Group, Cranfield University.

[3] Walsh P.P., Fletcher P., 2004, GAS TURBINE PERFORMANCE, Black-well science, 2nd Ed.

[4] Research and Technology Organization, 2002, Performance Prediction and Simulation of Gas Turbine Engine Operation, RTO-TR-044

[5] Pachidis V.A., 2006, Gas Turbine Advanced Performance Simulation, PhD Thesis, Cranfield University.

[6] Reed J.A., Afjeh A.A., 1997, A Comparative Study of High and Low Fidelity Fan Models for Turbofan Engine System Simulation, IASTED Int Conference on Applied Modeling & Simulation, Banff, Canada, July 1997.

[7] Rolls-Royce, 1996, THE JET ENGINE, 5th Edn, The Technical Publications Department, Rolls-Royce plc, Derby, England.

[8] [online] Available at: http://student-pilots.com/what-is-an-epregt-and-fod [Accessed 29 Jul. 2015].

[9] Saravanamuttoo H.I.H., Rogers G.F.C., Cohen H., Straznicky P.V., 2009, GAS TURBINE THEORY, 6th Ed.

[10] Technical Committee S-16, 2013, Inlet Total Pressure Distortion Considerations for Gas Turbine Engines, SAE AIR 1419, May 1983, revised 2013-05.

[11] Shevel R.S., 1989, FUNDAMENTALS OF FLIGHT, 2nd Ed, Prentice-Hall, USA.

[12] Mahoney J.J., 1990, INLETS FOR SUPERSONIC MISSILES, AIAA Education Series.

[13] El-Sayed A.F., 2008, AIRCRAFT PROPULSION AND GAS TURBINE ENGINES, CRC Press.

[14] Laruelle G., 2002, Air Intakes: Role, Constraints and Design, ICAS 2002 CONGRESS.

[15] Seddon J., Goldsmith E.L., 1993, PRACTICAL INTAKE AERODYNAMIC DESIGN, Blackwell Scientific Publications, Oxford.

[16] Williams D., 2010, Airframe Engine Integration, Propulsion System Performance and Integration, MSc Thermal Power Course Notes, Cranfield University.

[17] Seddon J., Goldsmith E.L., 1999, INTAKE AERODYNAMICS, Blackwell Science ltd.

[18] Bissinger N. C., Breuer T., 2010, Basic Principles–Gas Turbine Compatibility–Intake Aerodynamic Aspects, Encyclopedia of Aerospace Engineering, Volume 8, Chapter EAE487.

[19] Kurzke J., 2008, Effects of Inlet Flow Distortion on the Performance of Aircraft Gas Turbines, *Journal of Engineering for Gas Turbines and Power*, 130, July 2008.

[20] Technical Committee S-16, 2002, Gas Turbine Engine Inlet Flow Distortion Guidelines, SAE AIR 1420, Rev B, 2002-02.

[21] Yadlin, Y., 2006, Simulation of Vortex Flows for Airplanes in Ground operations, AIAA, 2006-0056.

[22] 'F-16 Intake Vortex', [Online] Available: https://www.reddit.com/r/AirForce/comments/347nfg/f16_intake_vortex. [Accessed: 23-Jun-2011].

[23] Allan B. G., Owens L. R., Berrier B. L., 2004, Numerical Modeling of Active Flow Control in a Boundary Layer Ingesting Offset Inlet, *2nd AIAA Flow Control Conference*, 28 June - 1 July 2004, Portland, Oregon.

[24] Mund F.C., 2006, Coordinated Application of CFD and Gas Turbine Performance Methods, PhD Thesis, Cranfield University.

[25] Jiyuan Tu; Guan Heng Yeoh; Chaoqun Liu, 2008, COMPUTATIONAL FLUID DYNAMICS A PRACTICAL APPROACH, Elsevier.

[26] Hawkins J. E., 1974, YF-16 Inlet Design and Performance, AIAA/SAE 10th Propulsion Conference, San Diego, California, Oct 21-23 1974, AIAA 74-1062.

[27] 'Airwar.ru', [Online] Available: http://www.airwar.ru/other/draw/f16cb52_aiv.html. [Accessed: 04-Nov-2010]., 4-11-2010

[28] 'Aerospaceweb.org, Aircraft Museum - F-16 Fighting Falcon', [Online] Available at: http://www.aerospaceweb.org/aircraft/fighter/f16/ [Accessed: 4 November 2010].

[29] GAMBIT 2.4, 2007, User's Guide, Fluent, Incorporated.

[30] [online] Available at: http://www.cranfield.ac.uk/~cfdcour [Accessed 20 Mar 2010].

[31] U.S. Standard Atmosphere, 1976, NASA-TM-X-74335

[32] ANSYS FLUENT 12.0, Theory Guide, ANSYS Inc, 2009-01-23.

[33] Ibrahim I.H., Ng E.Y.K., Wu Y.L., Wong L.W.K., 2009, The Swirl Flow Analysis of the Port Side F-5E Intake Using CFD, *Progress in Computational Fluid Dynamics:An International Journal*, Vol 9, No 2, pp 109-115.

[34] Doulgeris G.C., 2008, Modeling and Integration of Advanced Propulsion Systems, PhD Thesis, Cranfield University.

[35] ANSYS FLUENT 12.0, User's Guide, ANSYS Inc, 2009-01-23

[36] Davis M., Hale Al., Beale D., 2002, *An Argument for Enhancement of the Current Inlet Distortion Ground Test Practice for Aircraft Gas Turbine Engines*, Journal of Turbomachinery, Vol. 124, pp 235-241, April 2002.

[37] Reid C., 1969, *The Response of Axial Flow Compressors to Intake Flow Distortion*, THE AMERICAN SOCIETY OF MECHANICAL ENGINEERS, ASME Paper 69-GT-29.

[38] Li Zhipeng, Lu Chao, Wu Hui, Liu Xiaopeng, Zhang Guowang, 2014, *Applying CFD Technology to Determine the Effect of Two New Designed Fan Inlet Distortion Generators,* 2014 Asia-Pacific International Symposium on Aerospace Technology, APISAT2014, Procedia Engineering 99 (2015) 646 – 653.

[39] Mehalic M. C., 1988, *Effect of Spatial Inlet Temperature and Pressure Distortion on Turbofan Engine Stability*, NASA-TM-100850.

[40] P. C. Learner and I. G. Kennon, 1978, Experimental Investigation of a 0.15-Scale Model of an Underfuselage Normal-Shock Inlet, NASA Contractor Report 3049.

[41] Bissinger C. N., Jost M., 2000, *Thrust Vectoring for Advanced Fighter Aircraft - High Angle of Attack Intake Investigations,* RTO MP-051.

[42] Kevin R. Walsh, Andrew J. Yuhas, John G. Williams, William G. Steenken, 1997, *Inlet Distortion for an F/A-18A Aircraft During Steady Aerodynamic Conditions up to 60˚ Angle of Attack*, NASA Technical Memorandum 104329.

[43] Voytovych D., Merkle C., Xia G., 2010, *Effects of Radial Distortion on Performance of a Fan*, AIAA 2010-745.

[44] Williams D., 1986, *Review of Current Knowledge on Engine Response to Distorted Inflow Conditions,* AGARD-CP-400.

[45] ANSYS ICEM CFD Help Manual, 2012, ANSYS, Inc.

[46] 'Lect-28-NPTEL', [Online] Available at: http://nptel.ac.in/courses/101101002/downloads/Lect-28.pdf [Accessed 25 Jul 2015].

[47] Thomas J. Anderson, 2013, How Supersonic Inlets Work, Details of the Geometry and Operation of the SR-71 Mixed Compression Inlet, 8/19/13, http://www.enginehistory.org/Convention/2013/HowInletsWork8-19-13.pdf/26-7-15

[48] 'CFD Class', [Online] Available at: http://www.bakker.org/dartmouth06/engs150/10-rans.pdf [Accessed 26 Jul 2015].

[49] P. Hendrick, K. Bourdiaudhy, J-F. Herbiet, 2008, *A Flight Thrust Deck for the F100 Turbofan of the F-16 Aircraft,* 26TH International Congress of the Aeronautical Sciences, ICAS 2008.

[50] Bernie MacIsaac, Roy Langton, GAS TURBINE PROPULSION SYSTEMS, AIAA Education Series, 2011, John Wiley & Sons, 2011, Reston VA USA.

[51] Hale A., Davis M., Sirbaugh J., 2006, A Numerical Simulation Capability for Analysis of Aircraft Inlet-Engine Compatibility, *Journal of Engineering for Gas Turbines and Power*, 128, 3, pp 473-481.

[52] Andreadis E., 2009, Upgrade Evaluation of a Military Turbofan Engine, Msc Thesis, Cranfield University.

[53] András Sóbester, 2007, *Tradeoffs in Jet Inlet Design: A Historical Perspective*, JOURNAL OF AIRCRAFT, Vol. 44, No. 3, May–June 2007

[54] Kenneth C. Weston, 1992, ENERGY CONVERSION, Ch. 5, Electronic Edition, http://www.saylor.org/content/weston_energy/Energy_Conversion.pdf.

[55] Delaunay, B., 1934, *Sur la sphere vide*, Izvestia Akademii Nauk SSSSR, Mathematical and Natural Sciences Division, No. 6, 793-800

[56] Jane's AERO-ENGINES, 2003, Issue 14, Jane's Information Group.

[57] A. S. Lee, R. Singh, S. D . Probert, 2009, *Modeling of the Performance of a F100-PW229 Equivalent Engine under Sea-level Static Conditions*, 45th AIAA/ASME/SAE/ASEE Joint Propulsion Conference & Exhibit, AIAA 2009-5018.

[58] Salim .M. Salim, S.C. Cheah, 2009, *Wall Y+ Strategy for Dealing with Wall-bounded Turbulent Flow*, Proceedings of the International Multi Conference of Engineers and Computer Scientists 2009 Vol II, IMECS 2009, March 18 - 20, 2009, Hong Kong

[59] Gilles Eggenspieler, Turbulence Modeling, ANSYS presentation, May 14, 2012.

[60] G. W. Huband, J. S. Shang, M. J. Aftosmis, 1990, *Numerical Simulation of an F-16A at Angle of Attack*, J. Aircraft, Vol. 27, No 10.

[61] Reue, G. L., Doberenz, M. E., Wilkins, D. D., 1976, *Component Aerodynamic Load from 1/9-Scale F-16A Loads Model*, General Dynamics Report 16PR316, Fort Worth, Tex., May 1976.

[62] Crites R. C., Heckert M. V., 1970, *Application of Random Data Techniques on Aircraft Inlet Diagnostics*, AIAA70-597, May 1970.

[63] Johnson R. H., Bayati J. E., Lum E. L., Martin A. W., 1972, *Compressor Stability Assessment Program. Final Technical Report Air Induction System Considerations*, Rockwell Report No. NA-70-615, February 1972.

[64] Rudolf P.M. Rademakers, Thomas Kachele, Stefan Bindl, Reinhard Niehuis, 2014, *Approach for an Optimized Evaluation of Pressure and Swirl Distortion in S-Shaped Engine Inlet Configurations,* Propulsion and Energy Forum, 50th AIAA/ASME/SAE/ASEE Joint Propulsion Conference, July 28-30, 2014, Cleveland, OH.

[65] T. Triantafyllou, T. Nikolaidis, M. Diakostefanis, P. Pilidis, 2015, *Total Pressure Distortion Levels at the Aerodynamic Interface Plane of a Military Aircraft*, The Aeronautical Journal, Volume 119, No 1219, September 2015.

[66] T. Triantafyllou, T. Nikolaidis, M. Diakostefanis, P. Pilidis, 2015, *Effect of Inlet Flow Distortion on Installed Gas Turbine Performance*, Submitted for Publication In Journal of Propulsion and Power, Nov 2015, 2015-10-B36051.

[67] T. Triantafyllou, T. Nikolaidis, M. Diakostefanis, P. Pilidis, 2015, *Numerical Simulation of the Airflow over a Military Aircraft with Active Intake*, Submitted for Publication In Journal of Aerospace Engineering., Dec 2015, JAERO-15-0691.

[68] Li Zhipeng, Lu Chao, Wu Hui, Liu Xiaopeng, Zhang Guowang, 2014, *Applying CFD Technology to Determine the Effect of Two New Designed Fan Inlet Distortion Generators,* Procedia Engineering 99 (2015) 646 – 653, APISAT2014, ELSEVIER.

[69] Sebastian Brehm, Thomas Kachele, Reinhard Niehuis, 2014, *CFD Investigations on the Influence of varying Inflow Conditions on the Aero dynamics in an S-*

Shaped Inlet Duct, Propulsion and Energy Forum, 50th AIAA/ASME/SAE/ASEE Joint Propulsion Conference, July 28-30, 2014, Cleveland, OH.

[70] The Turbomatch Scheme, Cranfield University Handbook, Edition 1, March 2015.

[71] Pachidis, V. A., "*Gas-Turbine Performance Simulation*", M.Sc. Course Notes, Cranfield University, 2006/2007.

[72] Chapter from the book Aeronautics and Astronautics, Downloaded from: http://www.intechopen.com/books/aeronautics-and-astronautics/5-2-2018.

[73] 'Pitot Intake Operating Modes', [Online] Available at: https://en.wikipedia.org/wiki/Components_of_jet_engines#/media/File:Pitotintake.svg [Accessed 5 Feb 2018].

[74] William T Cousins, Milt W. Davis, 2011, Evaluating complex inlet distortion with a parallel compressor model: part 1 – concepts, theory, extensions, and limitations, Proceedings of ASME Turbo Expo 2011, GT2011-45067, June 6-10, 2011, Vancouver, Canada.

[75] Pearson, H. and McKenzie, A.B., 1959, "Wakes in Axial Compressors," Journal of the Royal Aeronautical Society, 63, July, pp. 415-416.

[76] 'F-16 Aircraft Flight Manual', [Online] Available at: https://info.publicintelligence.net/HAF-F16.pdf [Accessed 25 Feb 2018].

[77] 'Ram Recovery', [Online] Available at: http://www.flight-mechanic.com/gas-turbine-engine-performance [Accessed 07 Mar 2018].

APPENDIX A

DISTORTION DESCRIPTOR DATA

The process described herein provides the means to quantify the distortion levels at the AIP of a flying military aircraft. The source of distortion is merely the aircraft's flight attitude with varying AOA and AOSS. The total pressure nonuniformities at the AIP stem from the fact that the intake is a long curved duct highly embedded in the airframe. The quantified distortion results were also used to estimate how the gas turbine engine's performance was affected due to the distorted conditions that experienced.

In the context of the present work 27 different flight attitudes have been tested. Tables A-1 through A-3 below contain all the data related to the Distortion Descriptor Elements referring to the 0.35M, 0.6M and 0.85M flight attitudes. The data are quoted on a ring by ring basis for each flight attitude.

Table A-1. Distortion Descriptor Elements Data for the 0.35M Flight Attitudes

DISTORTION DESCRIPTORS FOR THE 0.35M FLIGHT ATTITUDES									
	0_0	**0_8**	**0_16**	**8_8**	**8_16**	**16_8**	**8_0**	**16_0**	**16_16**
RING_1									
CIRCUMFERENTIAL_EXTENT	111.38	178.09	153.50	127.80	148.92	144.47	122.87	142.16	149.90
CIRCUMFERENTIAL INTENSITY	0.003	0.005	0.031	0.014	0.031	0.025	0.015	0.024	0.031
RADIAL INTENSITY	-0.022	-0.020	-0.008	-0.019	-0.011	-0.011	-0.016	-0.006	-0.012
MPR	1	1	1	1	1	1	1	1	1
RING_2									
CIRCUMFERENTIAL_EXTENT	86.02	169.52	151.18	118.12	149.73	137.61	105.12	132.42	150.44
CIRCUMFERENTIAL INTENSITY	0.007	0.012	0.037	0.026	0.038	0.031	0.021	0.027	0.039
RADIAL INTENSITY	-0.016	-0.011	-0.003	-0.010	-0.004	-0.006	-0.011	-0.006	-0.004
MPR	1.25	1	1	1	1	1	1	1	1
RING_3									
CIRCUMFERENTIAL_EXTENT	102.3	179.77	150.26	161.93	127.20	130.29	97.17	113.85	150.98
CIRCUMFERENTIAL INTENSITY	0.015	0.018	0.038	0.014	0.031	0.033	0.030	0.030	0.040
RADIAL INTENSITY	0	0.002	0.001	-0.001	0.001	-0.001	-0.001	-0.004	0.001
MPR	1.09	1	1	1	1	1	1.04	1	1
RING_4									
CIRCUMFERENTIAL_EXTENT	98.34	182.00	150.12	165.49	137.33	125.10	88.10	94.43	152.97
CIRCUMFERENTIAL INTENSITY	0.015	0.021	0.035	0.015	0.030	0.030	0.032	0.031	0.038
RADIAL INTENSITY	0.013	0.010	0.002	0.003	0.009	0.004	0.008	0.002	0.004
MPR	1.24	1	1	1	1	1.02	1.18	1.02	1
RING_5									
CIRCUMFERENTIAL_EXTENT	104.73	182.51	153.21	170.51	142.16	113.26	87.15	84.73	154.30
CIRCUMFERENTIAL INTENSITY	0.013	0.019	0.031	0.014	0.025	0.025	0.028	0.029	0.033
RADIAL INTENSITY	0.026	0.020	0.009	0.013	0.020	0.015	0.020	0.013	0.012
MPR	1.26	1	1	1	1	1.09	1.25	1.1	1

Table A-2. Distortion Descriptor Elements Data for the 0.6M Flight Attitudes

DISTORTION DESCRIPTORS FOR THE 0.6M FLIGHT ATTITUDES									
	0_0	**0_8**	**0_16**	**8_8**	**8_16**	**16_8**	**8_0**	**16_0**	**16_16**
RING_1									
CIRCUMFERENTIAL_EXTENT	121.76	137.31	166.95	107.46	148.96	126.43	76.16	123.32	150.89
CIRCUMFERENTIAL INTENSITY	0.005	0.011	0.031	0.004	0.026	0.011	0.003	0.013	0.025
RADIAL INTENSITY	-0.015	-0.013	0.002	-0.015	-0.007	-0.012	-0.014	-0.010	-0.011
MPR	1.00	1	1	1.28	1	1.00	1.64	1.00	1
RING_2									
CIRCUMFERENTIAL_EXTENT	122.06	131.84	158.98	103.48	148.51	82.90	79.27	103.54	151.65
CIRCUMFERENTIAL INTENSITY	0.010	0.017	0.036	0.007	0.032	0.024	0.008	0.018	0.032
RADIAL INTENSITY	-0.010	-0.007	0.001	-0.010	-0.002	-0.007	-0.010	-0.007	-0.004
MPR	1.00	1	1	1.35	1	1.00	1.38	1.00	1
RING_3									
CIRCUMFERENTIAL_EXTENT	117.75	123.65	153.37	98.96	148.87	106.80	77.63	87.28	150.33
CIRCUMFERENTIAL INTENSITY	0.014	0.022	0.036	0.011	0.031	0.023	0.012	0.028	0.034
RADIAL INTENSITY	-0.001	0.001	-0.001	0.000	0.001	0.000	0.000	-0.001	0.001
MPR	1.05	1	1	1.72	1	1.00	1.86	1.00	1
RING_4									
CIRCUMFERENTIAL_EXTENT	119.00	124.25	147.55	187.45	151.54	101.93	76.08	83.76	150.64
CIRCUMFERENTIAL INTENSITY	0.017	0.023	0.034	0.050	0.028	0.024	0.015	0.028	0.033
RADIAL INTENSITY	0.007	0.006	-0.002	0.008	0.002	0.005	0.007	0.005	0.004
MPR	1.06	1.01	1	1.00	1	1.05	1.96	1.07	1
RING_5									
CIRCUMFERENTIAL_EXTENT	115.10	182.34	144.34	189.02	157.47	97.37	82.24	82.83	152.56
CIRCUMFERENTIAL INTENSITY	0.016	0.016	0.031	0.018	0.025	0.023	0.014	0.026	0.031
RADIAL INTENSITY	0.018	0.014	0.000	0.017	0.006	0.013	0.017	0.014	0.009
MPR	1.12	1.00	1	1	1	1.13	1.99	1.14	1

Table A-3. Distortion Descriptor Elements Data for the 0.85M Flight Attitudes

DISTORTION DESCRIPTORS FOR THE 0.85M FLIGHT ATTITUDES									
	0_0	**0_8**	**0_16**	**8_8**	**8_16**	**16_8**	**8_0**	**16_0**	**16_16**
RING_1									
CIRCUMFERENTIAL_EXTENT	138.07	146.40	170.75	120.29	149.02	109.54	111.59	105.86	156.51
CIRCUMFERENTIAL INTENSITY	0.006	0.011	0.028	0.005	0.021	0.003	0.004	0.003	0.015
RADIAL INTENSITY	-0.011	-0.008	0.003	-0.010	-0.009	-0.011	-0.010	-0.010	-0.012
MPR	1.00	1	1	1	1	1.23	1.00	1.18	1
RING_2									
CIRCUMFERENTIAL_EXTENT	135.99	141.64	165.35	116.18	148.73	101.34	107.65	86.19	156.76
CIRCUMFERENTIAL INTENSITY	0.009	0.015	0.033	0.009	0.027	0.005	0.007	0.005	0.021
RADIAL INTENSITY	-0.007	-0.004	0.001	-0.007	-0.003	-0.007	-0.007	-0.007	-0.005
MPR	1.00	1	1	1	1	1.40	1.01	1.42	1
RING_3									
CIRCUMFERENTIAL_EXTENT	131.08	133.50	159.00	106.71	147.87	102.98	93.86	83.67	152.60
CIRCUMFERENTIAL INTENSITY	0.012	0.018	0.035	0.011	0.030	0.011	0.010	0.012	0.025
RADIAL INTENSITY	0.000	0.000	-0.001	0.000	0.001	-0.000	0.000	0.000	0.001
MPR	1.00	1	1	1.14	1	1.16	1.24	1.21	1
RING_4									
CIRCUMFERENTIAL_EXTENT	129.88	130.54	151.31	102.60	147.60	100.57	93.99	80.07	152.55
CIRCUMFERENTIAL INTENSITY	0.015	0.019	0.035	0.014	0.029	0.013	0.013	0.014	0.027
RADIAL INTENSITY	0.005	0.003	-0.002	0.005	0.003	0.005	0.005	0.005	0.005
MPR	1.00	1	1	1.16	1	1.31	1.25	1.38	1
RING_5									
CIRCUMFERENTIAL_EXTENT	126.57	132.27	146.48	101.35	149.93	99.56	88.62	79.67	154.54
CIRCUMFERENTIAL INTENSITY	0.015	0.019	0.034	0.014	0.028	0.014	0.014	0.015	0.028
RADIAL INTENSITY	0.012	0.009	-0.000	0.012	0.008	0.013	0.012	0.012	0.011
MPR	1.03	1	1	1.31	1	1.37	1.34	1.46	1

APPENDIX B

ENGINE'S PERFORMANCE SIMULATION MODEL

For the purposes of the present study, a model similar to F100-PW-229 gas turbine engine has been chosen as the baseline engine.

The F100-PW-229 is a low bypass, dual-spool turbofan engine, which was first qualified in 1989[8] and ever since it has been chosen by many F-16 users to power their fleet.

It comprises of a three-stage fan and a ten-stage high-pressure compressor (HPC). The HPC is driven by a two-stage high-pressure turbine (HPT) and a two-stage low pressure turbine (LPT) drives the fan.

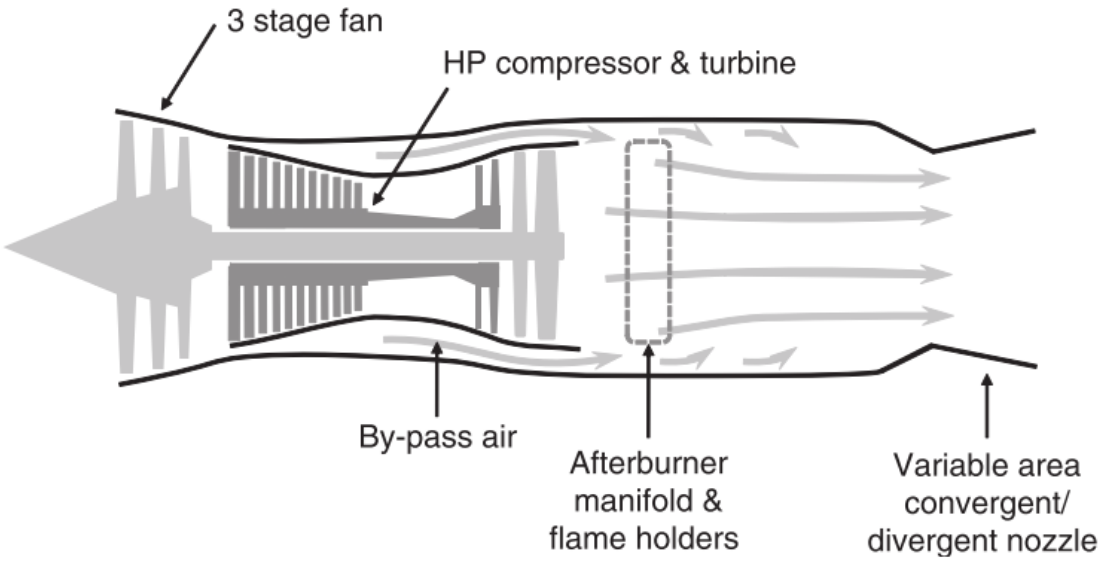

The gas turbine engine's performance simulation model was created in the way described below. The model's parameters, e.g. FAN pressure ratio, overall pressure ratio, bypass ratio, TET, were based on information found in the open literature [56], [57]. As for the important parameters that we did not have any information about, e.g. component efficiencies, pressure losses, cooling flows, these were continuously adjusted, through engineering judgments and optimization techniques, in order to match the engine's DP known output (net thrust and SFC).

Consequently, an engine with performance closely approximating that of F100-PW-229 engine was finally modelled. Table B-1 presents the baseline engine's design point performance data that were used for the validation of the performance simulation model.

Table B- 1 The F100-PW-229 Engine's Design Point Performance Data [56], [57]

Dry Thrust (Nt)	79200
SFC (lb/hr/lbf)	0.74
Dry Fuel Flow (Kg/s)	1.67

Also fig. 2 presents a layout of the baseline engine's components (''bricks'' in Turbomatch) which was primarily used in the creation of the engine's simulation model. On this figure and for the components that they are not self explanatory:

- MIXEES, refers to the ''brick'' that Turbomatch uses to calculate the outlet conditions resulting from the mixing of two flows with given inlet conditions and with no allowance for total pressure change.
- MIXFUL, refers to the ''brick'' that Turbomatch uses to calculate the outlet conditions resulting from mixing of two flows with given inlet conditions, with full allowance for total pressure change resulting from momentum balance.
- PREMAS, refers to the ''brick'' that Turbomatch uses to calculate the outlet conditions from a component such as a splitter, bleed, bypass duct or jet pipe, given the absolute and/or relative changes of mass flow and total pressure.
- DUCTER, refers to the ''brick'' that Turbomatch uses to calculate the outlet conditions from a duct, given the inlet conditions and relative total pressure loss; also, if called for, to calculate the reheat fuel flow, given the outlet total temperature and combustion efficiency.

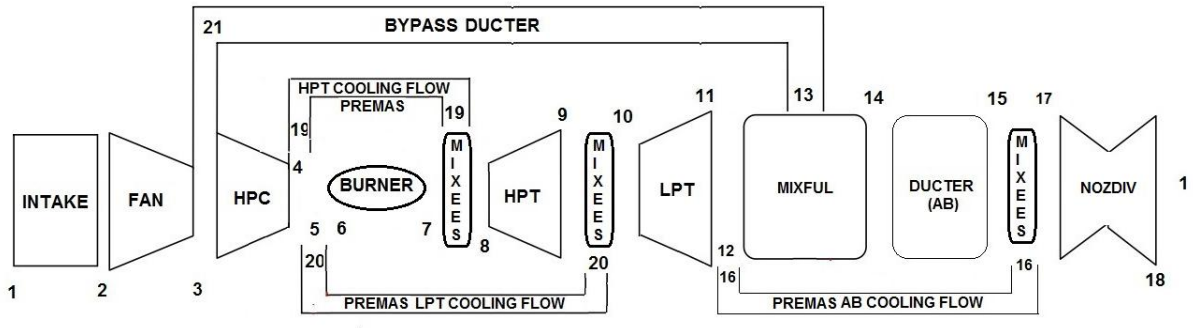

Figure B-1 Sketch of the F100-PW-229 Turbofan Engine's Components

```
Engine: F100-PW-229
Design Point-Dry (without AB)
////
DP SI KE VA XP
-1
-1
INTAKE S1,2            D1-6       R300
FANBRI S2,3,21         D7-22      R301     V9  V7  V8
COMPRE S3,4            D23-34     R302     V23  V24
PREMAS S4,5,19         D35-38
PREMAS S5,6,20         D39-42
BURNER S6,7            D43-50     R303
MIXEES S7,19,8
TURBIN S8,9            D51-66              V52
MIXEES S9,20,10
TURBIN S10,11          D67-82              V68
PREMAS S11,12,16    D83-86
DUCTER S21,13          D87-91     R304
MIXFUL S13,12,14       D92-94
DUCTER S14,15          D95-99     R305
MIXEES S15,16,17
NOZDIV S17,18,1        D100-102  R306
PERFOR S1,0,0          D103-106,306,300,303,0,0,304,0,0,305
CODEND
DATA ITEMS////

!INTAKE
1 0.0 !Altitude [m]
2 0.0 !Dev from ISA temperature [K]
3 0.0 !Flight Mach number
4 0.99 !Pressure recovery
5 0.0 !Dev from ISA pressure [Atm]
```

6 0.0 !Relative humidity [%]

!FAN

7 0.36 !BPR

8 -1.0 !Z

9 -1.0 !Relative rotational speed PCN

10 3.2 !DP BP Pressure ratio

11 0.82 !DP BP Isentropic efficiency

12 3.1 !DP CORE Pressure ratio

13 0.8 !DP CORE Isentropic efficiency

14 2.0 !MAP number

15 1.0 !Shaft number

16 1.0 !Degradation factor for PR

17 1.0 !Degradation factor for NDMF

18 1.0 !Degradation factor for ETA

19 0.44 !Tip radius

20 0.3 !Hub/Tip ratio

21 0.0 !Error selection

22 0.0 !Volume

!HP COMPRESSOR

23 -1.0 !Z

24 -1.0 !Relative rotational speed PCN

25 10.6 !DP Pressure ratio

26 0.85 !DP Isentropic efficiency

27 0.0 !Error selection(0.0:Error is not required)

28 3.0 !Compressor map number

29 2.0 !Shaft number

30 1.0 !Degradation factor for PR

31 1.0 !Degradation factor for NDMF

32 1.0 !Degradation factor for ETA

33 -1.0 !Volume

34 0.0 !Stator angle relative to DP

!PREMAS (HPT COOLING FLOW)

35 0.83 !Lambda(W)

36 0.0 !Delta(W)

37 1.0 !Lambda(P)

38 0.0 !Delta(P)

!PREMAS (LPT COOLING FLOW)

39 0.871 !Lambda(W)

40 0.0 !Delta(W)

41 1.0 !Lambda(P)

42 0.0 !Delta(P)

!BURNER

43 0.05 !BURNER:Total pressure loss/Inlet total pressure

44 0.99 !Combustion efficiency

45 -1.0 !Fuel flow(=-1.0:the outlet total temperature must be stated)

46 0.0 !(>0) Water flow [kg*s-1 or lb*s-1] or (<0) Water to air ratio

47 288.0 !Temperature of water stream [K]

48 0.0 !Phase of water (0=liquid, 1=vapour)

49 1.0 !Scaling factor of ETAb (combustion efficiency) – Degradation factor

50 -1.0 !Effective component volume [m^3]

!HP TURBINE

51 0.0 !TURBIN:Auxiliary work

52 -1.0 !Relative enthalpy drop to temperature ratio (when “-1.0”, a design default value of 0.8 is invoked)

53 -1.0 !Relative non-dimensional speed (when “-1.0”, a design default value of 0.6 is invoked)

54 -0.87 !Isentropic efficiency

55 -1.0 !Relative rotational speed (-1.0 for compressor turbine)

56 2.0 !Shaft number

57 5.0 !Turbine map number

58 -1.0 !Power law index

59 1.0 !Degradation factor for TF (non-D inlet W)

60 1.0 !Degradation factor for DH (enthalpy change)

61 1.0 !Degradation factor for ETA (isentropic eff)

62 -1.0 !Rotor rotational speed [rps] – only for TR, else -1.0

63 -1.0 !Rotor moment of inertia [kg.m^2]] – only for TR, else -1.0

64 -1.0 !Effective component volume [m^3]] – only for TR, else -1.0

65 -1.0

66 0.0 !NGV angle relative to D.P., always 0.0 at D.P.

!LP TURBINE

67 0.0 !TURBIN:Auxiliary work

68 -1.0 !Relative enthalpy drop to temperature ratio (when "-1.0", a design default value of 0.8 is invoked)

69 -1.0 !Relative non-dimensional speed (when "-1.0", a design default value of 0.6 is invoked)

70 0.88 !Isentropic efficiency

71 -1.0 !Relative rotational speed (-1.0 for compressor turbine)

72 1.0 !Shaft number

73 4.0 !Turbine map number

74 -1.0 !Power law index

75 1.0 !Degradation factor for TF (non-D inlet W)

76 1.0 !Degradation factor for DH (enthalpy change)

77 1.0 !Degradation factor for ETA (isentropic eff)

78 -1.0 !Rotor rotational speed [rps] – only for TR, else -1.0

79 -1.0 !Rotor moment of inertia [kg.m^2]] – only for TR, else -1.0

80 -1.0 !Effective component volume [m^3]] – only for TR, else -1.0

81 -1.0

82 0.0 !NGV angle relative to D.P., always 0.0 at D.P.

!PREMAS (AB COOLING FLOW)

83 0.9 !Lambda(W)

84 0.0 !Delta(W)

85 1.0 !Lambda(P)

86 0.0 !Delta(P)

!DUCTER

87 0.0 !DUCTER:Switch set (=0.0:no reheating)

88 0.01 !Total pressure loss/Inlet total pressure

89 0.99 !Combustion efficiency

90 100000.0 !Limiting value of fuel flow

91 -1.0 !Effective component volume [m^3]

!MIXFUL

92 1.0 !MIXFUL:Number of compressor providing stream number 2

93 1.0 !Switch set (=1.0:Mach number)

94 0.45 !Mach number of stream number 1

!DUCTER

95 0.0 !DUCTER:Switch set (=0.0:no reheating)

96 0.01 !Total pressure loss/Inlet total pressure

97 0.99 !Combustion efficiency

98 100000.0 !Limiting value of fuel flow(=100000.0:not needed)

99 -1.0 !Effective component volume [m^3]

!NOZDIV

100 -1.0 !NOZDIV:Switch set (=-1.0:throat and exit areas FIXED)

101 -1.0 !Throat area

102 1.0 !Scaling factor

!PERF

103 -1.0 !Power output for power turbine (or -1.0 for turbofan)

104 -1.0 !Propeller efficiency (or -1.0 for turbofan)

105 0.0 !Scaling Index (“1.” = Scaling needed, “0.” = no scaling)

106 0.0 !Required thrust

-1

1 2 114.1

7 6 1750.0

-1

-3

APPENDIX C

TURBOMATCH INPUT FILE FOR DISTORTED ENGINE'S PERFORMANCE

Engine: F100-PW-229

Off Design-Dry (without AB)

PCN Handle

////

OD SI KE VA FP

-1

-1

INTAKE S1,2 D1-6 R300

FANBRI S2,3,21 D7-22 R301 V7 V8

COMPRE S3,4 D23-34 R302 V23 V24

PREMAS S4,5,19 D35-38

PREMAS S5,6,20 D39-42

BURNER S6,7 D43-50 R303 W7,6

MIXEES S7,19,8

TURBIN S8,9 D51-66 V52

MIXEES S9,20,10

TURBIN S10,11 D67-82 V68

PREMAS S11,12,16 D83-86

DUCTER S21,13 D87-91 R304

MIXFUL S13,12,14 D92-94

DUCTER S14,15 D95-99 R305

MIXEES S15,16,17

NOZDIV S17,18,1 D100-102 R306

PERFOR S1,0,0 D103-106,306,300,303,0,0,304,0,0,305

CODEND

DATA ITEMS////

!INTAKE

1 0.0 !Altitude [m]

2 0.0 !Dev from ISA temperature [K]

3 0.0 !Flight Mach number

4 0.99 !Pressure recovery

5 0.0 !Dev from ISA pressure [Atm]

6 0.0 !Relative humidity [%]

!FAN

7 0.36 !BPR

8 -1.0 !Z

9 -1.0 !Relative rotational speed PCN

10 3.2 !DP BP Pressure ratio

11 0.82 !DP BP Isentropic efficiency

12 3.1 !DP CORE Pressure ratio

13 0.8 !DP CORE Isentropic efficiency

14 2.0 !MAP number

15 1.0 !Shaft number

16 1.0 !Degradation factor for PR

17 1.0 !Degradation factor for NDMF

18 1.0 !Degradation factor for ETA

19 0.44 !Tip radius

20 0.3 !Hub/Tip ratio

21 0.0 !Error selection

22 0.0 !Volume

!HP COMPRESSOR

23 -1.0 !Z

24 -1.0 !Relative rotational speed PCN

25 10.6 !DP Pressure ratio

26 0.85 !DP Isentropic efficiency

27 0.0 !Error selection(0.0:Error is not required)

28 3.0 !Compressor map number

29 2.0 !Shaft number

30 1.0 !Degradation factor for PR

31 1.0 !Degradation factor for NDMF

32 1.0 !Degradation factor for ETA

33 -1.0 !Volume

34 0.0 !Stator angle relative to DP

!PREMAS (HPT COOLING FLOW)

35 0.83 !Lambda(W)

36 0.0 !Delta(W)

37 1.0 !Lambda(P)

38 0.0 !Delta(P)

!PREMAS (LPT COOLING FLOW)

39 0.871 !Lambda(W)

40 0.0 !Delta(W)

41 1.0 !Lambda(P)

42 0.0 !Delta(P)

!BURNER

43 0.05 !BURNER:Total pressure loss/Inlet total pressure

44 0.99 !Combustion efficiency

45 -1.0 !Fuel flow(=-1.0:the outlet total temperature must be stated)

46 0.0 !(>0) Water flow [kg*s-1 or lb*s-1] or (<0) Water to air ratio

47 288.0 !Temperature of water stream [K]

48 0.0 !Phase of water (0=liquid, 1=vapour)

49 1.0 !Scaling factor of ETAb (combustion efficiency) – Degradation factor

50 -1.0 !Effective component volume [m^3]

!HP TURBINE

51 0.0 !TURBIN:Auxiliary work

52 -1.0 !Relative enthalpy drop to temperature ratio (when “-1.0”, a design default value of 0.8 is invoked)

53 -1.0 !Relative non-dimensional speed (when “-1.0”, a design default value of 0.6 is invoked)

54 -0.87 !Isentropic efficiency

55 -1.0 !Relative rotational speed (-1.0 for compressor turbine)

56 2.0 !Shaft number

57 5.0 !Turbine map number

58 -1.0 !Power law index

59 1.0 !Degradation factor for TF (non-D inlet W)

60 1.0 !Degradation factor for DH (enthalpy change)

61 1.0 !Degradation factor for ETA (isentropic eff)

62 -1.0 !Rotor rotational speed [rps] – only for TR, else -1.0

63 -1.0 !Rotor moment of inertia [kg.m^2]] – only for TR, else -1.0

64 -1.0 !Effective component volume [m^3]] – only for TR, else -1.0

65 -1.0

66 0.0 !NGV angle relative to D.P., always 0.0 at D.P.

!LP TURBINE

67 0.0 !TURBIN:Auxiliary work

68 -1.0 !Relative enthalpy drop to temperature ratio (when “-1.0”, a design default value of 0.8 is invoked)

69 -1.0 !Relative non-dimensional speed (when “-1.0”, a design default value of 0.6 is invoked)

70 0.88 !Isentropic efficiency

71 -1.0 !Relative rotational speed (-1.0 for compressor turbine)

72 1.0 !Shaft number

73 4.0 !Turbine map number

74 -1.0 !Power law index

75 1.0 !Degradation factor for TF (non-D inlet W)

76 1.0 !Degradation factor for DH (enthalpy change)

77 1.0 !Degradation factor for ETA (isentropic eff)

78 -1.0 !Rotor rotational speed [rps] – only for TR, else -1.0

79 -1.0 !Rotor moment of inertia [kg.m^2]] – only for TR, else -1.0

80 -1.0 !Effective component volume [m^3]] – only for TR, else -1.0

81 -1.0

82 0.0 !NGV angle relative to D.P., always 0.0 at D.P.

!PREMAS (AB COOLING FLOW)

83 0.9 !Lambda(W)

84 0.0 !Delta(W)

85 1.0 !Lambda(P)

86 0.0 !Delta(P)

!DUCTER

87 0.0 !DUCTER:Switch set (=0.0:no reheating)

88 0.01 !Total pressure loss/Inlet total pressure

89 0.99 !Combustion efficiency

90 100000.0 !Limiting value of fuel flow

91 -1.0 !Effective component volume [m^3]

!MIXFUL

92 1.0 !MIXFUL:Number of compressor providing stream number 2

93 1.0 !Switch set (=1.0:Mach number)

94 0.45 !Mach number of stream number 1

!DUCTER

95 0.0 !DUCTER:Switch set (=0.0:no reheating)

96 0.01 !Total pressure loss/Inlet total pressure

97 0.99 !Combustion efficiency

98 100000.0 !Limiting value of fuel flow(=100000.0:not needed)

99 -1.0 !Effective component volume [m^3]

!NOZDIV

100 -1.0 !NOZDIV:Switch set (=-1.0:throat and exit areas FIXED)

101 -1.0 !Throat area

102 1.0 !Scaling factor

!PERF

103 -1.0 !Power output for power turbine (or -1.0 for turbofan)

104 -1.0 !Propeller efficiency (or -1.0 for turbofan)

105 0.0 !Scaling Index (“1.” = Scaling needed, “0.” = no scaling)

106 0.0 !Required thrust

-1

1 2 114.1

7 6 1750.0

-1

1 6096.0 !0.35M 0_0

3 0.35

4 0.973

9 0.9399

17 0.9967

-1

-1

1 6096.0 !0.35M 0_8

3 0.35

4 0.97

9 0.9399

17 0.9887

-1

-1

1 6096.0 !0.35M 0_16

3 0.35

4 0.959

9 0.9399

17 0.9667

-1

-1

1 6096.0 !0.35M 8_8

3 0.35

4 0.968

9 0.9399

17 0.9879

-1

-1

1 6096.0 !0.35M 8_16

3 0.35

4 0.959

9 0.9399

17 0.9694

-1

-1

1 6096.0 !0.35M 16_8

3 0.35

4 0.965

9 0.9399

17 0.9808

-1

-1

1 6096.0 !0.35M 8_0

3 0.35

4 0.971

9 0.9399

17 0.9936

-1

-1

1 6096.0 !0.35M 16_0

3 0.35

4 0.968

9 0.9399

17 0.9840

-1

-1

1 6096.0 !0.35M 16_16

3 0.35

4 0.958

9 0.9399

17 0.9657

-1

-1

1 6096.0 !0.6M 0_0

3 0.6

4 0.977

9 0.9613

17 0.99164

-1

-1

1 6096.0 !0.6M 0_8

3 0.6

4 0.972

9 0.9613

17 0.98133

-1

-1

1 6096.0 !0.6M 0_16

3 0.6

4 0.953

9 0.9613

17 0.9385

-1

-1

1 6096.0 !0.6M 8_8

3 0.6

4 0.975

9 0.9613

17 0.9899

-1

-1

1 6096.0 !0.6M 8_16

3 0.6

4 0.962

9 0.9613

17 0.9605

-1

-1

1 6096.0 !0.6M 16_8

3 0.6

4 0.973

9 0.9613

17 0.9838

-1

-1

1 6096.0 !0.6M 8_0

3 0.6

4 0.979

9 0.9613

17 0.9947

-1

-1

1 6096.0 !0.6M 16_0

3 0.6

4 0.975

9 0.9613

17 0.9890

-1

-1

1 6096.0 !0.6M 16_16

3 0.6

4 0.961

9 0.9613

17 0.9594

-1

-1

1 6096.0 !0.85M 0_0

3 0.85

4 0.974

9 0.9931

17 0.99403

-1

-1

1 6096.0 !0.85M 0_8

3 0.85

4 0.968

9 0.9931

17 0.9816

-1

-1

1 6096.0 !0.85M 0_16

3 0.85

4 0.945

9 0.9931

17 0.92865

-1

-1

1 6096.0 !0.85M 8_8

3 0.85

4 0.975

9 0.9931

17 0.9936

-1

-1

1 6096.0 !0.85M 8_16

3 0.85

4 0.96

9 0.9931

17 0.9644

-1

-1

1 6096.0 !0.85M 16_8

3 0.85

4 0.975

9 0.9931

17 0.9953

-1

-1

1 6096.0 !0.85M 8_0

3 0.85

4 0.978

9 0.9931

17 0.9991

-1

-1

1 6096.0 !0.85M 16_0

3 0.85

4 0.977

9 0.9931

17 0.9993

-1

-1

1 6096.0 !0.85M 16_16

3 0.85

4 0.962

9 0.9931

17 0.9703

-1

-1

-3

APPENDIX D

DISTORTION DESCRIPTOR GRAPHICAL RESULTS

All distortion descriptor elements for each tested flight attitude are summarized herein and illustrated on a ring by ring basis using a bar graph display, where circumferential extent, circumferential intensity and radial intensity are displayed respectively.

- **0.35M 0˚ AOA 0˚ AOSS**

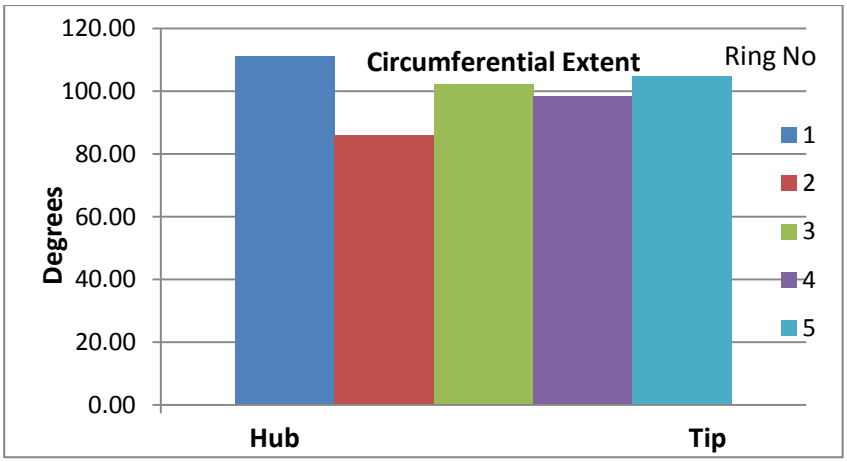

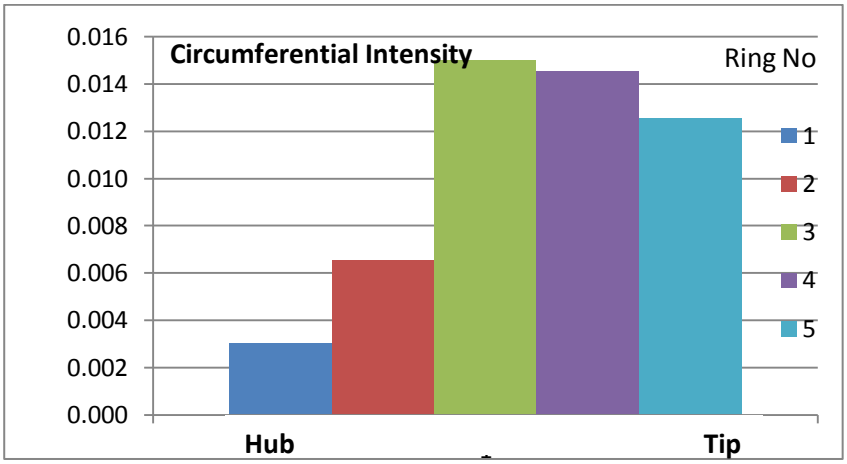

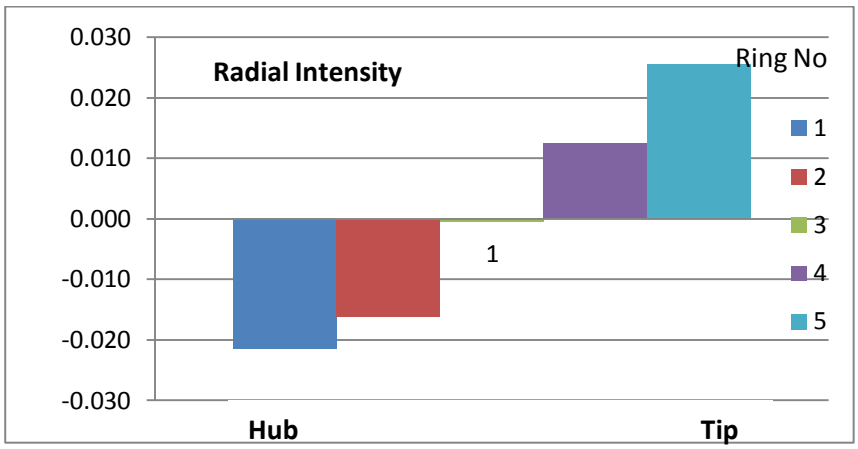

- **0.35M 0˚ AOA 8˚ AOSS**

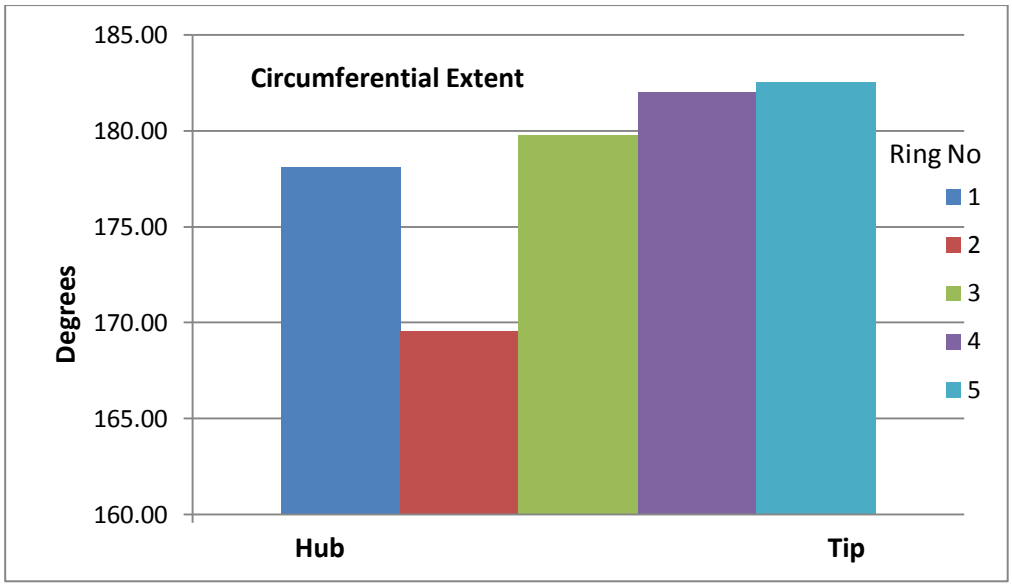

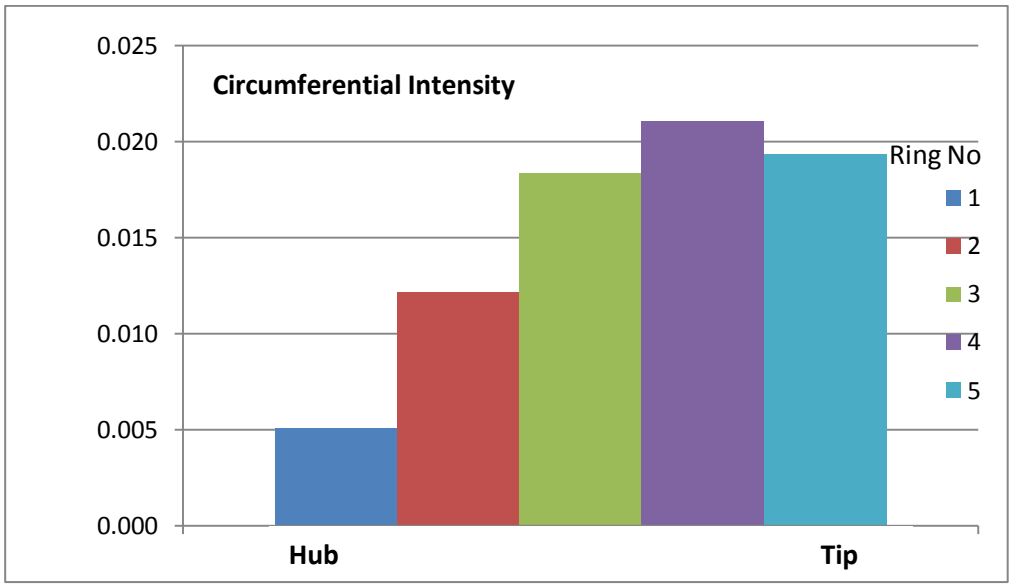

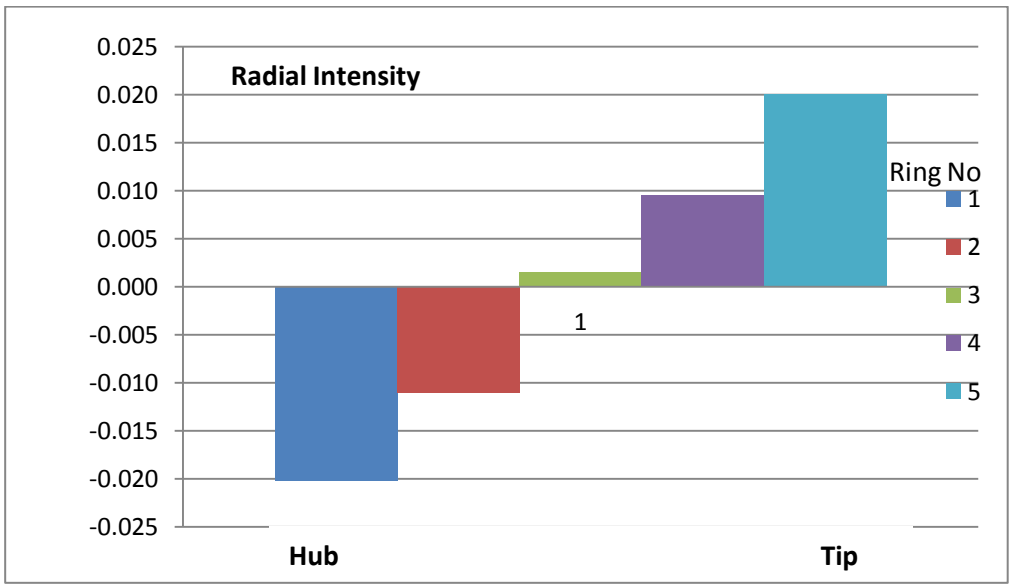

- **0.35M 0˚ AOA 16˚ AOSS**

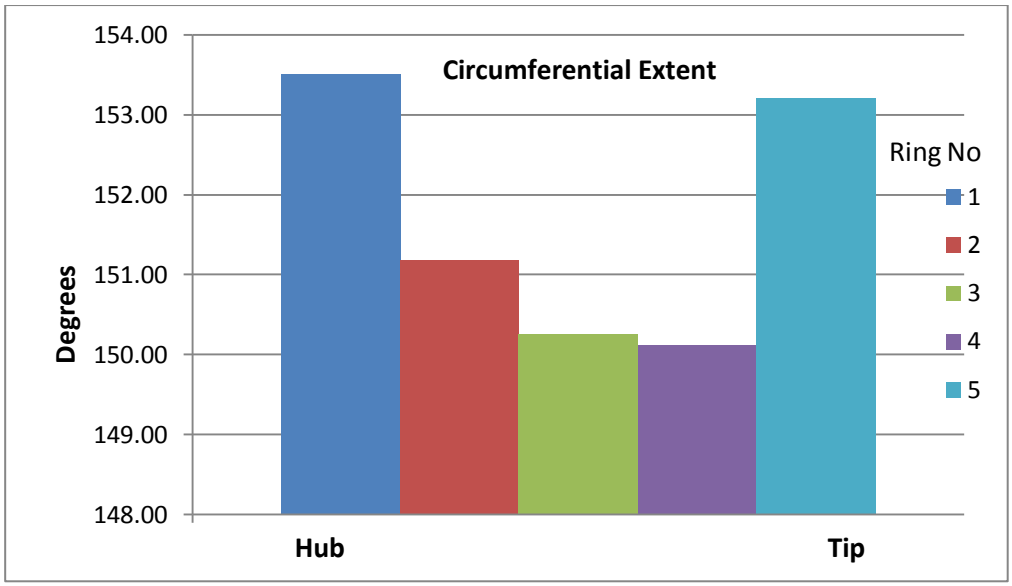

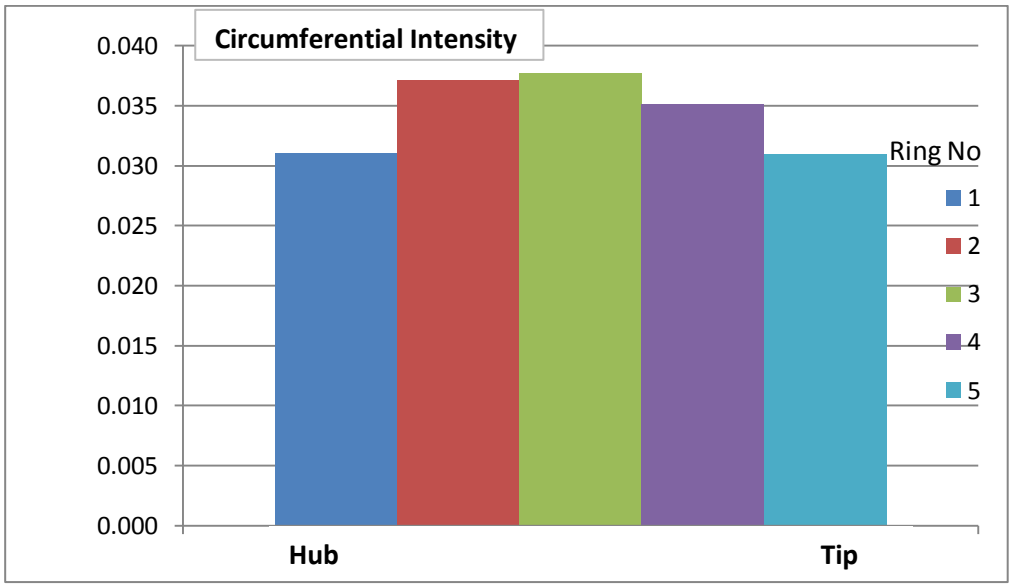

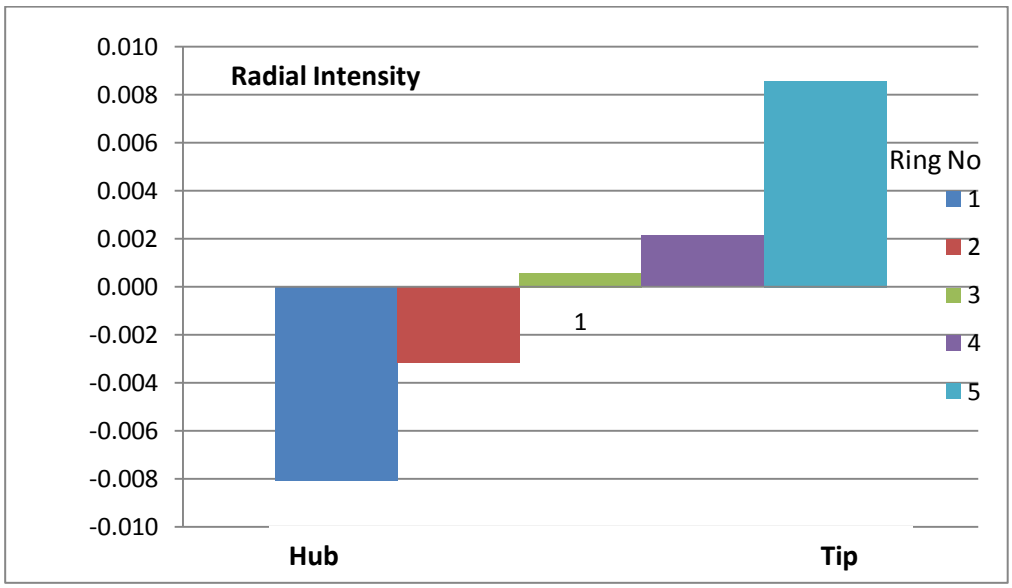

- **0.35M 8˚ AOA 0˚ AOSS**

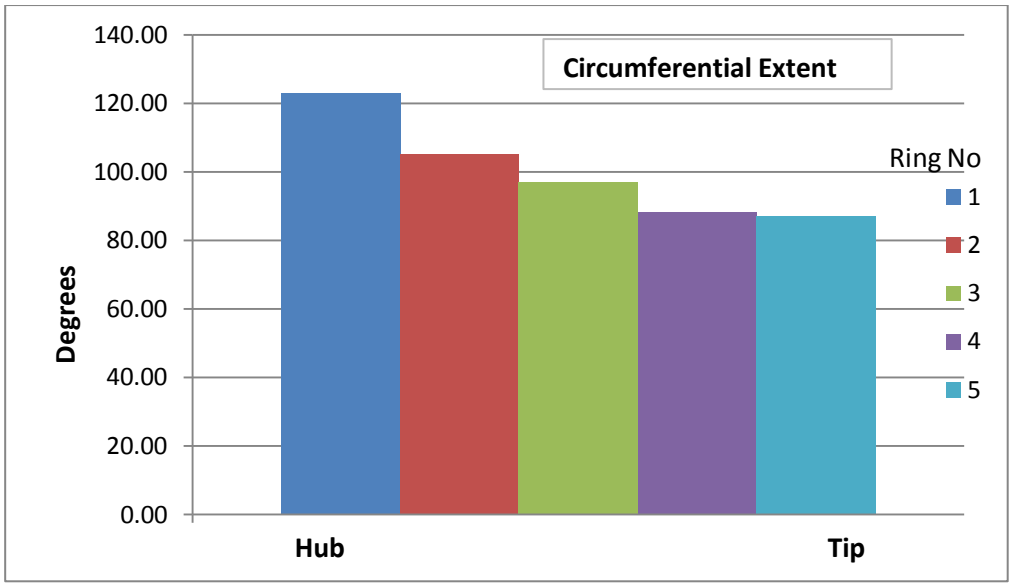

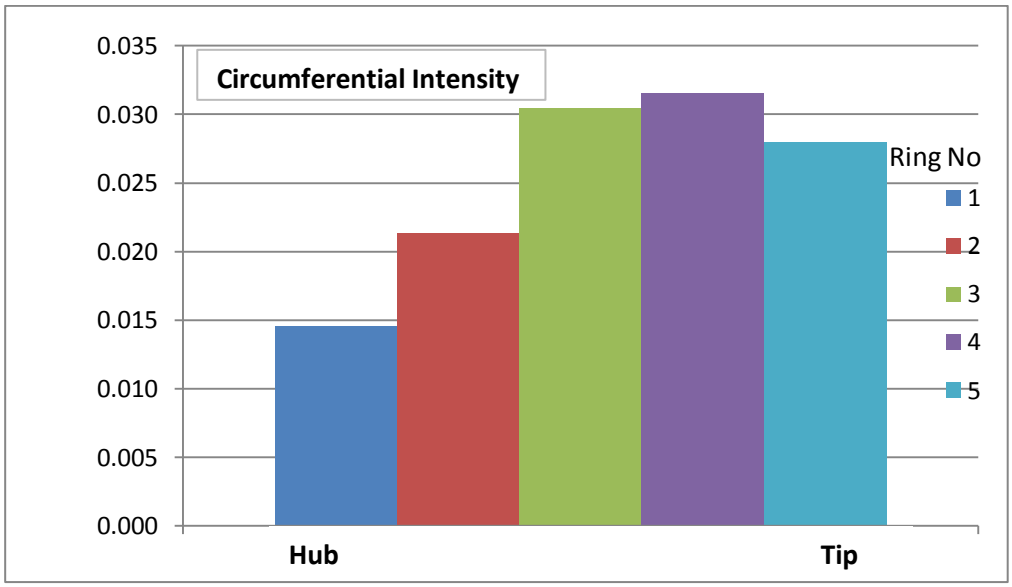

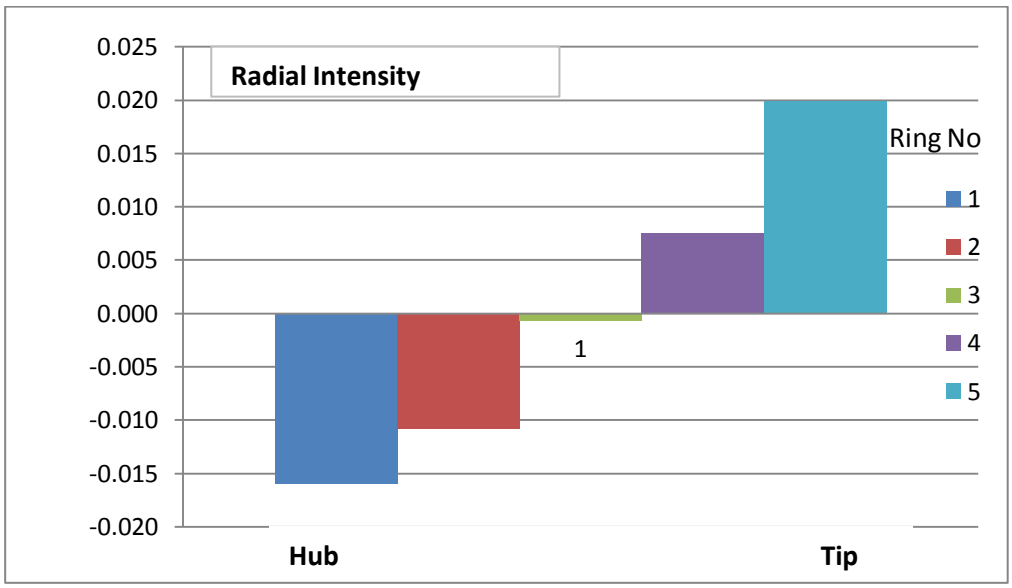

- **0.35M 8˚ AOA 8˚ AOSS**

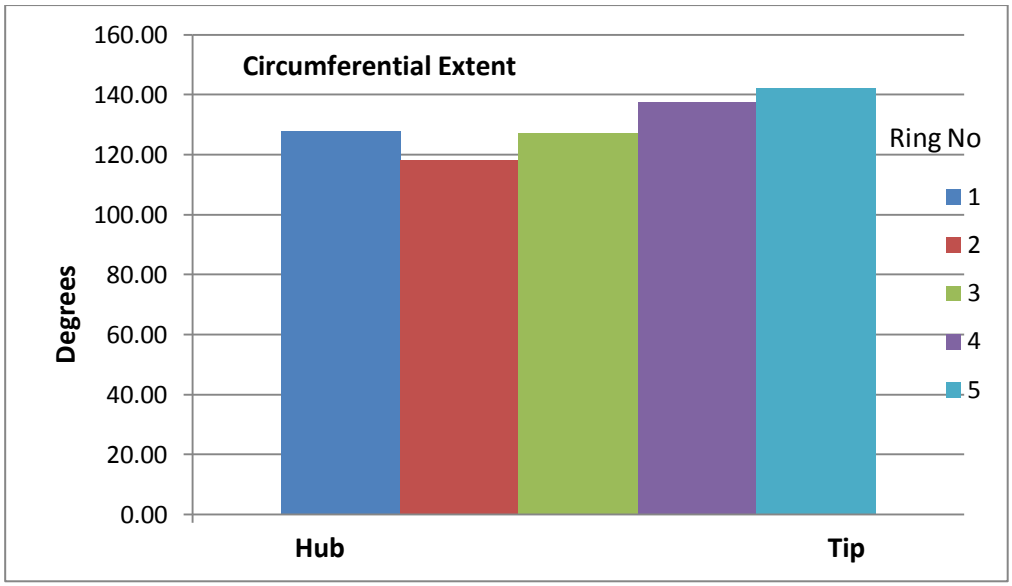

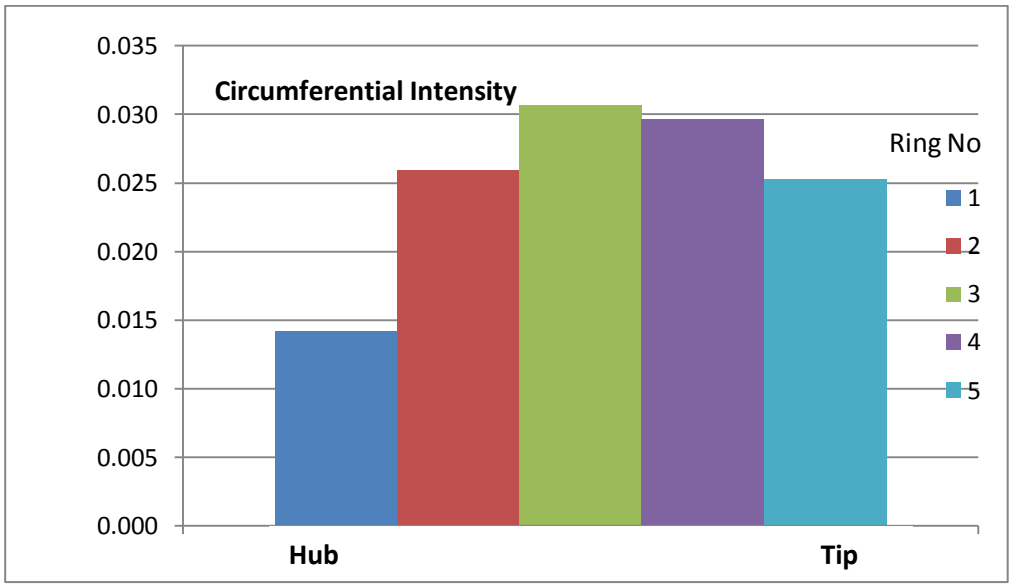

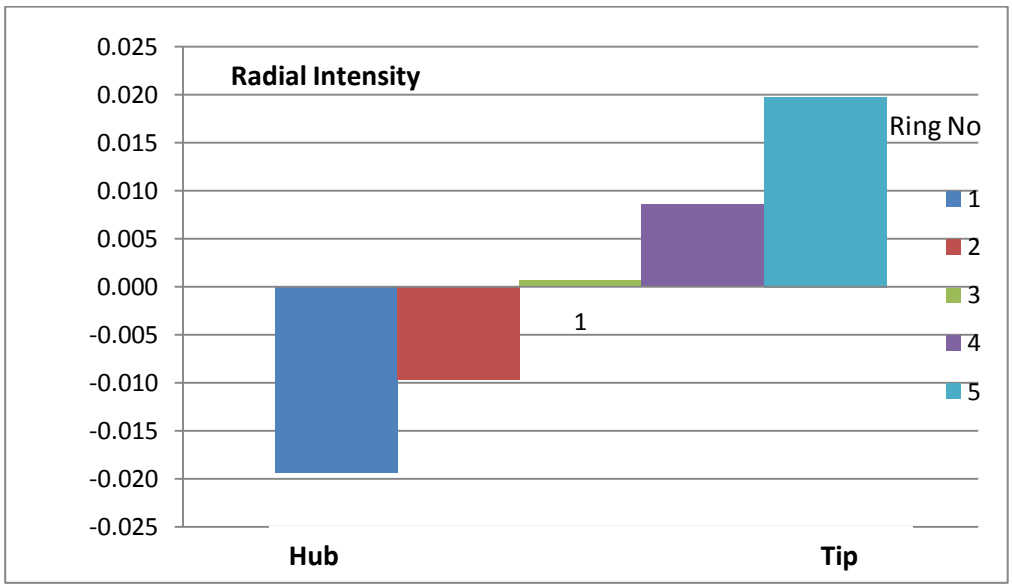

- **0.35M 16˚ AOA 0˚ AOSS**

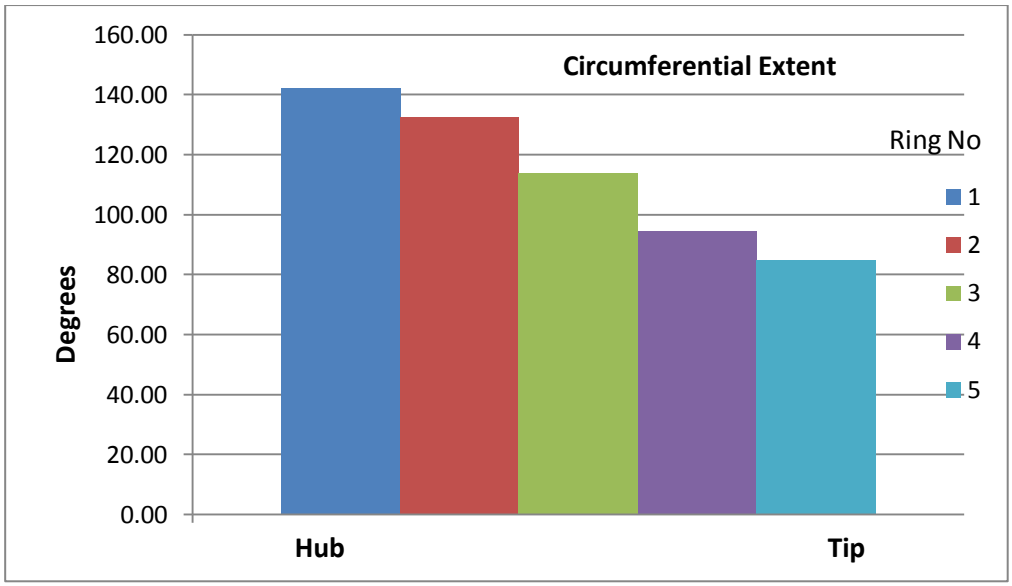

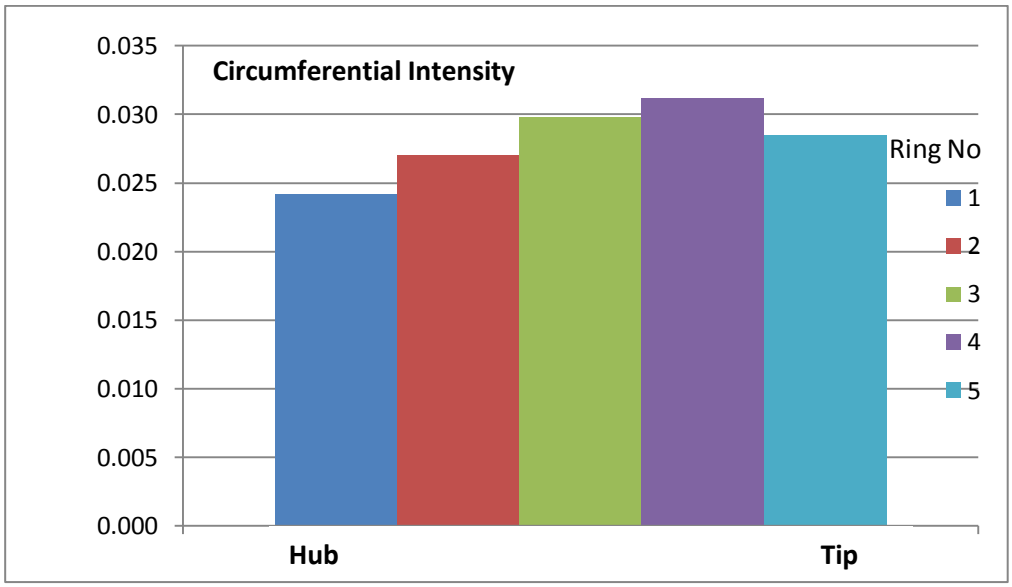

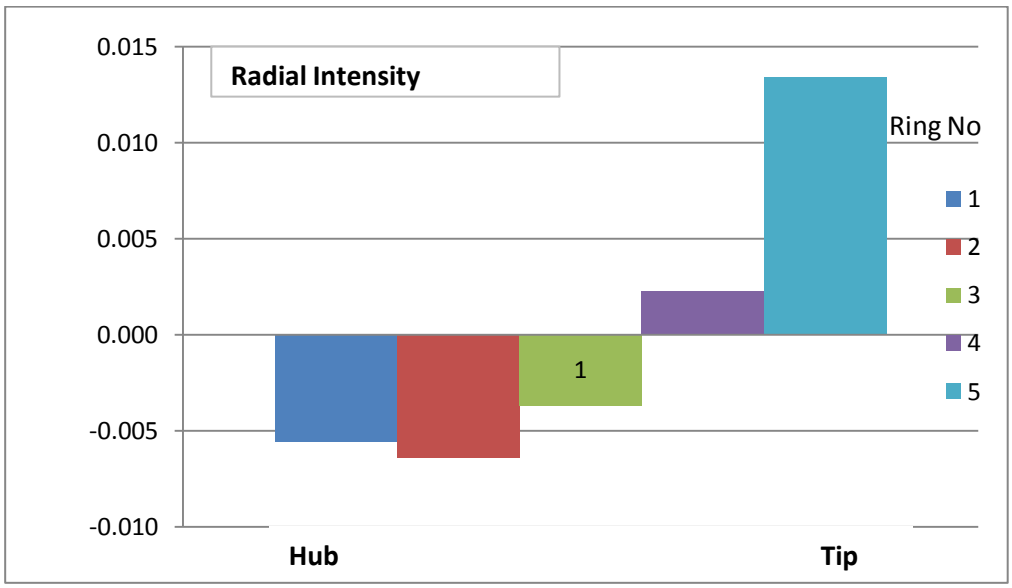

- **0.35M 16˚ AOA 8˚ AOSS**

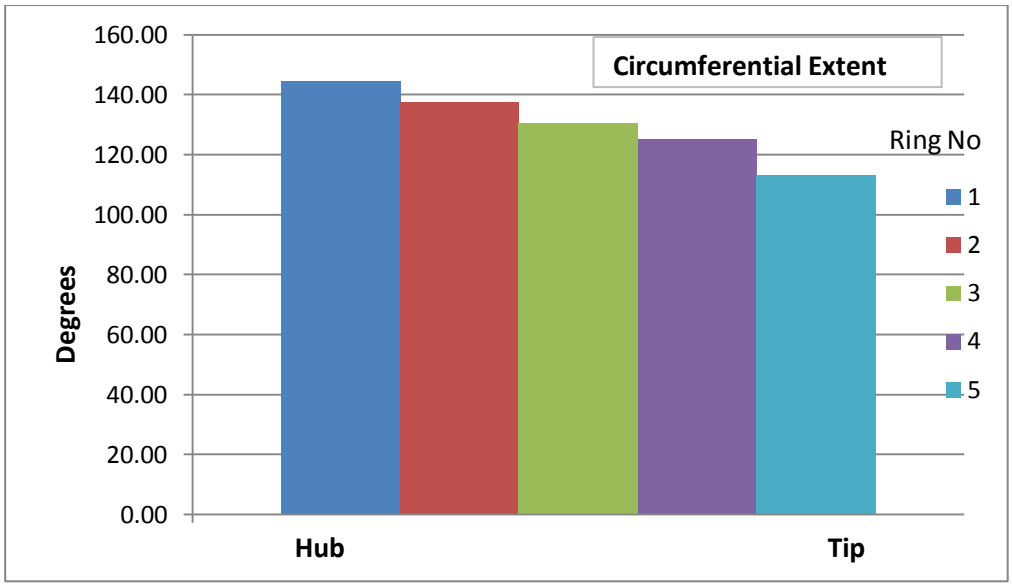

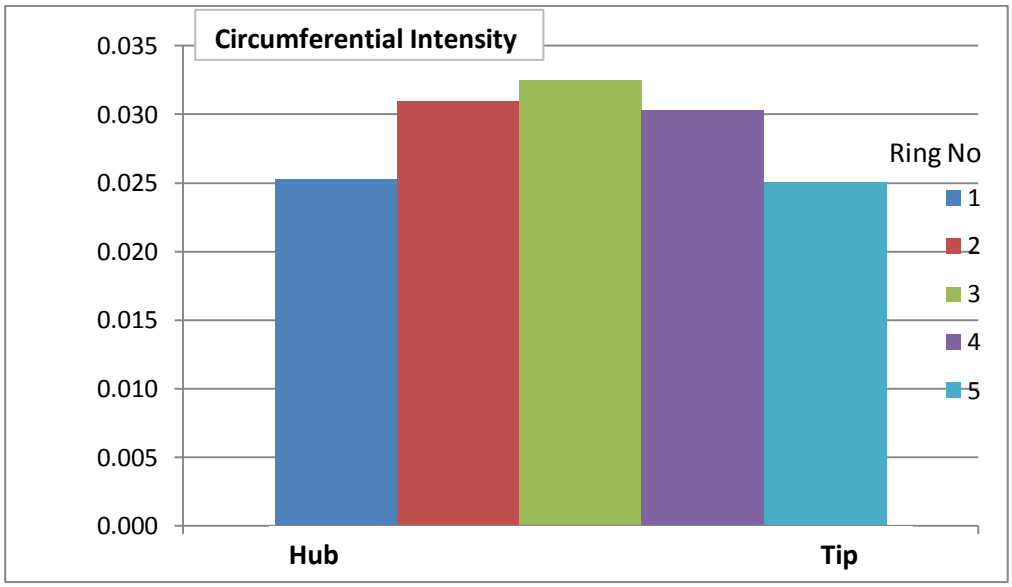

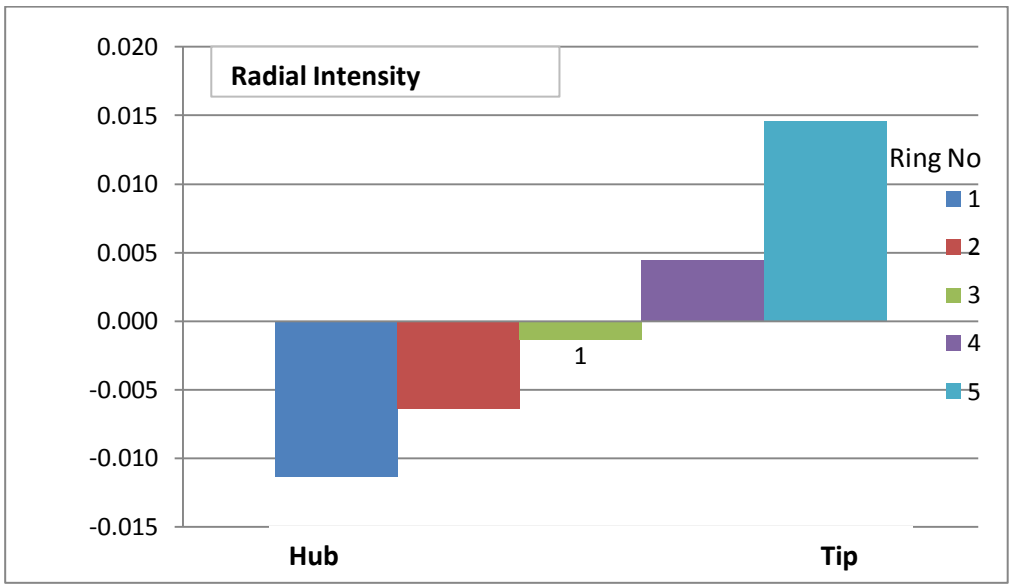

- **0.35M 8˚ AOA 16˚ AOSS**

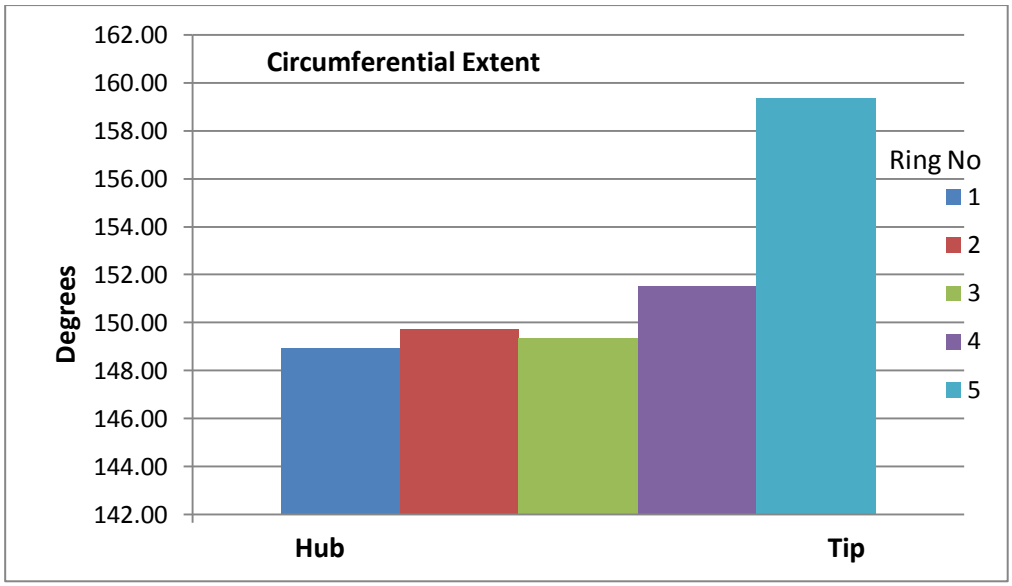

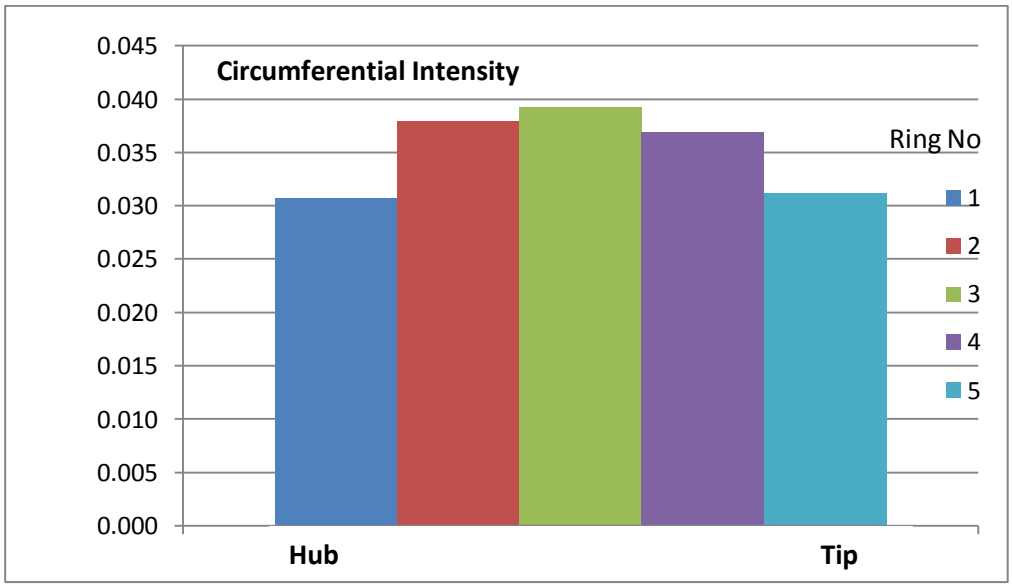

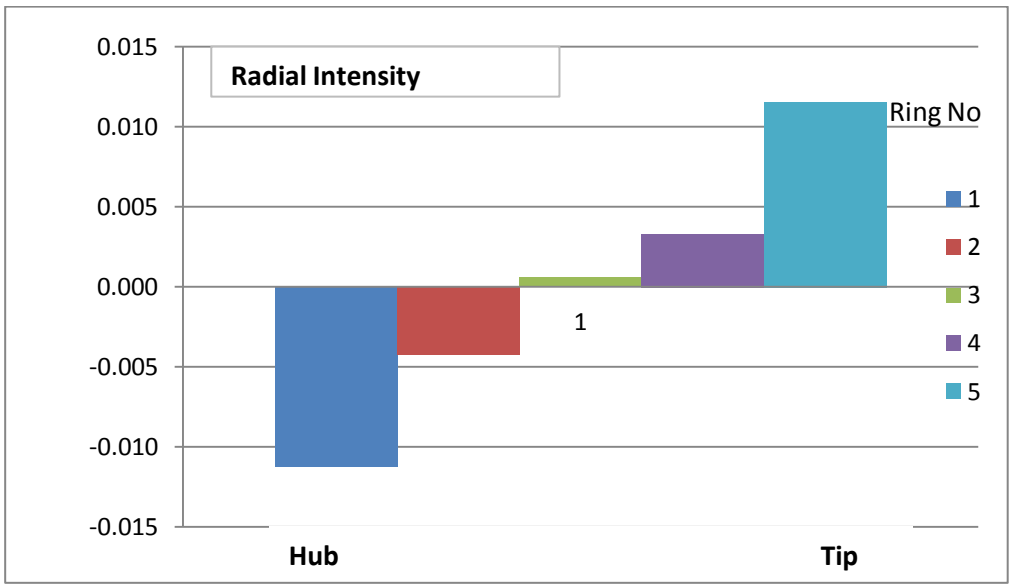

- **0.35M 16˚ AOA 16˚ AOSS**

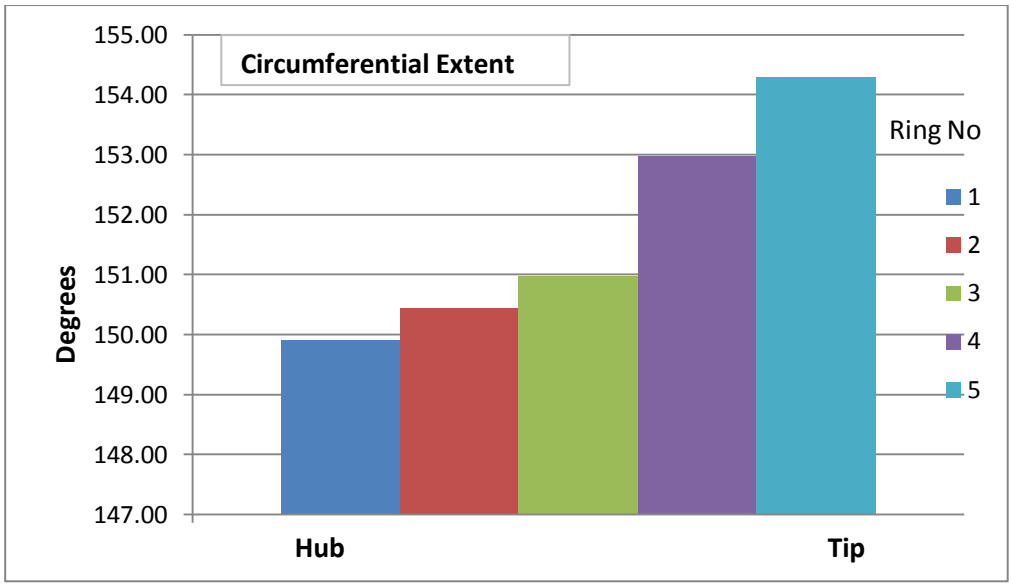

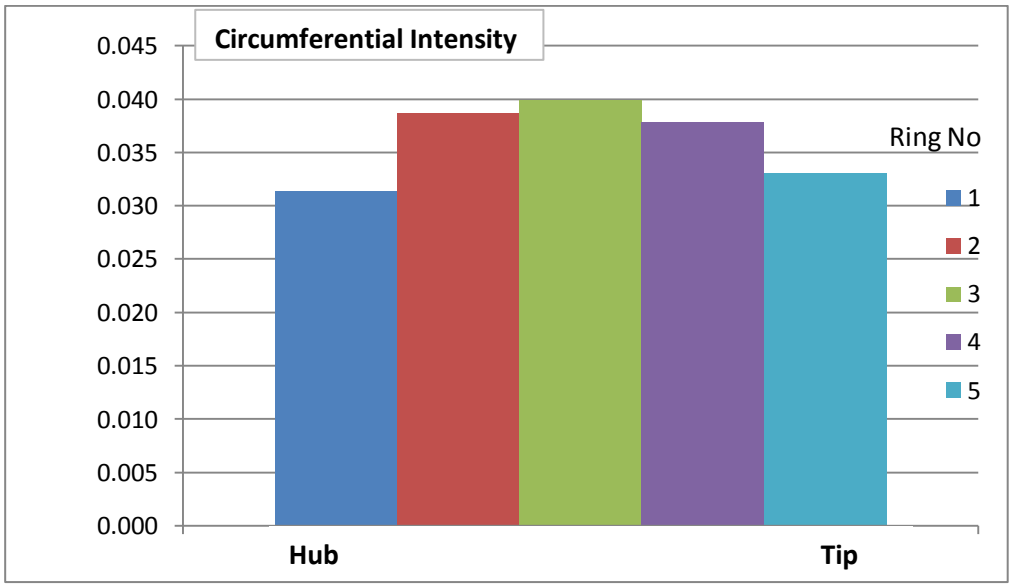

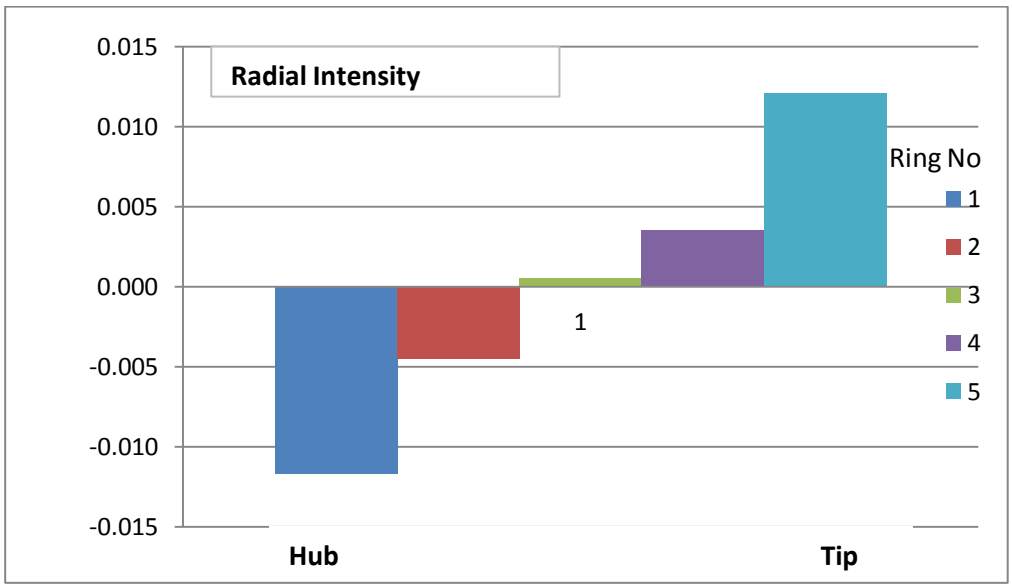

- **0.6M 0˚ AOA 0˚ AOSS**

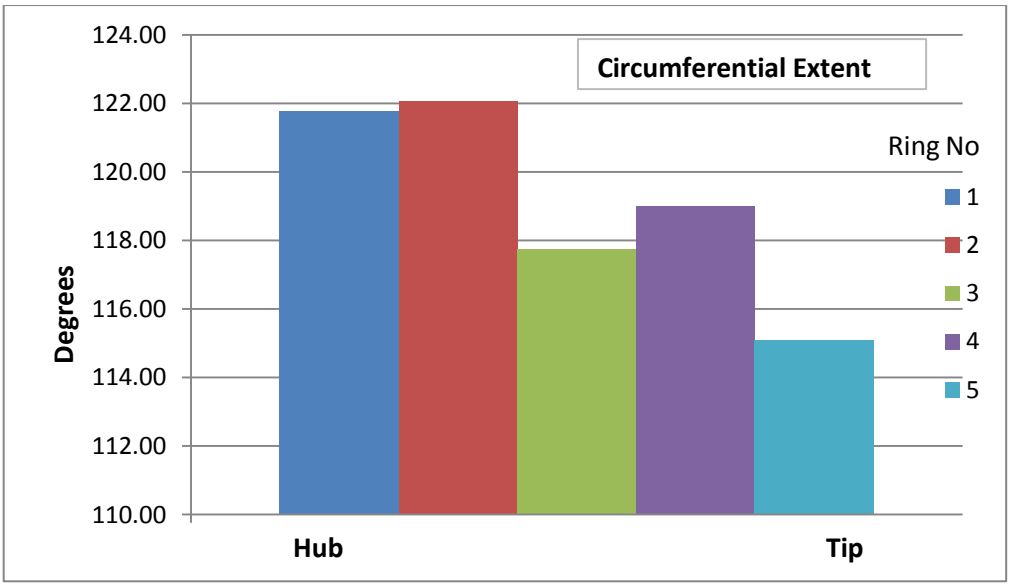

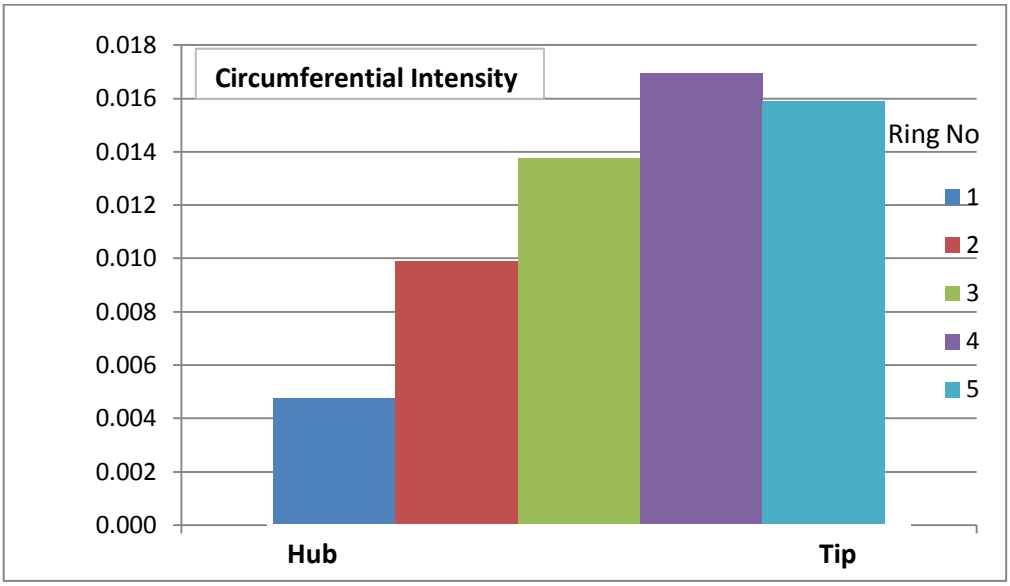

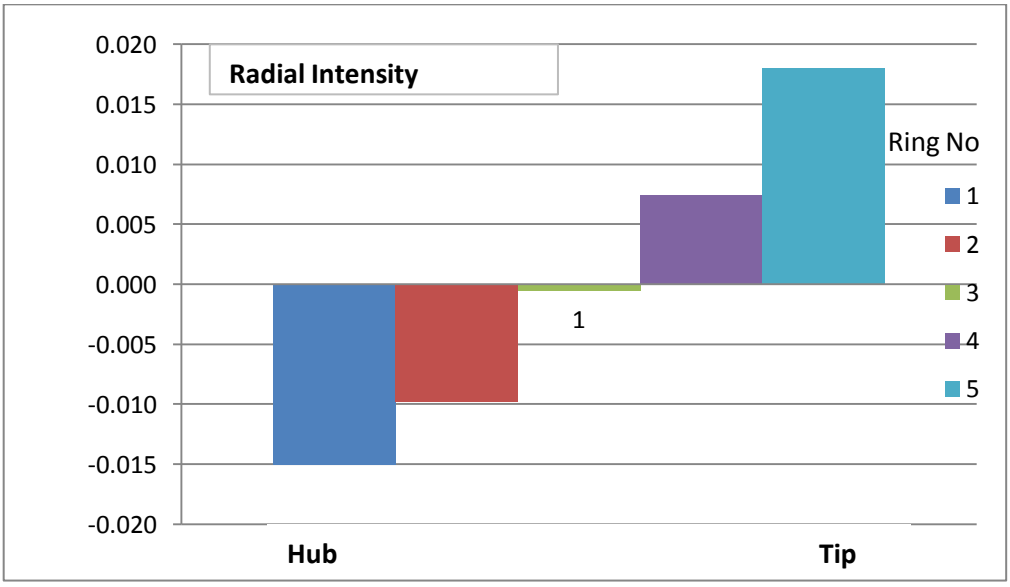

- **0.6M 0˚ AOA 8˚ AOSS**

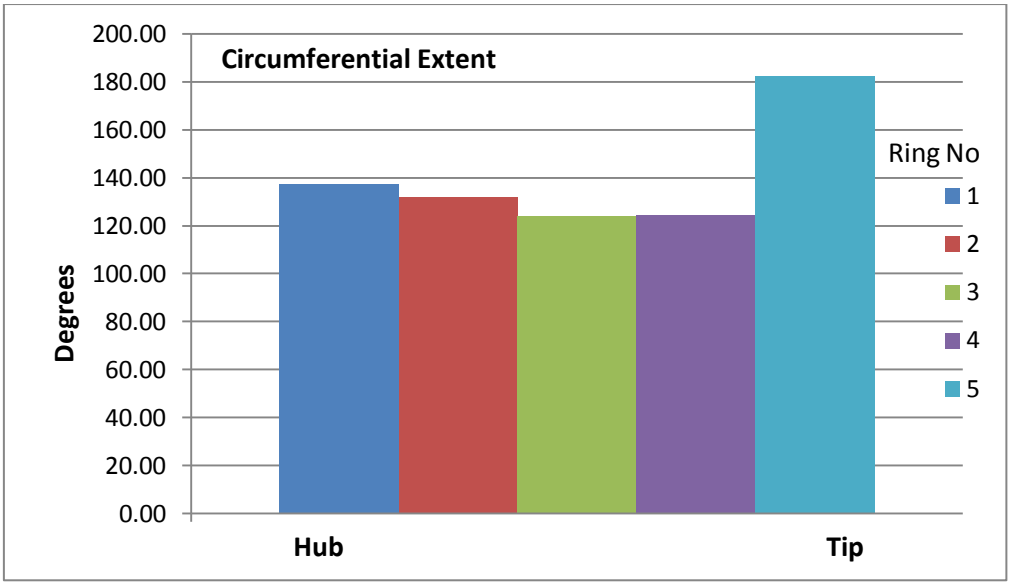

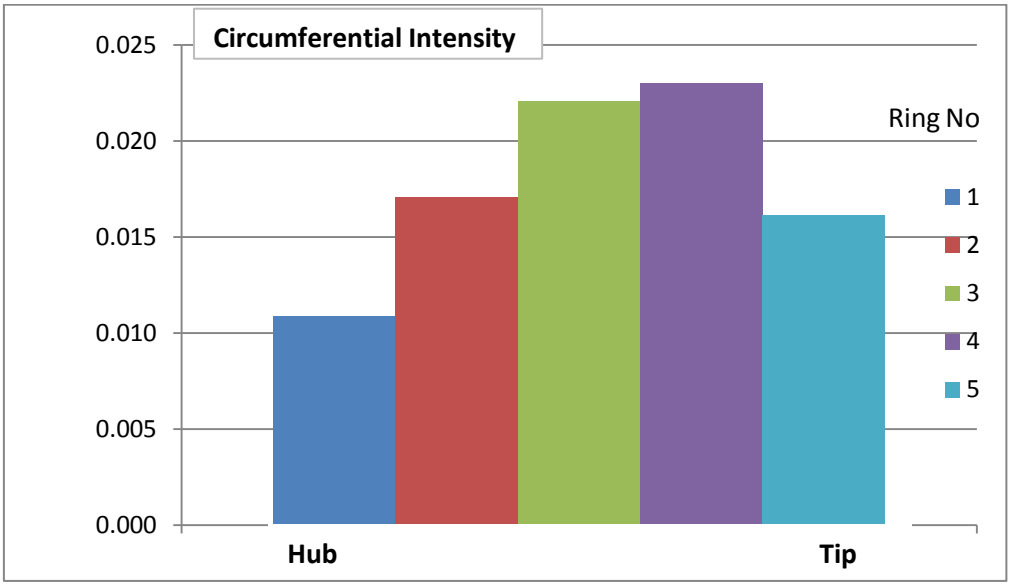

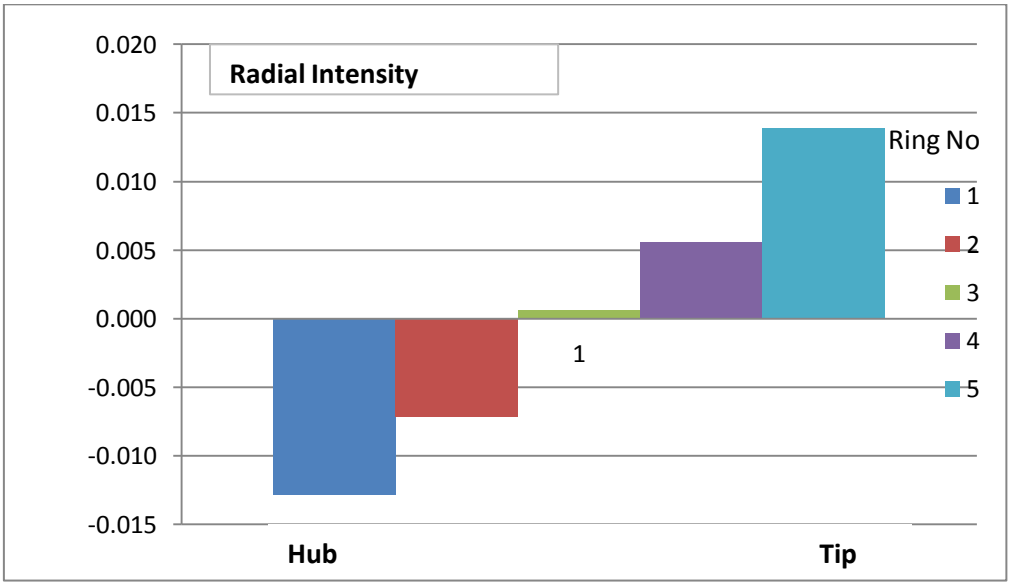

- **0.6M 0˚ AOA 16˚ AOSS**

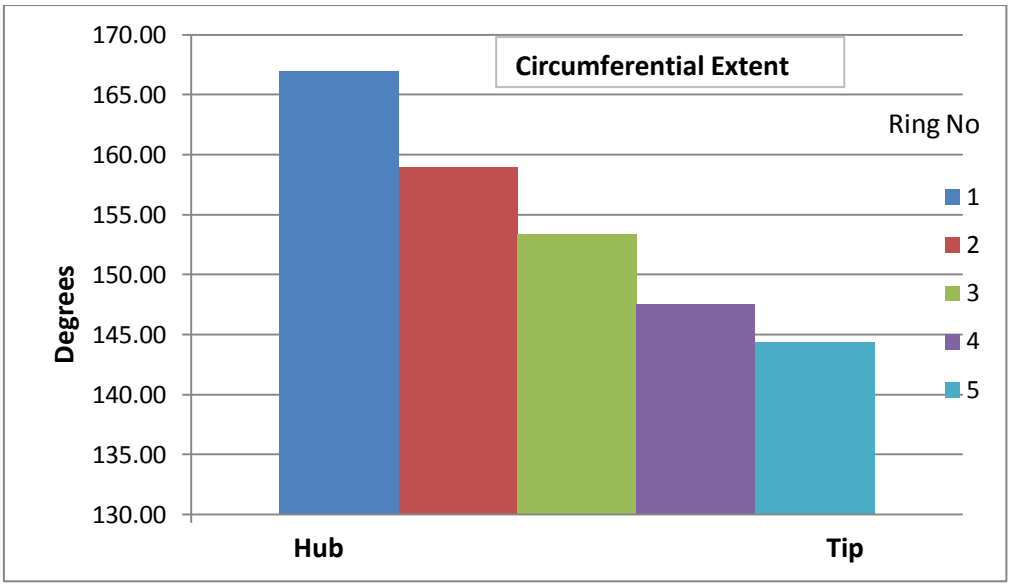

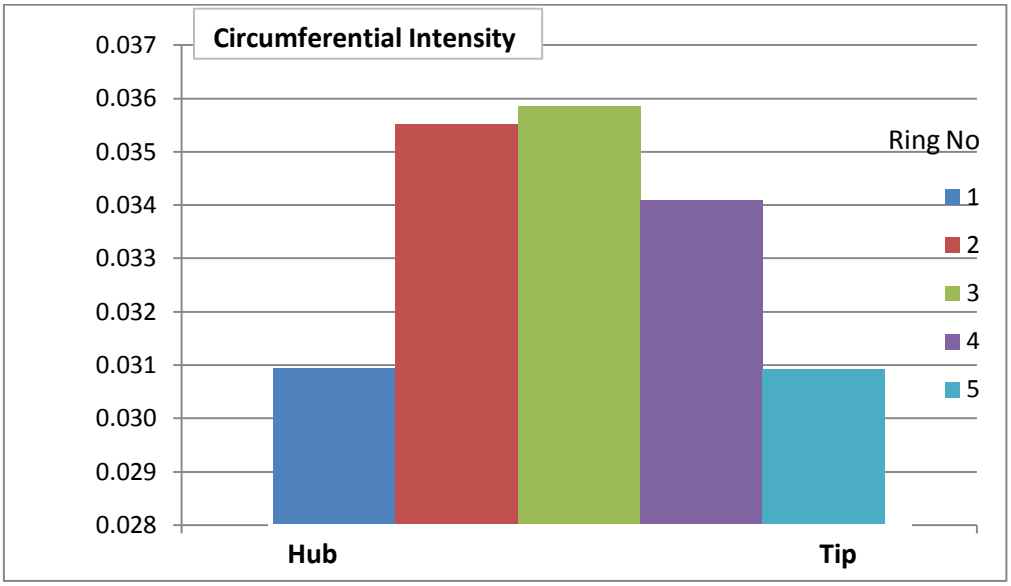

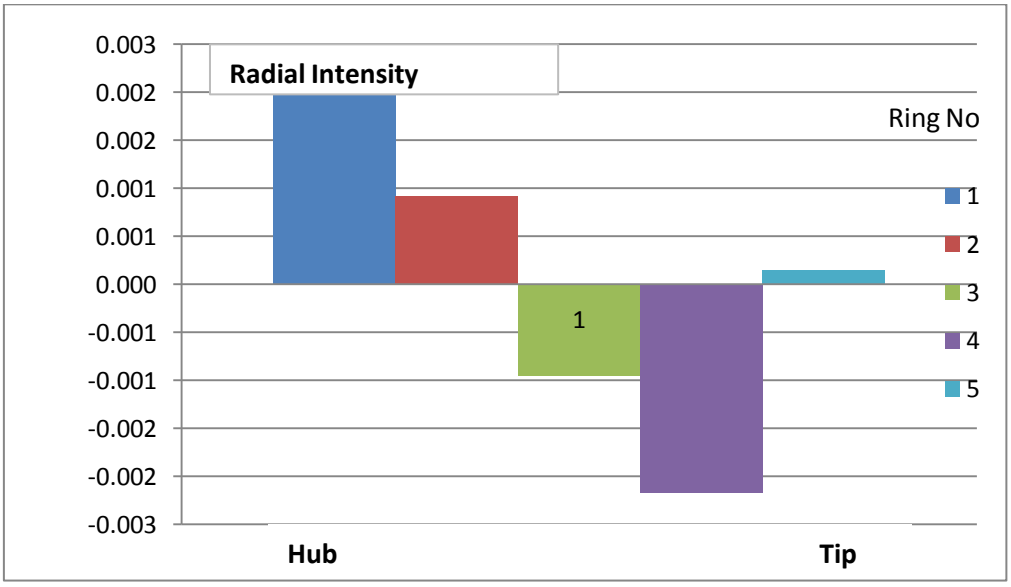

- **0.6M 8˚ AOA 0˚ AOSS**

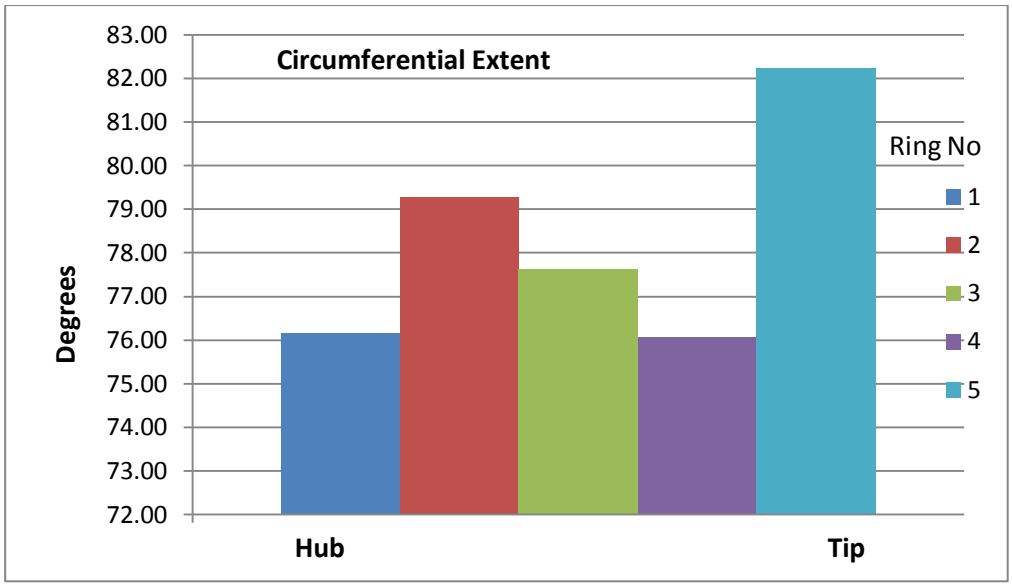

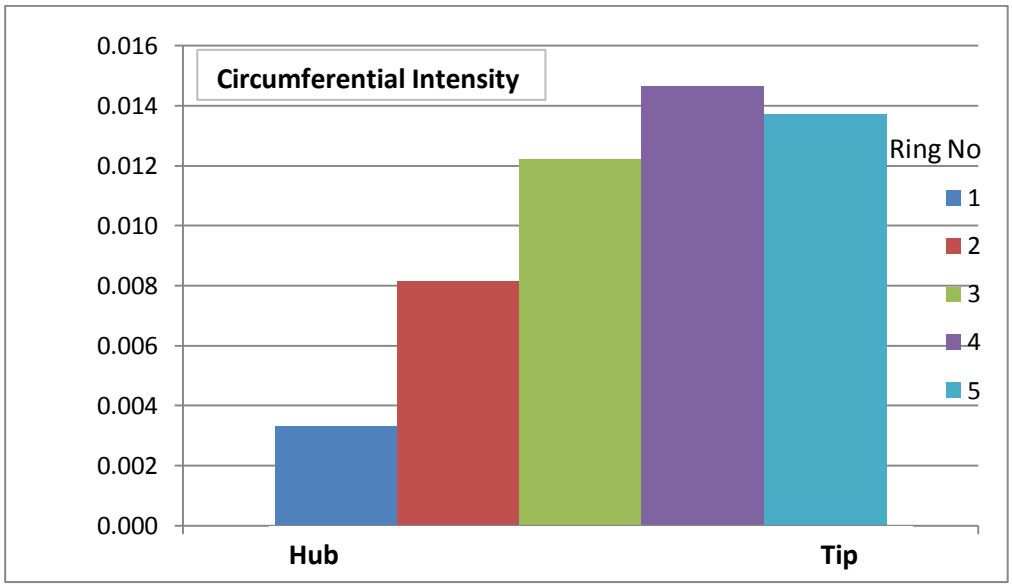

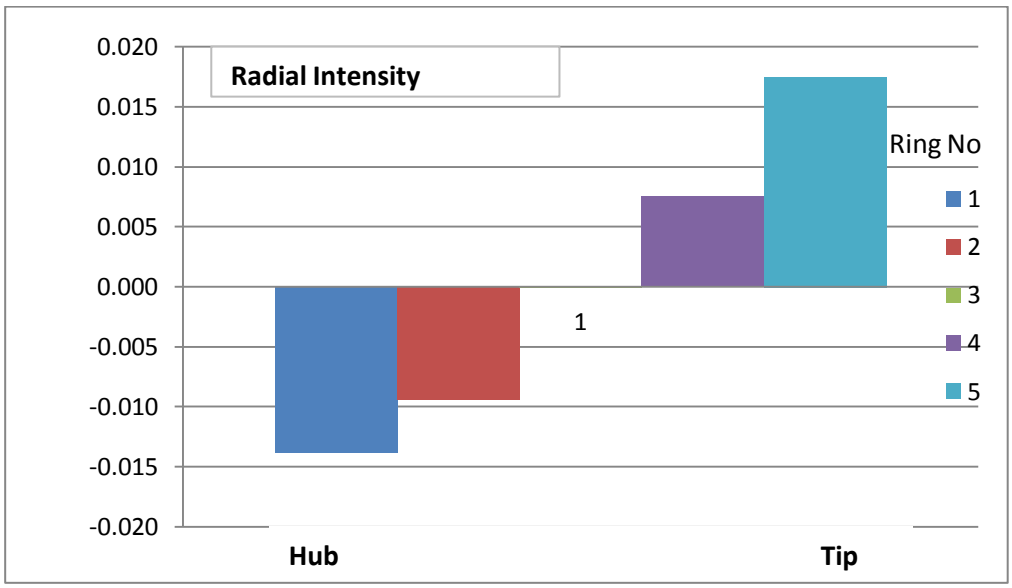

- **0.6M 8˚ AOA 8˚ AOSS**

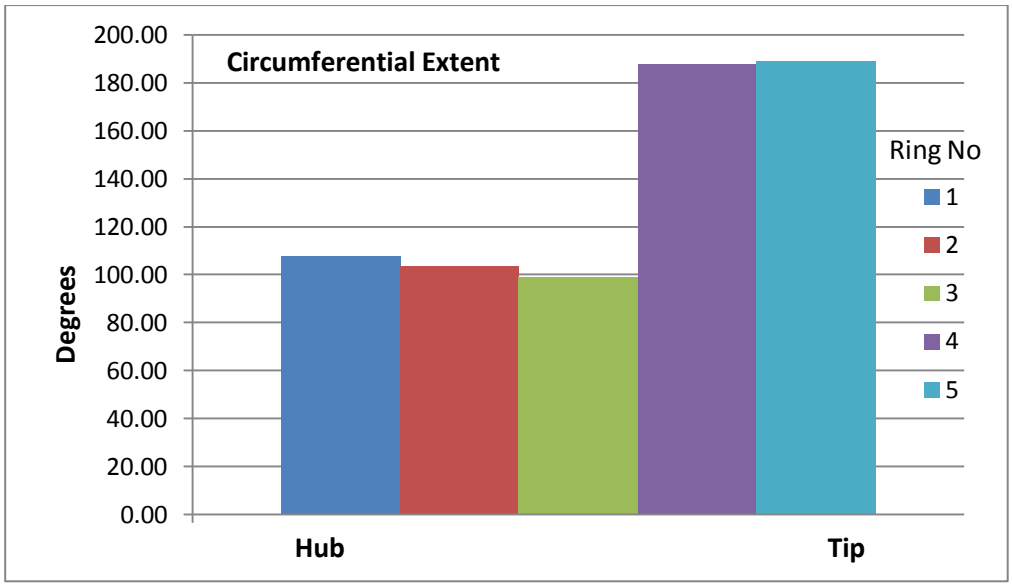

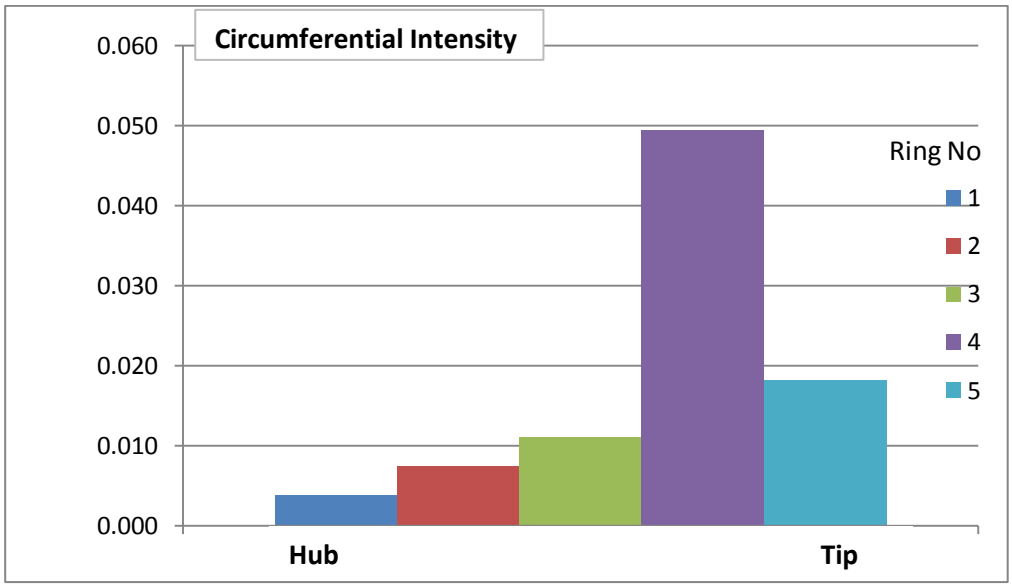

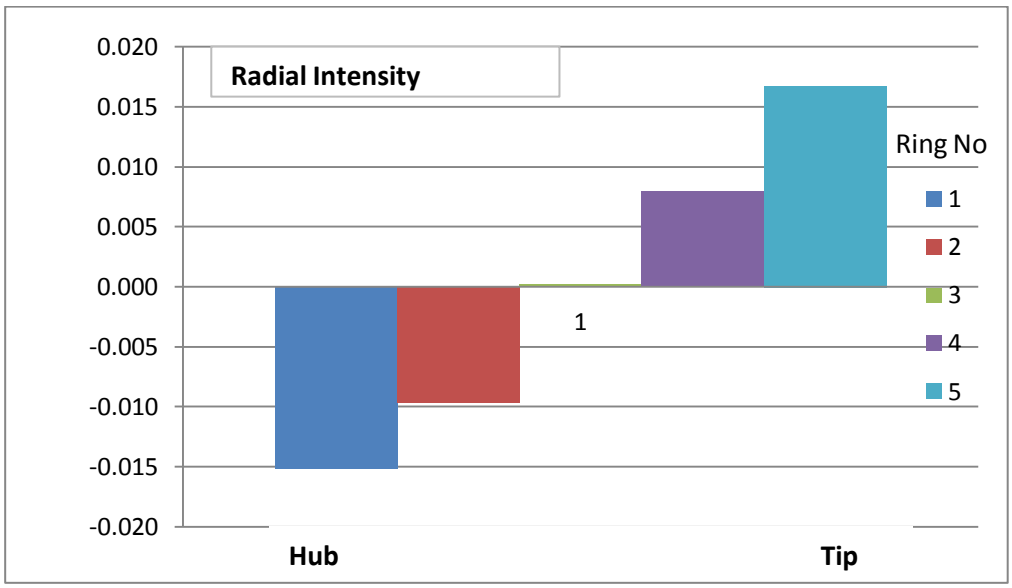

- **0.6M 8˚ AOA 16˚ AOSS**

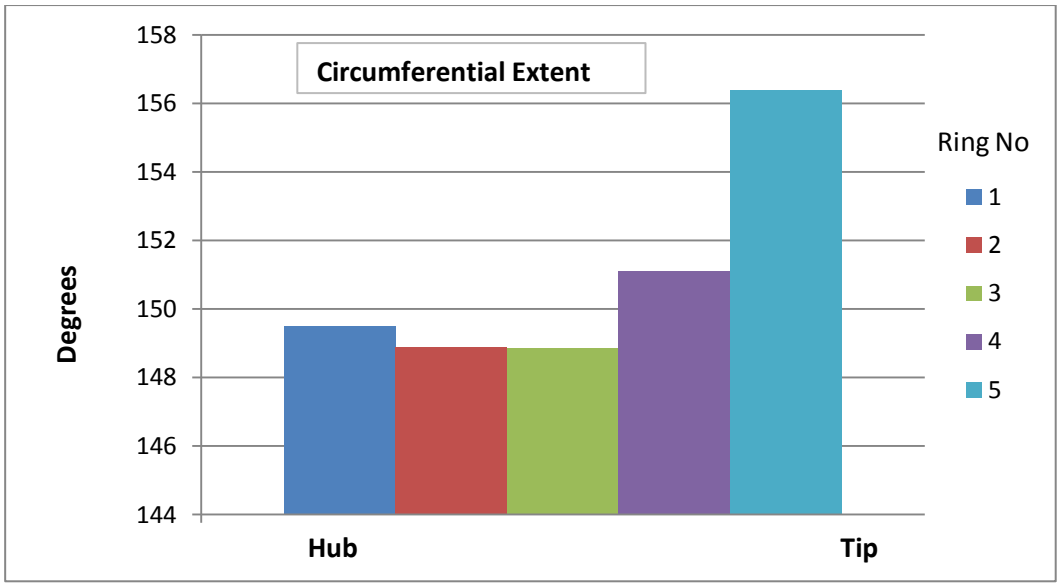

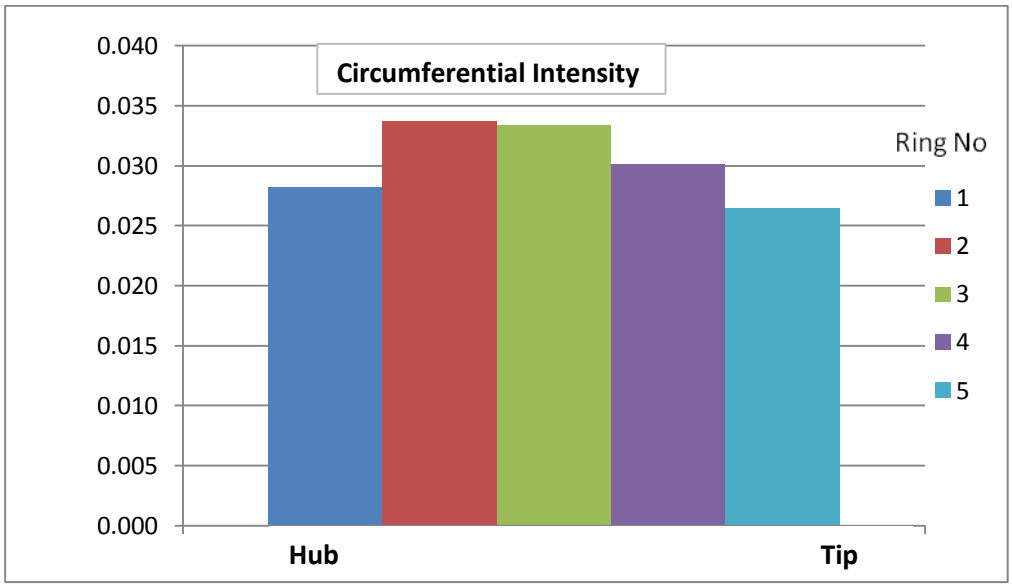

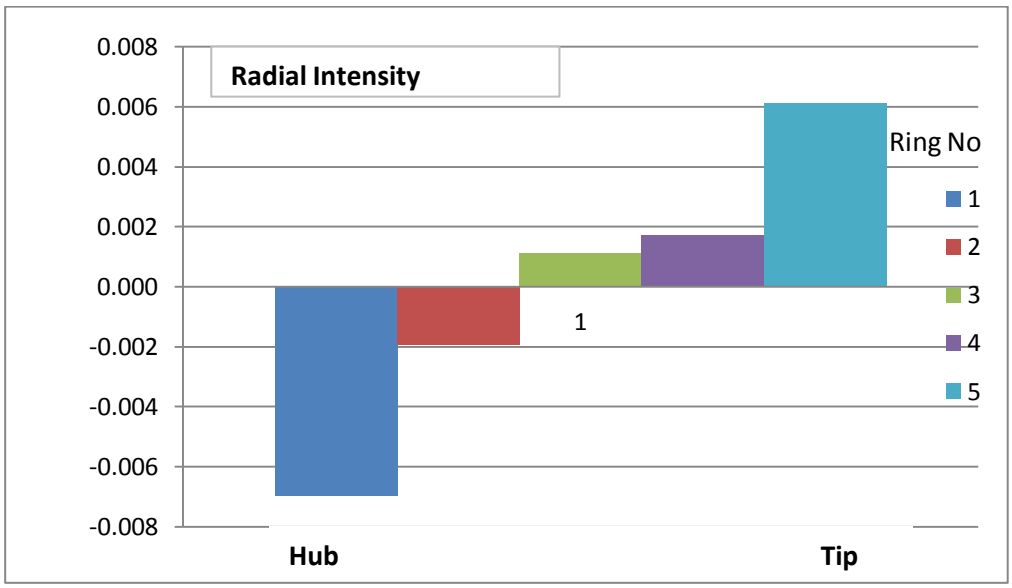

- **0.6M 16˚ AOA 0˚ AOSS**

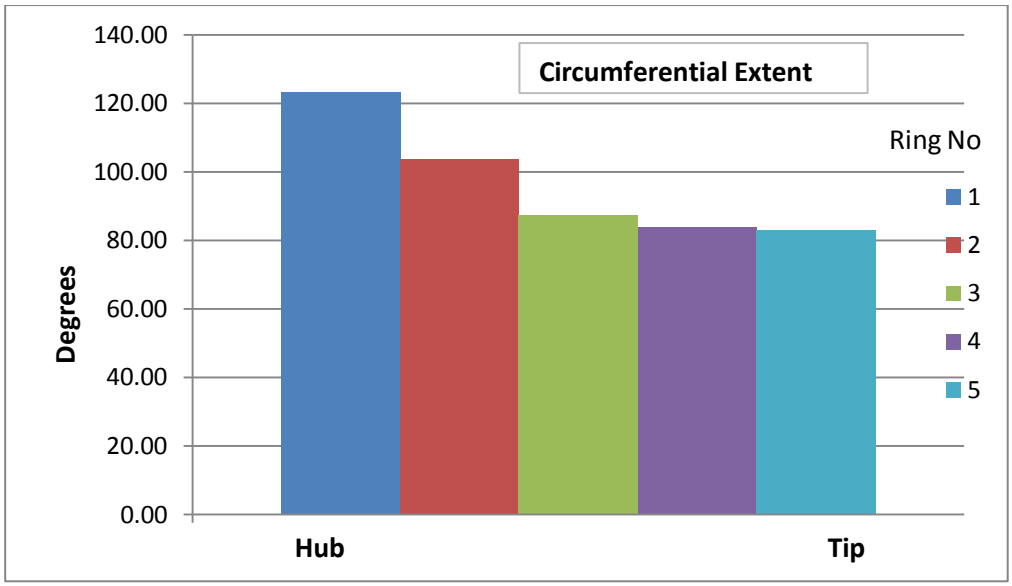

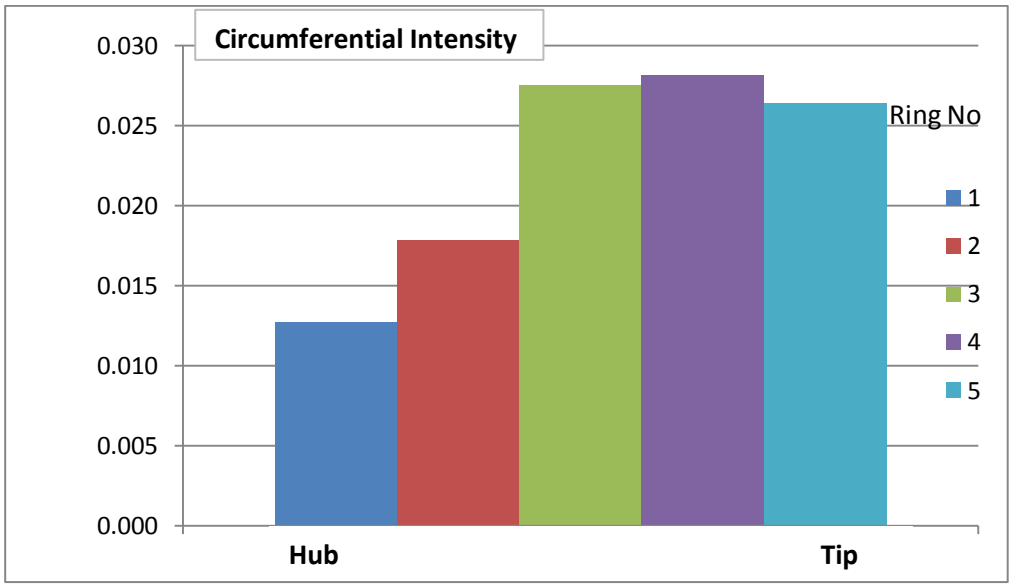

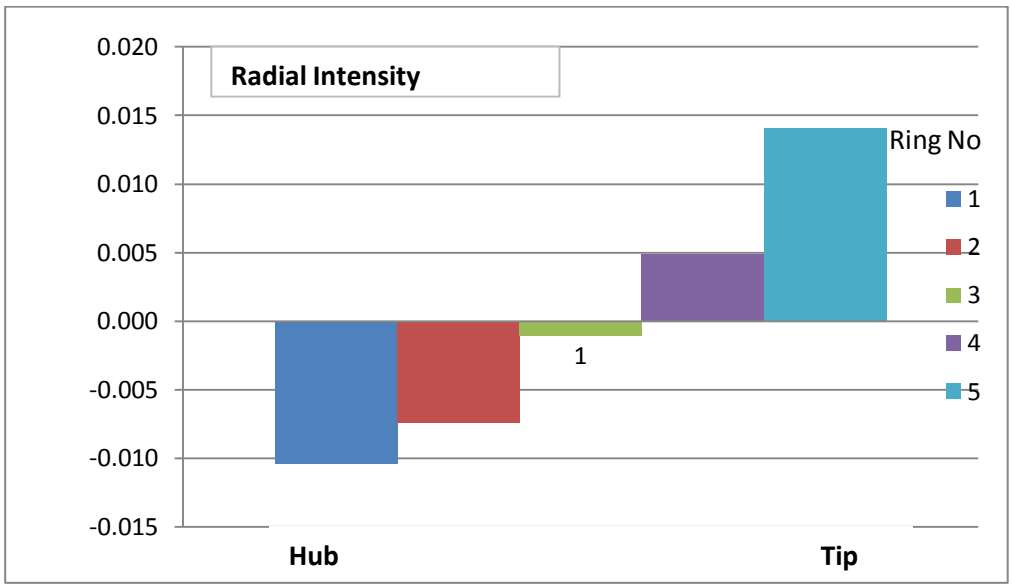

- **0.6M 16˚ AOA 8˚ AOSS**

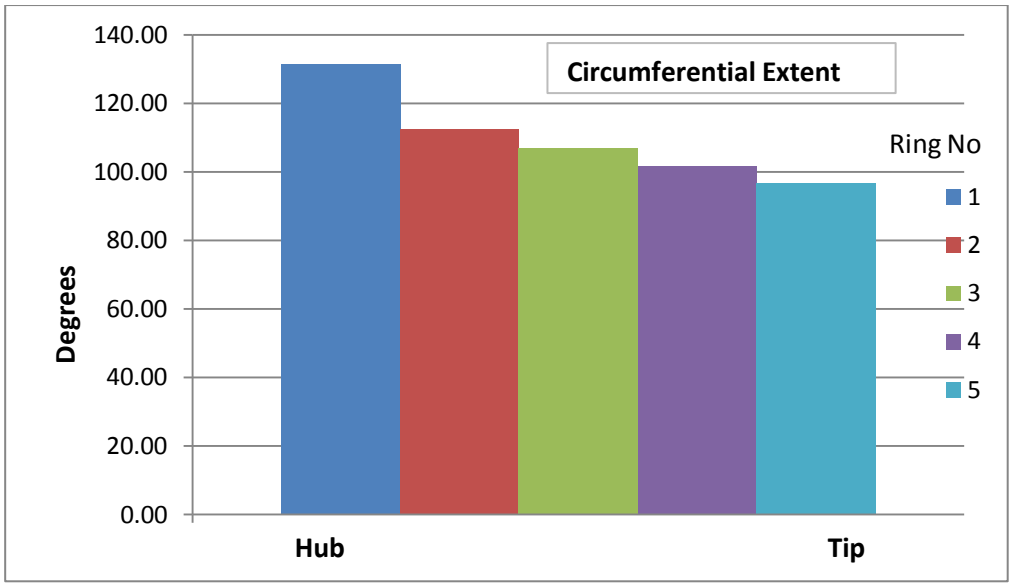

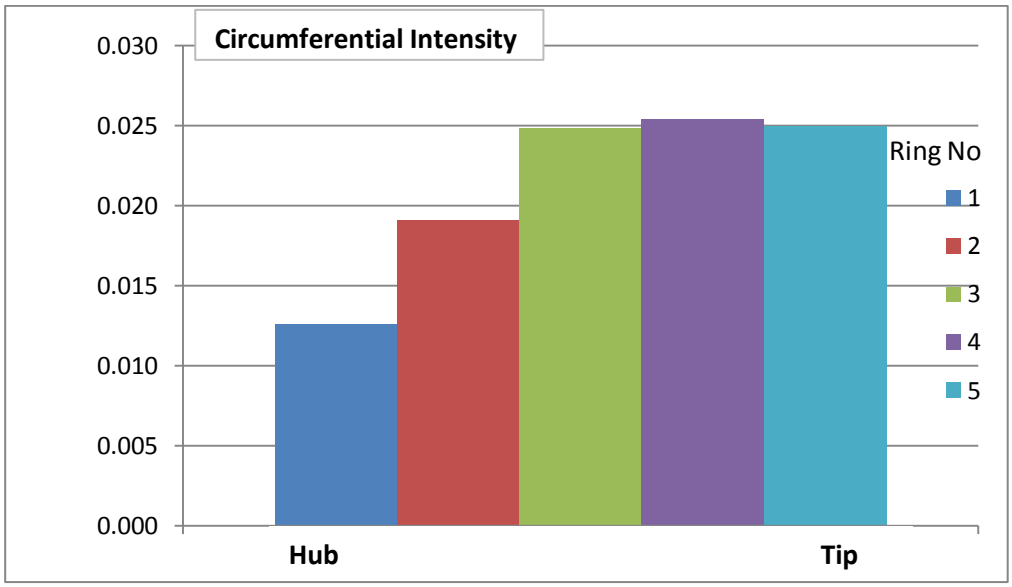

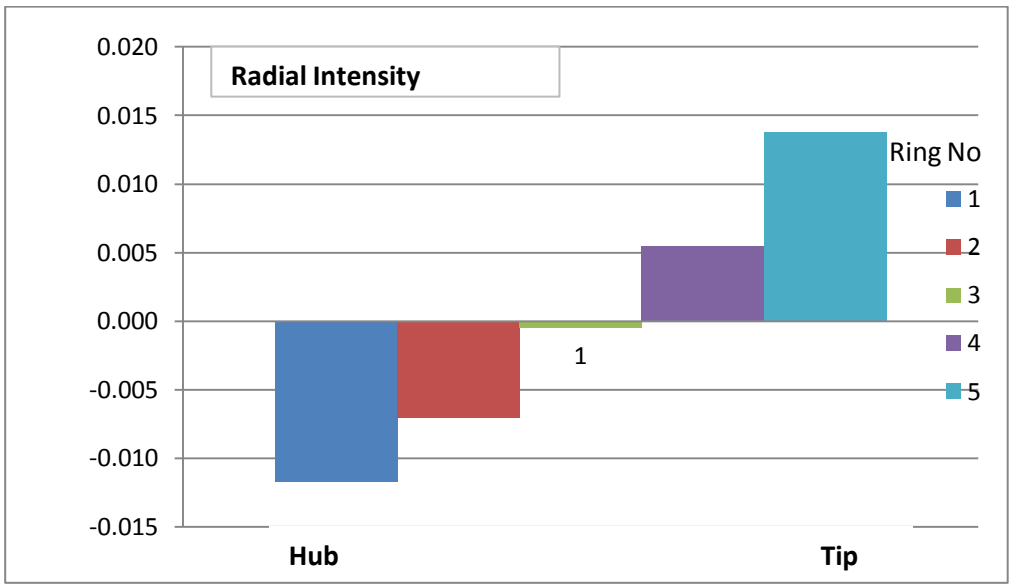

- **0.6M 16˚ AOA 16˚ AOSS**

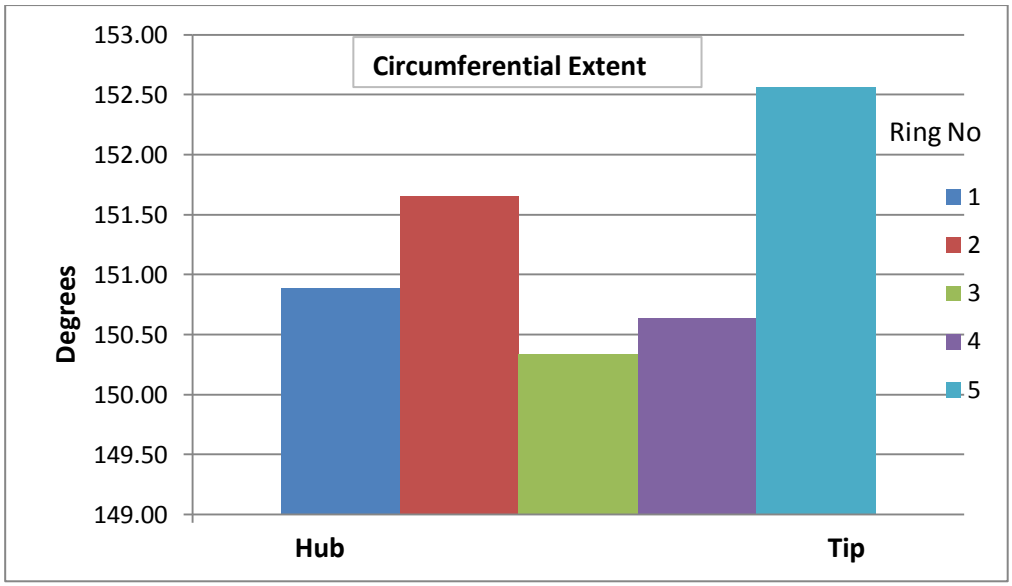

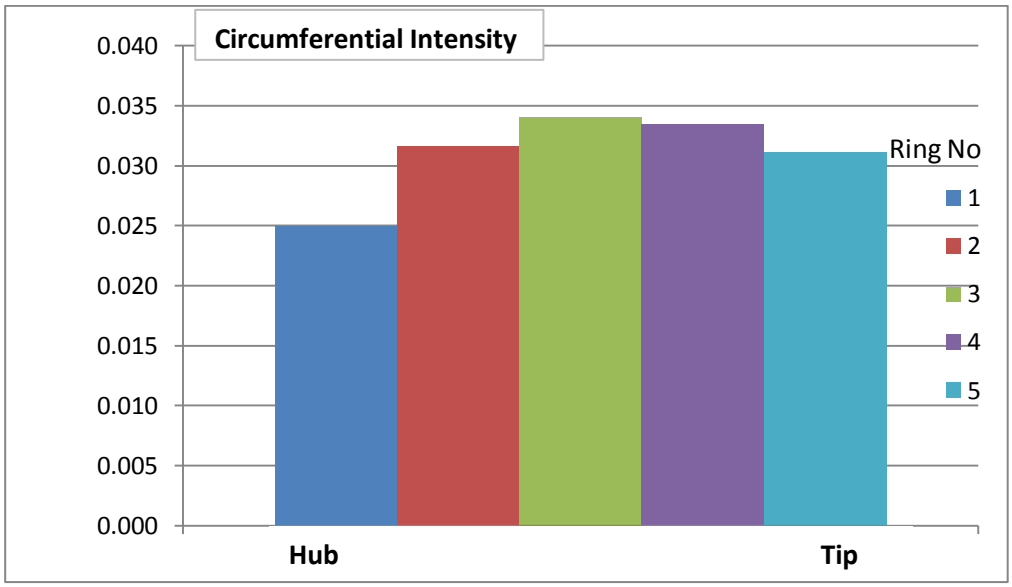

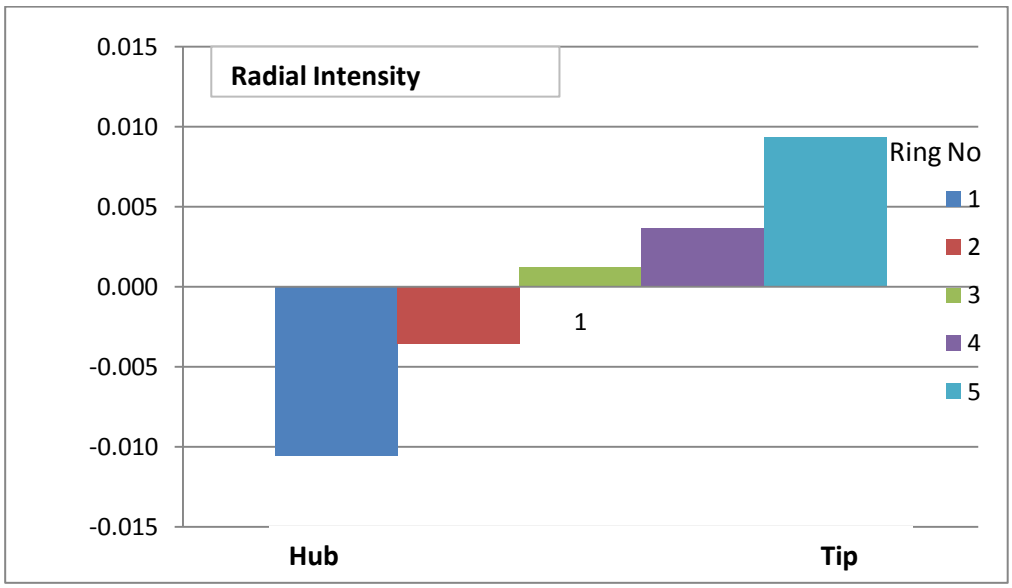

- **0.85M 0˚ AOA 0˚ AOSS**

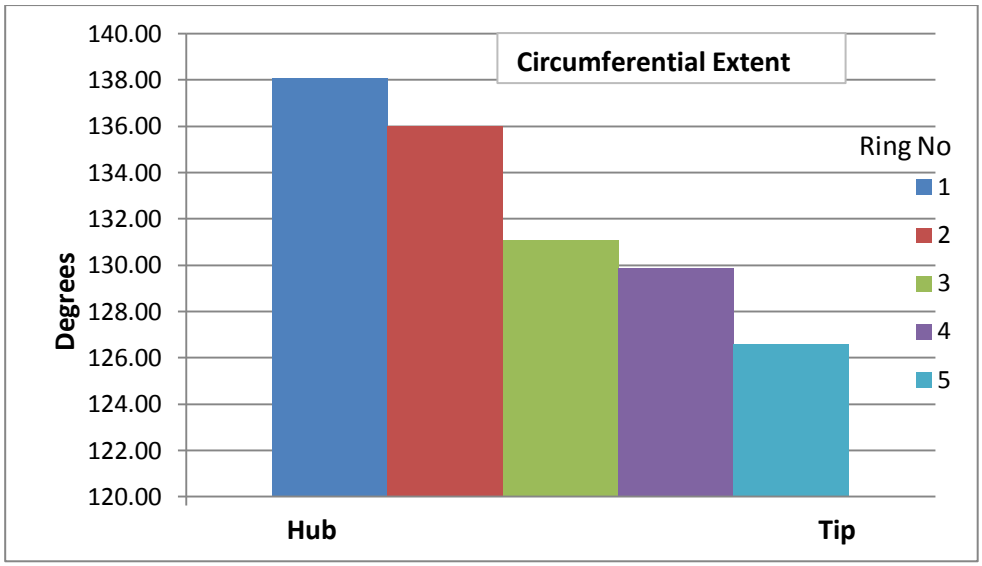

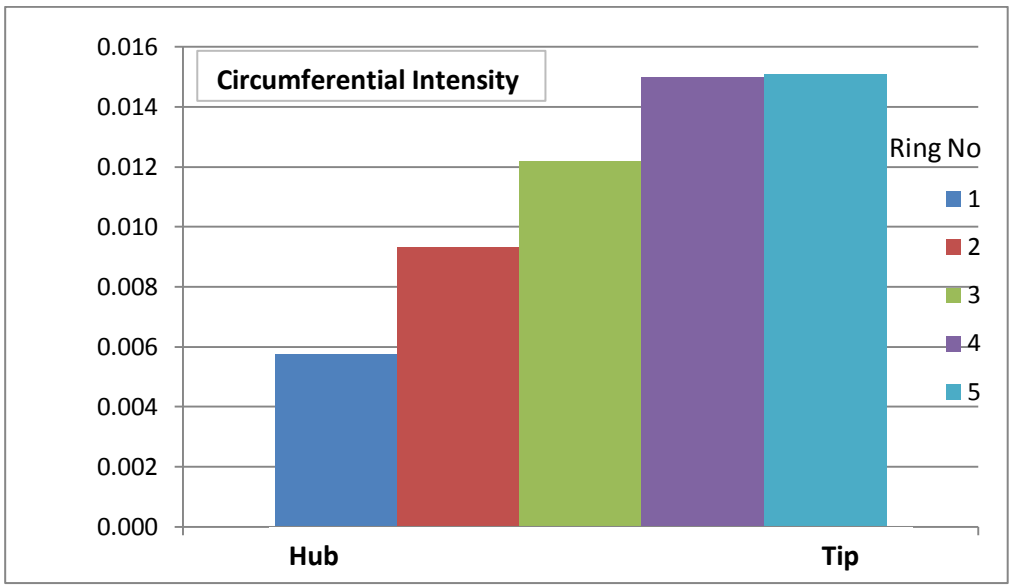

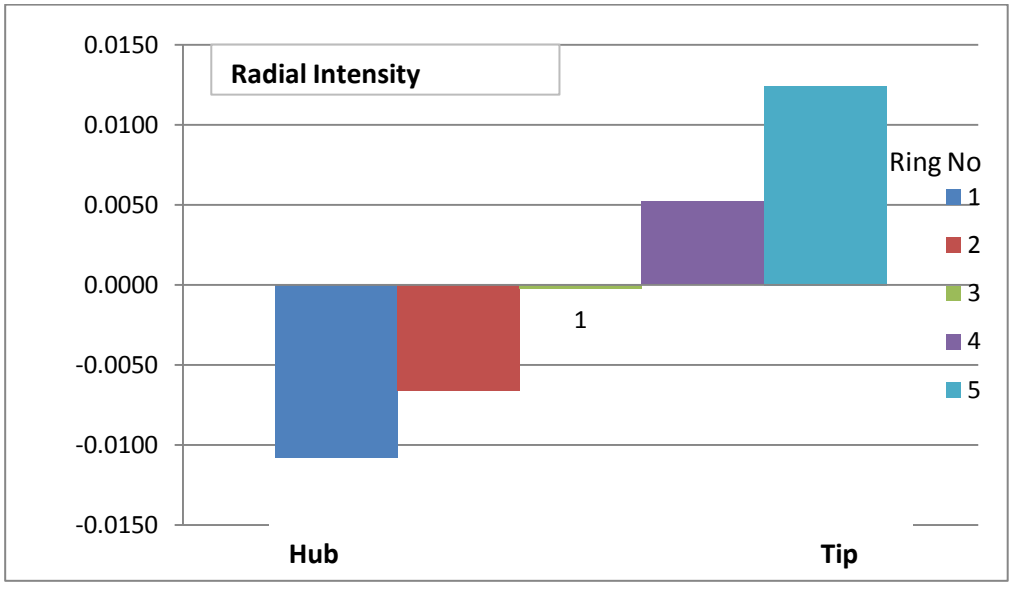

- **0.85M 0˚ AOA 8˚ AOSS**

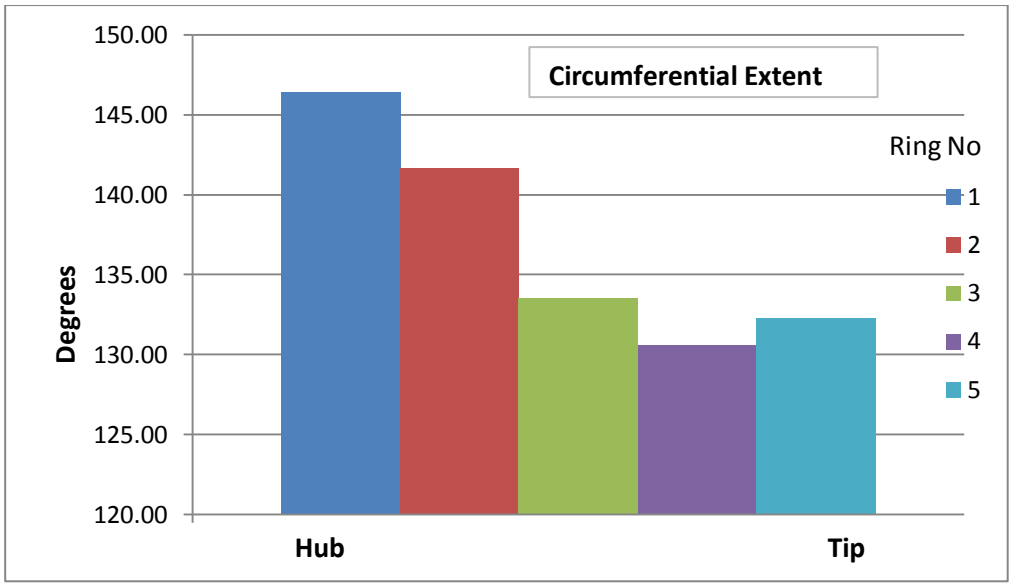

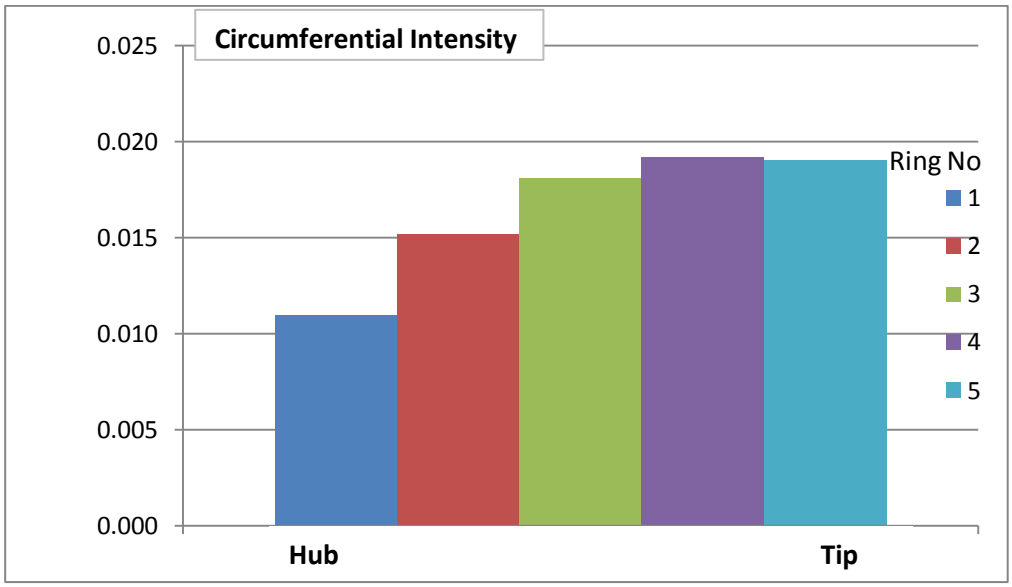

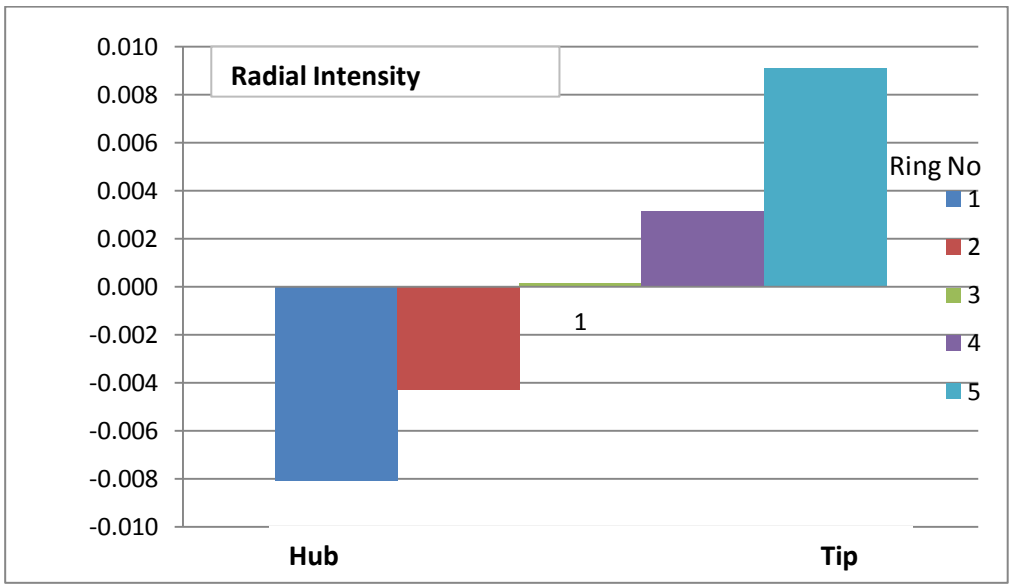

- **0.85M 0˚ AOA 16˚ AOSS**

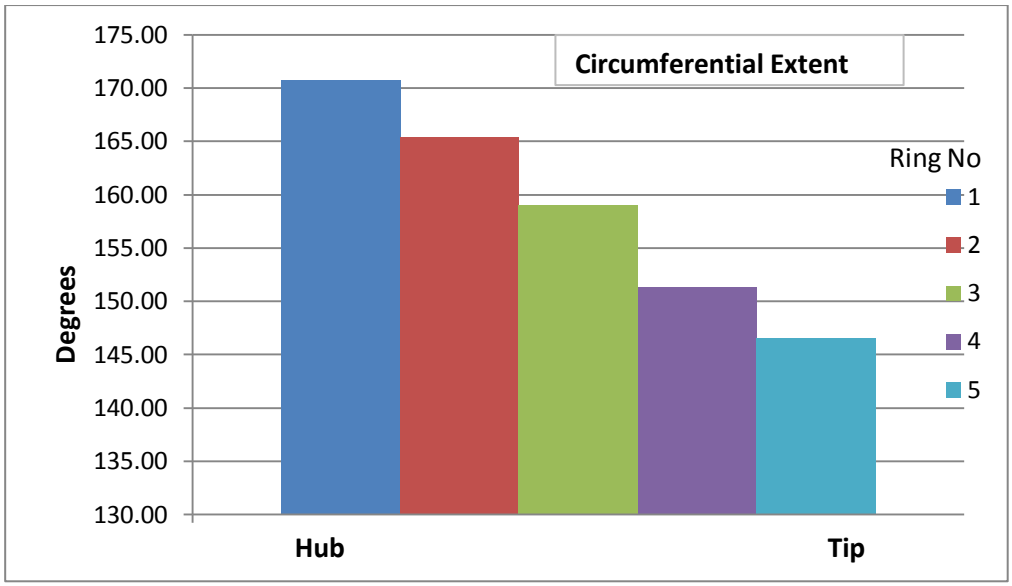

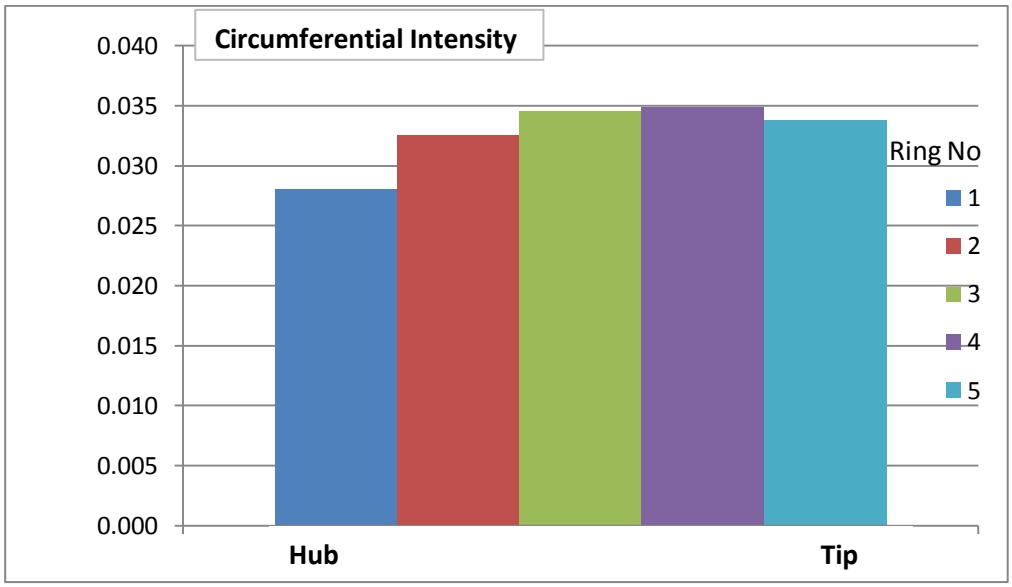

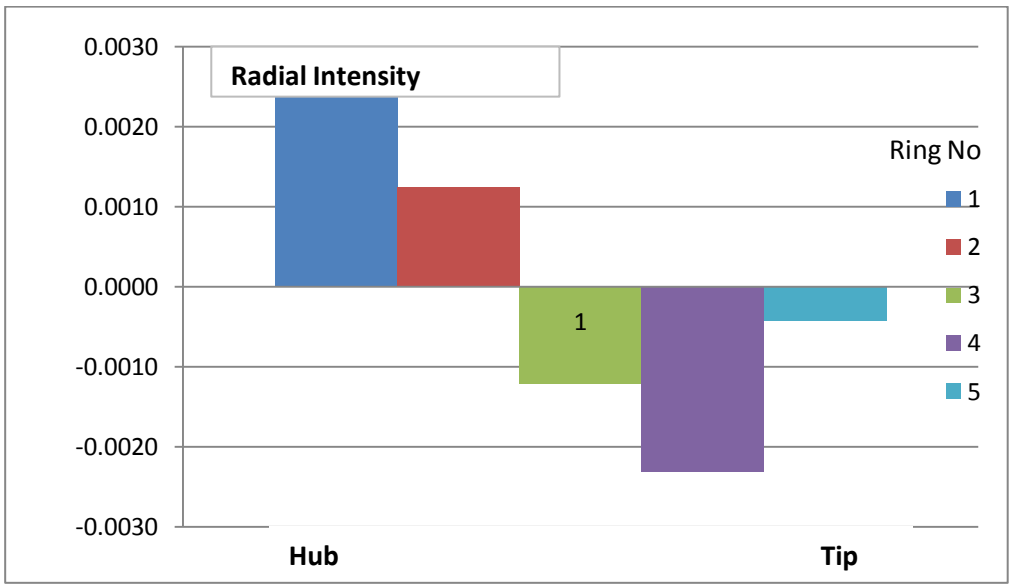

- **0.85M 8˚ AOA 0˚ AOSS**

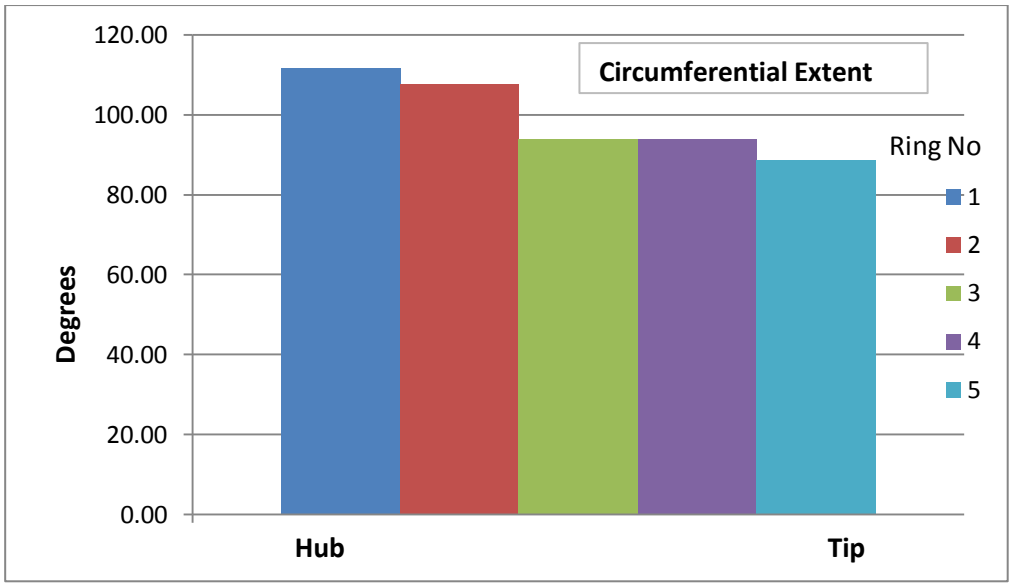

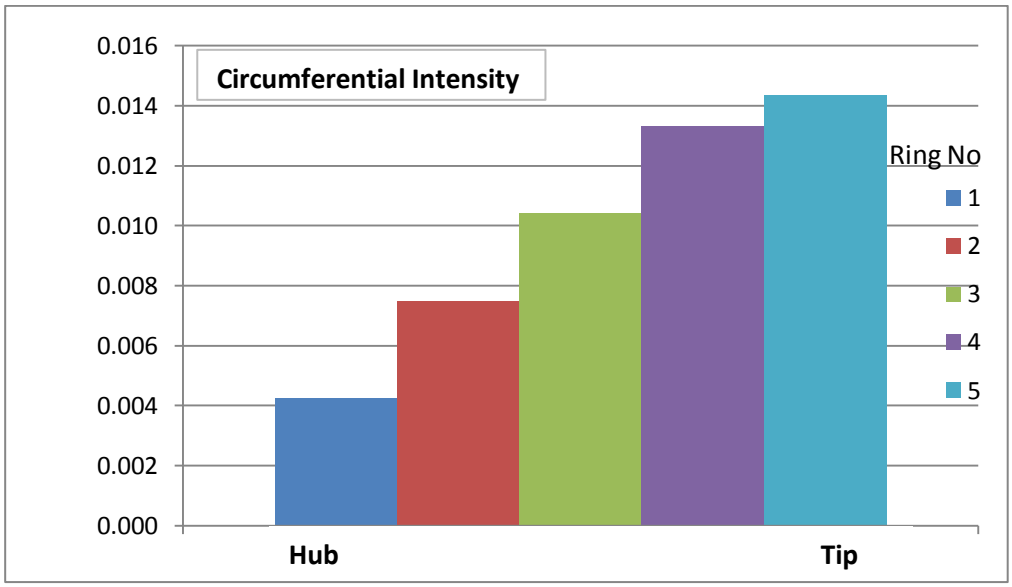

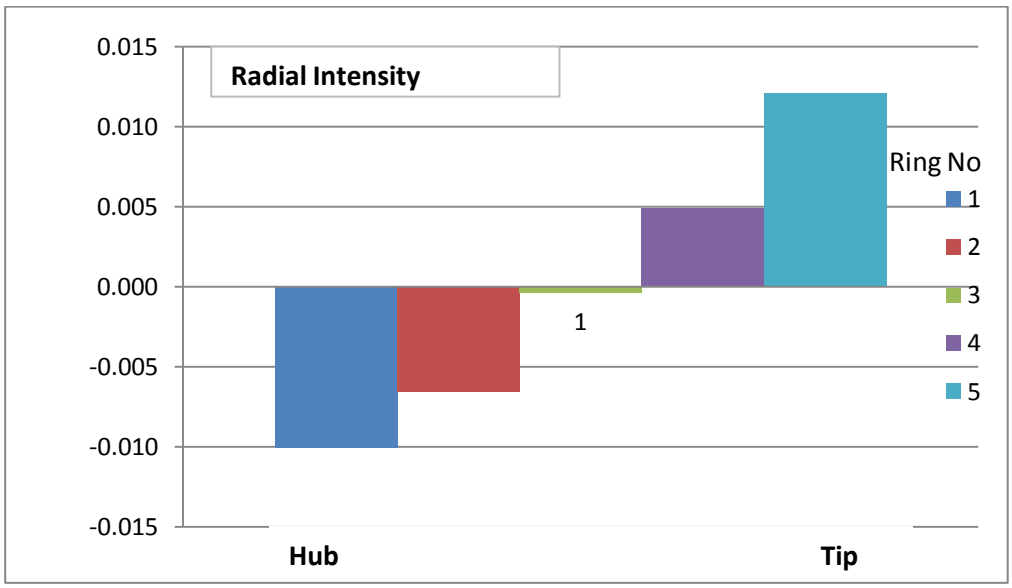

- **0.85M 8˚ AOA 8˚ AOSS**

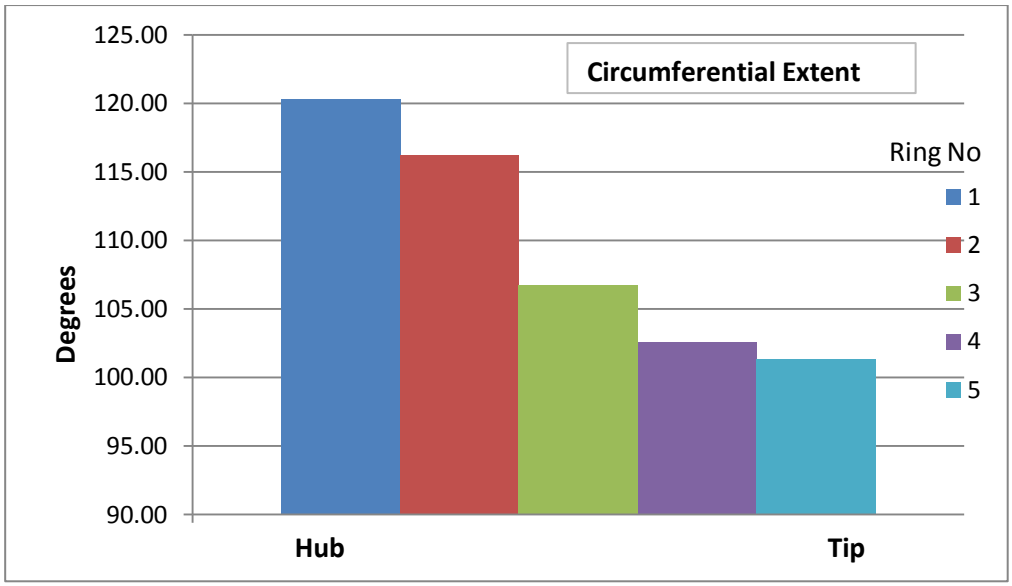

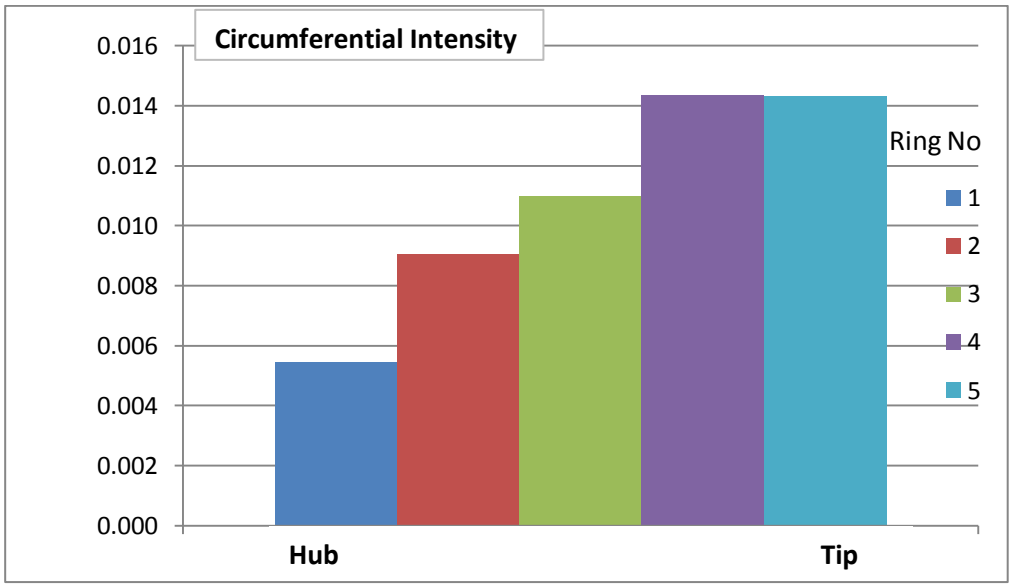

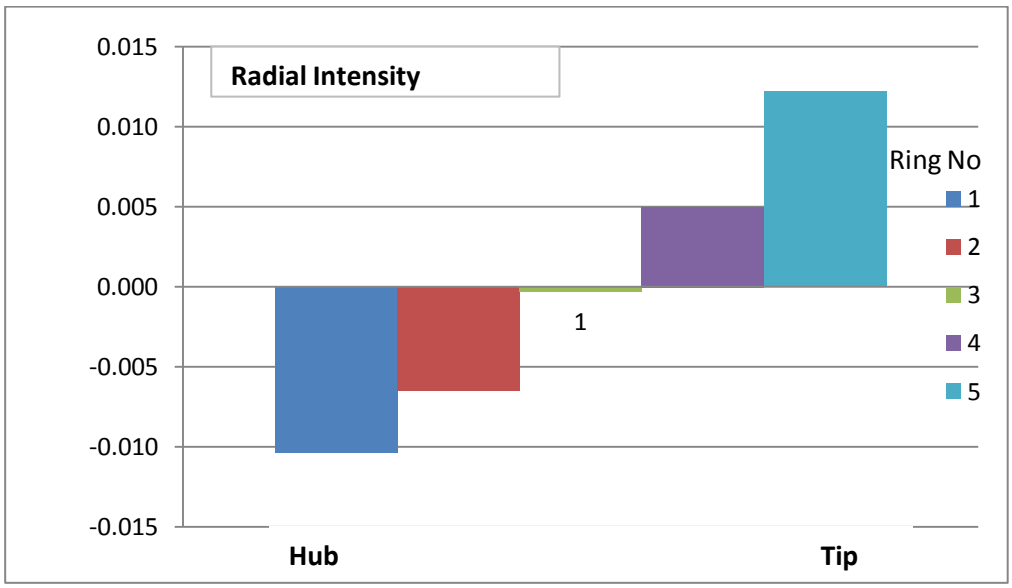

- **0.85M 8˚ AOA 16˚ AOSS**

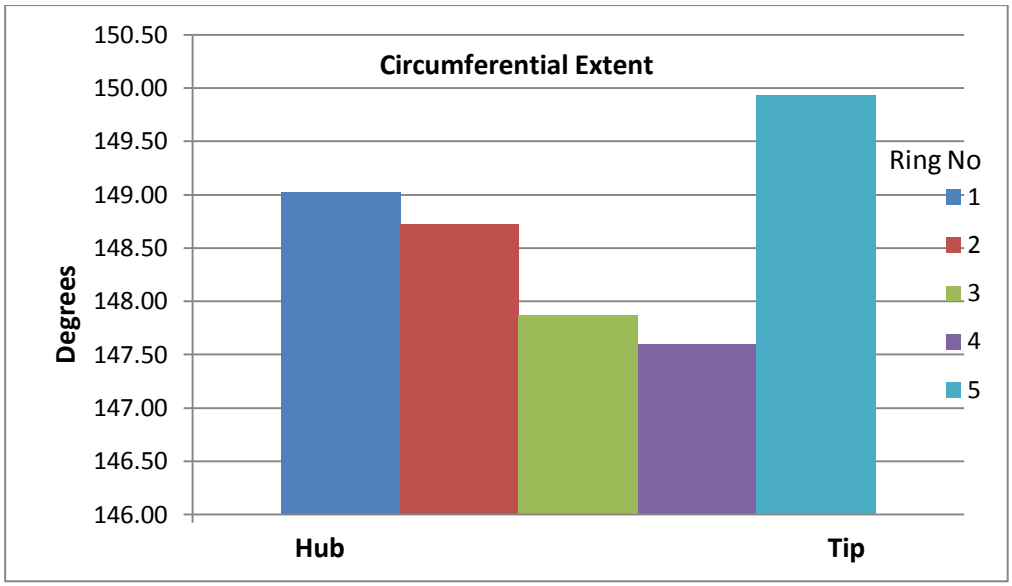

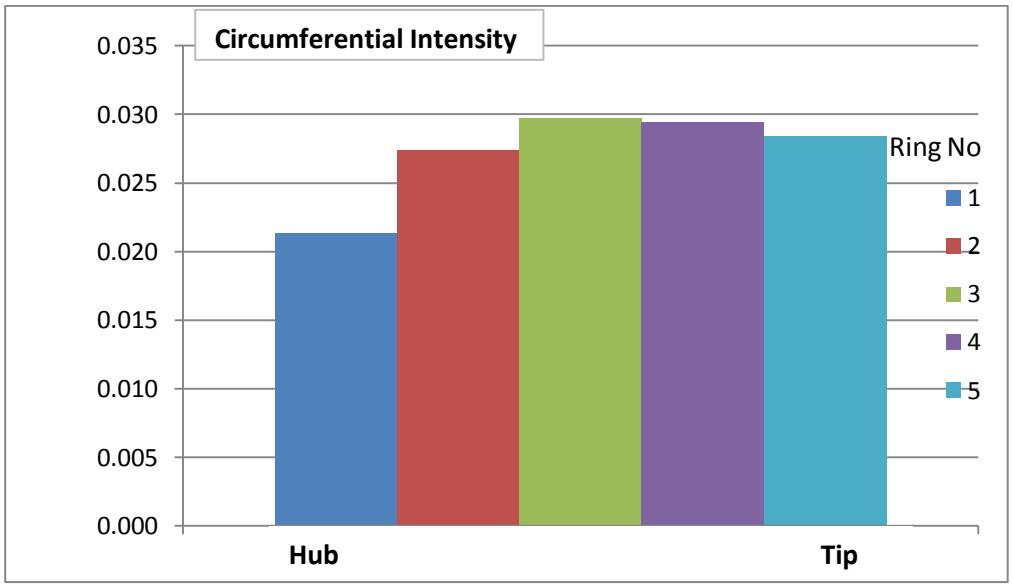

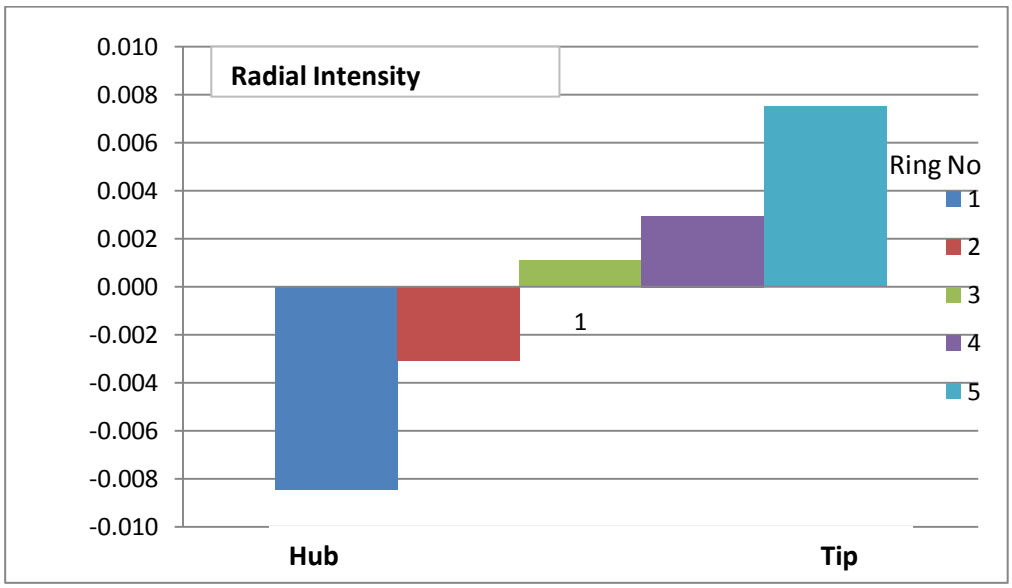

- **0.85M 16˚ AOA 0˚ AOSS**

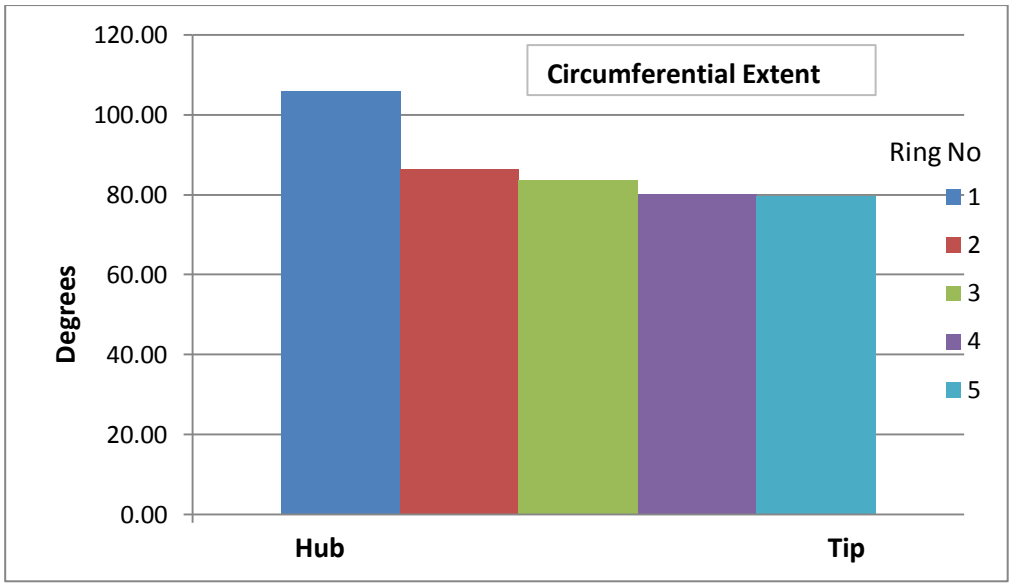

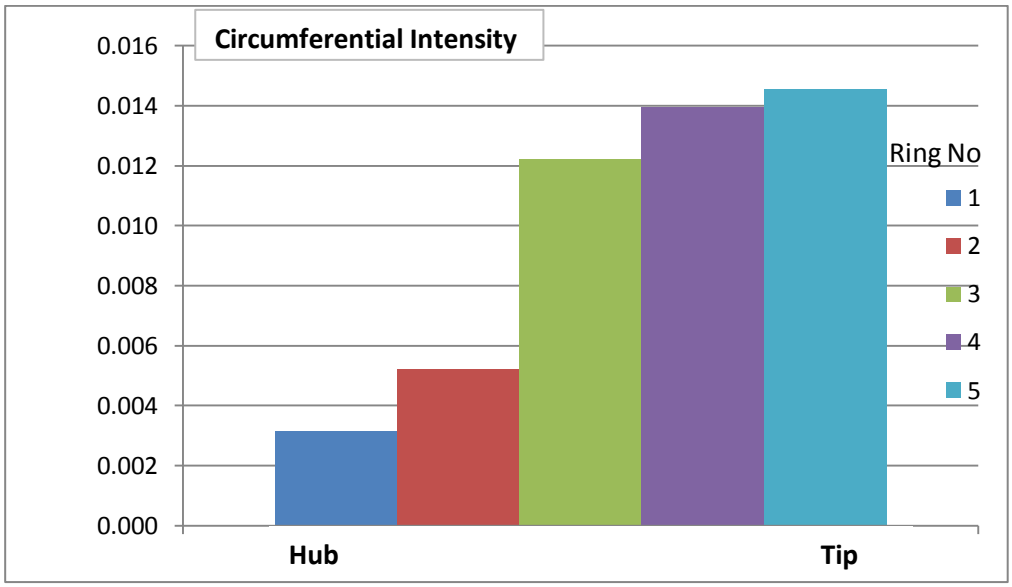

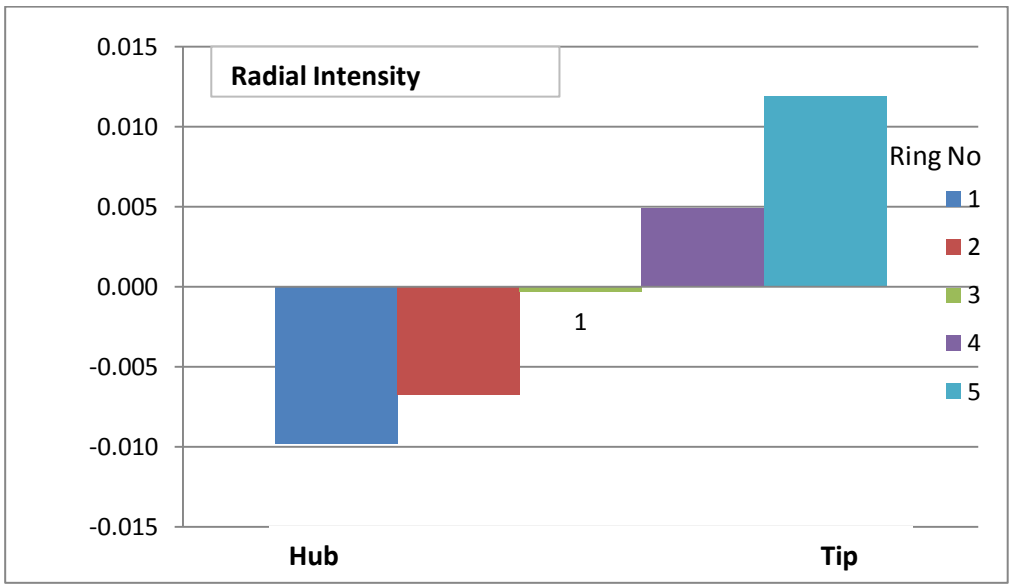

- **0.85M 16˚ AOA 8˚ AOSS**

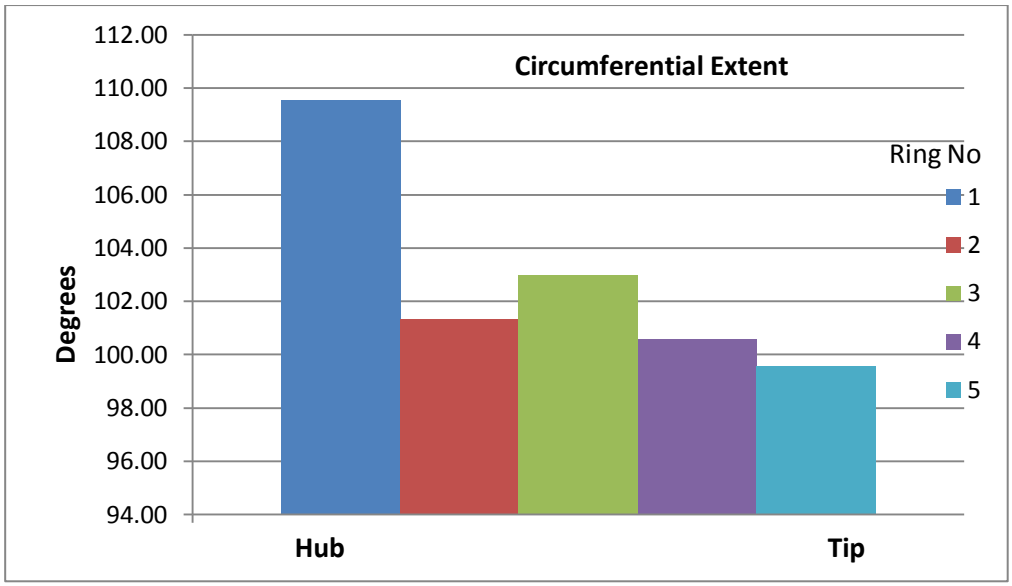

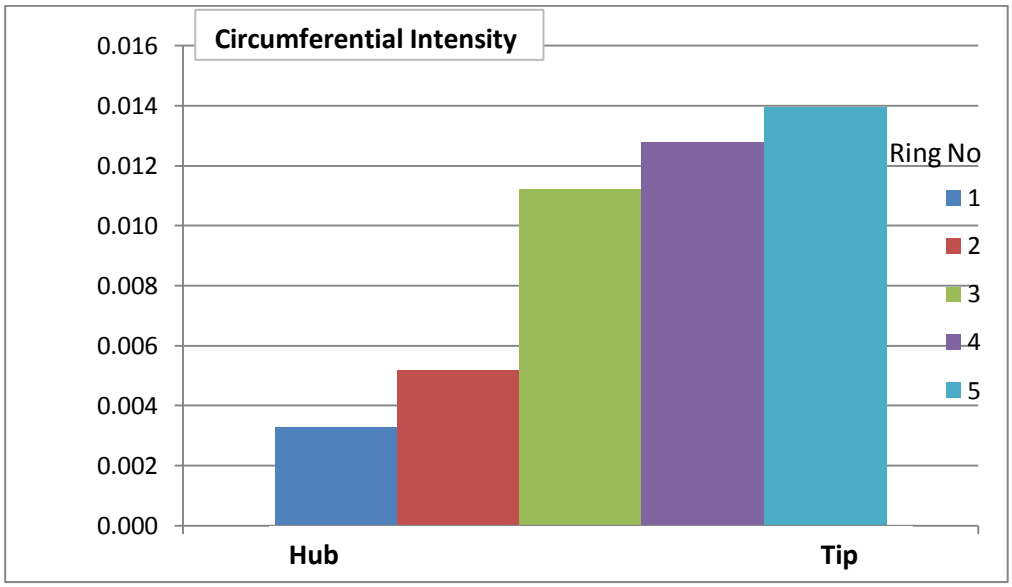

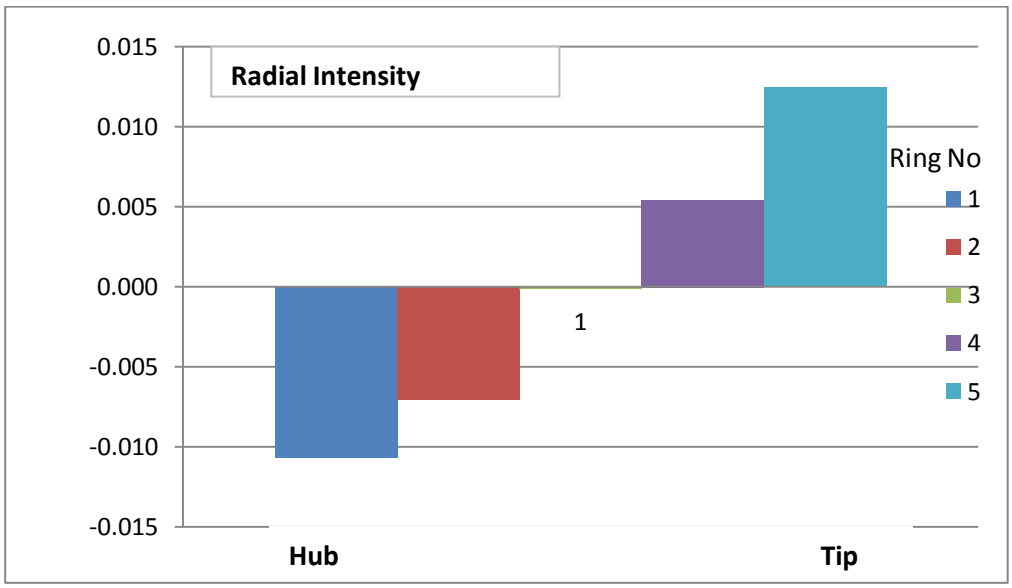

- **0.85M 16˚ AOA 16˚ AOSS**